

Processing, Crystallization and Oxidation of the Ni-Nb(-Sn) Refractory Alloy Glass System

Dissertation

Zur Erlangung des Grades

Doktor der Ingenieurwissenschaften (Dr. -Ing)

der

Naturwissenschaftlich-Technischen Fakultät III Chemie, Pharmazie und
Werkstoffwissenschaften

der

Universität des Saarlandes

vorgelegt von

Sanja Stanojevic

Saarbrücken

2013

Tag des Kolloquiums: 30.10.2013.....

Dekan: Prof. Dr. Volkhard Helms.....

1. Gutachter: Prof. Dr. rer. nat. Ralf Busch.....

2. Gutachter: Prof. Dr.-Ing. Frank Mücklich.....

Vorsitz: Prof. Dr. Ing. Markus Stommel.....

Akad. Mitarbeiter: Dr. Michael Schmitt.....

Abstract

In this work, the topics of processing, crystallization and isothermal oxidation, below the glass transition temperature, of Ni-Nb(-Sn) based bulk metallic glasses are studied. In addition to the as-cast amorphous structures, the thermally treated amorphous structures, as well as the nanocrystalline and microcrystalline structures are studied. Characterizations were conducted by employing various experimental techniques, such as differential thermal analysis, x-ray diffraction, thermogravimetry, electron microscopy and atom probe tomography. The results show that the microcrystalline structures obey purely parabolic laws. The as-cast amorphous structures of $\text{Ni}_{59.35}\text{Nb}_{34.45}\text{Sn}_{6.2}$, $\text{Ni}_{57}\text{Nb}_{34}\text{Sn}_9$ and $\text{Ni}_{58.85}\text{Nb}_{34.45}\text{Sn}_{6.2}\text{Si}_{0.5}$ oxidize in a parabolic manner, while $\text{Ni}_{70}\text{Nb}_{30}$, $\text{Ni}_{62}\text{Nb}_{38}$ and $\text{Ni}_{60}\text{Nb}_{36}\text{Sn}_3\text{B}_1$ oxidize parabolically. The microcrystalline samples have lower parabolic oxidation rates than the as-cast amorphous structures with the same composition. Thermally treated amorphous- and especially the nanocrystalline- structures show significantly better oxidation resistance than the as-cast structures. The oxidation of the amorphous structure is accompanied by crystallization of Ni-rich intermetallics, among which Ni_3Sn is found. Ni_3Sn is not found as a product of devitrification in Ar. The results are discussed in terms of thermodynamics and kinetics of oxidation and crystallization.

Zusammenfassung

Die Themen dieser Arbeit sind die Herstellung, die Kristallisation und das Oxidationsverhalten von Ni-Nb(-Sn)-basierten metallischen Massivgläsern. Die Oxidationsstudien wurden mit Proben amorpher, mikrokristalliner und nanokristalliner Struktur durchgeführt. Als Methoden der Materialcharakterisierungen dienten die Differentialthermoanalyse, Röntgenbeugung, thermogravimetrische Analyse, Elektronenmikroskopie und tomographische Atomsonde. Die Ergebnisse zeigen, dass das zeitliche Oxidationsverhalten bei mikrokristallinen Strukturen parabolischen Gesetzen folgt. Amorphe Proben der Legierungen $\text{Ni}_{59.35}\text{Nb}_{34.45}\text{Sn}_{6.2}$, $\text{Ni}_{57}\text{Nb}_{34}\text{Sn}_9$ und $\text{Ni}_{58.85}\text{Nb}_{34.45}\text{Sn}_{6.2}\text{Si}_{0.5}$ oxidieren nach einem parabolischen Gesetz, während $\text{Ni}_{70}\text{Nb}_{30}$, $\text{Ni}_{62}\text{Nb}_{38}$ und $\text{Ni}_{60}\text{Nb}_{36}\text{Sn}_3\text{B}_1$ parabolischen Zeitgesetzen folgen. Die parabolischen Oxidationsraten der mikrokristallinen Proben sind niedriger als die der amorphen Proben mit gleicher Zusammensetzung. Die thermisch behandelten amorphen Proben sowie die nanokristallinen Proben zeigen einen höheren Oxidationswiderstand als die im Gusszustand amorphen Proben. Die Oxidation amorpher Proben findet mit Kristallisation in Ni-reichen intermetallischen Phasen, insbesondere Ni_3Sn , statt. Bei einer Kristallisation in Ar-Atmosphäre wird die Entstehung von Ni_3Sn nicht beobachtet. Die Ergebnisse werden hinsichtlich kinetischer und thermodynamischer Aspekte diskutiert.

Acknowledgements

My sincerest gratitude goes first of all to my mentor Prof. Dr. Ralf Busch for giving me the opportunity to pursue my doctorate under his guidance, at the Lehrstuhl für Metallische Werkstoffe (LMW) of the Saarland University.

I greatly appreciate the help that Dr. Isabella Gallino has given me throughout all phases of my work.

Special thanks goes to Dr. Zachary Evenson, Dr. F. Aubertin, , Frau M. Stemmler, Dipl.-Ing H. Altmeyer, Herrn J. Eiden, Dipl. Ing. Jörg Schmauch and Metin Sahin who were helping me in different aspects of my work.

I would like to thank, the colleagues from the Lehrstuhl für Funktionswerkstoffe with whom I have collaborated regarding Atom Probe Microscopy experiments, especially M.Sc. Hisham Aboufadel, Dipl. Ing. Jenifer Barrierero and M. Sc. Isabella Schramm

To my colleagues and co-workers at the LMW I would like to thank for their cooperation and the friendship over the last three years.

My graduate work in Saarbrücken would not have been possible without the AMASE Master Program and the financial support provided by the Erasmus Mundus Program. In this regard I would especially like to thank Prof. Dr.-Ing. Frank Mücklich and Dr.-Ing. Flavio Soldera.

I am very grateful for the love and support of my partner Zach.

Thank you

Table of Contents

Abstract	3
Zusammenfassung	4
Acknowledgements	5
1. Introduction	9
2. Theoretical Foundations	11
2.1. Bulk Metallic Glasses.....	11
2.1.1. Thermodynamics and Kinetics of Glass Formation	11
2.1.2. Thermodynamics and Kinetics of Glass Crystallization	15
2.2. Ni-Nb(-Sn) Based Refractory Alloy Glasses	18
2.3. Oxidation	21
2.3.1. Thermodynamics of Oxidation.....	22
2.3.2. Kinetics of Oxidation	23
2.3.3. Initial Stages of Oxidation and Scale Growth	24
2.3.4. Oxidation of Alloys	26
2.3.4.1. Oxidation of Crystalline and Amorphous Alloys	26
3. Experimental Methods	29
3.1. Processing Methods.....	29
3.1.1. Alloying of Pure Elements	29
3.1.2. Suction Casting of Amorphous Specimens	31
3.2. Characterization Methods.....	31
3.2.1. Microscopy	31
3.2.1.1. Scanning Electron Microscopy (SEM).....	31
3.2.1.2. Transmission Electron Microscopy (TEM).....	33
3.2.1.3. Atom Probe Tomography (APT).....	34
3.2.2. X-Ray Diffraction (XRD).....	39
3.2.3. Calorimetry: Differential Thermal Analysis (DTA) and Differential Scanning Calorimetry (DSC)	40
3.2.4. Thermo Gravimetric Method of Oxidation (TGA).....	42
3.3. Sample Treatments	44
4. Results	48
4.1. Amorphous Structure	48
4.1.1. XRD Characterization	48
4.1.2. APT Characterization	50
4.2. Crystallization	52
4.2.1. Calorimetric Characterizations	52
4.2.1.1. Ni-Nb.....	52
4.2.1.2. Ni-Nb-Sn	53

4.2.1.3.	Ni ₆₀ Nb ₃₆ Sn ₃ B ₁	58
4.2.1.4.	Ni _{58.85} Nb _{34.45} Sn _{6.2} Si _{0.5}	60
4.2.2.	XRD Characterizations.....	61
4.2.2.1.	Solidification Structures.....	61
4.2.2.2.	Devitrification Structures.....	62
4.2.3.	Microscopy Characterizations.....	65
4.3.	Oxidation.....	68
4.3.1.	Thermogravimetric Characterizations.....	68
4.3.1.1.	Oxidation of Ni-Nb.....	68
4.3.1.2.	Oxidation of Ni-Nb-Sn.....	69
4.3.1.3.	Oxidation of Ni ₆₀ Nb ₃₆ Sn ₃ B ₁	73
4.3.1.4.	Oxidation of Ni _{58.85} Nb _{34.34} Sn _{6.2} Si _{0.5}	75
4.3.2.	XRD Characterizations.....	77
4.3.3.	Microstructure Characterizations.....	81
4.3.3.1.	Binary Ni-Nb Alloys.....	81
4.3.3.2.	Microstructure of the Oxidized Ternary Ni-Nb-Sn Alloys.....	83
4.3.3.3.	Microstructure of the Oxidized Quaternary Ni _{58.85} Nb _{34.45} Sn _{6.2} Si _{0.5} Alloy.....	93
4.3.3.4.	Microstructure of the Oxidized Quaternary Ni ₆₀ Nb ₃₄ Sn ₃ B ₁ Alloy.....	94
4.3.4.	Calorimetric Characterizations of the Oxidized Ni-Nb-Sn Alloys.....	96
4.3.5.	Atom Probe Microscopy Characterization of the Oxidized Ni-Nb-Sn RAG Alloys.....	97
5.	Discussion.....	100
5.1.	Processing.....	100
5.2.	Crystallization.....	101
5.2.1.	Solidification.....	101
5.2.2.	Amorphous Structure and Devitrification.....	104
5.2.2.1.	Devitrification of binary Ni-Nb Alloys.....	104
5.2.2.2.	Amorphous Structure of Ternary Ni-Nb-Sn Alloys.....	106
5.2.2.3.	Devitrification of Ni-Nb-Sn Based Alloys.....	107
5.3.	Oxidation.....	113
5.3.1.	Oxidation of the Binary Ni-Nb RAG.....	116
5.3.2.	Oxidation of the Amorphous Ni-Nb(-Sn) Based Alloys.....	120
5.3.2.1.	Driving Forces for Nucleation of Different Phases at the Oxidation Front....	122
5.3.2.2.	Oxidation Mechanism.....	124
5.3.2.3.	Influence of the Thermal Treatment on the Oxidation Behavior of the Amorphous Structure.....	126
5.3.3.	Oxidation of the Quaternary Ni-Nb-Sn-X (X=Si, B).....	128
5.3.4.	Oxidation of the Micro- and Nanocrystalline Ni-Nb-Sn Alloys.....	130
6.	Conclusions.....	133
	Appendix.....	136
A1.	Suction Casting - Experimental Difficulties.....	136
A2.	Gibbs Free Energy Functions and Coefficients.....	139
A3.	XRD Pattern of Different Phases.....	141
A4.	XRD Pattern of the Oxidized Ni _{59.35} Nb _{34.45} Sn _{6.2} Alloy.....	143

A5. Overview on E_a of Various Processes	146
Reference List	148

1. Introduction

The first metallic alloy to be successfully formed into an amorphous, 10 μm thick foil, was the binary Au-Si eutectic alloy in 1960 [1]. An extremely high cooling rate of 10^6 K/s, achieved by splat-quenching, was necessary in order to bypass the crystallization of the undercooled liquid and form a glass. The intensive research that followed during the 1970s and the 1980s has led to the discovery of new compositions, requiring much lower cooling rates on the order of 100 K/s to 0.1 K/s. This new class of bulk metallic glasses (BMGs) can be characterized as having, in general, critical casting thicknesses greater than ~ 1 mm. As a further result, the easily processable Zr-based BMGs (Vitreloy) [2] have recently been commercially produced in bulk dimensions for various technological applications (cell phone-, computer- or golf club parts). It is of general interest to expand the field of application to other compositions, where the alloys of so-called common materials like Fe, Ni, and Co, to name a few, are of special interest. In terms of technological application, characteristics of BMGs such as large critical casting thicknesses, advantageous mechanical properties, a large and stable supercooled liquid region and resistance to oxidation have to be taken into consideration.

Among Ni-based BMGs, the family of Ni-Nb-Sn based alloys was extensively studied [3–10] in the first decade of 21st century. Compared to critical casting thicknesses (t_c) of some BMGs, like the Zr-based Vitreloy 1 ($\text{Zr}_{41.2}\text{Be}_{22.5}\text{Ti}_{13.8}\text{Cu}_{12.5}\text{Ni}_{10}$) (25 mm [11,12]) or the Pd-based $\text{Pd}_{40}\text{Cu}_{30}\text{Ni}_{10}\text{P}_{20}$ (72 mm [13–15]), the critical thicknesses of Ni-Nb(Sn) based BMGs are relatively low. The reported t_c for the binary Ni-Nb is close to 2 mm, for the ternary Ni-Nb-Sn 2–3 mm and up to 4 mm in the quinary Ni-Nb-Sn-Hf-Co [3,16,17]. These relatively low critical casting thicknesses are one of the main limiting factors for the application of the alloy systems based on Ni-Nb. On the other hand, very high hardnesses (up to 1280HV), estimated yield strengths (up to 3.8 GPa) and elastic moduli (up to 200 GPa) have been reported for this particular BMG family [5], making them especially interesting for technological applications. In addition to this these alloys possess a generally very high glass transition temperature, T_g (~ 895 K), which is almost 200 K greater than that of Zr-based BMGs. The application of BMG alloys based on Ni-Nb-Sn can therefore be found not only at room temperatures but also up to much higher temperatures of around 873 K.

In this thesis the topics of processing, crystallization and oxidation behavior of the Ni-Nb(-Sn) family of BMG-forming alloys will be introduced and discussed, with emphasis on the phenomenon of oxidation-induced crystallization from the glassy state. Section 5.1 discusses processing using arc-melting and suction casting methods. In particular, the effectiveness and potential problems when using these methods for alloying Ni-Nb-Sn alloys will be discussed. The

main part of this study will be dedicated to characterization and interpretation of the crystallization and oxidation behavior of Ni-Nb(-Sn) alloys, employing the use of various experimental techniques, such as Differential Thermal Analysis (DTA), thermogravimetry (TGA), optical and electron microscopy methods, as well as Atom Probe Microscopy. The crystallization behavior will be characterized in terms of solidification through crystallization from the melt and in terms of crystallization from the glassy state (devitrification). The isothermal oxidation behavior is studied using TGA, at different temperatures below the T_g , under a flow of dry oxygen. The results will be discussed in terms of thermodynamics and kinetics, with special attention being devoted to establishing the interaction between oxidation and crystallization. In addition to the as-cast amorphous structures of different Ni-Nb(-Sn) compositions, namely binary Ni-Nb, ternary Ni-Nb-Sn and the quaternary Ni-Nb-Sn-Si and Ni-Nb-Sn-B families, the oxidation behavior of different thermally treated amorphous structures, as well as the nanocrystalline and microcrystalline structures are studied and compared with that of the corresponding as-cast amorphous structures.

2. Theoretical Foundations

2.1. Bulk Metallic Glasses

The amorphous structure of BMGs can be characterized by lacking the long-range periodicity that is common to conventional crystalline materials. BMGs represent a relatively newly discovered group of materials in the much larger group of structural amorphous solids, to which silicate glasses and most polymers belong. Amorphous alloys are typically produced by quenching from the molten state but other production paths, like solid-state amorphization or vapor deposition, can also be used. Due to the structural similarities with the liquid, the glassy structure is often referred to as being “frozen-in” from the undercooled liquid.

2.1.1. Thermodynamics and Kinetics of Glass Formation

The phase transformation from a crystalline solid to non-crystalline liquid (melt) is referred to as melting and, in the case of a pure metal, this occurs at a well defined melting temperature, T_m . Since even many pure metals can be undercooled from the liquid state [18], the solidification temperature is not in these cases well-defined. In the case of multicomponent metallic systems (alloys), the melt and crystalline fractions of the solid can coexist within a certain temperature interval between the T_m and liquidus temperature, T_l . T_l represents the maximum temperature at which the solid crystals are still stable in melt. Upon slow (equilibrium) cooling, the solidification process starts when temperature reaches the T_l and ends at T_m . To cool liquid below T_l without crystallizing is referred to as the process of undercooling and the undercooled melt is considered to be in metastable equilibrium. In terms of the Gibbs free energy of the system, a metastable equilibrium represents local minimum value of the Gibbs free energy, for which the system stays stable against small compositional fluctuations but will generally tend to transform to a state corresponding to a global Gibbs free energy minimum, if enough time is allowed for.

At temperatures below T_l , the Gibbs free energy of the solid phase, $G^S(T)$, becomes lower than that of the liquid, $G^L(T)$. If the melt is undercooled by ΔT , the process of solidification then corresponds to a Gibbs free energy decrease, which can be approximated as the driving force for solidification [19]:

$$\Delta G^{L-S}(T) = G^L(T) - G^S(T), \quad (1)$$

The process of solidification begins by formation of solid phase nuclei in the melt. The formation of solid phase nuclei results in free energy change [19]:

$$\Delta G = -V_S \Delta G_V + A_{SL} \gamma_{SL} \quad (2)$$

$$\Delta G_V = G_V^L - G_V^S, \quad (3)$$

where V_S is the volume of the solid nuclei, A_{SL} and γ_{SL} are the solid/melt interfacial area and the interfacial free energy, respectively. G_V^L and G_V^S are the free energies per unit volume of solid and melt. Assuming a spherical shape of the solid nuclei with a radius r , Eq. (2) becomes:

$$\Delta G_n = -\frac{4}{3} \pi r^3 \Delta G_V + 4 \pi r^2 \gamma_{SL}, \quad (4)$$

Eq. (4) shows that the term connected to the volume free energy changes with r^3 and the term connected to interfacial energy with r^2 . Therefore, for some given undercooling ΔT , there is a radius r^* , for which ΔG_n has a maximum value. This value is referred to as nucleation barrier (ΔG^*) and r^* as the critical nucleus radius. Only solid particles with $r > r^*$ will further grow in the melt, since as a result the free energy of the system will decrease. Conversely, for values of $r < r^*$, such nuclei will dissolve back into the melt.

Since for $r = r^*$, ΔG_n has a maximum ($dG=0$), and by employing approximation [19]:

$$\Delta G_V = \frac{\Delta H_f \Delta T}{T_l}, \quad (5)$$

where ΔH_f is a latent heat of fusion per unit volume, the expressions for ΔG^* and r^* are obtained as:

$$\Delta G^* = \left(\frac{16 \pi \gamma_{SL}^3 T_l^2}{3 \Delta H_f^2} \right) \frac{1}{(\Delta T)^2} \quad (6)$$

$$r^* = \left(\frac{2 \gamma_{SL} T_l}{\Delta H_f} \right) \frac{1}{\Delta T}, \quad (7)$$

It can be seen from Eqs. (6) and (7) that both ΔG^* and r^* decrease with increasing undercooling, hence nucleation is favored.

The diffusivity, D , which reflects the atomic transport necessary for the growth of nuclei, also decreases with decreasing temperature. Even though the nucleation barrier decreases as the undercooling increases, crystallization can be inhibited by low atomic mobility. At low undercoolings, on the other hand, the atomic mobility is high but also the thermodynamic factors (large ΔG^* and r^*) tend to make crystallization improbable. Due to the opposing effects of these thermodynamic and the kinetic factors, the shortest time to crystallization can be expected at intermediate values of the undercooling.

The progress of a phase transformation such as crystallization is often plotted as a time-temperature-transformation (TTT) diagram (Fig. 1), with the curves representing times to onset of crystallization having a typical nose-like shape. The melt must be cooled rapidly enough to bypass the temperature interval where the maximal nucleation rate occurs, in order to avoid crystallization and reach the glassy state. It follows from this that rapid cooling is usually connected with glass formation. However, the selection of better glass forming compositions can push the nose of the TTT diagram to longer times (curve *a* to curve *b* in Fig. 1), i.e. lower cooling rates are sufficient to bypass the crystallization ($R_1 > R_2$, Fig. 1).

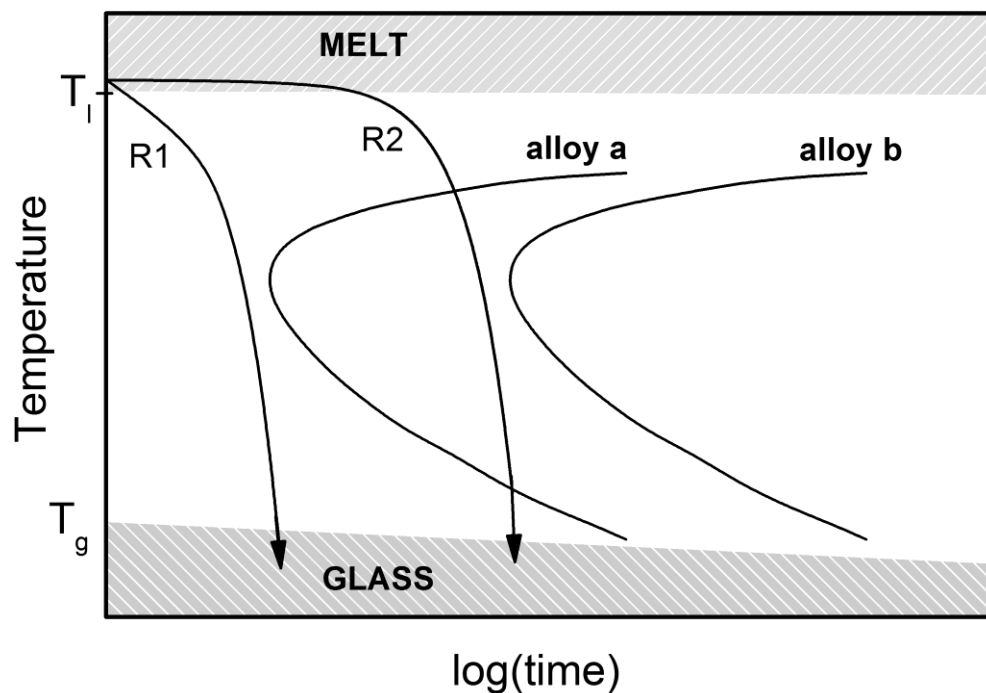


Fig. 1 Schematic representation of TTT diagrams for alloys *a* and *b*. R_1 and R_2 are cooling rates, where $R_1 > R_2$. Glassy and melted states are also indicated.

The three basic principles for the formation of BMGs, according to Inoue [20] are: 1) multi component systems, 2) a size difference between the atomic species in the alloy greater than 12 % and 3) a negative enthalpy of mixing. In addition, production of metallic glasses by melt quenching was found to be favored in compositions near deep eutectics. Eutectic compositions are characterized by having a large temperature region, over which the melt is thermodynamically stable. In addition to this, eutectic crystallization is accompanied by compositional changes, which require long range diffusion [21]. This process is slow compared to that of polymorphic crystallization, where only topological reconstruction of the atomic arrangement is required for crystallization and no compositional changes are necessary. For polymorphic crystallization, the Gibbs free energy curve of the crystalline phase, at a given composition must be below the liquid

phase curve. The characteristic compositions, at which the free energy curves of the crystalline and the liquid phase intersect, at given temperatures, are used for the T_0 -line construction [21]. The polymorphic liquid-crystal transformation is thermodynamically possible only inside of the T_0 -line. One side of an equilibrium binary eutectic diagram is schematically shown in Fig. 2 (with solid lines and notations of the one- and two phase regions). The composition-dependent glass transition temperatures and the T_0 -line for the α - phase are shown with the dash-dot and dashed line, respectively. When upon the rapid cooling of the eutectic melt at composition X_B^E , the glass transition occurs before the conditions for the fast polymorphic formation of the crystalline phases are reached (like shown in Fig. 2 for the α phase), the crystallization then proceeds according to the slower, diffusion controlled, non-polymorphic reaction. This type of situation, for example, is favorable for glass formation.

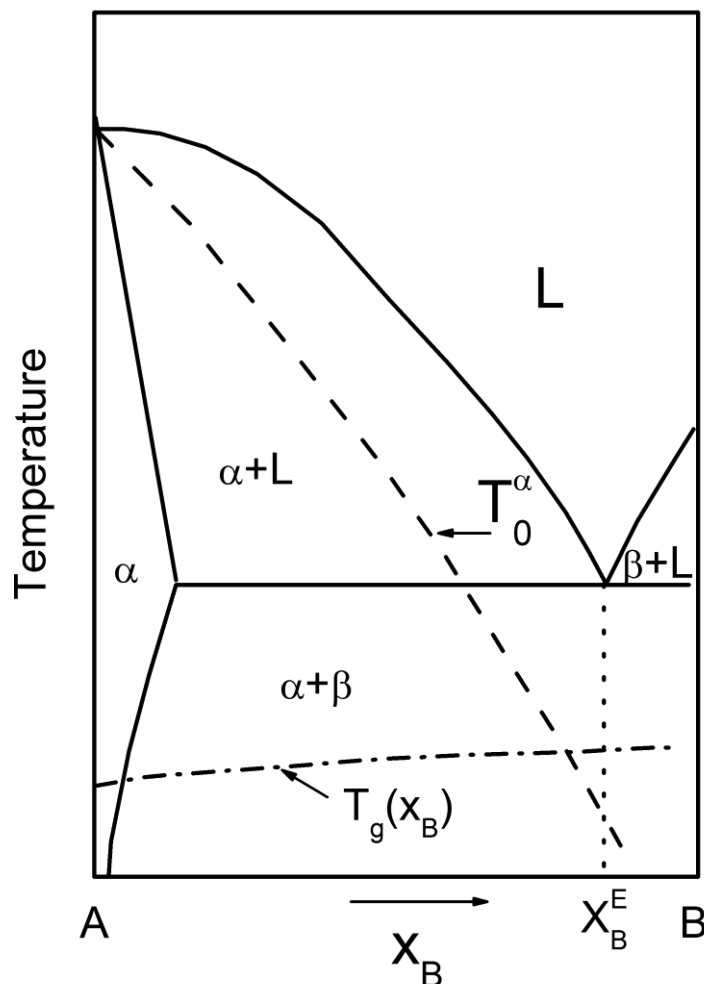


Fig. 2 Schematic representation of one side of the eutectic binary phase diagram. X_B^E represents the eutectic composition, $T_g(X_B)$ is the composition-dependent glass transition and T_0^a is a T_0 -curve for the α phase.

2.1.2. Thermodynamics and Kinetics of Glass Crystallization

BMGs, being in their nature non-equilibrium materials, upon exposure to elevated temperatures undergo significant rearrangement processes within the experimental time scale, such as structural relaxation, crystallization and possible phase separation/decomposition. The isothermal annealing of a glass slightly below T_g allows the material to relax and recover the metastable equilibrium structure of the deeply undercooled liquid. This process is connected with a decrease in the excess values of enthalpy, entropy and volume in comparison to those of the crystalline state.

It is commonly observed in as-cast glassy alloys that atomic diffusivities are due to structural relaxation events that are not only temperature but also time dependent [22]:

$$D(t, T) = D_R(T) + \Delta D(t, T), \quad (8)$$

where $D_R(T)$ is the temperature dependent diffusivity of the relaxed state and $\Delta D(t, T)$ is the time and temperature dependent diffusivity enhancement of the unrelaxed state. At some elevated temperature, the atomic diffusivity of the as-cast amorphous structure will decrease with time, until a saturation level is reached, which represents the atomic diffusivity in the relaxed structure. This decrease in diffusivity as the result of relaxation is correlated to the process of annealing out the excess volume, which was “frozen” into the as-cast structure during casting.

Diffusion in crystalline and glassy materials is very different. While diffusion in crystalline materials involves single atom jump processes, in glassy alloys diffusion proceeds by highly collective atom hopping [22]. Diffusion coefficients in the fully relaxed glassy state show an Arrhenius-type temperature dependence:

$$D = D_0 \exp\left(\frac{-E_a}{RT}\right), \quad (9)$$

where D_0 , E_a and R are the pre-exponential factor, activation enthalpy for diffusion and ideal gas constant (8.314 J/(mol K)), respectively. In various amorphous alloys D_0 is found to lie between 10^{15} m²/s and 10^{13} m²/s and in crystalline alloys between 10^{-6} m²/s and 10^2 m²/s [22]. The values of E_a for diffusion of different atoms in amorphous alloys lie between 1 - 3 eV, which is similar to those found in crystalline alloys. A general trend in crystalline and in amorphous alloys is that E_a increases with the increasing atom size [22].

Given a sufficient time and high enough temperature, devitrification (solid-state crystallization) of glassy alloys is eminent. Since most BMGs are multicomponent systems, the process of devitrification is often complex and involves the formation of multiple crystalline phases. There are three modes of devitrification: polymorphic, primary and eutectic [23]. In the polymorphic mode, the glass transforms into a crystalline phase with the same composition, where at a constant

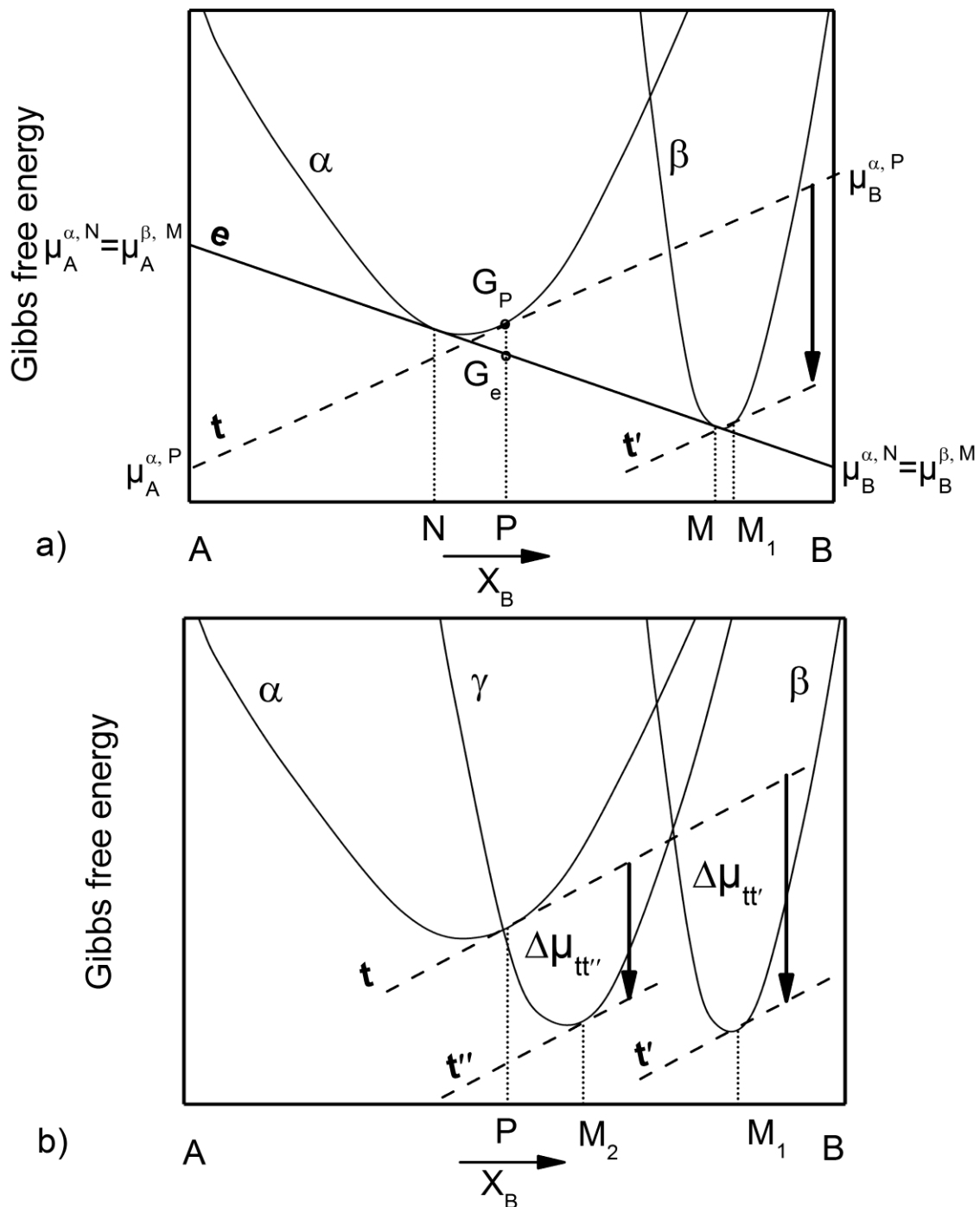


Fig. 3 Free energy diagrams illustrating in **a)** the α and β phases and their common tangent e . The alloy with composition P has a free energy G_P in the α phase. At equilibrium, the alloy P has a free energy G_e and it is composed of the $\alpha + \beta$ mixture, where α and β phases have compositions N and M , respectively. Chemical potentials, μ , of A and B are shown for the α and β phases in equilibrium with compositions M and N , as well as for the α phase with composition P . In **b)** the parallel tangent construction over the α , β and γ phases are shown along with driving forces for nucleation of the β and γ phases (with compositions M_1 and M_2) from the α phase with composition P indicated with $\Delta\mu_{tt'}$ and $\Delta\mu_{tt''}$, respectively.

temperature the growth is interface controlled. In primary crystallization, the crystalline phase forms with a composition different from that of the glass and consequently, a compositional gradient forms around the growing crystalline phase. The residual glassy matrix can further undergo different transformation modes. In the eutectic mode, two crystalline phases form simultaneously and solute partitioning is limited to the interfacial regions between the glass and two crystalline phases [23].

Since the devitrification often involves formation of multiple crystalline phases, a simple geometric construction (*parallel tangent construction*) can be used to determine the maximum driving force for a particular reaction [21]. An illustration of free energy curves of α and β phases are shown in Fig. 3a. An alloy with a composition P where A and B atoms are arranged as a α phase will have free energy of G_p . This alloy can decrease its free energy to minimum (G_e) by rearranging into two phases, α and β , with compositions N and M, respectively.

The *chemical potential* is defined as [19]

$$\mu_A = \left(\frac{\partial G'}{\partial n_A} \right)_{T, P, n_B}, \quad (10)$$

under constant values of temperature, pressure and number of moles of atoms B. G' is the free energy of the alloy and n_A is a number of moles of atoms A. The chemical potentials of atoms A and B in the α phase with a composition P are represented in free energy diagram, as illustrated in Fig. 3a by the intersection of tangent t with pure A and B ($\mu_A^{\alpha, P}$ and $\mu_B^{\alpha, P}$, respectively). In equilibrium, the chemical potentials of A and B in the α phase with composition N and β phase with composition M must be equal. Hence, the driving force for any reaction in general is given the difference in chemical potential, $\Delta\mu$, between two phases at a given composition.

Although the minimization of the free energy by achieving an equilibrium structure is a main goal of restructuring, the first phase to nucleate is often not that having the equilibrium composition. The phase composition which provides the maximal decrease in chemical potential per atom in a particular reaction is considered to have the maximum driving force [21]. Geometrically, the parallel tangent construction is used to determine this, as shown in Fig. 3a. The tangent over phase β (t') is constructed parallel to that over α phase with a P composition (t). The intersection point of this tangent (M_1) with the β phase represents the β phase composition with the highest driving force for nucleation from the α phase with a composition P. The driving force for nucleation represents the vertical difference between the tangents t and t' . In systems with more numerous phases, the parallel tangent construction provides a way to determine which phases are more likely to nucleate. This is illustrated in Fig. 3b, where the γ phase is added to the free energy diagram in Fig. 3a. The corresponding driving forces for nucleation of the β and γ phases from the α phase with composition P are indicated as $\Delta\mu_{t'}$ and $\Delta\mu_{t''}$, respectively. From this illustration, it

appears that the higher driving force for nucleation corresponds to the β phase with a composition M_1 than for the γ phase with composition M_2 .

2.2. Ni-Nb(-Sn) Based Refractory Alloy Glasses

A certain subset of BMGs is known as Refractory Alloy Glasses (RAG). The high melting temperatures of the constituent elements are used in RAGs to produce alloys with the high thermal stabilities, glass transition temperatures and yield strengths. The binary Ni-Nb system is an important sub-system in many multicomponent Ni-based alloys. The Ni-Nb phase diagram is shown in Fig. 4 [24]. The equilibrium phases in this binary system are the terminal fcc Ni-rich and

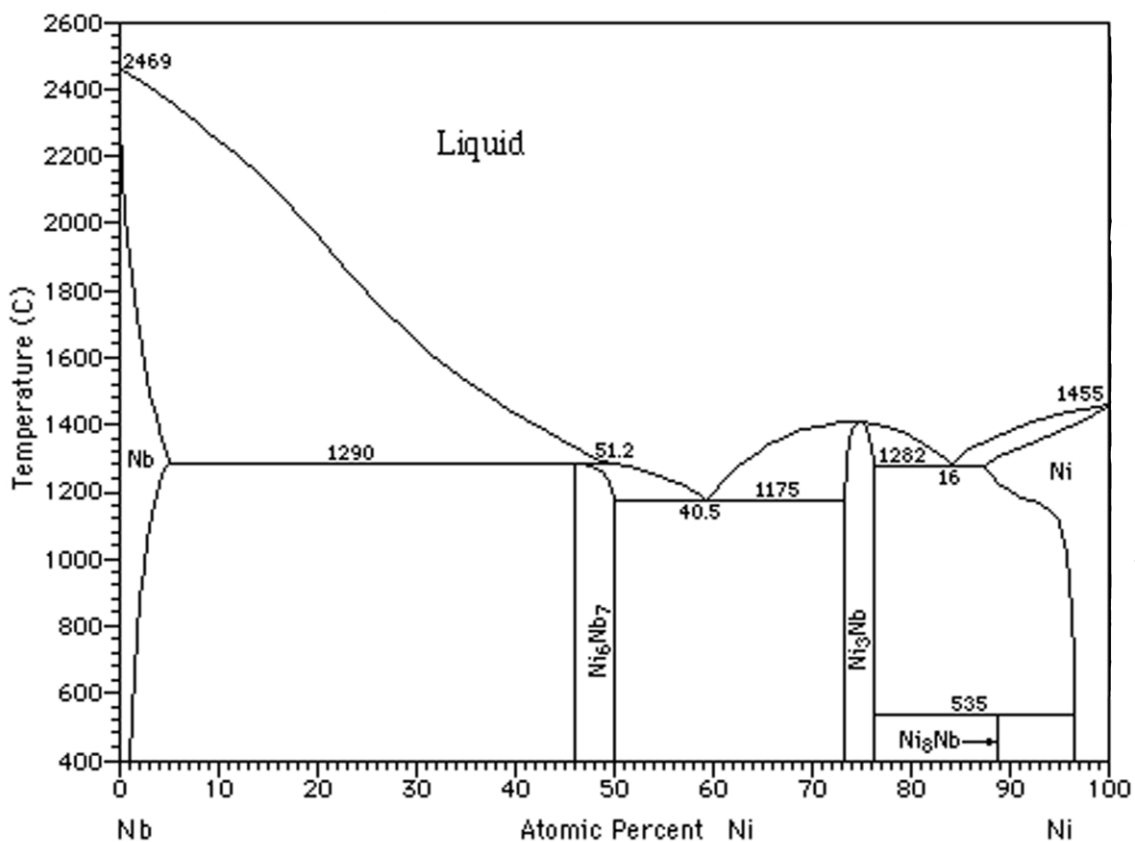


Fig. 4 Ni-Nb phase diagram [24].

bcc Nb-rich solid solutions, along with the three intermetallic phases: Ni_8Nb , Ni_3Nb and Ni_6Nb_7 . Ni_8Nb belongs to the group of ordered phases, with a critical ordering temperature of 808 K. Ni_3Nb is an orthorhombic phase with the Cu_3Ti -type of structure that forms within a very narrow concentration range around its stoichiometric concentration (~ 1 at.% [25]). Ni_6Nb_7 , often referred to as $NiNb$ or μ -phase, has a crystal structure of the Fe_7W_6 -type. The experimental data indicates a phase stability range of 50-57 at.% Nb [26]. The binary Ni-Nb diagram (Fig. 4) is characterized by two eutectics, one at the $Ni_{84}Nb_{16}$ and other at the $Ni_{59.5}Nb_{40.5}$ composition. In the conditions of equilibrium solidification, the eutectic $Ni_{84}Nb_{16}$ melt solidifies into the Ni-rich fcc solid solution

and Ni_3Nb phase, and the eutectic $\text{Ni}_{59.5}\text{Nb}_{40.5}$ melt solidifies into the Ni_3Nb and Ni_6Nb_7 phases. It was experimentally found that in the binary Ni-Nb system, in the case of rapid quenching conditions, such as melt-spinning, the completely amorphous structure could be achieved in a large compositional range between 27.5- 75 at.% Ni [27]. This is in agreement with the positions of the T_0 -lines of different phases also calculated in Ref. [27] for cooling rates of 10^6 K/s . The maximal solubility of the bcc and fcc solid solution was calculated as 26 at.% and 85 at.% Ni, respectively. The phase stability range of the Ni_3Nb phase was calculated as 67.5- 82.5 at.% Ni. The composition with the best glass forming ability in the binary Ni-Nb system was reported to be the near eutectic composition $\text{Ni}_{62}\text{Nb}_{38}$, with a critical casting thickness of 2 mm [16]. The crystallization of amorphous binary Ni-Nb alloys was extensively studied in Refs. [27,28] and the reported results of these studies will be briefly discussed below.

It was reported in Ref. [27] that amorphous binary Ni-Nb alloys with the intermediate compositions of 45 to 70 at.% Ni crystallize into two equilibrium intermetallic phases, Ni_3Nb and Ni_6Nb_7 . The first product of decomposition of the amorphous binary alloys with 60 to 75 at.% Ni is Ni_3Nb . In addition to these two equilibrium phases, in the compositions with 45 to 60 at.% Ni, metastable M- and η -phases were also found. Both of these metastable phases are rich in Nb. The M phase was first observed in the ternary Ni-Nb-Al system. The crystalline structure of the M phase contains blocks of Ni_6Nb_7 and it forms at 48 at.% Nb which shows that it is closely related to Ni_6Nb_7 . In the ternary Ni-Nb-Al system, the M phase forms with 13 at.% Al, and it was shown that the Al atoms replace Ni at some positions [29]. The η -phase is a Ti_2Ni type phase with a composition close to NiNb_5 . It was also shown in Ref. [27] that when precipitated, both metastable phases M and η have significant stability.

In Ref. [28], the isothermal crystallization behavior of the amorphous binary $\text{Ni}_{60}\text{Nb}_{40}$ composition at 871 K was studied. The M phase was reported to be the first phase to form from the amorphous matrix. It was suggested that the formation of the metastable M phase instead of one of the stable phases is favored by the formation of the interface with a smaller surface energy, which especially in the case of homogeneous nucleation plays an important role. During crystallization, equilibrium Ni_3Nb forms in the structure from the remaining amorphous matrix, on the M phase/amorphous interfaces. During further crystallization, Ni_6Nb_7 formation is favored in comparison to the M phase, due to the Ni_3Nb /amorphous interfaces.

The Ni-Nb-Sn RAG family is a new family of BMGs, which is based on the binary Ni-Nb system having the $\text{Ni}_{59.5}\text{Nb}_{40.5}$ eutectic composition. In the Ni-Nb-Sn system the ternary eutectic was found close to the composition 54 at.% Ni 35 at.% Nb and 11 at.% Sn (Liquid \rightarrow Ni_3Nb + Ni_6Nb_7 + Ni_2NbSn) [10]. The temperature of the ternary eutectic was reported to be about 85 K lower than the eutectic temperature of the corresponding binary eutectic [3]. This was an indication of the better glass forming ability (GFA) in the ternary system than in the binary, since the liquid remains stable to lower temperatures than in the binary system. The glass transition temperatures

in the binary Ni-Nb compositions are generally slightly higher than in the ternary Ni-Nb-Sn compositions (Table 1). The supercooled liquid regions are often not observable in the binary compositions and in any case are smaller than those found in the ternary compositions (see Table 1). The TTT diagrams of the binary $\text{Ni}_{60}\text{Nb}_{40}$ and the ternary $\text{Ni}_{60}\text{Nb}_{35}\text{Sn}_5$ can be compared in Fig. 5. The binary $\text{Ni}_{60}\text{Nb}_{40}$ diagram shown in Fig. 5 is according to the diagram modeled in Ref. [30]. The lower half of the TTT diagram, of the ternary $\text{Ni}_{60}\text{Nb}_{35}\text{Sn}_5$, is constructed according to the data obtained from the isothermal DSC measurements in the interval 880-940 K and extrapolated to broader time-temperature interval, as reported in Ref. [31]. For $\text{Ni}_{60}\text{Nb}_{35}\text{Sn}_5$ alloy, in addition to 1% and 99 % crystallization, the isothermal glass transition time, which represents an approximate relaxation time at T_g [8], is indicated. The upper part and the position of the nose of the TTT diagram are not yet available for the ternary composition.

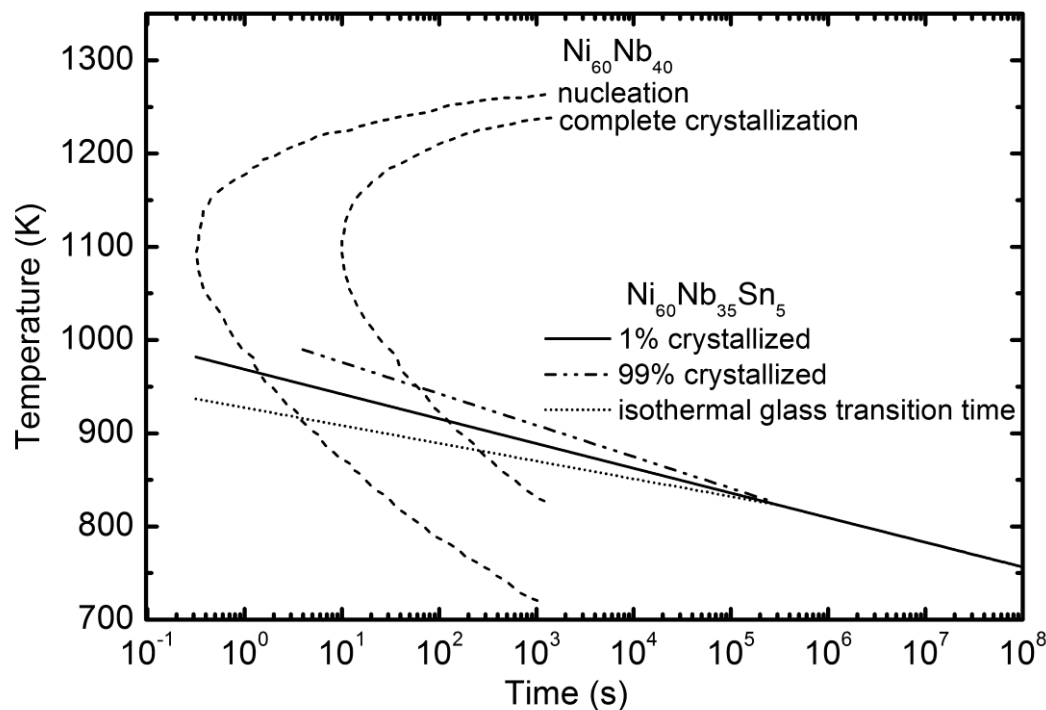


Fig. 5 The TTT diagrams of the binary $\text{Ni}_{60}\text{Nb}_{40}$ and the ternary $\text{Ni}_{60}\text{Nb}_{35}\text{Sn}_5$ alloys. The binary TTT diagram is according to the calculated diagram published in Ref. [30] and the estimated $\text{Ni}_{60}\text{Nb}_{35}\text{Sn}_5$ is according to the isothermal calorimetric measurements, as published in Ref. [31]. For $\text{Ni}_{60}\text{Nb}_{35}\text{Sn}_5$ alloy, in addition to 1% and 99 % crystallization, the isothermal glass transition time [8] is indicated.

The glass-forming compositional range of the ternary Ni-Nb-Sn alloys is reported as 54-62 at.% Ni, 32-36 at.% Nb and 3-11 at.% Sn [10]. This compositional range is at or in the vicinity of the ternary eutectic. The t_c for the ternary Ni-Nb-Sn compositions is 2 mm, except for $\text{Ni}_{59.35}\text{Nb}_{34.45}\text{Sn}_{6.2}$ and $\text{Ni}_{59.5}\text{Nb}_{33.6}\text{Sn}_{6.9}$, where a t_c of 3 mm was reported [3]. Various quaternary and quinary amorphous compositions, where elements like B, Fe, Cu, Ta, Co or Hf were added to

the ternary Ni-Nb-Sn were also reported on [3,4,10]. In terms of increasing t_c , the best results were found by alloying with B, Co and Hf (see Table 1 and references therein).

The ternary Ni-Nb-Sn glasses have a high Young's modulus of ~ 180-200 GPa and hardness of 1000-1280 kg/mm² [3]. The yield strength of 3-3.8 GPa was estimated from the hardness, according to the relation $\sigma_y = 3HV$ [3]. Compressive tests have shown, later on, that the measured strength is lower than the estimated (2.8-1.8 GPa) and that it is a function of Sn concentration, where the strength decreases with the increasing Sn concentration [3,4]. This was initially assumed to be connected with phase separation that the Ni-Nb-Sn alloys may undergo during annealing in the supercooled liquid region [4].

Table 1 Critical thickness (t_c), onset of glass transition (T_g) and onset of crystallization (T_x) temperatures of different reported Ni-Nb(-Sn) based compositions

<i>Composition</i>	<i>t_c (mm)</i>	<i>T_g (K)</i>	<i>T_x (K)</i>	<i>Ref.</i>
<i>Ni₆₂Nb₃₈^{a)}</i>	2	892	932	[16]
<i>Ni₆₀Nb₃₇Sn₃</i>	2	895	943	[3]
<i>Ni₆₀Nb₃₅Sn₅</i>	2	885	943	[3]
<i>Ni_{59.35}Nb_{34.45}Sn_{6.2}</i>	3	882	930	[3]
<i>Ni₅₇Nb₃₅Sn₅Fe₃</i>	2	886	915	[3]
<i>Ni₆₀Nb₃₆Sn₃B₁</i>	3	882	940	[3]
<i>Ni₅₁Nb₃₃Sn₇Co₉</i>	3	872	922	[10]
<i>Ni₅₆Nb₂₈Sn₅Co₃Hf₈</i>	4	864	919	[10]

a- Best reported glass forming alloy in the binary Ni-Nb system

2.3. Oxidation

The term oxidation refers to the process where the element in consideration loses one or more electrons. Oxidation is also used in a more specific sense to describe the reaction between a metal and oxygen. The total reaction of oxidation can be written as:



where M is a metal and a and b are stoichiometric coefficients.

The oxidation behavior of a metal or an alloy is described, in general, by analyzing the:

- thermodynamics of oxidation;
- kinetics of oxidation;
- morphology of the oxide scale.

2.3.1. Thermodynamics of Oxidation

The Gibbs free energy change connected with the metal-oxygen reaction (ΔG_r) represents the thermodynamic driving force for oxidation. When the Gibbs free energy change of the reaction is negative, i.e. $\Delta G_r < 0$, the reaction of oxidation occurs spontaneously until the equilibrium state is reached, i.e. $\Delta G_r = 0$. For Eq. (11) the ΔG_r can be written as:

$$\Delta G_r = \Delta G^0 + RT \ln K_r, \quad (12)$$

where ΔG^0 and K_r are the standard free energy difference and the reaction constant, respectively, T is the absolute temperature. The reaction constant of the oxidation shown in the Eq. (11) can be expressed as:

$$K_r = \frac{a_{M_aO_b}^{2/b}}{a_M^{2a/b} p_{O_2}}, \quad (13)$$

where $a_{M_aO_b}$, a_M and p_{O_2} represent the activities of the M_aO_b , M and the partial pressure of O_2 , respectively. At equilibrium oxidation conditions ($\Delta G_r = 0$) of the pure metal M ($a_{M_aO_b} = a_M = 1$), Eq. (13) becomes:

$$K_{eq} = \frac{1}{p(O_{2,eq})}, \quad (14)$$

where K_{eq} is the equilibrium constant and $p(O_{2,eq})$ is the oxygen partial pressure in equilibrium with the oxide, which can be expressed as:

$$p(O_{2,eq}) = \exp\left(\frac{\Delta G^0}{RT}\right) \quad (15)$$

The values of the ΔG^0 as a function of temperature are usually graphically presented in the form of the so-called *Ellingham/Richardson diagram* from which the relative stabilities of different oxides can be assessed.

In the case of alloy oxidation the activities of the elements are $a_M < 1$ and the precise values of the activities are expressed as:

$$a_M = \gamma_M X_M, \quad (16)$$

where the γ_M and X_M are the activity coefficient and the molar fraction of the metal M in the alloy, respectively. This expression shows that the activity is a function of concentration and, if the value for γ_M is not available, ideal solution behavior is assumed, $\gamma_M = 1$, i.e. the a_M can be approximated to X_M [32]. For a regular solution the activity is expressed as:

$$\mu_M = G_M + RT \ln a_M, \quad (17)$$

where the μ_M represents the chemical potential of the metal M and the G_M is the free energy of M in its standard state at the temperature in question. This expression shows the relationship between the activity and the molar free energy [19].

2.3.2. Kinetics of Oxidation

With the exception of the noble metals, the free energy change for the formation of most oxides is negative. The thermodynamic considerations can in this respect point to the more stable products of oxidation but the final outcome may be considerable limited by the overall kinetics of the process. The oxidation rate depends of many parameters, e.g. temperature, oxygen pressure, surface pre-polarization and microstructure, and may be an indicator of the oxidation mechanisms taking place [32]. The equations used to describe the most often encountered oxidation behavior will be briefly discussed below.

Logarithmic equation

The logarithmic oxidation behavior is most often applied to oxidation behavior at low temperatures or to fit any thin oxide film growth. In the case of logarithmic oxidation, the reaction rate rises fast at the beginning and then slows down rapidly as soon as the oxide scale forms a protective film. The logarithmic oxidation behavior can be described with direct or inverse logarithmic equations, Eq. (18) and Eq. (19), respectively.

Direct logarithmic equation

$$Y = K \log t + A \quad (18)$$

Inverse logarithmic equation

$$Y^{-1} = B + K_i \log t, \quad (19)$$

where Y can represent the oxidation parameter, like mass gain or oxide thickness, and t represents the isothermal time. K and K_i are the direct and inverse logarithmic rate constants, respectively, and A and B are integration constants.

Parabolic equation

The high temperature oxidation behavior, where the thermal diffusion is the rate determining process, can in many cases be described with the parabolic equation

$$Y^2 = K_p t + C \quad , \quad (20)$$

where the K_p and C are the parabolic rate constant and the integration constant, respectively.

Linear equation

The linear oxidation law, Eq. (21), describes the oxidation behavior when the oxidation rate remains constant with time

$$Y = K_l t + D, \quad (21)$$

where K_l is the linear rate constant and the D is the integration constant. The linear oxidation behavior is often an indication that some surface reaction is the rate determining factors. The combinations of different equations are also commonly used, e.g. parabolic behavior is characterized by a parabolic oxidation followed by a linear oxidation. Formation of a continuous, dense (pore and crack free), well-adherent scale, which results in the kinetic slowing down of oxidation (to a complete stop) is considered oxidation passivation and represents desirable oxidation behavior.

Activation energy for oxidation, E_a

The temperature dependence of the oxidation rate can be expressed with the Arrhenius equation:

$$K = A \exp\left(\frac{-E_a}{RT}\right), \quad (22)$$

where K is the rate constant, the E_a is the activation energy (J/mol) and A is a pre-exponential. The oxidation rate constant (K) can be determined by isothermal oxidation experiments by means of a $\log(K)$ vs. $(1/T)$ plot. The E_a can be determined from the line slope ($-E_a/2.303R$). If $\log(K)$ vs $(1/T)$ exhibits a changing slope, a change in the oxidation mechanism, in the temperature interval in question, may be occurring.

2.3.3. Initial Stages of Oxidation and Scale Growth

The reaction between the oxygen and the bare metal surface is rapid, even at room temperature. The initial stages of oxidation are very complicated and will be therefore summarized in only general terms.

When the oxygen comes into contact with the bare metal surface, the process of physical adsorption of oxygen molecules on the surface takes place. With an adsorption energy of 20-25 kJ/mol, this is considered to be a weak bond [33]. After dissociation of the physisorbed molecules, the process of chemisorption follows, which results in a stronger bond (~ 600 kJ/mol) [33]. The formation of the thin layer of adsorbed oxygen is shown schematically in Fig. 6 (I). The following step, shown in Fig. 6 (II) is the formation of oxide nuclei and their lateral growth, which can result in the formation of a continuous oxide layer. The process of nucleation can then proceed through heterogeneous or homogeneous nucleation. Heterogeneous nucleation proceeds usually in the conditions of low temperature and low supersaturation, whereas under the opposite conditions homogeneous nucleation is more likely.

After a continuous thin oxide layer is formed, oxide layer growth, i.e. thickening, proceeds as shown in Fig. 6 (III). When the oxide layer becomes thicker the term 'scale' is more frequently used. The scale growth is connected to the following reactions [34]:

- at the gas-oxide interface, oxygen reacts with electrons to form O^{2-} ;
- at the metal-oxide interface the metal atoms (M) form metal ions (M^{n+}) and electrons (ne^-);
- the O^{2-} ions diffuse from the gas-oxide interface inwards and the metal ions (M^{n+}) and electrons (ne^-) from the metal-oxide interface outwards. The outward electron transport by the ions is accompanied by the electron countercurrent or by the inward vacancy diffusion;

Finally, as the oxide scale thickens, due to the cell volume differences between the metal and the oxide, the formation of pores and cracks may occur leading to breakaway oxidation. The cracking is especially expected in the case when the oxide scale grows inwards.

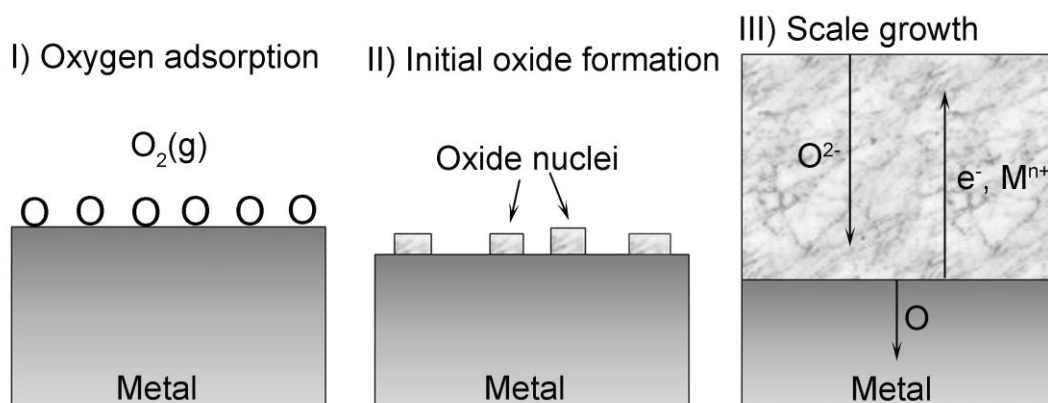


Fig. 6 Schematic representation of some aspects of the oxide scale formation.

2.3.4. Oxidation of Alloys

The issue of good oxidation resistance must often be addressed when designing a new alloy. It would be therefore of significant interest to be able to predict the influence of alloying elements on oxidation behavior. At present, such a unified theory is not available. However, factors to be considered when an alloy is being oxidized are [35]:

- Affinity of the component metal atoms to oxygen and to each other
- Diffusion rates of atoms in the alloy and ions in oxides
- Mutual solubilities of oxidation products
- Relative volumes of different phases

It is important first of all to decide which of the elements in the alloy are likely to be oxidized by comparing ΔG^0 values. Knowing this, the binary alloys A-B, where B is the less noble metal, can be classified into three concentration ranges [35]:

1. Alloys with a composition at the A-rich end of the system, which form only A oxides at the surface. Maximum concentration of the less noble element B, for this type of oxidation to occur, depends on oxygen affinities of A and B, temperature and mutual solubilities of oxides;
2. Alloys with a composition at the B-rich side of the system, which form only B oxides;
3. Intermediate compositions (between those in 1. and 2.), where oxides of both A and B can form either as separate layers or as mixtures. Even layers of double oxides such as CrNbO_4 in Nb-Cr alloys can form.

2.3.4.1. Oxidation of Crystalline and Amorphous Alloys

The only stable Ni oxide at high temperatures is NiO. The growth of a NiO scale is governed by Ni-ion diffusion through the scale and the oxidation reaction takes place at the oxide-gas interface [36]. In Refs. [37,38] the important contribution of the Ni grain boundary diffusion in NiO was also reported on. This type of growth is favorable in terms of lower stress concentration in the oxide layer and consequently lower tendency for crack formation.

The oxidation behavior of Nb is considered complex, not only because it involves three different stable Nb oxides: NbO, NbO₂ and Nb₂O₅, but also because Nb₂O₅ can form in different polymorphic forms. In the initial stages of oxidation the formation of different metastable phases of the form NbO_x, NbO_y, and Nb_yO is also possible [32]. The oxidation behavior of Nb is

characterized by two main stages. In the first stage, oxygen dissolves in Nb and forms metastable NbO_x , NbO_y , Nb_yO phases. The acceleration of the oxidation rate in the second stage is associated with the nucleation and growth of Nb_2O_5 , which is well known to form porous scales, which offer poor protection against oxidation.

Ni-rich Ni-Nb crystalline alloys follow an approximately parabolic law of oxidation. Alloys with an fcc (Ni, Nb) solid solution structure oxidize slower than pure Ni. Further increase of Nb concentration, to a two phase region, results in a decrease of oxidation resistance, which is above 25 at.% Nb lower than that of pure Ni [39,40]. In alloys containing up to 25 at.% Nb, the formation of an external NiO layer and inner zone rich in Nb oxides was reported [40,41], except in the case of low oxygen pressure where only oxidation of Nb was observed [42]. In some instances [40] the formation of double oxide NiNb_2O_6 , in an inner part of the external NiO scale was apparent [40]. The oxidation behavior of the two-phase polycrystalline Ni-Nb alloy containing 21.3 at.% Nb showed a typical in situ-type of oxidation, where neither of the constituent elements (Ni and Nb) was observed to diffuse extensively [40].

Oxidation studies on the as-cast amorphous $\text{Ni}_{62}\text{Nb}_{38}$ [43] and $\text{Ni}_{65}\text{Nb}_{35}\text{Sn}_5$ [31] compositions have also been carried out. The short time oxidation study [43] conducted at room temperature and 339 K below T_g , gave insight into the initial stages of oxidation of the amorphous $\text{Ni}_{62}\text{Nb}_{38}$. It was observed that thin oxide layers may start to form as amorphous and only after prolonged oxidation (30 min at 573 K) start to crystallize. The as-cast surface of $\text{Ni}_{62}\text{Nb}_{38}$ oxidized at room temperature consisted mainly of Nb oxides, while after only 5 and 10 min of oxidation at 573 K the surface compositions started to enrich in NiO [43]. These results confirm the earlier proposed mechanisms for the initial oxidation in Ni-Nb alloys [31,41], where a simultaneous nucleation of Ni and Nb oxides with a later NiO overgrowth was proposed. The oxidation of the ternary $\text{Ni}_{65}\text{Nb}_{34}\text{Sn}_5$ [31] was studied in synthetic air, in the temperature range between the 20 and 60 K below the T_g , where $T_g = 883$ K. The oxidation kinetics was shown to be parabolic, with oxidation rates close to that of Zr-based BMGs (when measured 20 to 60 K below T_g). The oxide scale was reported as consisting of a NiO outer scale and a continuous inner layer of Nb oxides, mostly Nb_2O_5 with some NbO_2 . In the matrix, underneath the scale the formation of a Nb depletion layer was observed and thought to destabilize of the amorphous matrix and induce crystallization of the Ni-rich intermetallic phases such as Ni_3Nb and Ni_2NbSn [44].

Oxidation studies on some other amorphous alloys, such as Zr- Fe- and Co-based alloys have also been reported on [45–51]. It was observed that the crystallization processes often accompany oxidation and that in some instances intermetallic phases different from those found after crystallization in vacuum environment can form [46]. In comparison to their microcrystalline counterparts, amorphous alloys often exhibit more intense oxidation [48,51,52]. Furthermore, the microstructures observed in the oxidation penetration distance and the identified oxide phases may differ significantly from those observed on microcrystalline samples. On the other hand $\text{Fe}_{78}\text{Si}_9\text{B}_{13}$,

for example, shows the opposite effect—the amorphous structure was more oxidation resistant than the crystalline. Although the same phases were found in both oxidized microstructures, Fe_3O_4 , Fe_2O_3 and SiO_2 , the amorphous structure was richer in SiO_2 and the particle size was smaller, which was believed to be the reason for better oxidation resistance. Some studies on Zr-based alloys have also showed [47,50,53] that in comparison with the amorphous structure, the nanocrystalline structure of the same composition has a pronounced oxidation resistance due to the lower driving force for oxidation of the nanocrystalline compared to amorphous structure.

3. Experimental Methods

In Section 3.1, processing methods and experimental difficulties encountered during alloying and suction casting of amorphous plates are described. Characterization methods and detailed descriptions of various specimens used throughout this work are given in Sections 3.2 and 3.3, respectively.

3.1. Processing Methods

3.1.1. Alloying of Pure Elements

Master alloys of various compositions were produced from elements with purities of 99.95 at.% or higher. The pure elements were weighed out to the precision of ± 0.001 g, in the amounts necessary for 20 g batches and cleaned ultrasonically in acetone and then in ethanol. In order to remove any remaining liquid from its porous structure, the elemental B was additionally thermally treated before alloying, first at 463 K for 1 h under 10^{-1} mbar and then at 1273 K for 1 h under 10^{-4} mbar.

The pure elements were alloyed together in a custom-made arc melting furnace. The melting of the pure elements in the arc melter is realized under the influence of an electric arc formed between two electrodes: a negative W-cathode and a positive Cu-anode, which are connected to a DC generator. The bottom of the furnace is a Cu-anode in the form of a water-cooled plate and has spherical impressions on its upper surface for placing and melting the material. The W-cathode is positioned vertically on top of the furnace onto the Cu-plate. Both the W-cathode and Cu-anode are water cooled. For better control of the melting process both electrodes are constructed to be maneuverable. Before melting, the atmosphere of the chamber was evacuated to 10^{-3} mbar and back filled with Argon 4.6 ($\geq 99,996$ % purity). This process was repeated three times in succession. The residual oxygen in the atmosphere was then gettered by melting a piece of pure Ti placed in a separate impression of the copper plate (see Fig. 7).

Master alloys of the binary Ni-Nb compositions were produced by direct melting together of the pure Ni and Nb. After the initial melting, the ingot was left to solidify and cool down. Using a manipulator the solidified ingot was turned and then re-melted. The process of turning and re-melting was repeated three to five times, until the alloy ingot appeared homogeneous by visual inspection.

During the first alloying trials of the ternary Ni-Nb-Sn compositions, the positioning of Ni, Nb and Sn in the spherical impression of the arc melting chamber (see Fig. 7a) was chosen based on the melting temperatures of these elements. The Sn ($T_m = 505$ K) was placed on the bottom of the spherical impressions in the Cu-plate and the Ni ($T_m = 1726$ K) pieces were placed on top of the Sn. Since Nb has the highest melting temperature of each of the three elements ($T_m = 2750$ K), the Nb pieces were placed lastly, on top of the Ni. In this way the Nb is closest to the W-electrode and it is the first element to melt. The formed melt then flows and slowly incorporates the Ni and Sn. It was attempted by this order of element positioning to shield the low melting Sn from the extreme temperatures that are necessary while melting Nb and which may cause the Sn to evaporate ($T_b = 2543$ K). After the melt solidified a strong adhesion between the ingot and the Cu-plate was sometimes formed. These ingots were considered to be contaminated with the Cu atoms after detachment from the Cu-plate and were therefore not further used.

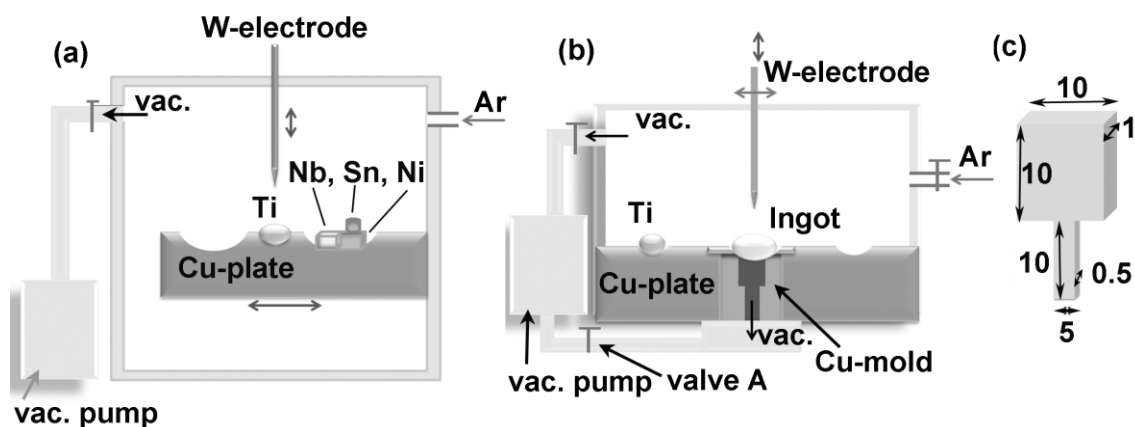


Fig. 7 A schematic representations of: **a)** arc melting furnace used for alloying, **b)** suction casting setup and **c)** typical geometry of the plate-like castings with its dimensions indicated in the image in units of mm.

In the next alloying trials, the three elements to be alloyed were ordered in the spherical impression of the Cu-plate as follows: the Sn pieces were placed on the top of Ni pieces and the Nb pieces were placed next to the Ni and Sn (see Fig. 7a). The process of melting would start with the melting of Nb. At the same time, the Sn would also slowly melt and simultaneously mix with the underlying pieces of Ni. Finally, the melted Nb mixed with Ni and Sn into one ingot. After solidification the ingot was turned upside down and re-melted. This process was repeated three to five times. No practical problems (e.g. adhesion between the ingot and Cu-plate) were encountered during melting.

In the case of the quaternary $\text{Ni}_{60}\text{Nb}_{36}\text{Sn}_3\text{B}_1$ composition, B was directly alloyed with the other elements, where the relative position of Ni, Nb, and Sn was maintained as in the ternary alloys and

the B was placed directly underneath the Nb. In the case of the Ni-Nb-Sn-Si alloys, Si and Ni were pre-alloyed together and subsequently melted with Nb and Sn.

3.1.2. Suction Casting of Amorphous Specimens

The Buehler MAM 1 arc melting furnace with a suction casting inset, schematically shown in Fig. 7b, was used for casting plate-like specimens (Fig. 7c). The suction casting inset has a specially designed Cu-plate underneath the ingot material. Instead of the simple spherical impressions, which are characteristic of an arc melter (Fig. 7a), a Cu-mold with a cavity geometry of the desired castings is placed in the Cu-plate of the suction casting setup. Underneath the Cu-mold a connection with a vacuum system can be established by opening the valve A (Fig. 7b). Before melting, the atmosphere of the chamber was successfully evacuated three times to 7×10^{-3} mbar and back-filled with Argon 4.6. Finally, after Ti-gettering the atmosphere, the ingot prepared in the arc melter was melted and cast by applying suction from underneath the Cu-mold, i.e. by forming a pressure difference above and beneath the Cu-mold. This can be achieved by opening the valve A, which establishes a connection to the vacuum pump (Fig. 7b).

3.2. Characterization Methods

3.2.1. Microscopy

In order to characterize the structure of the samples at various size scales, different microscopy methods were applied, such as scanning electron microscopy, transmission electron microscopy and the atom probe microscopy.

3.2.1.1. Scanning Electron Microscopy (SEM)

SEM is a microscopy technique based on scanning the sample surface with an electron beam. A typical SEM is schematically shown in Fig. 8a. It consists of an electron gun, which either thermally or by field emission produces monochromatic electrons. The electron beam is then formed and focused onto the sample surface by a number of lenses and apertures. The energy transfer from the primary electron beam to the sample results in various types of signals coming from the sample (Fig. 8b). These signals are detected by appropriate detectors and analyzed. In this way various types of information can be obtained about the sample.

Secondary electrons (SE) are inelastically scattered sample electrons and the orientation of the sample surface determines the number of electrons reaching the detector. Therefore, the obtained contrast reveals information about the topography of the sample. Backscattered electrons (BS) are elastically scattered sample electrons, which, compared to secondary electrons, come from deeper regions within the sample. This signal therefore has a lower topographical resolution but is useful in distinguishing one material from another. Energy dispersive x-ray analysis (EDX) is a technique used to determine the chemical composition of a sample. As the incoming electrons collide with the sample some of the sample electrons from the inner electron shells are ejected, leaving a vacancy in their place. When an electron from an outer, higher-energy shell then fills the vacated position, a characteristic x-ray is emitted. By analyzing the emitted x-rays, the elemental composition of the sample can be determined. Electron backscatter diffraction (EBSD) provides information about crystallographic nature of the sample. After the electron beam strikes a tilted crystalline sample, the diffracted electrons form a diffraction pattern that is detected on a phosphorous screen. This diffraction pattern characterizes a crystal structure (and its orientation) of the sample region from which it originates. By processing crystallographic information obtained by the scanning electron beam in a grid on a sample surface, different types of maps can be

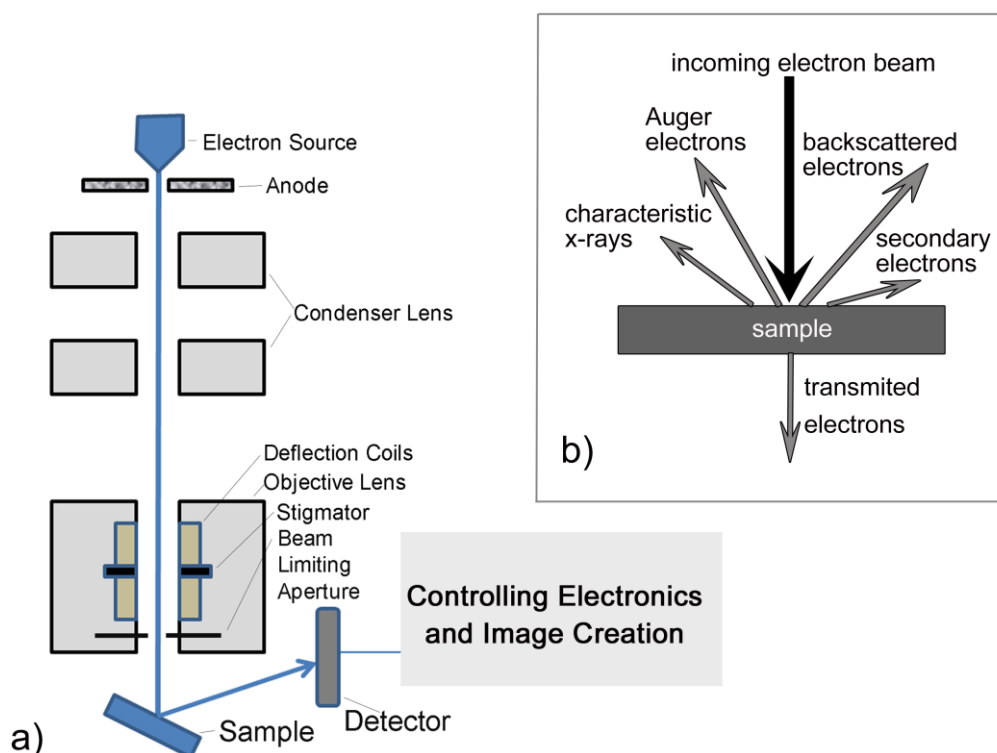


Fig. 8 a) Schematic representation of a SEM and b) electron beam-sample interactions.

constructed. A phase map, for example, allows discrimination between different phases present in the sample on a scanned area.

Metallographic sample preparation for SEM was conducted according to a standard mechanical polishing procedure down to a colloidal silica suspension, OPS, of 0.05 μm particle size. SEM images were acquired in SE mode, when the topography of the sample surface was the main concern. In the cases where compositional contrast was of interest, BS mode was used. The BS images were used to determine the volume fraction of different phases in the structure. Using the areal method of stereological quantitative analysis [54,55], the areal fraction of one phase A in the structure is calculated as a ratio between area of phase A and the measuring area, multiplied by 100. According to the Delesse principle [56], the areal fraction (A_A) equals the volume fraction (V_V) of the same microstructural element. Finally, crystallographic information on different phases was obtained by EBSD and the chemical analysis was performed by EDX. Depending on availability, SEM images were taken using one of the following microscopes: Helios Nanolab 600 (FEI), ZEISS Supra 55VP and CAMSCAN-FE by CAMSCAN Ltd.

3.2.1.2. Transmission Electron Microscopy (TEM)

An electron beam is used in the TEM to illuminate a thin sample of less than 100 nm thickness. Similar to SEM, the electron beam is generated by an electron gun. Electromagnetic lenses are used to focus the transmitted electrons and to magnify and project the image onto a recording device. The contrast observed in the image is determined by the interaction of the electron beam with the sample. The diffraction pattern of the sample allows characterization of the structure and orientation of the crystal. Two other types of imaging modes are bright-field (BF) and dark-field (DF) imaging. The BF image is made with an objective aperture selecting only the direct beam (undiffracted electrons). In the DF image, the objective aperture is positioned in such a way that only electrons scattered in a specific direction; i.e. only crystals which fulfill a specific diffraction condition contribute to the image. BF mode is often used for characterization of size and morphology of the nanostructures and DF mode for imaging precipitates of a second phase and crystal defects.

Oxide samples were characterized in the TEM in order to obtain more detailed information about the structure of the oxide layer. Sample preparation was carried out using a focused ion beam (FIB) technique, in a Helios Nanolab 600 (FEI) dual beam workstation. After applying a double Pt-layer onto the polished cross-section of the surface, two trenches were milled around the area of interest (Fig. 9). The thickness of the area between trenches was gradually reduced by fine milling up to 1 μm . An L-shaped pattern (marked schematically in Fig. 9) was used to partially cut out the TEM foil. A micro-manipulator was then attached to the TEM foil with a Pt-layer and the

remaining connection between TEM foil and a bulk sample was finally cut off. The TEM foil was then transferred and connected to a pre-cut Cu grid and further thinned to a thickness of approximately 100 nm.

The bright field image and the diffraction pattern images were made using a Jeol JEM 2010 microscope and used for sample characterization at a voltage of 200 kV. Additionally, the chemical composition of different phases was characterized by EDX.

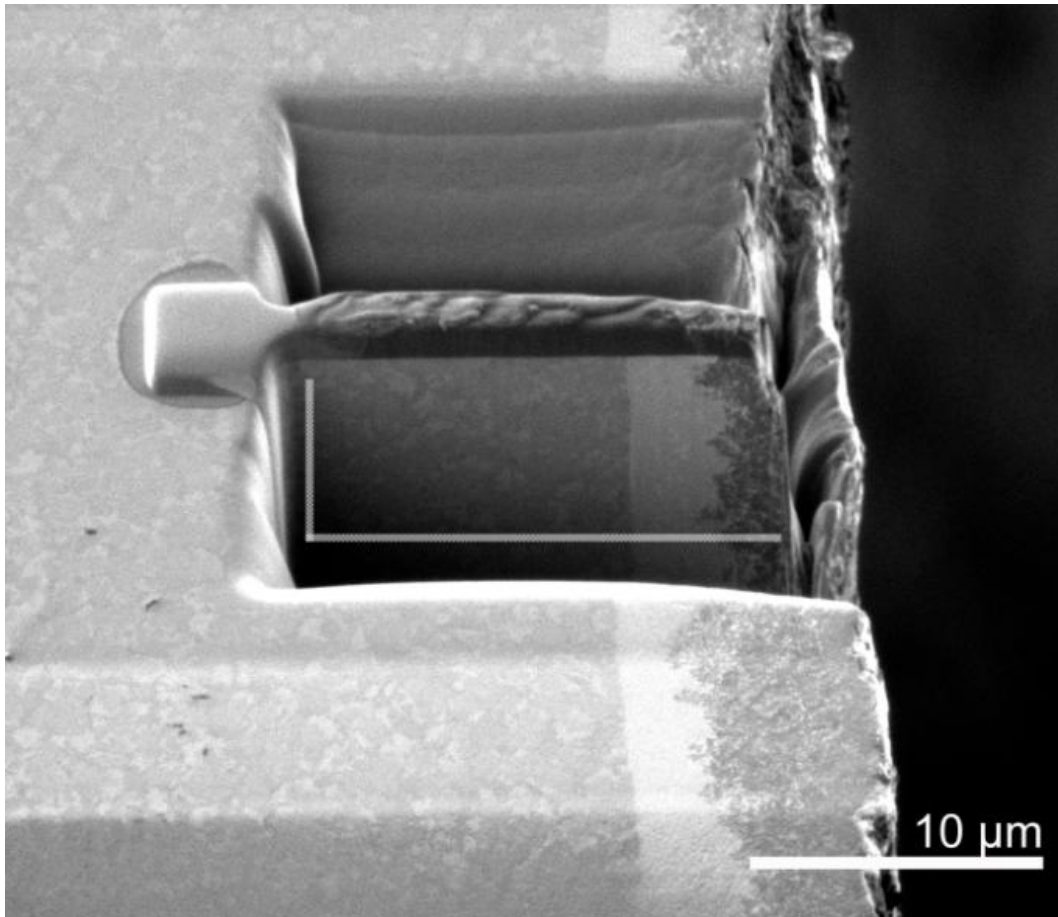


Fig. 9 The partially cut-out TEM sample taken from the surface of the nanocrystalline $\text{Ni}_{59.35}\text{Nb}_{34.45}\text{Sn}_{6.2}$ oxidized at 831 K for 19 h in dry oxygen. The oxide layer is visible on the surface (on the right of the image).

3.2.1.3. Atom Probe Tomography (APT)

In APT, an atom probe tip is mounted in a chamber, which is cooled to a low temperature ~ 20 K and equipped with a high vacuum system. A counter electrode is positioned in front of the tip. The tip is connected to a high voltage power supply and field evaporation of surface atoms can be induced by high voltage or laser pulsing. The generated ions are collected on a detector, where the

time-of-flight (t_f) and position of impact are recorded. For each detected ion, based on its t_f , a mass-to-charge ratio (M) is calculated by the relation

$$M = \frac{m}{n} = 2eV \left(\frac{t_f - t_0}{L_f} \right)^2, \quad (23)$$

where m and n are the mass and charge of the ion, respectively and e , V , t_0 and L_f are the electron charge, total voltage, time shift and flight distance, respectively. The M values of the detected ions are represented in the form of mass spectrum (histogram). Based on the mass spectrum, the chemical composition of the specimen can be determined. APT also offers the ability to map atom positions in 3D. The 3D reconstruction is built atom-by-atom by reverse projecting the detected ion positions onto the surface of a virtual specimen [57].

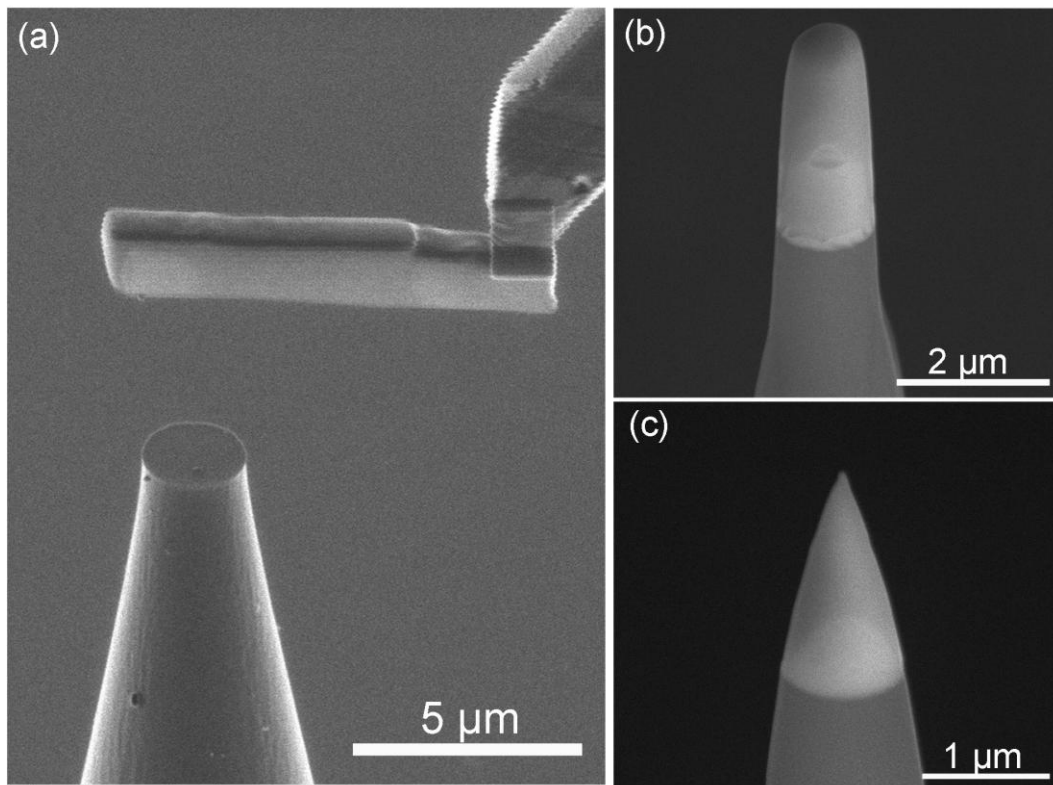


Fig. 10 Application of the FIB technique for atom probe sample preparation: **a)** wedge cut out of the sample and positioned on top of the Si post, **b)** intermediate shape of the tip, after a series of annular milling patterns were applied, **c)** final shape of the tip made from the as-cast amorphous sample of the $\text{Ni}_{59.35}\text{Nb}_{34.45}\text{Sn}_{6.2}$ composition.

The APT measurements were performed on four specimens (tips) of the as-cast amorphous $\text{Ni}_{59.35}\text{Nb}_{34.45}\text{Sn}_{6.2}$ composition and ten tips made from $\text{Ni}_{58.85}\text{Nb}_{34.45}\text{Sn}_{6.2}\text{Si}_{0.5}$ oxidized at $T_g - 50$ K (820 K) for 17 h. The preparation of tips was performed using a FIB technique, in a Helios Nanolab 600 (FEI) dual beam workstation. After protecting the surface of interest with a layer of Pt, a wedge shaped bar (15 μm long) was cut-out with an appropriately angled ion beam and transferred with a micro-manipulator to an array of Si posts (Fig. 10a). The wedge was positioned on top of

one of the Si posts, attached to it with a Pt-layer and a slice cut off. The remaining length of the wedge bar was sliced in the same way. Slices of the wedge bar were then milled with a series of annular milling patterns, with decreasing inner milling diameter and a progressively smaller electron beam current. The tip shape after milling with one of the intermediate milling patterns is shown in Fig. 10b. As a final milling step, a circle milling pattern and a very small electron beam current of 2 kV were used for milling across the entire tip surface in order to remove any implanted Ga⁺ ions, remaining Pt-layer or any other impurities and defects caused by the previous milling steps. The final tip shape of the amorphous sample is shown in Fig. 10c.

The method of random comparators is based on the comparison of the experimentally measured data to the simulated data of the theoretical system with the hypothetical properties. In this work the element frequency distribution analysis of the measured as-cast amorphous tips was compared to the simulated atom distribution in the system with the same composition as the real sample and the random atom distribution, i.e. binomial distribution based on the Bernoulli trial [57]:

$$f_b(n) = NP_b(n) = N \frac{n_d!}{n!(n_d - n)!} x_A^n (1 - x_A)^{(n_d - n)}, \quad (24)$$

where N is the number of blocks in which the reconstruction is divided into, P_b is the theoretical probability distribution, n_d is a total number of atoms in voxel, x_A is concentration of element A in the material and f_b(n) is number of blocks each containing n atoms of element A.

The statistical departure of the experimental frequency distribution, f_b(n), from the value estimated by the binomial frequency distribution, e(n) can be quantified by χ^2 and the Pearson coefficient, μ :

$$\chi_e^2 = \sum_{n=0}^{n_b} \frac{(e(n) - f_b(n))^2}{f_b(n)} \quad (25)$$

$$\mu = \sqrt{\frac{\chi_e^2}{N + \chi_e^2}}. \quad (26)$$

By comparing these two data sets even slight correlations in the atom distributions can be detected. The frequency distribution analysis of the as-cast amorphous specimens in this work was performed using 12334 blocks with a block size of 200 ions.

The atom probe characterization was also performed on the as-cast amorphous $\text{Ni}_{58.85}\text{Nb}_{34.45}\text{Sn}_{6.2}\text{Si}_{0.5}$ composition, oxidized at T_g-50 K (820 K) for 17 h. The wedges for the tip preparation were cut-out from the deeper parts of the oxide layer, which is shown in Fig. 11 (*inset*) with the white rectangle pattern. The final geometry of the tips is also shown in Fig. 11.

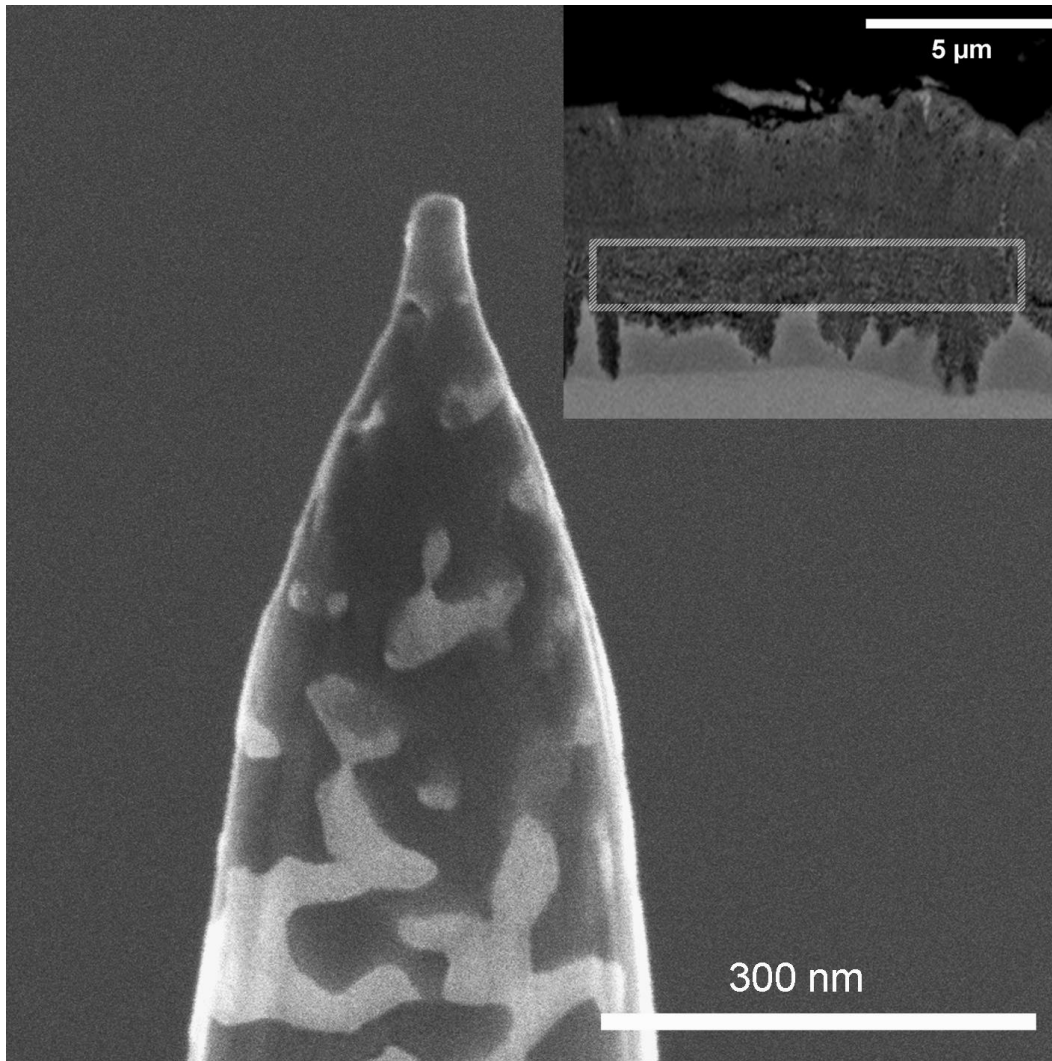


Fig. 11 SEM micrograph of a tip used for APT characterization for the as-cast amorphous $\text{Ni}_{58.85}\text{Nb}_{34.45}\text{Sn}_{6.2}\text{Si}_{0.5}$, oxidized at 820 K for 17 h. The tip was milled out from an internal scale area, as indicated with a white rectangle pattern in the *inset*.

Artifacts

Upon analysis of the data obtained from the APT measurements of the oxidized tips (Fig. 11), different field evaporation rates were observed at the interface between the darker and lighter phase and within the lighter phase itself. Due to this, different artifacts appeared in the reconstructions of the tips. First, a locally faster evaporation rate was observed along the interfaces due to the trajectory aberrations between the darker and the lighter phases. Secondly, due to the different evaporation rates of Sn and Ni (12 V/nm and 35 V/nm, respectively), the Ni was retained longer on the tip than Sn, resulting in the appearance of an inhomogeneous distribution of Ni and Sn in the

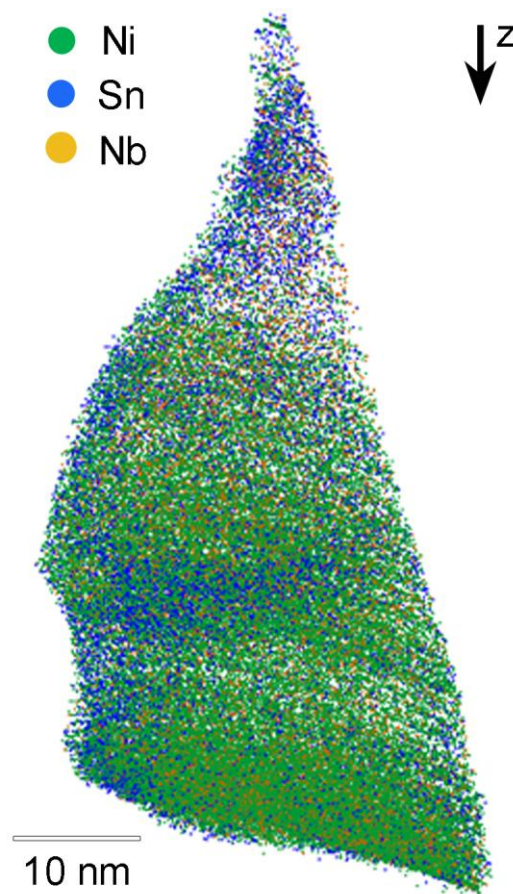


Fig. 12 Artifacts observed on the Ni-Nb-Sn based intermetallic phase measured on one of the tips extracted from the oxidized sample, as shown in Fig. 11. Different evaporation rates of Ni and Sn lead to the faster Sn evaporation (high Sn concentration on the top of the phase) and non-ordered evaporation of Ni and Sn leads to geometric artifacts (the phase appears elongated in the z direction). Furthermore, retention issues of different elements also result in the higher and lower density region within this phase.

reconstruction (Fig. 12), as well as a geometric distortion, i.e. phase elongation in the z direction (measurement direction). Density issues in the measurement direction were also observed. In the mass spectrum analysis the overlaps of Ni^{++} and O_2^+ at 32 a.m.u. and of Ni^+ and Sn^{++} at 58, 60 and

62 a.m.u., presented an additional difficulty. These difficulties and artifacts were taken in consideration when the material characteristic information was extracted from the measurement data. To avoid the trajectory aberration effect, interface analysis could not be performed and the interface regions were altogether avoided. Compositional analysis of the two phases was performed separately. In the case of the Ni-Nb-Sn based phase, where inhomogeneous distribution of the Ni and Sn as the result of different evaporation rates was observed, only the overall phase composition could be determined by eliminating 2-3 nm from the interface. The Nb-rich oxide phase is characterized with the evaporation of different complex ions. The decomposed values of the complex ion concentrations were used for determining the oxide phase stoichiometry.

3.2.2. X-Ray Diffraction (XRD)

The method of XRD was used to identify crystalline phases present in the samples and to verify the amorphicity of the glassy specimens. In some cases this method was used to estimate the size of crystalline phases. The characterization was conducted with the PANalytical X'Pert Pro diffractometer, using copper K_{α} ($\lambda = 1.154$ nm) radiation, at 45 kV and 40 mA. All samples were measured simultaneously. Due to the small size of some samples, lower maximum intensities in the XRD pattern were obtained. A putty, which was used to hold the sample, was separately measured and used as a reference to determine if the putty was measured together with the sample.

After background subtraction and the elimination of the $K_{\alpha 2}$ lines, the crystalline reflections and the amorphous halos were fitted with the Voigt function, $I(2\theta)_V$, which represents the linear combination of the Gauss, $I(2\theta)_G$ and Lorenz, $I(2\theta)_L$ functions:

$$I(2\theta)_V = (1 - M_v)I(2\theta)_G + M_v I(2\theta)_L \quad (27)$$

$$I(2\theta)_G = \frac{I_c}{\exp\left(4 \ln 2 \left(\frac{2\theta - x_c}{w_G}\right)^2\right)} \quad (28)$$

$$I(2\theta)_L = \frac{I_c}{1 + (2\theta - x_c)^2 w_L^2}, \quad (29)$$

where M_v is a linear factor, I_c and x_c are the intensity and 2θ position of the maximum, respectively, and w is the full width at half maximum [58]. Using Scherrer equation, Eq. (30) [58], the size, D , of the crystalline phases was estimated as

$$D = \frac{K\lambda}{w_L \cos(x_c)}, \quad (30)$$

where K is a constant which depends on the shape of the particle. In this case, a K value of 0.89 was used, which is derived from a spherical particle geometry. The Scherrer equation is considered to be applicable for a particle size $D < 150\text{-}200$ nm.

3.2.3. Calorimetry: Differential Thermal Analysis (DTA) and Differential Scanning Calorimetry (DSC)

Calorimetry is a method based on the measurement of heat exchange (ΔQ), which is related to temperature change as described by the equation

$$\Delta Q = mc\Delta T, \quad (31)$$

where m (kg) and c (J/kg·K) are mass and specific heat capacity of the material, respectively.

In DTA, a common furnace delivers a heat flow, \dot{Q} , to the sample a reference, and the temperature difference between the two is measured by separate thermocouples. During a reaction, heat is either released (exothermic) or taken in (endothermic), which is manifested by a change in slope of the measured signal, ΔT .

DSC is a method based on the measurement of the change in \dot{Q} to the sample and to the reference while each are subjected to a controlled temperature program [59]. Two different types of DSCs must be distinguished: 1) power-compensated DSC and 2) heat-flux DSC. In power-compensated DSC, the sample and references are placed into mutually isolated furnaces. The temperatures of the sample and the reference are maintained equal by regulating delivered heating power to their separate furnaces. Since thermal symmetry is applicable between the sample and the reference, any event causing the change of the sample's heat capacity will disrupt the temperature equality between the sample and the reference. In order to compensate the temperature difference between the sample and reference, a change in heating power is needed. This heating power is directly proportional to the heat flow (\dot{Q}) in or out of the sample,

$$\dot{Q} = mc \frac{dT}{dt}, \quad (32)$$

where dT/dt is the applied heating rate.

In heat flux DSC, the measured signal is, similar to DTA, the temperature difference between the sample and the reference. This temperature difference (ΔT) is then used to determine heat flow (\dot{Q}) through the equation

$$\dot{Q} = K\Delta T, \quad (33)$$

where K is a calibration constant. Different designs of heat flux DSC exist. In the case of the disc-type design used in this work, the main heat flow from the furnace to the sample and reference is provided by a disk having good thermal conductivity. Due to the presence of the thermally conducting disc, changes in sample temperature can influence the reference temperature. The disc-type DSC is therefore not a real twin-furnace design, in contrast to power-compensated DSC, and care must be taken when interpreting results.

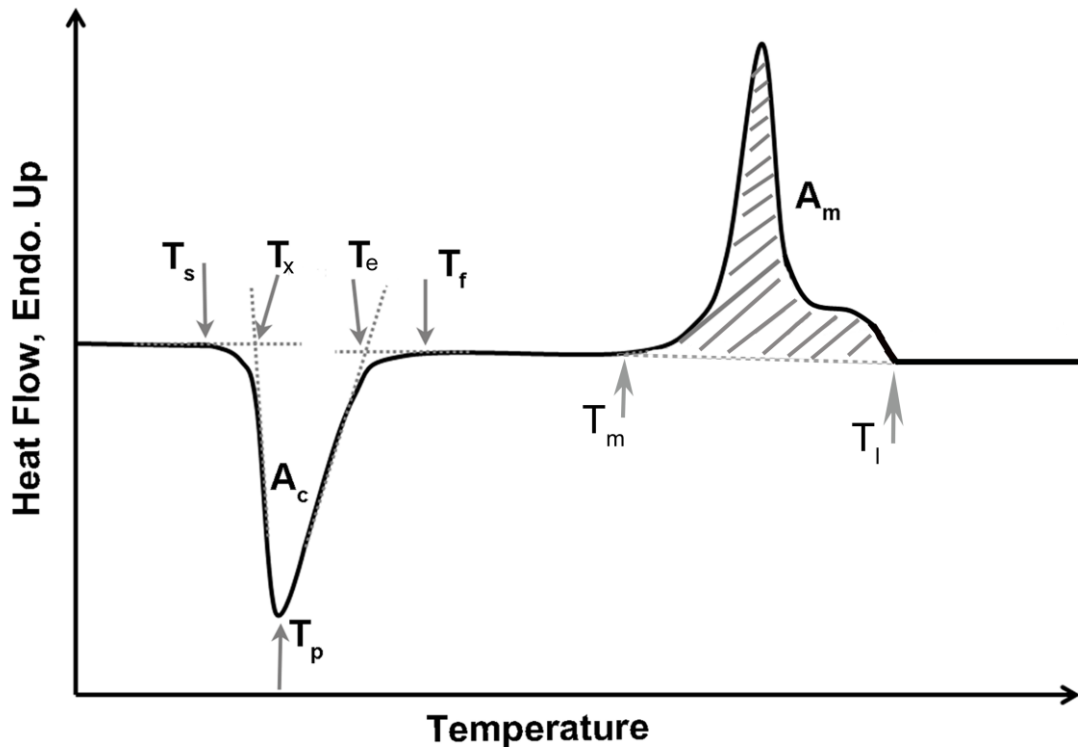


Fig. 13 Schematic representation of a heat flow curve measured under a constant heating rate. The exothermic crystallization and the endothermic melting events are marked with A_c and A_m .

DSC measurements can be conducted as isothermal or constant heating/cooling rate measurements. The results are usually presented in the form of a heat flow (\dot{Q}) vs. time (t) or temperature (T) curve. A schematic presentation of a constant heating (up-scan) measurement with crystallization and melting events is presented in Fig. 13. Exothermic crystallization and endothermic melting events, marked in Fig. 13 with areas A_c and A_m , respectively, occur in the form of peaks. The glass transition region is not shown in Fig. 13 but it has a form of a step-like endothermic event, which forms due to the change in the heat capacity of the sample before and after the glass transition. The characterization of the above mentioned events is conducted after subtraction of the baseline.

In this thesis the baseline corresponds to a subsequent, identical measurement of the already crystallized sample. Since the melting event is a reversible process, no baseline was able to be subtracted for measurements in this temperature range. The characteristic temperatures of an event are schematically presented in Fig. 13. Taking the crystallization event as an example, T_s and T_f are the temperatures where measured curve starts and stops to deviate from the baseline, respectively. T_x and T_e are the temperatures where the interpolated baseline is intersected by the tangents placed on the peak slopes. T_p is the position of the center of the peak of the event. Although the glass transition region is not schematically shown in Fig. 13, the onset and the end temperature of glass transition region (T_g and T_g^{end}) are also defined as the temperatures where the interpolated baseline and the tangent placed on the glass transition slope intersect. The area of crystallization (A_c) and melting peak (A_m) are proportional to the enthalpy of crystallization and fusion, respectively.

Each specimen was heated with a constant heating rate of 0.33 K/s under constant flow (50 ml/min) of argon 6.0, from room temperature up to the set temperature above the liquidus and then cooled to room temperature also with the cooling rate of 0.33 K/s. Measurements were conducted in a NETZSCH STA 449/C/6/MFC/G Jupiter Differential Thermal Analyzer with a TG-DSC head, i.e. a heat-flux DSC design. For every up-scan the baseline was also measured under identical conditions and subtracted from the initial scan.

3.2.4. Thermo Gravimetric Method of Oxidation (TGA)

The TGA method is based on monitoring the sample mass as a function of time or temperature while having the sample subjected to a set temperature program under a specific gas flux. In the case of isothermal oxidation, a sample of precisely measured mass, surface area and well-defined surface quality is placed in the sample holder on top of a precision balance. The sample holder resides in a furnace, which is provided with a constant flow of gas. Prior to oxidation, the samples were mechanically ground on SiC papers of 320 and 600 fines. After measuring the surface areas of the samples and cleaning them in an ultrasonic bath of acetone and then ethanol, the samples were weighed and inserted into the oxidation chamber.

In this study a NETZSCH STA 449/C/6/MFC/G Jupiter Differential Thermal Analyzer with a TG head was used for oxidation. The oxidation chamber was flushed for 10 min with Ar 4.6 (50 ml/min) and another 10 min with pure dry O₂ (50 ml/min). In 10 min, under a 50 ml/min gas flow, a volume of gas equal to the three times the volume of the oxidation chamber passes through. After flushing the chamber, the sample was heated with 0.83 K/s up to the oxidation temperature and then held isothermally in dry O₂ while measuring mass gain (mg) with time (s). At the end of the isothermal oxidation time, the sample was cooled to room temperature with 0.57 K/s under a flow of Ar. In addition to the sample measurement, a baseline with no sample under identical

experimental conditions was measured and then subtracted from the raw measurement data. After subtracting the baseline, the mass gain was normalized by the oxidizing surface area. The initial heating time to reach the oxidation temperature corresponds to the incubation time (t_h) having a corresponding mass gain (m_h). Both were then subtracted from the normalized curve in order to show *isothermal behavior* only. It was determined, based on the isothermal oxidation of five samples with the same preparation and structure that the mass gain measurements are reliable with a tolerance of 0.1 mg/cm^2 .

The samples were oxidized at different temperatures below the glass transition. For the same composition, micro- and nanocrystalline samples, as well as the thermally treated amorphous samples were oxidized at the same set of temperatures as the as-cast amorphous samples.

The oxidation times for different Ni-Nb-Sn based compositions were determined according to the TTT diagram of the $\text{Ni}_{60}\text{Nb}_{35}\text{Sn}_5$ composition [31] shown in Fig. 5. The TTT diagram of the $\text{Ni}_{60}\text{Nb}_{35}\text{Sn}_5$ composition was first modified for the composition in question. The procedure of modification is shown in Fig. 14, in the case of the $\text{Ni}_{57}\text{Nb}_{34}\text{Sn}_9$ composition. Lines marked with 1% and 99 % correspond to the onset and end times of crystallization, respectively, of the $\text{Ni}_{60}\text{Nb}_{35}\text{Sn}_5$ composition, estimated from isothermal DSC measurements [31]. The line marked with b in Fig. 14 represents an approximate relaxation time, τ_{rel} , at T_g [8], where T_g and τ_{rel} were determined from constant heating rate up-scans. τ_{rel} is calculated as:

$$\tau_{rel} = \frac{T_g^{end} - T_g}{q_h} = \frac{\Delta T_g}{q_h}, \quad (34)$$

where q_h represents the heating rate. In Fig. 14, the point A represents τ_{rel} at T_g , determined for the $\text{Ni}_{60}\text{Nb}_{35}\text{Sn}_5$ composition for $q_h = 0.33 \text{ K/s}$. Point B, in Fig. 14, represents τ_{rel} at T_g , determined here for the composition $\text{Ni}_{57}\text{Nb}_{34}\text{Sn}_9$, also with $q_h = 0.33 \text{ K/s}$. Lines marked with b, 1 % and 99 % are then shifted for the same increment, so that the point A coincides with point B, as shown in Fig. 14. The lines obtained in this way are marked with b', (1%)' and (99 %)', and represent the TTT diagram modified for the $\text{Ni}_{57}\text{Nb}_{34}\text{Sn}_9$ composition. Using the (1%)' line, the time to the onset of crystallization, τ_c , at the temperature chosen for isothermal oxidation, T_{ox} , was determined, as illustrated in Fig. 14. The oxidation time is then chosen to be 75 % of τ_c , i.e. 25 % shorter than τ_c .

The oxidation times of the binary Ni-Nb compositions are chosen in this work independently from the expected time for the onset of crystallization. The reason for that decision is that the times to the onset of crystallization at the temperatures of interest (50 to 80 K below T_g) according to the TTT diagram of the binary Ni-Nb system (Fig. 5 and Ref. [30]), are very short, on the order of a few tens of seconds.

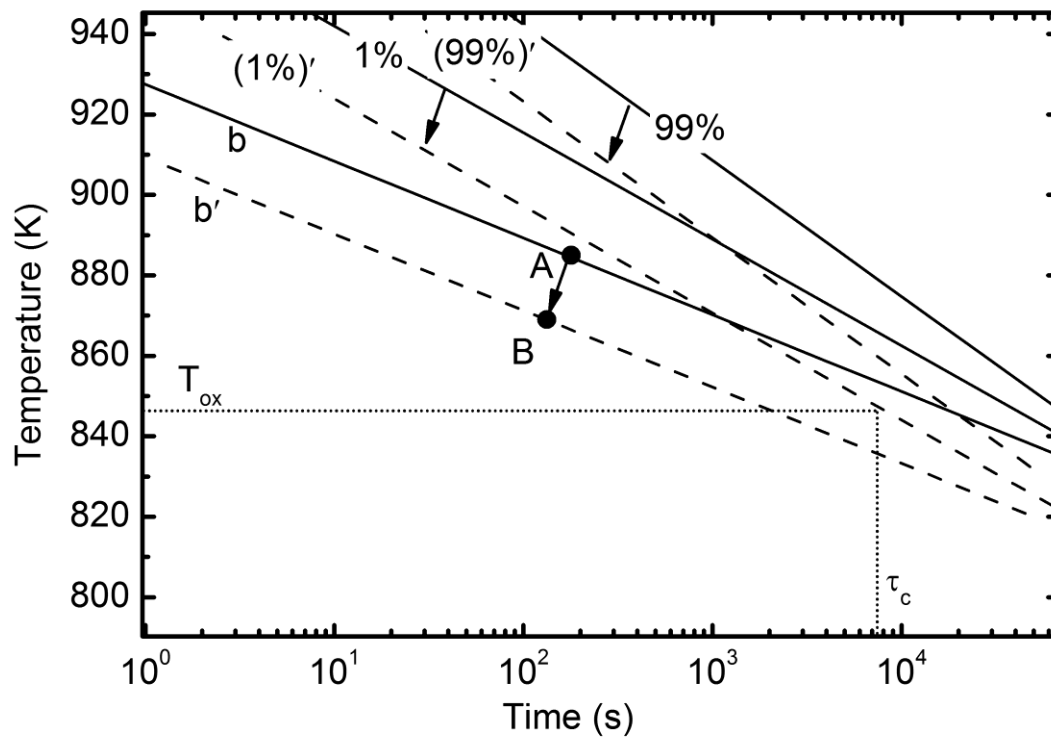


Fig. 14 TTT diagram of $\text{Ni}_{60}\text{Nb}_{35}\text{Sn}_5$ [31] and the *modification procedure* for the $\text{Ni}_{57}\text{Nb}_{34}\text{Sn}_9$ composition. Line b is the approximated τ_{rel} , at T_g , determined from constant heating rate up-scans in Ref [8] and lines 1 % and 99 % represent the onset and the end of crystallization, respectively. Points A and B represent τ_{rel} at T_g determined with $q_h = 0.33$ K/s for $\text{Ni}_{60}\text{Nb}_{35}\text{Sn}_5$ and $\text{Ni}_{57}\text{Nb}_{34}\text{Sn}_9$, respectively. Lines b', (1 %) ' and (99 %) ' represent the TTT diagram modified for $\text{Ni}_{57}\text{Nb}_{34}\text{Sn}_9$ composition. T_{ox} and τ_c are the illustrations of oxidation temperature and time to onset of crystallization.

3.3. Sample Treatments

Description of the various samples and applied heat treatments are described in this section. The samples, applied heat treatments, assigned labels and experiments, in which these samples were used, are listed in Table 2.

Eight different Ni-Nb(-Sn) compositions, from the binary $\text{Ni}_{70}\text{Nb}_{30}$, $\text{Ni}_{62}\text{Nb}_{38}$ and $\text{Ni}_{59.5}\text{Nb}_{40.5}$ to the ternary $\text{Ni}_{62}\text{Nb}_{35}\text{Sn}_3$, $\text{Ni}_{59.35}\text{Nb}_{34.45}\text{Sn}_{6.2}$ and $\text{Ni}_{57}\text{Nb}_{34}\text{Sn}_9$ and quaternary $\text{Ni}_{58.85}\text{Nb}_{34.45}\text{Sn}_{6.2}\text{Si}_{0.5}$ and $\text{Ni}_{60}\text{Nb}_{36}\text{Sn}_3\text{B}_1$, were studied. The amorphous samples of each composition were produced by suction casting, with the exceptions of $\text{Ni}_{70}\text{Nb}_{30}$, which was melt-spun in 1987 by R. Busch [27].

The ingots, produced by melt solidification on a water cooled Cu-plate in the arc melter, were also characterized and used in the oxidation experiments. These microcrystalline specimens are hereafter referred to as the *master alloy*. The heat treatments, which were applied to the as-cast amorphous and the master alloy specimens, are discussed below.

A horizontal quartz tube furnace, equipped with a vacuum system (10^{-4} mbar) was used for isothermal vacuum heat treatments of the as-cast amorphous Ni-Nb-Sn samples. In *heat treatment 1 (HT1)*, the samples were heated with a rate of 0.45 K/s up to the hold temperature (T_{iso}) and then held isothermally (± 1 K) for a set time. After that, the furnace was switched off and the samples were left to cool under vacuum. The cooling rate decreased from 0.54 K/s at high temperatures ($T > 573$ K) to 0.17 K/s at low temperatures ($T < 573$ K). *Heat treatment 2 (HT2)* differs from *HT1* only where the temperature during heating approaches T_{iso} . In *HT2*, the temperature rises to 7 K above T_{iso} and then decreases to T_{iso} , where it stays constant within ± 1 K during remaining isothermal time. The process of overheating and returning to T_{iso} lasts a total of 15 min.

Specimens of the crystalline master alloy were melted in a NETZSCH STA 449/C/6/MFC/G Jupiter Differential Thermal Analyzer with a TG head, in an Al_2O_3 beaker, under an Ar (4.6) flow of 50 ml/min. Pieces of the master alloy were heated up with 0.83 K/s to a temperature 30 K above the liquidus temperature (T_l) and then cooled with 0.1 K/s to 1073 K and with 0.57 K/s further to the room temperature. Specimens treated with this type of thermal regime will be referred to as *equilibrium cooled*.

A second type of treatment in the DTA was carried out using a heat-flux DSC sample holder. This type of treatment was performed in order to observe possible crystallization events as they occur during annealing on a \dot{Q} vs. t or \dot{Q} vs. T curve. An amorphous sample was heated with a constant rate of 0.33 K/s up to the temperature at which one of the crystallization events was finished, or in the case when two events partially overlapped, to the temperature before the onset of the next crystallization event. After reaching this set temperature, the sample was cooled with a maximum cooling rate, which was 0.75 K/s at higher temperatures and 0.52 K/s at ~ 573 K. The samples annealed in this way will be referred to as being annealed with *heat treatment 3 (HT3)*.

The isothermal heat treatments of as-cast amorphous $Ni_{57}Nb_{34}Sn_9$ composition were carried out in a power-compensated Perkin-Elmer Diamond DSC. The measurement was performed in Al pans under a constant flow (50 ml/min) of ultra high purity Ar-gas (6.0). This sample is indicated in Table 2 as *heat treatment 4 (HT4)*.

Table 2 Experimental sample compositions, heat treatments, labels and experiments for which the samples were used.

<i>Composition</i>	<i>Heat treatment/ Description</i>	<i>Label</i>	<i>Experiments</i>	<i>Experiments after TGA</i>
$Ni_{70}Nb_{30}^{a)}$	Melt spun/amorphous	Ni70A	XRD, DTA,	SEM, EDX
$Ni_{62}Nb_{38}$	Suction cast/amorphous	Ni62A	TGA ^{b)}	XRD, SEM,
	Master alloy	Ni62M	XRD, TGA	EDX
$Ni_{59.5}Nb_{40.5}$	Suction cast/amorphous	Ni59.5A	XRD, DTA	
$Ni_{62}Nb_{35}Sn_3$	Suction cast/amorphous	Sn3A		
	Master alloy	Sn3M	XRD	
$Ni_{59.35}Nb_{34.45}Sn_{6.2}$	Suction cast/amorphous	Sn6.2A	XRD, DTA, APT, TGA	XRD, SEM, EDX
	HT1 at 831 K for 2.5 h	R2.5h	DTA, TGA	XRD, SEM, EDX, EBSD
	HT1 at 831 K for 15 h	R15h	XRD, DTA, TGA	
	HT3 up to 933 K	Nq933K	XRD, DTA, TGA	XRD ^{c)} , SEM, EDX
	HT3 up to 983 K	Nq983K	XRD	
	HT3 up to 1073 K	Nq1073K		
	HT3 up to 1223 K	Nq1223K		
	HT2 at 831 K for 15 h	Ni15h	XRD, TGA	XRD ^{c)} SEM, EDX, TEM
	HT2 at 831 K for 19 h	Ni19h		XRD ^{c)}
	Master alloy	Sn6.2M	XRD, SEM, EDX, TGA	XRD ^{c)} , SEM, EDX
Equilibrium cooled	Sn6.2E	SEM, EDX, TGA	XRD ^{c)} , SEM, EDX	
$Ni_{57}Nb_{34}Sn_9$	Suction cast/amorphous	Sn9A	XRD, DTA, TGA at 80, 50 and 20 K below the T_g	XRD
	HT4 at 846 K for 28 h	Ni28h	XRD, TGA	XRD, DTA
	HT3 up to 933 K	Sn9Nq933K	XRD	
	Master alloy	Sn9M	XRD, SEM, EDX, TGA	XRD

<i>Composition</i>	<i>Heat treatment/ Description</i>	<i>Label</i>	<i>Experiments</i>	<i>Experiments after TGA</i>
	Equilibrium cooled	Sn9E	SEM, EDX, TGA	XRD
$Ni_{58.85}Nb_{34.45}Sn_{6.2}Si_{0.5}$	Suction cast/amorphous	Si0.5A	XRD, DTA, TGA	XRD, SEM, EDX, APT
$Ni_{60}Nb_{36}Sn_3B_1$	Suction cast/amorphous	B1A	XRD, DTA, TGA at 80, 50 and 20 K below the T_g	XRD, SEM, EDX
	Master alloy	B1M	TGA	XRD

- a- The $Ni_{70}Nb_{30}$ sample was melt-spun into thin ribbons by R. Busch in 1988 (see [27])
- b- Unless otherwise indicated in the table, TG measurement was conducted at T_g-50 K
- c- XRD pattern can be found in Appendix A4

4. Results

4.1. Amorphous Structure

The amorphous structure of the suction cast plates belonging to the $\text{Ni}_{59.5}\text{Nb}_{40.5}$, $\text{Ni}_{62}\text{Nb}_{38}$, $\text{Ni}_{70}\text{Nb}_{30}$, $\text{Ni}_{62}\text{Nb}_{35}\text{Sn}_3$, $\text{Ni}_{59.35}\text{Nb}_{34.45}\text{Sn}_{6.2}$, $\text{Ni}_{57}\text{Nb}_{34}\text{Sn}_9$, $\text{Ni}_{58.85}\text{Nb}_{34.45}\text{Sn}_{6.2}\text{Si}_{0.5}$ and $\text{Ni}_{60}\text{Nb}_{36}\text{Sn}_3\text{B}_1$ compositions is characterized by means of XRD and the results are presented in Section 4.1.1. In Section 4.1.2, the results of the APT investigations will be presented for the $\text{Ni}_{59.35}\text{Nb}_{34.45}\text{Sn}_{6.2}$ composition.

4.1.1. XRD Characterization

The XRD pattern obtained from the ground surfaces of the as-cast alloys of different compositions are shown in Fig. 15. For better overview the curves have been vertically shifted, the XRD pattern of $\text{Ni}_{62}\text{Nb}_{38}$ and $\text{Ni}_{58.85}\text{Nb}_{34.45}\text{Sn}_{6.2}\text{Si}_{0.5}$ compositions are magnified 2 \times and of the $\text{Ni}_{59.5}\text{Nb}_{40.5}$ composition 4 \times . All samples show a broad amorphous halo occurring from between 35 $^\circ$ to 55 $^\circ$. Reflections of crystalline phases were not observed on any of these XRD pattern, hence these samples are considered to be x-ray amorphous. However, slight deviations from the broad peak can be observed in the XRD pattern of the $\text{Ni}_{62}\text{Nb}_{35}\text{Sn}_3$ specimen, which may indicate the presence of small amounts of crystalline volume fractions in the sample. Table 3 reports the 2θ values of the amorphous halo maximum, x_c ; the corresponding atomic distances, d_c ; and the thicknesses of the investigated plates, t . The fitting error for x_c was less or equal to 0.01 $^\circ$ except for the $\text{Ni}_{59.5}\text{Nb}_{40.5}$ sample where the error was 0.02 $^\circ$.

Table 3 The compositions and critical casting thicknesses, t_c , of the as-cast amorphous samples shown in Fig. 15, as well as the 2θ positions and the corresponding interatomic distances, d_c of the amorphous halo maxima, x_c .

Composition	t_c (mm)	x_c (degrees)	d_c (Å)
$\text{Ni}_{59.5}\text{Nb}_{40.5}$	0.5	42.52	2.12
$\text{Ni}_{62}\text{Nb}_{38}$	0.5	42.43	2.13
$\text{Ni}_{70}\text{Nb}_{30}$	0.02-0.05	43.29	1.68
$\text{Ni}_{62}\text{Nb}_{35}\text{Sn}_3$	0.5	42.57	2.12
$\text{Ni}_{59.35}\text{Nb}_{34.45}\text{Sn}_{6.2}$	1	42.26	2.14
$\text{Ni}_{57}\text{Nb}_{34}\text{Sn}_9$	1	42.07	2.15
$\text{Ni}_{58.85}\text{Nb}_{34.45}\text{Sn}_{6.2}\text{Si}_{0.5}$	0.5	42.18	2.14
$\text{Ni}_{60}\text{Nb}_{36}\text{Sn}_3\text{B}_1$	1	42.43	2.13

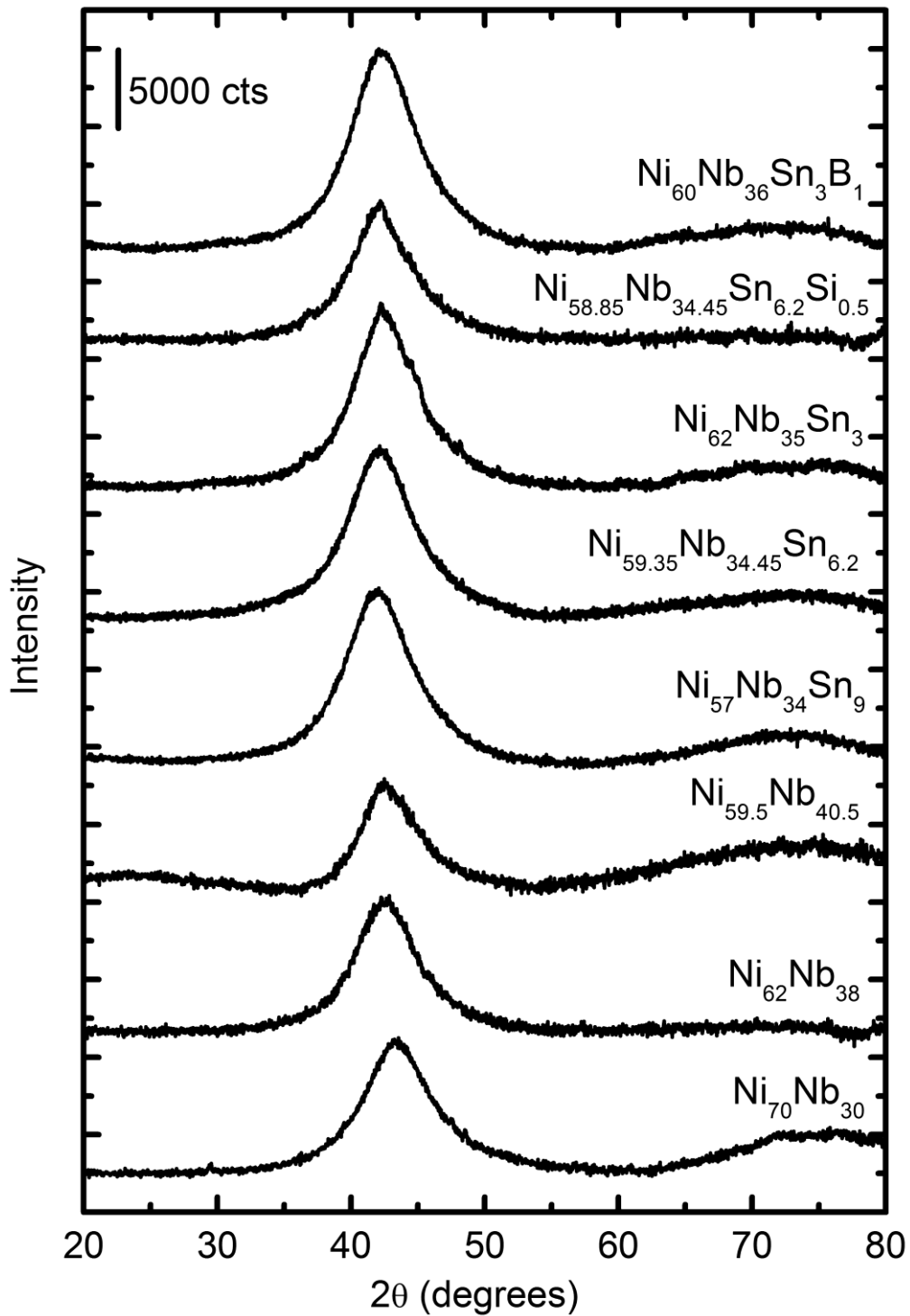


Fig. 15 The XRD patterns of the as-cast samples of different compositions. The curves have been vertically shifted for easier comparison. The thicknesses of the castings are given in Table 3.

4.1.2. APT Characterization

In Fig. 16 the atom probe mass spectrum of the suction cast amorphous $\text{Ni}_{59.35}\text{Nb}_{34.45}\text{Sn}_{6.2}$ alloy is shown along with its assessed baseline. The composition of the specimen, after applying a complete peak decomposition algorithm, was determined to be 58.18 ± 0.046 at.% Ni, 34.549 ± 0.041 at.% Nb and 6.396 ± 0.027 at.% Sn.

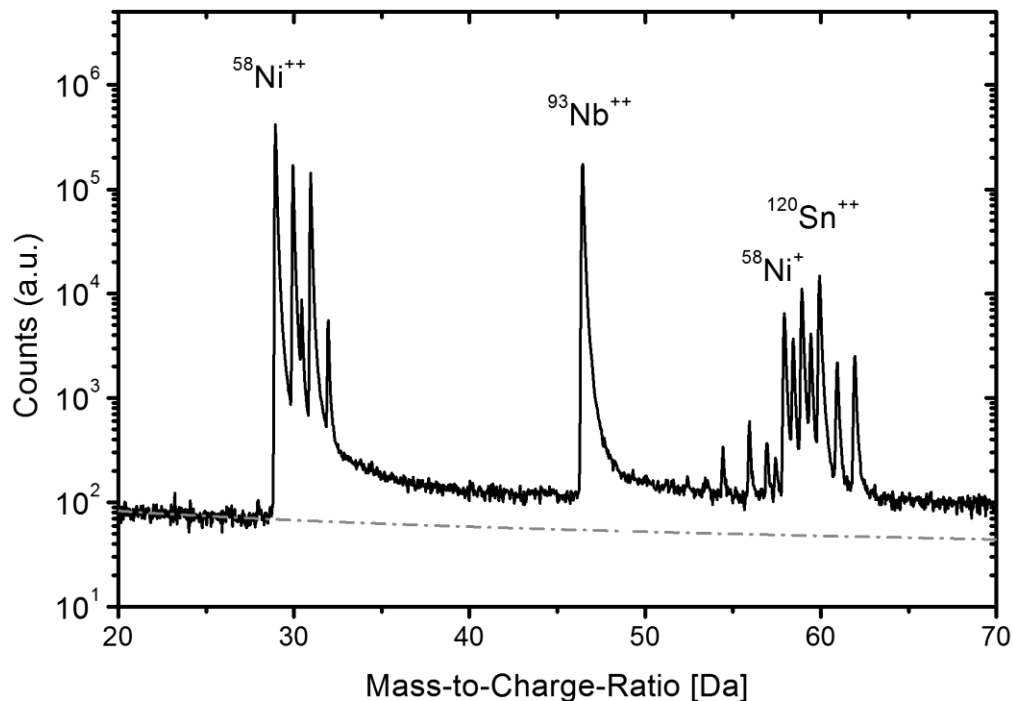


Fig. 16 The atom probe mass spectrum of as-cast amorphous $\text{Ni}_{59.35}\text{Nb}_{34.45}\text{Sn}_{6.2}$. The solid curve represents the mass spectrum and the gray dashed line is baseline.

One-dimensional concentration profiles of the as-cast amorphous $\text{Ni}_{59.35}\text{Nb}_{34.45}\text{Sn}_{6.2}$ sample are shown in Fig. 17. The profiles are determined in the lateral direction (x-direction) and in the direction of the tip depth (z-direction). Within the measured distances, the concentrations of Ni, Nb and Sn are observed to be relatively constant, with small local concentration fluctuations of ~ 1.5 at.%.

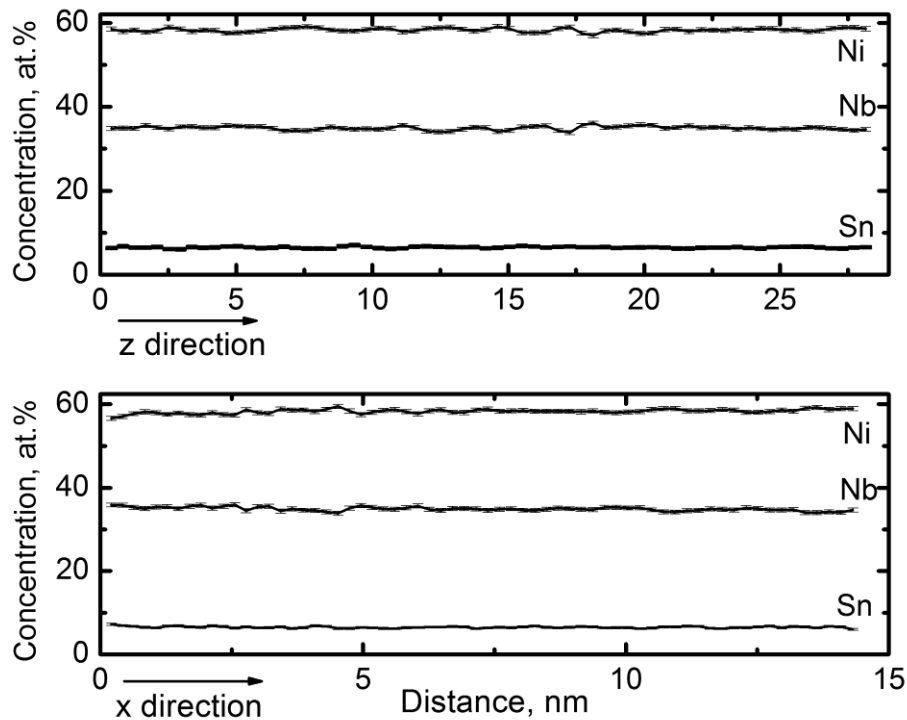


Fig. 17 1-dimensional concentration profiles, in the lateral and vertical directions of the tip (x- and z-directions, respectively) of as-cast amorphous $\text{Ni}_{59.35}\text{Nb}_{34.45}\text{Sn}_{6.2}$. Small composition fluctuations of ± 1.5 at.% are noticed throughout.

In Fig. 18 the results of the frequency distribution analysis of the elements in the amorphous $\text{Ni}_{59.35}\text{Nb}_{34.45}\text{Sn}_{6.2}$ sample (solid lines) are shown. The distribution of each element, as determined experimentally is compared to the calculated curves, which represent a random distribution of each element in the same composition (dashed lines). The experimental and calculated frequency distributions overlap ideally for all three elements in the alloy (Ni, Nb and Sn). The Pearson coefficient, μ , is not greater than 0.1 for distributions of all these elements, which implies a homogeneous structure.

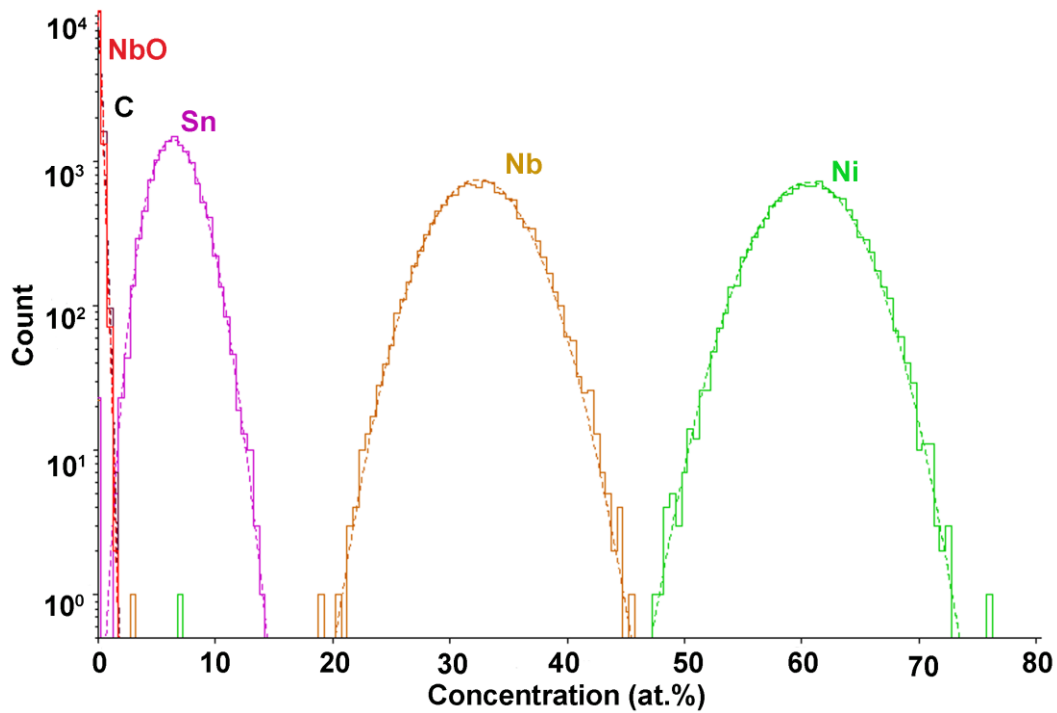


Fig. 18 Distribution functions of the elements in amorphous $\text{Ni}_{59.35}\text{Nb}_{34.45}\text{Sn}_{6.2}$. are shown with solid lines. Dashed lines represent distribution functions of elements in the case of random distribution.

4.2. Crystallization

4.2.1. Calorimetric Characterizations

4.2.1.1. Ni-Nb

Calorimetric up-scans (heat-flux DSC) of the three as-cast binary Ni-Nb alloys are shown in Fig. 19. The $\text{Ni}_{62}\text{Nb}_{38}$ and $\text{Ni}_{59.5}\text{Nb}_{40.5}$ compositions were suction cast (this work) into 0.5 mm thick plates and the $\text{Ni}_{70}\text{Nb}_{30}$ composition was melt spun into ribbons in 1987 by R. Busch [27]. The $\text{Ni}_{62}\text{Nb}_{38}$ up-scan shows a clearly observable step-like glass transition event (marked with an arrow in Fig. 19), after which crystallization proceeds in three events, where the first and the second events overlap significantly. Upon heating of $\text{Ni}_{70}\text{Nb}_{30}$ and $\text{Ni}_{59.5}\text{Nb}_{40.5}$, no glass transition region was observed, in contrast to $\text{Ni}_{62}\text{Nb}_{38}$ (see Fig. 19). The crystallization of $\text{Ni}_{70}\text{Nb}_{30}$ and $\text{Ni}_{59.5}\text{Nb}_{40.5}$ proceeds in three and four exothermal events, respectively. The up-scan of the $\text{Ni}_{70}\text{Nb}_{30}$ sample contained an exothermic slope, which was not completely eliminated by baseline subtraction. Therefore, for easier comparison with the other two scans in Fig. 19, an additional baseline was constructed using OriginPro 8.5 Software and subtracted. The characteristic thermophysical

properties of the $\text{Ni}_{59.5}\text{Nb}_{40.5}$, $\text{Ni}_{62}\text{Nb}_{38}$ and $\text{Ni}_{70}\text{Nb}_{30}$ alloys determined in Fig. 19 are given in Table 4.

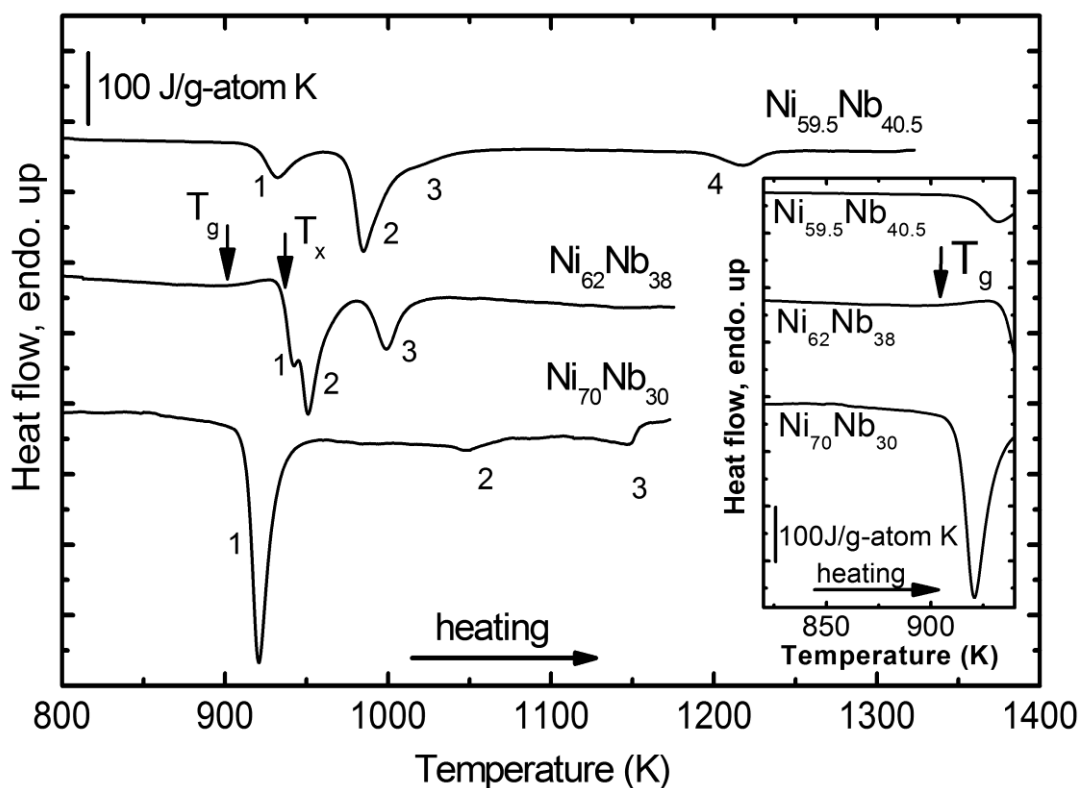


Fig. 19 The calorimetric up-scans of the amorphous binary Ni-Nb alloys determined with a constant heating rate of 0.33 K/s. The $\text{Ni}_{59.5}\text{Nb}_{40.5}$ and $\text{Ni}_{62}\text{Nb}_{38}$ compositions were suction cast into amorphous plates (this work) and the $\text{Ni}_{70}\text{Nb}_{30}$ was melt spun into amorphous strips (R. Busch [27]). The inset shows magnification of the temperature interval 820-940 K. The curves have been vertically shifted.

4.2.1.2. Ni-Nb-Sn

The calorimetric up-scans (heat-flux DSC) of the three as-cast amorphous Ni-Nb-Sn alloys are shown in Fig. 20a. All three thermograms show a well defined glass transition onset prior to crystallization. The onsets of the glass transition temperatures are marked with arrows. It is also observable in Fig. 20a that the onset of the glass transition (T_g) and crystallization (T_x), as well as the end of the crystallization (T_e) and the temperature interval T_x-T_e , increase in the order: $\text{Ni}_{57}\text{Nb}_{34}\text{Sn}_9 < \text{Ni}_{59.35}\text{Nb}_{34.45}\text{Sn}_{6.2} < \text{Ni}_{62}\text{Nb}_{35}\text{Sn}_3$. The crystallization of $\text{Ni}_{57}\text{Nb}_{34}\text{Sn}_9$ and $\text{Ni}_{59.35}\text{Nb}_{34.45}\text{Sn}_{6.2}$ proceeds in four exothermic events and in $\text{Ni}_{62}\text{Nb}_{35}\text{Sn}_3$ in three exothermic events.

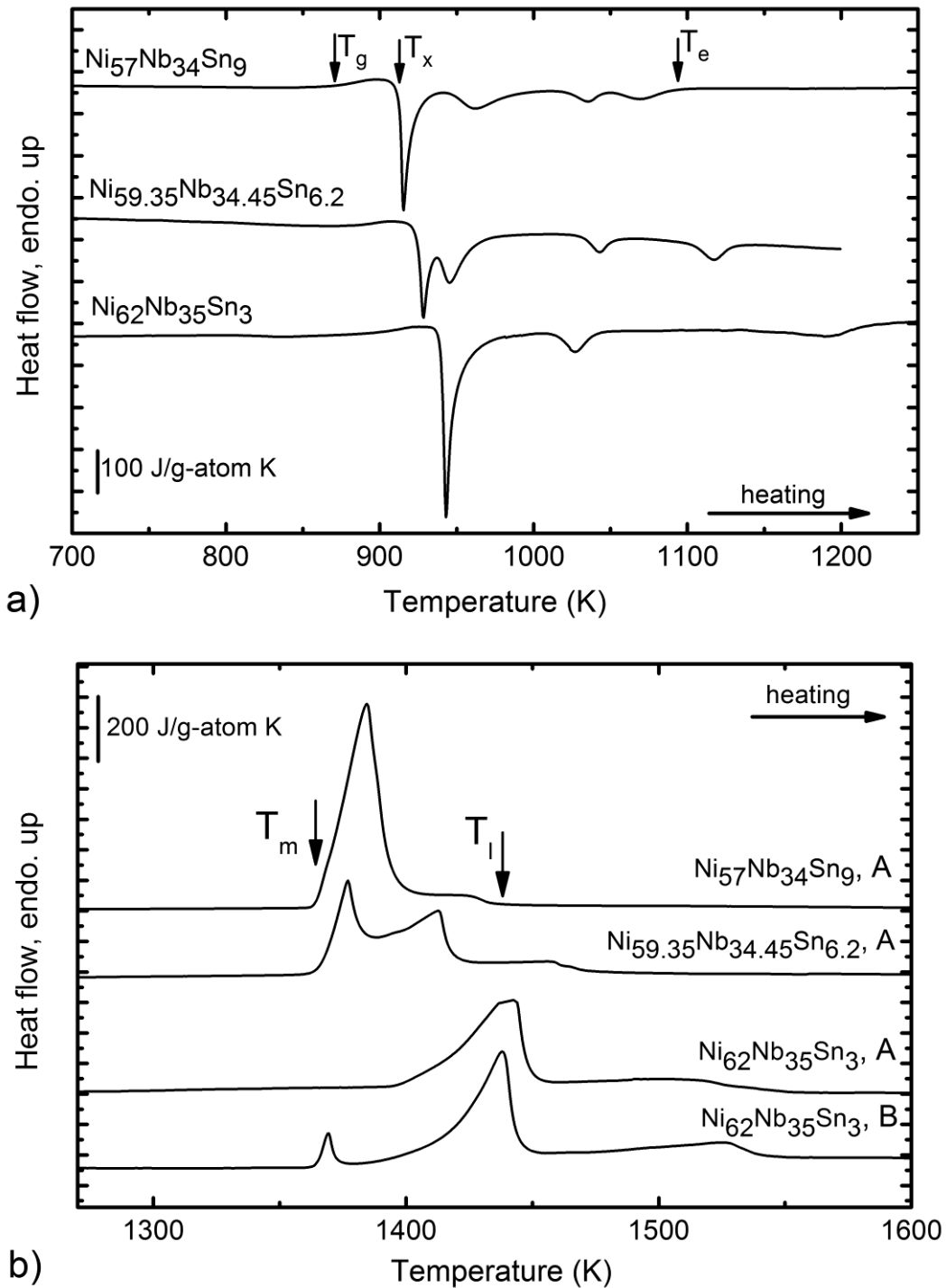


Fig. 20 The calorimetric up-scans of the ternary Ni-Nb-Sn alloys: **a)** upon heating from the as-cast amorphous state to the end of crystallization, **b)** upon heating through the melting region. The up-scans of the $\text{Ni}_{57}\text{Nb}_{34}\text{Sn}_9$, $\text{Ni}_{59.35}\text{Nb}_{34.45}\text{Sn}_{6.2}$ and $\text{Ni}_{62}\text{Nb}_{35}\text{Sn}_3$ compositions marked with A, represent the continuation of the heating process from a. The curve B of the $\text{Ni}_{62}\text{Nb}_{35}\text{Sn}_3$ composition represents the melting upon the second up-scan. The curves have been vertically shifted.

The primary crystallization event in $\text{Ni}_{57}\text{Nb}_{34}\text{Sn}_9$ is the most pronounced of all four events in that measurement. The first crystallization event in $\text{Ni}_{59.35}\text{Nb}_{34.45}\text{Sn}_{6.2}$ is smaller compared to second event, which is more pronounced than in $\text{Ni}_{57}\text{Nb}_{34}\text{Sn}_9$ and starts at lower temperatures. The primary crystallization event is shifted to higher temperatures in $\text{Ni}_{62}\text{Nb}_{35}\text{Sn}_3$, with respect to the other two compositions. The characteristic thermophysical values of the investigated composition in the ternary Ni-Nb-Sn system, as determined from the calorimetric measurements shown in Fig. 20, are given in Table 4.

In Fig. 20b, the melting regions of three ternary alloys: $\text{Ni}_{57}\text{Nb}_{34}\text{Sn}_9$, $\text{Ni}_{59.35}\text{Nb}_{34.45}\text{Sn}_{6.2}$ and $\text{Ni}_{62}\text{Nb}_{35}\text{Sn}_3$, are shown. The curves marked with A in Fig. 20b represent the melting peaks after crystallization of the as-cast amorphous alloys during heating through the glass transition (Fig. 20a). The onset temperature of melting, T_m , of $\text{Ni}_{59.35}\text{Nb}_{34.45}\text{Sn}_{6.2}$ and $\text{Ni}_{57}\text{Nb}_{34}\text{Sn}_9$ were observed to be equal and lower (by ~ 30 K) than the melting temperature of $\text{Ni}_{62}\text{Nb}_{35}\text{Sn}_3$. The differences between the liquidus temperatures, T_l , of the three ternary compositions are greater than the differences between their corresponding melting temperatures (see Table 5). As a result, the melting temperature range, $T_l - T_m$, increases in the order $\text{Ni}_{57}\text{Nb}_{34}\text{Sn}_9 < \text{Ni}_{59.35}\text{Nb}_{34.45}\text{Sn}_{6.2} < \text{Ni}_{62}\text{Nb}_{35}\text{Sn}_3$. The ternary $\text{Ni}_{57}\text{Nb}_{34}\text{Sn}_9$ melts in a single endothermic event. The $\text{Ni}_{59.35}\text{Nb}_{34.45}\text{Sn}_{6.2}$ shows three melting events, from which the second and third significantly overlap. The $\text{Ni}_{62}\text{Nb}_{35}\text{Sn}_3$ (curve A in Fig. 20b) melts in one endothermic event, which lies at a higher temperature than the melting events of the other two compositions ($\text{Ni}_{57}\text{Nb}_{34}\text{Sn}_9$ and $\text{Ni}_{59.35}\text{Nb}_{34.45}\text{Sn}_{6.2}$). Upon solidification by cooling with a rate of 0.33 K/s, the up-scans with 0.33 K/s heating rate, through their melting regions were repeated (curve B in Fig. 20b). A significant difference in the curve of the repeated up-scan compared to the first up-scan is noticed only for the $\text{Ni}_{62}\text{Nb}_{35}\text{Sn}_3$ composition (compare A and B curves for $\text{Ni}_{62}\text{Nb}_{35}\text{Sn}_3$ in Fig. 20b). The melting occurs in this case through two well distinguished endothermic events, where second event in the B curve corresponds to the second event of the A curve and the first event in the B curve corresponds to the position of the first melting events detected for $\text{Ni}_{57}\text{Nb}_{34}\text{Sn}_9$ and $\text{Ni}_{59.35}\text{Nb}_{34.45}\text{Sn}_{6.2}$ during the first up-scan. Since there were no significant differences in the first and second up-scans in the other two compositions ($\text{Ni}_{57}\text{Nb}_{34}\text{Sn}_9$ and $\text{Ni}_{59.35}\text{Nb}_{34.45}\text{Sn}_{6.2}$), the curves representing the second up-scans are not shown in Fig. 20b.

The calorimetric up-scans of the $\text{Ni}_{59.35}\text{Nb}_{34.45}\text{Sn}_{6.2}$ samples, which were thermally treated with different regimes (specimens R2.5h, R15h and Nq933K in Table 2), after casting them into amorphous plates, are shown in Fig. 21 (curves b, c and d, respectively). For comparison, the heat flow curve of the as-cast amorphous sample is also shown in Fig. 21 (curve a). The heat flow curves are shifted vertically for better overview. The inset of Fig. 21 is a magnified part of the heat flow curves in the vicinity of the glass transition. The as-cast sample shows a more pronounced enthalpic relaxation (heat release) before the onset of the glass transition than the thermally treated samples. The endothermic enthalpy recovery effect appears more pronounced in the specimen

R2.5h (curve b) than in R15h (curve c). The enthalpies of relaxation and recovery are, however, not quantitatively determined here because the measurements were performed in heat-flux DSC, which in comparison to the power-compensated DSC is less reliable, i.e. exhibits signal asymmetries between the sample and the reference. Furthermore, the end of the supercooled liquid region is obscured due to the intervening onset of crystallization, making an accurate determination of the enthalpy recovery impossible. Moreover, it appears that the glass transition region of the specimen Nq933K (curve d in Fig. 21) is absent. The glass transition temperature decreases in the order $R2.5h > \text{as-cast} > R15h$. The as-cast sample and the R2.5h have the corresponding four crystallization events (Fig. 21), with the same onset temperatures and the enthalpies of crystallization (see Table 6). The crystallization onset temperature and the enthalpy of crystallization of the first crystallization event of the sample R15h differ from the above discussed as-cast and R2.5h samples. The specimen Nq933K crystallizes in three exothermic events, where the onset temperature of the first event is lower than that of the other samples in Fig. 21. The temperature interval of the first peak ($T_{x1} - T_{e1} = 106$ K) is wider than the temperature interval of first and second peak combined ($T_{x1} - T_{e2}$), of the other three samples (39 K for as-cast, 40 for R2.5h and 48 K for R15h) shown in Fig. 21. The enthalpies of crystallization of the R2.5h, R15h

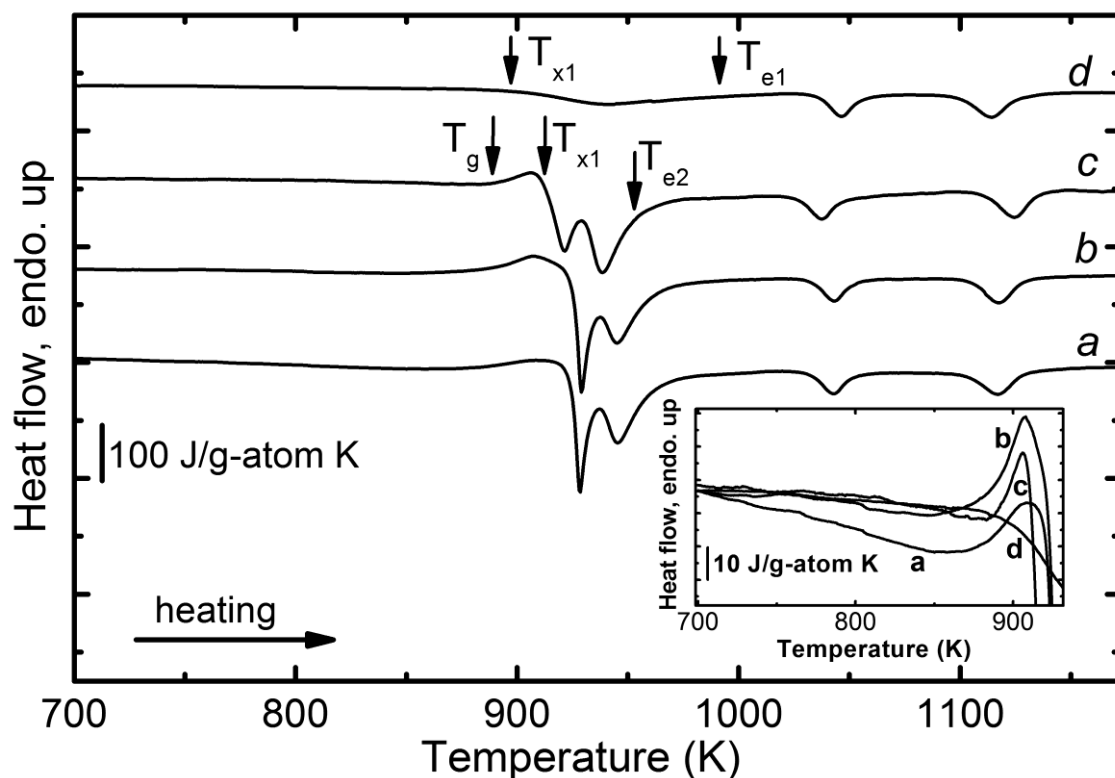


Fig. 21 The calorimetric up-scans of the as-cast amorphous and thermally treated $Ni_{59.35}Nb_{34.45}Sn_{6.2}$ specimens R2.5h, R15h and Nq933K (see Table 2), are shown in curves a, b, c and d, respectively. The inset shows magnified part of the heat flow curves in the vicinity of the glass transition. The curves are not vertically shifted in the inset.

and Nq933K represent 96, 94 and 53 % of the crystallization enthalpy of the as-cast sample, respectively.

Table 4 Thermophysical properties of different compositions in the glass transition and crystallization region. With ΔH_{x1} to ΔH_{x4} , the enthalpies of crystallization of separate crystallization events are shown and $\Delta H_{x(tot)} = \Delta H_{x1} + \Delta H_{x2} + \Delta H_{x3} + \Delta H_{x4}$

<i>Composition</i>	T_g	ΔT_g	T_x	T_e	ΔH_{x1}	ΔH_{x2}	ΔH_{x3}	ΔH_{x4}	$\Delta H_{x(tot)}$
	K				kJ/g-atom				
<i>Ni₇₀Nb₃₀</i>	N/A	N/A	913	1154	-4.6	-0.3	-0.8	N/A	-5.7
<i>Ni₆₂Nb₃₈</i>	900	37	937	1014	-0.5	-3.3	-1.7	N/A	-5.5
<i>Ni_{59.5}Nb_{40.5}</i>	N/A	N/A	918	1235	-1.0	-4.2	-0.7	N/A	-5.9
<i>Ni₅₇Nb₃₄Sn₉</i>	866	47	913	1092	-2.3	-1.6	-0.6	-0.7	-5.2
<i>Ni_{59.35}Nb_{34.45}Sn_{6.2}</i>	881	43	924	1131	-1.5	-2.5	-0.5	-0.7	-5.2
<i>Ni₆₂Nb₃₅Sn₃</i>	894	46	940	1219	-3.9	-0.9	-1.5	N/A	-6.3
<i>Ni₆₀Nb₃₆Sn₃B₁</i>	889	52	941	1245	-4.1	-1.3	-0.8	N/A	-6.2
<i>Ni_{58.85}Nb_{34.45}Sn_{6.2}Si_{0.5}</i>	870	41	911	1150	-0.9	-3.0	-0.8	-0.7	-5.9

Table 5 Thermophysical properties of different compositions in the melting region

<i>Composition</i>	T_m	T_l	ΔT_m	ΔH_m
	K			kJ/g-atom
<i>Ni₆₂Nb₃₈</i>	1463	1522	59	12.4
<i>Ni₅₇Nb₃₄Sn₉</i>	1365	1437	72	12.1
<i>Ni_{59.35}Nb_{34.45}Sn_{6.2}</i>	1368	1469	101	10.6
<i>Ni₆₂Nb₃₅Sn₃</i>	1397	1541	131	10.0
<i>Ni₆₀Nb₃₆Sn₃B₁</i>	1397	1502	85	10.2
<i>Ni_{58.85}Nb_{34.45}Sn_{6.2}Si_{0.5}</i>	1370	1480	110	12.6

Table 6 Thermophysical properties of the samples thermally treated before calorimetric characterization, of the composition $\text{Ni}_{59.35}\text{Nb}_{34.45}\text{Sn}_{6.2}$. With ΔH_{x1} to ΔH_{x4} , the enthalpies of crystallization of separate crystallization events are shown and $\Delta H_{x(\text{tot})} = \Delta H_{x1} + \Delta H_{x2} + \Delta H_{x3} + \Delta H_{x4}$

<i>Sample</i> (Table 2)	T_g	T_x	ΔH_{x1}	ΔH_{x2}	ΔH_{x3}	ΔH_{x4}	$\Delta H_{x(\text{tot})}$
	K		kJ/g-atom				
<i>As-cast</i>	881	924	-1.5	-2.5	-0.5	-0.7	-5.2
<i>R2.5h</i>	885	925	-1.4	-2.4	-0.5	-0.7	-5.0
<i>R15h</i>	889	912	-1.1	-2.5	-0.6	-0.7	-4.9
<i>Nq933K</i>	-	896	-1.5	-0.5	-0.8		-2.8

4.2.1.3. $\text{Ni}_{60}\text{Nb}_{36}\text{Sn}_3\text{B}_1$

The calorimetric up-scans of the quaternary $\text{Ni}_{60}\text{Nb}_{36}\text{Sn}_3\text{B}_1$ alloy are shown in Fig. 22 together with the up-scan of the $\text{Ni}_{62}\text{Nb}_{35}\text{Sn}_3$ (ternary alloy with similar composition) for comparison. The thermophysical properties determined from these measurements are shown in Tables 4 and 5. In Fig. 22a calorimetric up-scans of the as-cast $\text{Ni}_{60}\text{Nb}_{36}\text{Sn}_3\text{B}_1$ and $\text{Ni}_{62}\text{Nb}_{35}\text{Sn}_3$ are shown in their crystallization intervals. The quaternary $\text{Ni}_{60}\text{Nb}_{36}\text{Sn}_3\text{B}_1$ has a lower T_g and wider ΔT_g than the ternary $\text{Ni}_{62}\text{Nb}_{35}\text{Sn}_3$. The temperature interval of crystallization ($T_{e3}-T_{x1}$) of $\text{Ni}_{60}\text{Nb}_{36}\text{Sn}_3\text{B}_1$ is also wider than in the ternary $\text{Ni}_{62}\text{Nb}_{35}\text{Sn}_3$. In both of these alloys, crystallization proceeds in three exothermic events. The melting behavior of the $\text{Ni}_{60}\text{Nb}_{36}\text{Sn}_3\text{B}_1$ in the calorimetric sense is very similar to the melting of $\text{Ni}_{62}\text{Nb}_{35}\text{Sn}_3$ (Fig. 22b). When heated from the as-cast glassy state through crystallization (Fig. 22a) and further above melting (Fig. 22b), both compositions melt in one endothermic event followed by a typical melting shoulder. The temperature interval of melting is wider in ternary $\text{Ni}_{62}\text{Nb}_{35}\text{Sn}_3$ than in quaternary $\text{Ni}_{60}\text{Nb}_{36}\text{Sn}_3\text{B}_1$. After complete melting (above T_1) and consecutively solidification under cooling rate of 0.33 K/s, both alloys were reheated with the same heating rate of 0.33 K/s through the melting region and the observed melting behavior (curves B in Fig. 22b) was different than the melting behavior of the samples melted after crystallization from the as-cast amorphous state (curves A in Fig. 22b).

The second melting (curve B) proceeds in the two endothermic events instead of one, as was the case for the first melting (curve A). Furthermore, the second melting events shown in both B curves correspond to the melting event seen in both A curves.

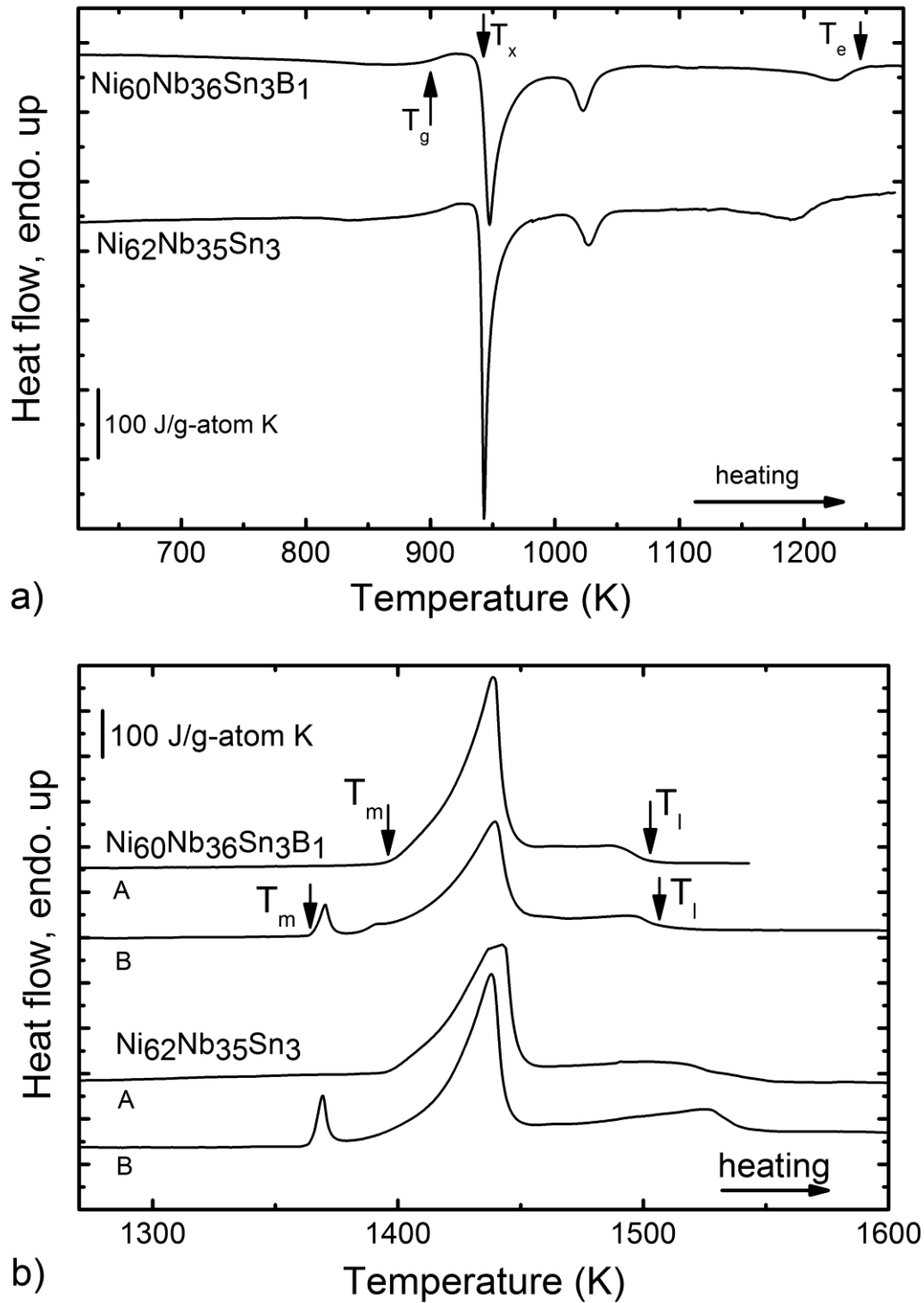


Fig. 22 The calorimetric up-scans of the quaternary $\text{Ni}_{60}\text{Nb}_{36}\text{Sn}_3\text{B}_1$ RAG and, for comparison, the ternary $\text{Ni}_{62}\text{Nb}_{35}\text{Sn}_3$ RAG alloy: **a)** upon heating from the as-cast amorphous state to the finish of the crystallization events, **b)** melting region, where the A curves represent the continuation of the heating process from *a*, and the B curves represent the melting upon second up-scan. The curves have been vertically shifted for better overview.

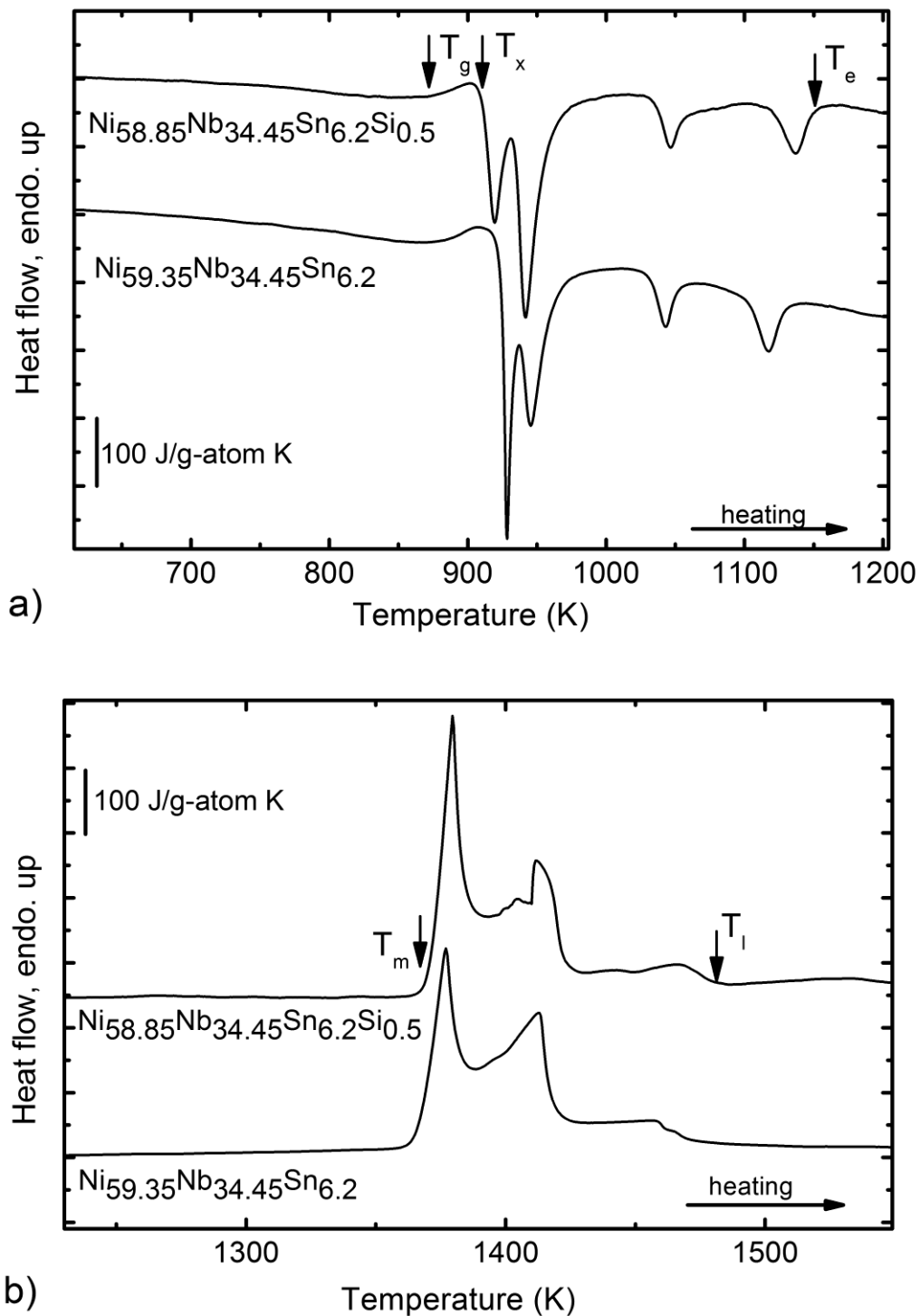
4.2.1.4. $\text{Ni}_{58.85}\text{Nb}_{34.45}\text{Sn}_{6.2}\text{Si}_{0.5}$ 

Fig. 23 The calorimetric up-scans of the quaternary $\text{Ni}_{58.85}\text{Nb}_{34.45}\text{Sn}_{6.2}\text{Si}_{0.5}$ and, for comparison, of the ternary $\text{Ni}_{59.35}\text{Nb}_{34.45}\text{Sn}_{6.2}$ RAG, alloy with similar composition: **a)** as-cast samples heated above crystallization, **b)** continuation of the curves shown in a, showing the melting region. The curves have been vertically shifted for better overview.

The calorimetric up-scans of the quaternary $\text{Ni}_{58.85}\text{Nb}_{34.45}\text{Sn}_{6.2}\text{Si}_{0.5}$ and the ternary $\text{Ni}_{59.35}\text{Nb}_{34.45}\text{Sn}_{6.2}$ alloys are shown together in Fig. 23, for comparison. Thermophysical properties determined from these measurements are shown in Tables 4 and 5. The up-scans of the as-cast samples, in the interval of crystallization, are shown in Fig. 23a. The quaternary $\text{Ni}_{58.85}\text{Nb}_{34.34}\text{Sn}_{6.2}\text{Si}_{0.5}$ has a lower T_g and T_x than the corresponding ternary $\text{Ni}_{59.35}\text{Nb}_{34.45}\text{Sn}_{6.2}$. The temperature interval of melting (Fig. 23b) is wider in $\text{Ni}_{58.85}\text{Nb}_{34.34}\text{Sn}_{6.2}\text{Si}_{0.5}$ than in $\text{Ni}_{59.35}\text{Nb}_{34.45}\text{Sn}_{6.2}$ due to its higher liquidus temperature (see Table 5).

4.2.2. XRD Characterizations

The results of XRD characterizations of the binary $\text{Ni}_{62}\text{Nb}_{38}$ and the ternary $\text{Ni}_{62}\text{Nb}_{35}\text{Sn}_3$, $\text{Ni}_{59.35}\text{Nb}_{34.45}\text{Sn}_{6.2}$ and $\text{Ni}_{57}\text{Nb}_{34}\text{Sn}_9$ master alloys are shown in Section 4.2.2.1. XRD results of the thermally treated as-cast amorphous specimens of the $\text{Ni}_{59.35}\text{Nb}_{34.45}\text{Sn}_{6.2}$ and $\text{Ni}_{57}\text{Nb}_{34}\text{Sn}_9$ compositions are shown in Section 4.2.2.2.

4.2.2.1. Solidification Structures

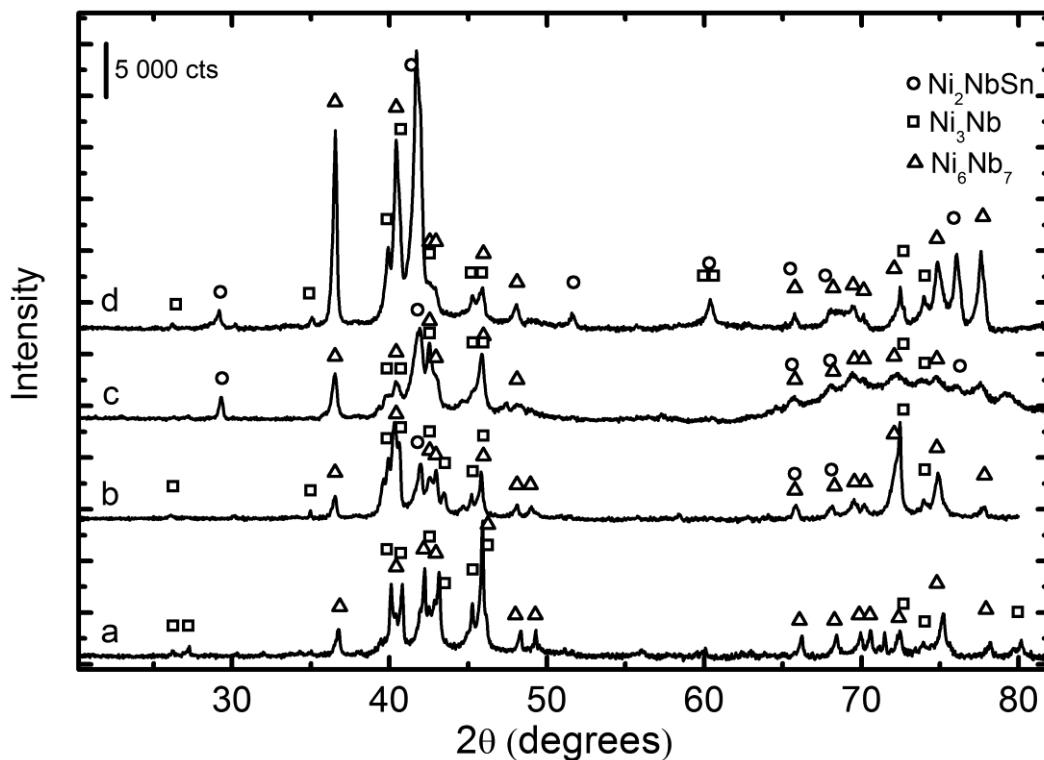


Fig. 24 XRD patterns of the master alloys: $\text{Ni}_{62}\text{Nb}_{38}$ (a), $\text{Ni}_{62}\text{Nb}_{35}\text{Sn}_3$ (b), $\text{Ni}_{59.35}\text{Nb}_{34.45}\text{Sn}_{6.2}$ (c) and $\text{Ni}_{57}\text{Nb}_{34}\text{Sn}_9$ (d).

The XRD patterns of the arc-melted master alloys of different compositions are shown in Fig. 24. In the XRD pattern of the binary $\text{Ni}_{62}\text{Nb}_{38}$ sample only the equilibrium Ni_3Nb (orthorhombic, $\beta\text{-Cu}_3\text{Ti}$ type) and Ni_6Nb_7 (hexagonal, W_6Fe_7 type) phases were identified. In the XRD patterns of the arc-melted structures of the three ternary Ni-Nb-Sn alloys (curves b-d in Fig. 24), in addition to the above mentioned Ni_3Nb and Ni_6Nb_7 , the ternary Ni_2NbSn (fcc, BiF_3 -type) phase was identified.

4.2.2.2. Devitrification Structures

The XRD patterns of the as-cast amorphous $\text{Ni}_{59.35}\text{Nb}_{34.45}\text{Sn}_{6.2}$ and $\text{Ni}_{57}\text{Nb}_{34}\text{Sn}_9$ specimens thermally treated with a constant heating rate (see Section 3.3) are shown in Fig. 25. The XRD pattern of the specimen Sn9Nq933K, of the $\text{Ni}_{57}\text{Nb}_{34}\text{Sn}_9$ composition (curve a in Fig. 25) shows reflections typical of the Ni_2NbSn phase along with an amorphous halo. The lattice parameter of the Ni_2NbSn phase was determined to be $a = 6.11 \text{ \AA}$ with a crystallite size of 7 nm. The maximum of the amorphous halo is seen at $2\theta = 44.85^\circ$ which corresponds to an interatomic distance of 2.02 \AA .

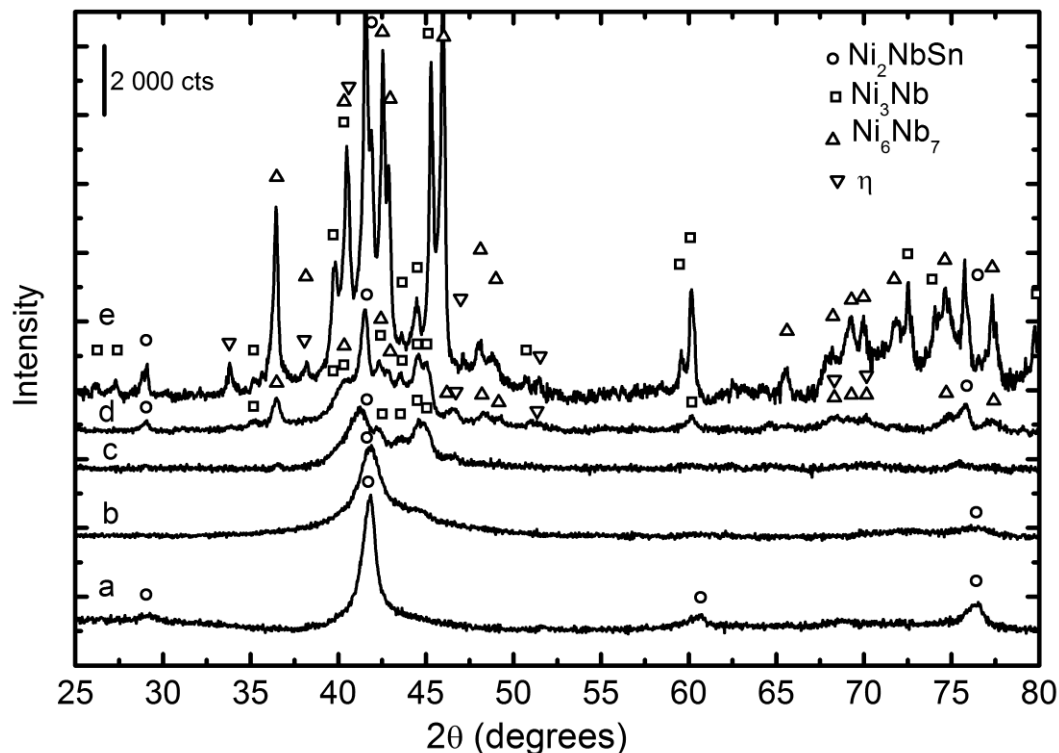


Fig. 25 XRD patterns of the amorphous specimens heat treated with the constant heating rate: (a) Sn9Nq933K of the $\text{Ni}_{57}\text{Nb}_{34}\text{Sn}_9$ composition and (b), (c), (d) and (e) are Nq933K, Nq983K, Nq1073K and Nq1223K specimens of the $\text{Ni}_{59.35}\text{Nb}_{34.45}\text{Sn}_{6.2}$ composition. The curves have been vertically shifted.

The XRD pattern of the specimen Nq933K of the $\text{Ni}_{59.35}\text{Nb}_{34.45}\text{Sn}_{6.2}$ composition is shown in curve b in Fig. 25. The peak at 41.81° corresponds to the highest reflection of the Ni_2NbSn -type phase with an interatomic distance of 2.16 \AA . Assuming that this peak belongs to the Ni_2NbSn phase, a lattice parameter of 6.11 \AA can be calculated. According to the Scherrer equation (Eq. 30), a crystallite size of 7 nm was determined. The maximum of the amorphous halo occurs at 43° , which corresponds to an interatomic distance of 2.10 \AA . This value of 2θ occurs at a position 0.74° greater than the maximum of the amorphous halo observed in the as-cast sample with the same composition (Table 3). This difference is suspected to be the result of different compositions of the as-cast and the amorphous phase remaining after the thermal treatment. This remaining amorphous phase will be hereafter referred to as A', for both Nq933K and Sn9Nq933K.

Curve c in Fig. 25 is the diffractogram of the specimen Nq983K of the $\text{Ni}_{59.35}\text{Nb}_{34.45}\text{Sn}_{6.2}$ composition. Here, in addition to the amorphous halo and a Ni_2NbSn -type phase, reflections characteristic of the Ni_3Nb phase are observed. The sizes of the crystallites of different phases observed in the curve c are up to 10 nm . The observed remaining amorphous phase is expected to have different composition than the as-cast amorphous phase or the A' amorphous phase. Therefore, it will be hereafter referred to as A''.

The diffractograms of the specimens Nq1073K and Nq1223K are also shown in Fig. 25 (curves d and e, respectively). In addition to the above mentioned Ni_2NbSn and Ni_3Nb phases, the reflections of two more crystalline phases, Ni_6Nb_7 and an η (Ti_2Ni -type) phase are observable in both d and e curves in Fig. 25. The amorphous halo in the specimen Nq1223K is no longer observable and the size of the crystallites is calculated to be up to 30 nm . The lattice parameters of the phases identified in the XRD pattern of the specimen Nq1223K are: $a = 6.14 \text{ \AA}$ for Ni_2NbSn ; $a = 5.07 \text{ \AA}$, $b = 4.66 \text{ \AA}$, $c = 4.53 \text{ \AA}$ for Ni_3Nb ; and $a = 4.93 \text{ \AA}$, $c = 26.64 \text{ \AA}$ for Ni_6Nb_7 .

The XRD patterns of the as-cast amorphous samples treated under different isothermal regimes are shown in Fig. 26 (see Table 2). The XRD pattern of sample R15h shows only a broad amorphous halo (curve a), with a maximum occurring at 42.28° (2.14 \AA), while the XRD pattern of Ni15h (curve b) shows crystalline reflections in addition to the amorphous halo. This XRD pattern appears similar to the diffractogram b in Fig. 25 – the structure of the sample heated with 0.33 K/s up to 933 K . However, in the XRD pattern of the Ni15h samples, in addition to the reflections of the amorphous and the Ni_2NbSn phases, some small additional reflections can be observed at 36.86° , 47.41° , 48.32° and 57.25° . These reflections cannot be assigned to any given specific phases with any certainty. The XRD pattern of sample Ni19h (curve c), Ni_3Nb and Ni_6Nb_7 can be identified in addition to Ni_2NbSn . The XRD pattern of the Ni28h sample (curve d) shows well defined Ni_2NbSn reflections as well as a broad amorphous halo. The lattice parameter for Ni_2NbSn

was calculated to be 6.13 Å and the position of the maximum of the amorphous halo was determined to be at 43.68° (2.07 Å).

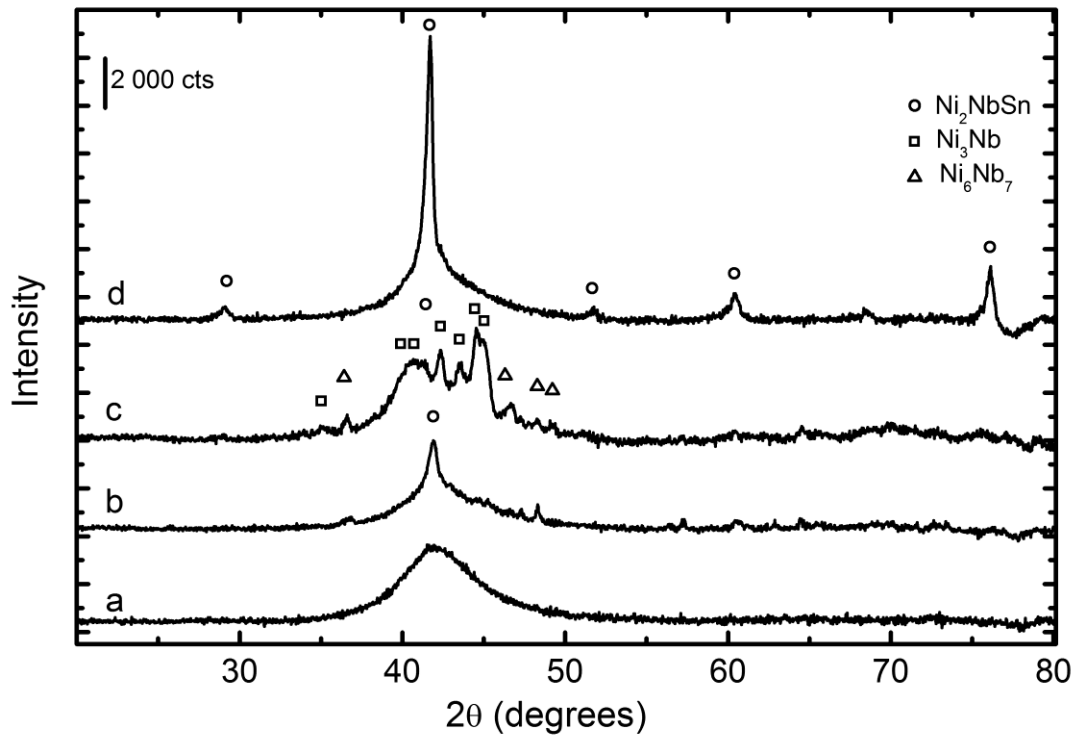


Fig. 26 XRD patterns of the amorphous samples isothermally treated with different regimes (see Section 3.3): (a) specimen R15h of the $\text{Ni}_{59.35}\text{Nb}_{34.45}\text{Sn}_{6.2}$ composition, (b) specimen Ni15h of the $\text{Ni}_{59.35}\text{Nb}_{34.45}\text{Sn}_{6.2}$ composition, (c) specimen Ni19h of the $\text{Ni}_{59.35}\text{Nb}_{34.45}\text{Sn}_{6.2}$ composition, and (d) specimen Ni28h of the $\text{Ni}_{57}\text{Nb}_{34}\text{Sn}_9$ composition.

The XRD pattern of isothermally vacuum treated as-cast amorphous $\text{Ni}_{60}\text{Nb}_{36}\text{Sn}_3\text{B}_1$ is shown in Fig. 27. The time of treatment was chosen to be 75% of the time to the onset of crystallization at 839 K (T_g-50), which was determined according to modified TTT diagram of the $\text{Ni}_{60}\text{Nb}_{35}\text{Sn}_5$ (see Section 3.2.4). In this diffractogram only the characteristic broad amorphous halo is observable.

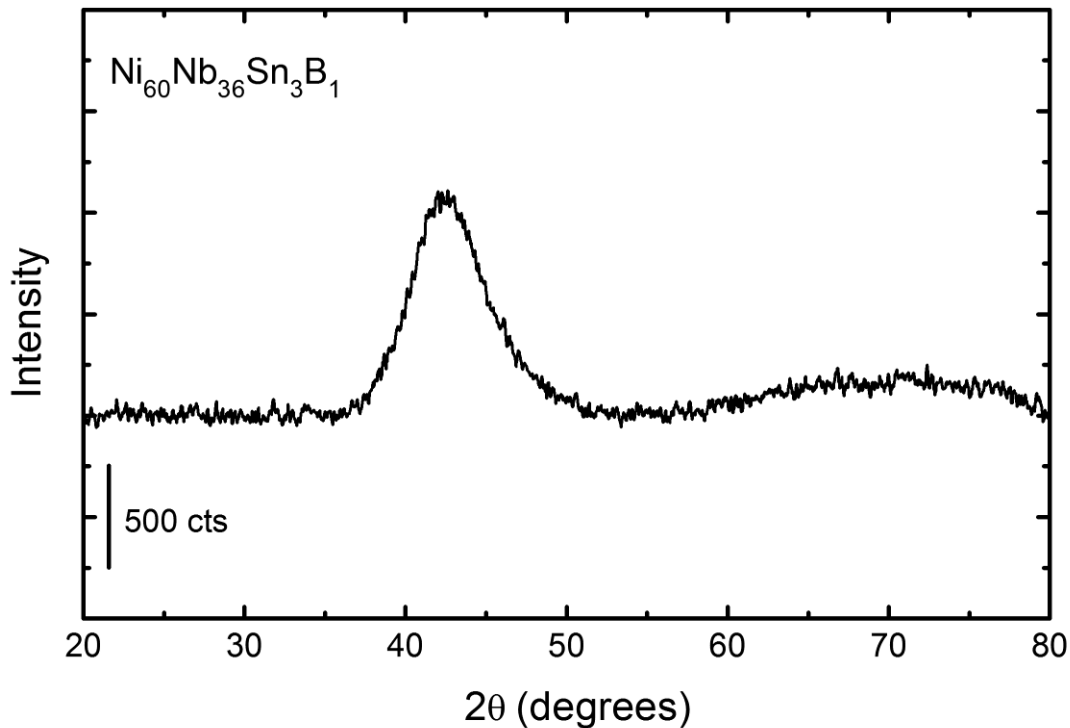


Fig. 27 XRD pattern of the as-cast amorphous $\text{Ni}_{60}\text{Nb}_{36}\text{Sn}_3\text{B}_1$ after vacuum treatment at 839 K for 20 h (75% of the time to the onset of crystallization at 839 K).

4.2.3. Microscopy Characterizations

The microstructures of the $\text{Ni}_{59.35}\text{Nb}_{34.45}\text{Sn}_{6.2}$ and $\text{Ni}_{57}\text{Nb}_{34}\text{Sn}_9$ alloys, obtained after equilibrium cooling from the molten state (Section 3.2.3), are presented in Fig. 28a and b, respectively. The arc melted master alloys of the same two compositions, $\text{Ni}_{59.35}\text{Nb}_{34.45}\text{Sn}_{6.2}$ and $\text{Ni}_{57}\text{Nb}_{34}\text{Sn}_9$, are shown in overview in Fig. 28c and e, and under higher magnifications in Fig. 28d and f, respectively. Based on the different contrasts observed in the BS electron images, five phases, marked with D, L, G, H and M in Fig. 28, can be distinguished, of which H (the phase with a darker gray contrast than the G phase) and M (brighter contrast phase than the L phase) are present in small amounts (less than 5 % volume fraction of the H and M phases combined). The compositions of these phases, as determined by EDX, are given in Table 7.

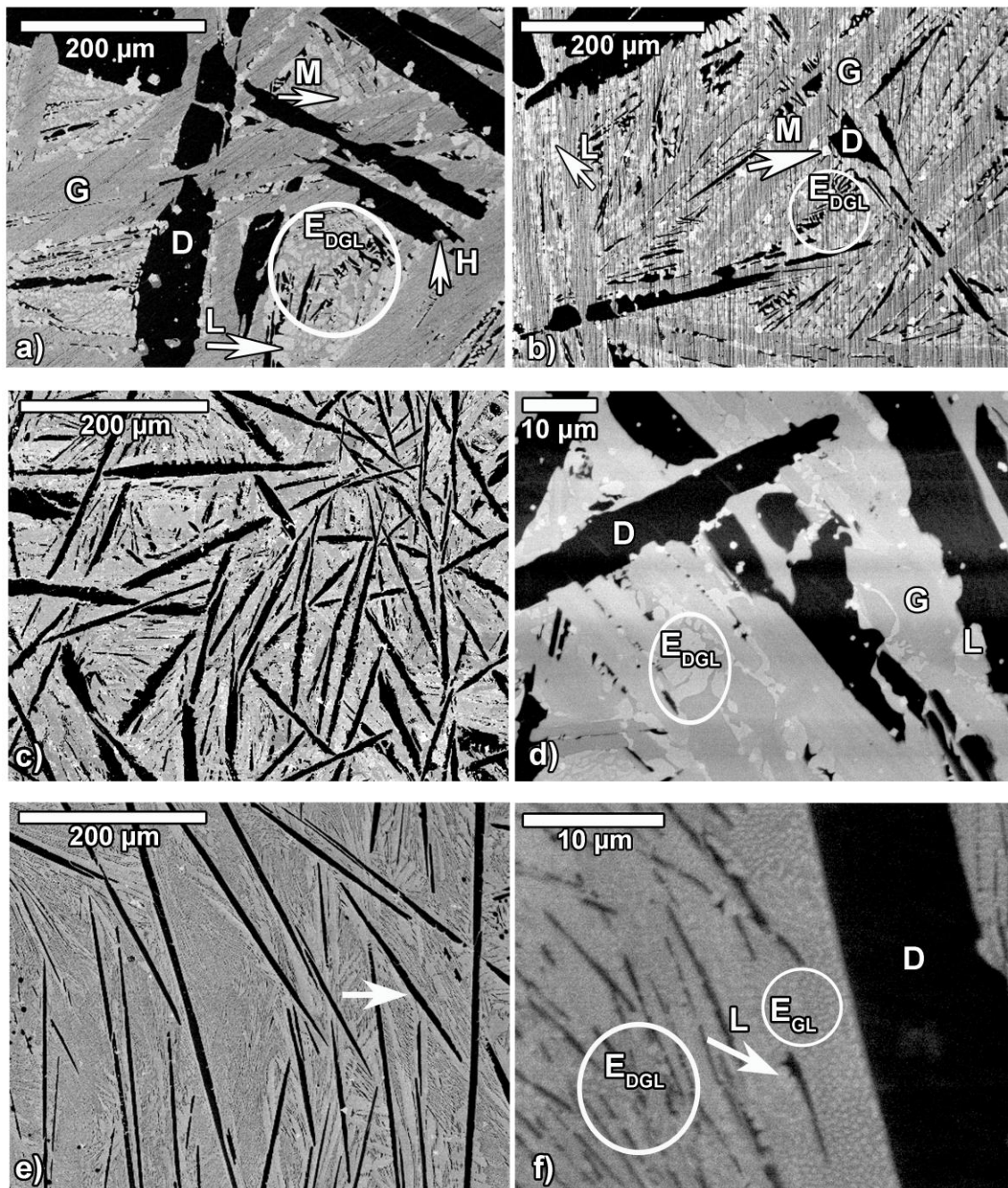


Fig. 28 BS images representing microstructures of the *equilibrium cooled* specimens: **a)** $\text{Ni}_{59.35}\text{Nb}_{34.45}\text{Sn}_{6.2}$ and **b)** $\text{Ni}_{57}\text{Nb}_{34}\text{Sn}_9$, and the *master alloy* specimens: **c)** $\text{Ni}_{59.35}\text{Nb}_{34.45}\text{Sn}_{6.2}$ in overview, **d)** $\text{Ni}_{59.35}\text{Nb}_{34.45}\text{Sn}_{6.2}$ in higher magnification, **e)** $\text{Ni}_{57}\text{Nb}_{34}\text{Sn}_9$ in overview and **f)** $\text{Ni}_{57}\text{Nb}_{34}\text{Sn}_9$ in higher magnification, at the position schematically presented with the *arrow* in *c*.

The phase D (Fig. 28) has a plate-like morphology in all four investigated specimens. In the master alloys, the phase D occupies a volume fraction of 31-37 % in $Ni_{59.35}Nb_{34.45}Sn_{6.2}$ and 18-27 % in the $Ni_{57}Nb_{34}Sn_9$ composition. The thickness of these plate-like crystals is observed to be the smallest in the master alloy specimen of the $Ni_{57}Nb_{34}Sn_9$ composition ($4 \pm 1 \mu m$), slightly bigger in arc melted $Ni_{59.35}Nb_{34.45}Sn_{6.2}$ ($8 \pm 3 \mu m$) and the coarsest in the equilibrium annealed samples of $Ni_{59.35}Nb_{34.45}Sn_{6.2}$ ($63 \pm 39 \mu m$) and $Ni_{57}Nb_{34}Sn_9$ ($67 \pm 17 \mu m$). Furthermore, it can be qualitatively observed that the coarseness of these structures, in general, increases in the same order.

The phase G was also found to form with a plate-like morphology in three out of four investigated specimens, with the exception of the master alloy of the $Ni_{57}Nb_{34}Sn_9$ composition (Fig. 28). In between the above described coarse plate-like D- and G-phase crystals, binary and ternary eutectic-like features are formed (marked with E_{GL} and E_{DGL} in Fig. 28). The bright phase, marked with L in Fig. 28 is generally observed to form with eutectic-like features.

Table 7 The chemical compositions of different phases, determined in at.% by EDX, of the arc melted master alloys and equilibrium cooled specimens, with $Ni_{59.35}Nb_{34.45}Sn_{6.2}$ and $Ni_{57}Nb_{34}Sn_9$ compositions

Phase	$Ni_{59.35}Nb_{34.45}Sn_{6.2}$			$Ni_{59.35}Nb_{34.45}Sn_{6.2}$			$Ni_{57}Nb_{34}Sn_9$			$Ni_{57}Nb_{34}Sn_9$		
	Master alloy			Equilibrium cooled			Master alloy			Equilibrium cooled		
	Ni	Nb	Sn	Ni	Nb	Sn	Ni	Nb	Sn	Ni	Nb	Sn
D	75	25	0	75	25	0	75	25	0	77	23	0
G	52	42	6	53	42	5				56	37	7
H				50	48	2						
L	35	49	16	53	25	22	35	48	17	56	23	21
M				38	47	16				38	45	17
E_{DGL}							55	33	12			
E_{GL}							52	35	13			

4.3. Oxidation

4.3.1. Thermogravimetric Characterizations

4.3.1.1. Oxidation of Ni-Nb

In Fig. 29 oxidation of two binary Ni-Nb alloys at 842 K is shown by thermogravimetric (TG) curves, representing mass gain as a function of isothermal annealing time. Oxidation of crystalline $\text{Ni}_{62}\text{Nb}_{38}$ (Ni62M) follows a single parabolic equation in the entire measurement range of 15 h, with a rate constant of $k_p = 2.68 \times 10^{-4} \text{ mg}^2\text{s}^{-1}\text{cm}^{-4}$. Amorphous $\text{Ni}_{62}\text{Nb}_{38}$ (Ni62A) follows the same parabolic oxidation behavior as crystalline $\text{Ni}_{62}\text{Nb}_{38}$ but only during the first 3 h of oxidation ($k_p = 2.32 \times 10^{-4} \text{ mg}^2\text{s}^{-1}\text{cm}^{-4}$). After 5 hours, the oxidation follows a new parabolic equation with a rate constant of $k_p = 1.36 \times 10^{-4} \text{ mg}^2\text{s}^{-1}\text{cm}^{-4}$ until the end of the oxidation measurement. The melt spun amorphous strip of the $\text{Ni}_{70}\text{Nb}_{30}$ composition (Ni70A) also follows a parabolic oxidation with a rate constant of $k_p = 1.09 \times 10^{-4} \text{ mg}^2\text{s}^{-1}\text{cm}^{-4}$ within the first 2.4 h of oxidation (Fig. 29). After going through a transition period, the oxidation curve reaches, after 4 hours of oxidation, a plateau of $\sim 1 \text{ mg/cm}^2$.

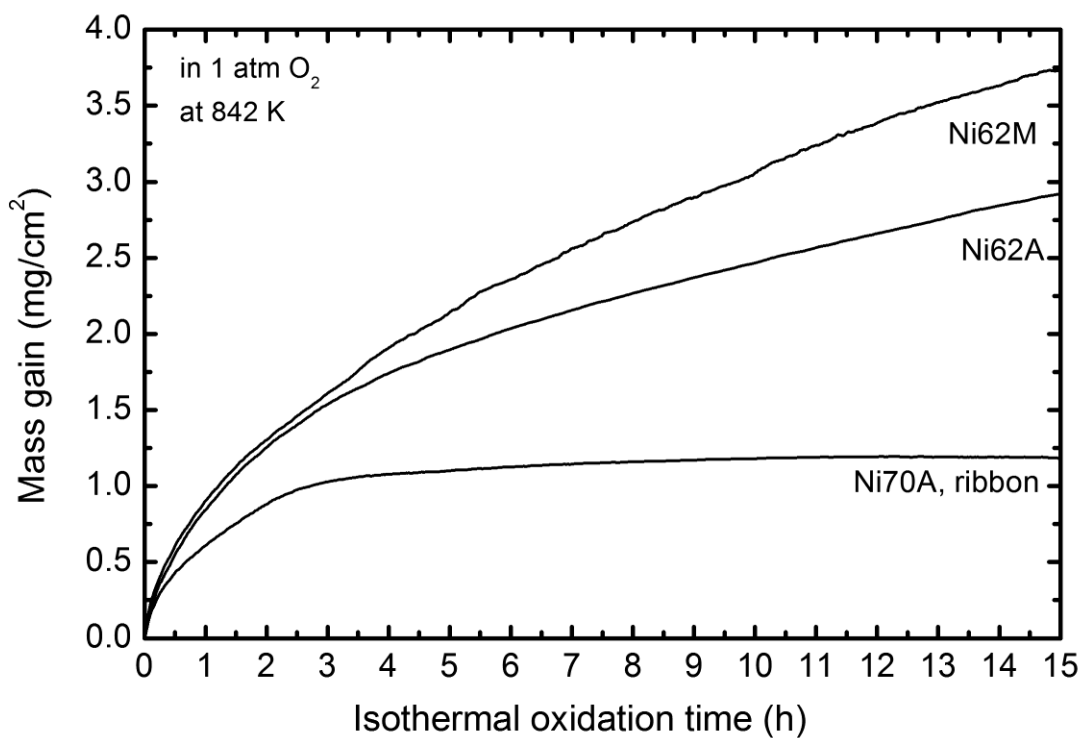


Fig. 29 Oxidation of the crystalline (Ni62M) and the amorphous (Ni62A) $\text{Ni}_{62}\text{Nb}_{38}$ alloy and the amorphous $\text{Ni}_{70}\text{Nb}_{30}$ (Ni70A) at 842 K for 15 h.

4.3.1.2. Oxidation of Ni-Nb-Sn

Oxidation of the as-cast amorphous $\text{Ni}_{57}\text{Nb}_{34}\text{Sn}_9$ alloy at three different temperatures, below the calorimetric glass transition, is presented in Fig. 30a. A magnification of the first two hours of oxidation is shown in Fig. 30b. All three TG curves show parabolic oxidation, eventually transitioning into linear oxidation. The parabolic rate constants increase and, at the same time, the time range of parabolic oxidation decreases as the temperature of oxidation increases (see Table 8). The plot of the parabolic rate constants as a function of reciprocal oxidation temperature and a corresponding Arrhenius fit from which E_a is calculated as 289 kJ/mol (or 3 eV/atom), is shown in Fig. 30c. The parabolic oxidation is followed by a transition period, which increases with the decrease of the oxidation temperature, from 0.23 h at 846 K to 1.53 h at 816 K and 18.8 h at 786 K. Most of the 18.8 h of the transition period at 786 K is the time when no mass gain during oxidation is observed. Therefore, much noise is evident in this part of the curve (indicated with * in Fig. 30a).

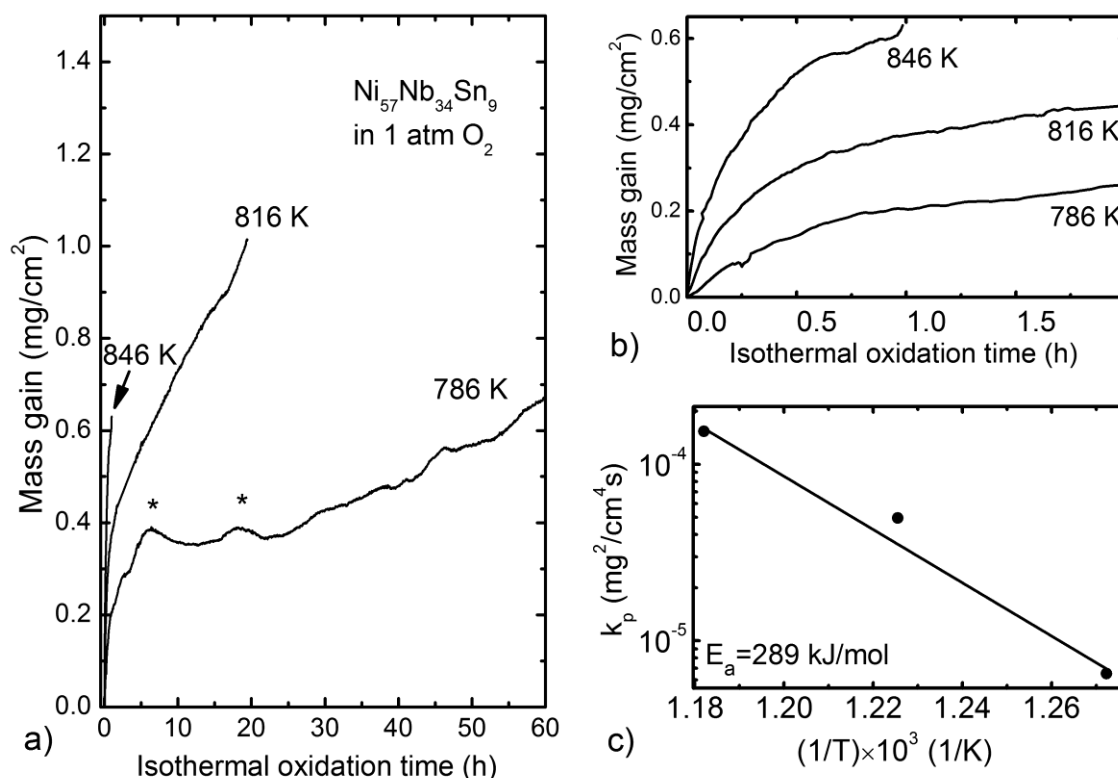


Fig. 30 Oxidation of the as-cast amorphous $\text{Ni}_{57}\text{Nb}_{34}\text{Sn}_9$: **a)** TG curves at three different temperatures below the glass transition: Tg-20 K (846 K), Tg-50 K (816 K) and Tg-80 K (786 K), **b)** magnification of the image in *a*, within the first two hours of oxidation, **c)** plot of the parabolic rate constants (k_p) as a function of $1/T$ and a corresponding Arrhenius fit.

The TG curves of the as-cast Sn6.2A, and two thermally treated amorphous specimens, R2.5h and R15h, of the $\text{Ni}_{59.35}\text{Nb}_{34.45}\text{Sn}_{6.2}$ composition, oxidized at 831 K for 19 h are shown in Fig. 31. The as-cast amorphous $\text{Ni}_{59.35}\text{Nb}_{34.45}\text{Sn}_{6.2}$ specimen shows parabolic oxidation behavior (Section 2.3.2), similar to the as-cast amorphous $\text{Ni}_{57}\text{Nb}_{34}\text{Sn}_9$ specimen (Fig. 30a). After initial parabolic oxidation, $k_p = 5.0 \times 10^{-5} \text{ mg}^2\text{s}^{-1}\text{cm}^{-4}$, and a transition period, the TG curve of Sn6.2A obeys a linear oxidation equation ($k_l = 6.36 \times 10^{-6} \text{ mgcm}^{-2}\text{s}^{-1}$). R2.5h and R15h show after initial parabolic growth and the transition period passivation at a mass gain of ~ 0.5 and $\sim 0.6 \text{ mg/cm}^2$ (Fig. 31), respectively.

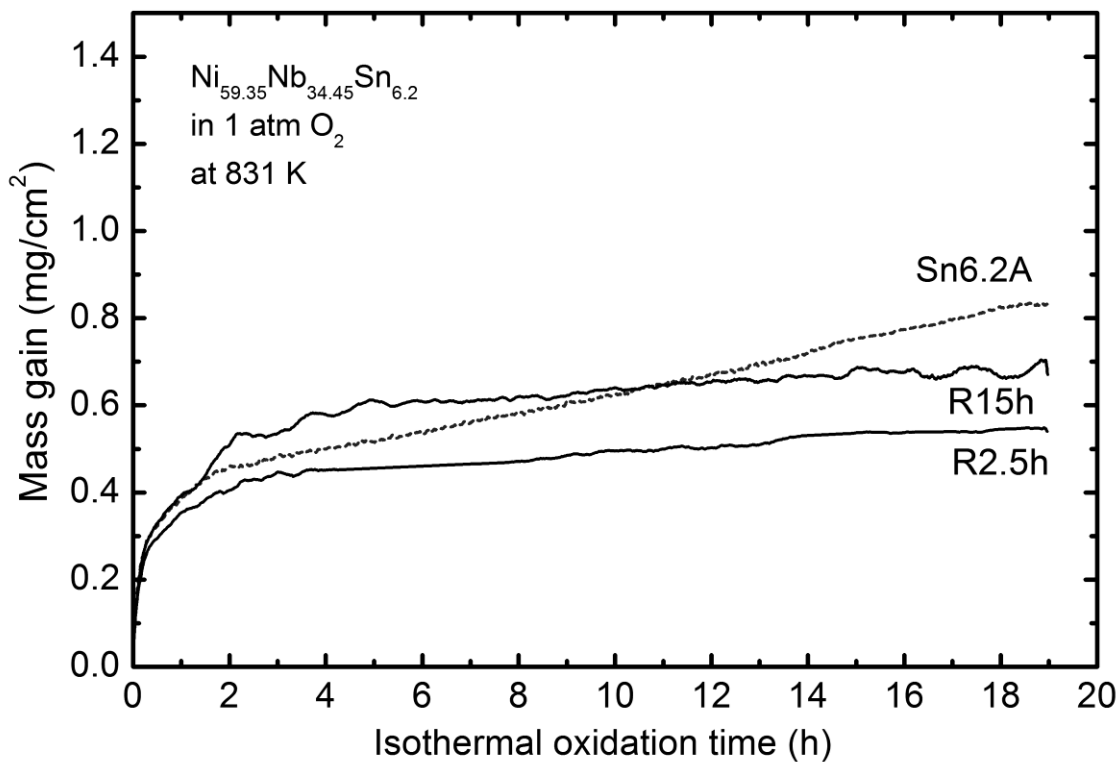


Fig. 31 Oxidation (at 831 K for 19h) of the as-cast amorphous (Sn6.2A, dashed line) and isothermally treated amorphous specimens R2.5h and R15h of the $\text{Ni}_{59.35}\text{Nb}_{34.45}\text{Sn}_{6.2}$ composition (see Table 2).

The TG curve of the specimen Ni28h with the composition $\text{Ni}_{57}\text{Nb}_{34}\text{Sn}_9$ (Table 2), oxidized at 816 K for 19.5 h is shown in Fig. 32a. After initial parabolic oxidation (between 0.1 and 2.5 h of oxidation), and short transition period, the passivation region is observed. The oxidation of the as-cast sample with the same composition (Sn9A in Table 2) is also shown in Fig. 32a, for comparison.

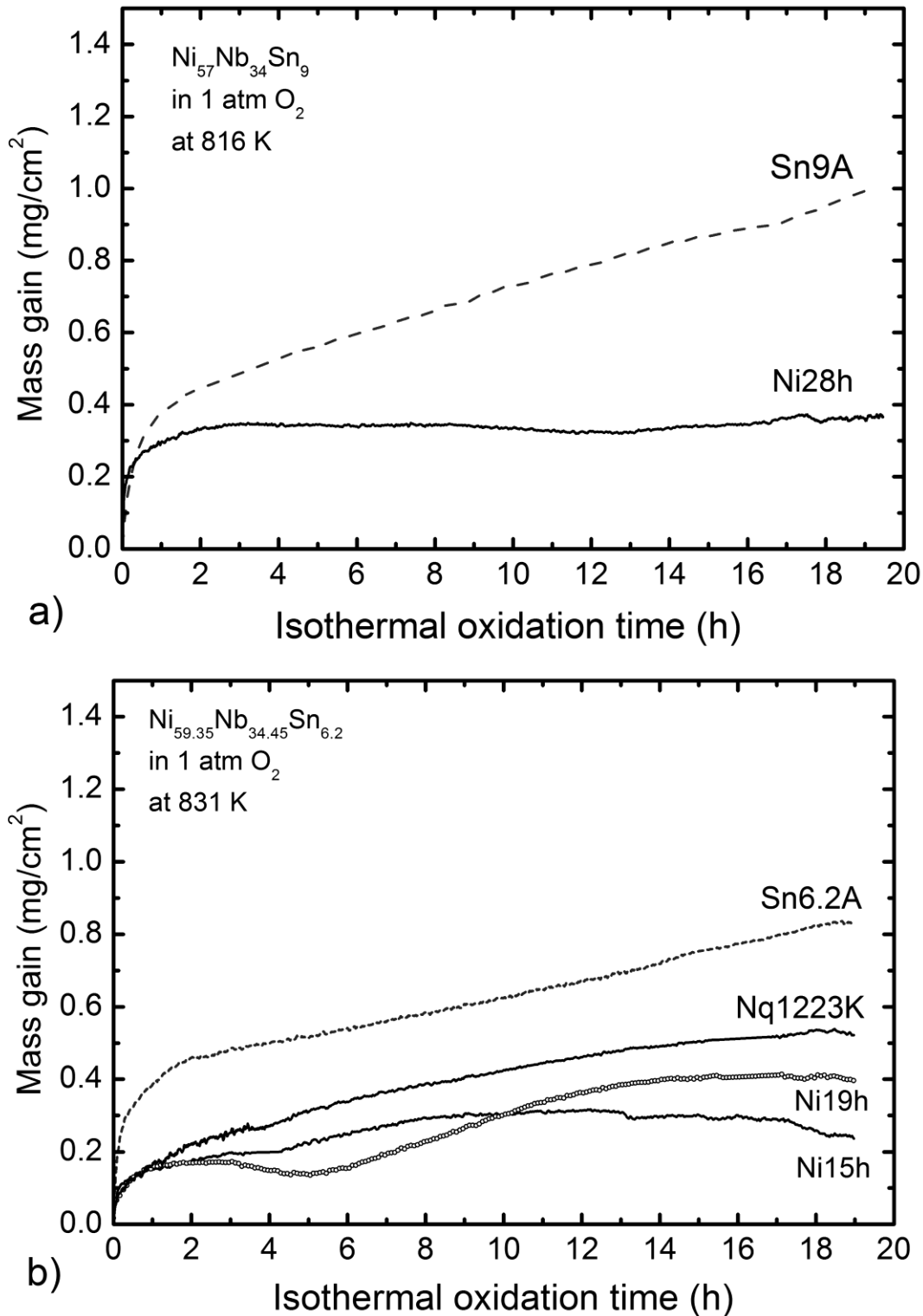


Fig. 32 Oxidation of nanocrystalline samples of the two ternary compositions: **a)** $\text{Ni}_{57}\text{Nb}_{34}\text{Sn}_9$ and **b)** $\text{Ni}_{59.35}\text{Nb}_{34.45}\text{Sn}_{6.2}$ alloys, at T_g-50 K (816 K and 831 K, respectively). The thermal treatment and the sample names are given in the Table 2. The TG curves of the as-cast samples oxidized under the same conditions as the nanocrystalline samples (Sn6.2A and Sn9A) are also shown here for comparison.

The TG curves of specimens Ni15h, Ni19h and Nq1223K, with the $\text{Ni}_{59.35}\text{Nb}_{34.45}\text{Sn}_{6.2}$ composition (Table 2), which were oxidized at 831 K, are shown in Fig. 32b. The TG curve of the as-cast amorphous specimen with the same composition is also shown in Fig. 32b for comparison (Sn6.2A in Table 8). The sample Ni15h oxidizes within the first 9.1 h according to the parabolic equation with a rate constant $k_p = 2.46 \times 10^{-6} \text{ mg}^2/\text{cm}^4\text{s}$. After 9.1 h, oxidation undergoes passivation, and no significant further mass gain is observed throughout the next 10 h of oxidation. The apparent decrease in the oxidation rate at about 4 h and the mass loss observed after 13 h of oxidation were determined to be artifacts from the baseline subtraction. After initial parabolic oxidation, within the first 0.83 h ($k_p = 7.67 \times 10^{-6} \text{ mg}^2/\text{cm}^4\text{s}$), the sample Ni19h undergoes a period of passivation between 0.83 and 5.9 h of oxidation. From 5.9 to 11.6 h, linear oxidation is observed in the TG curve of Ni19h and finally from 11.6 h to the end of the measurement another passivation region is observed.

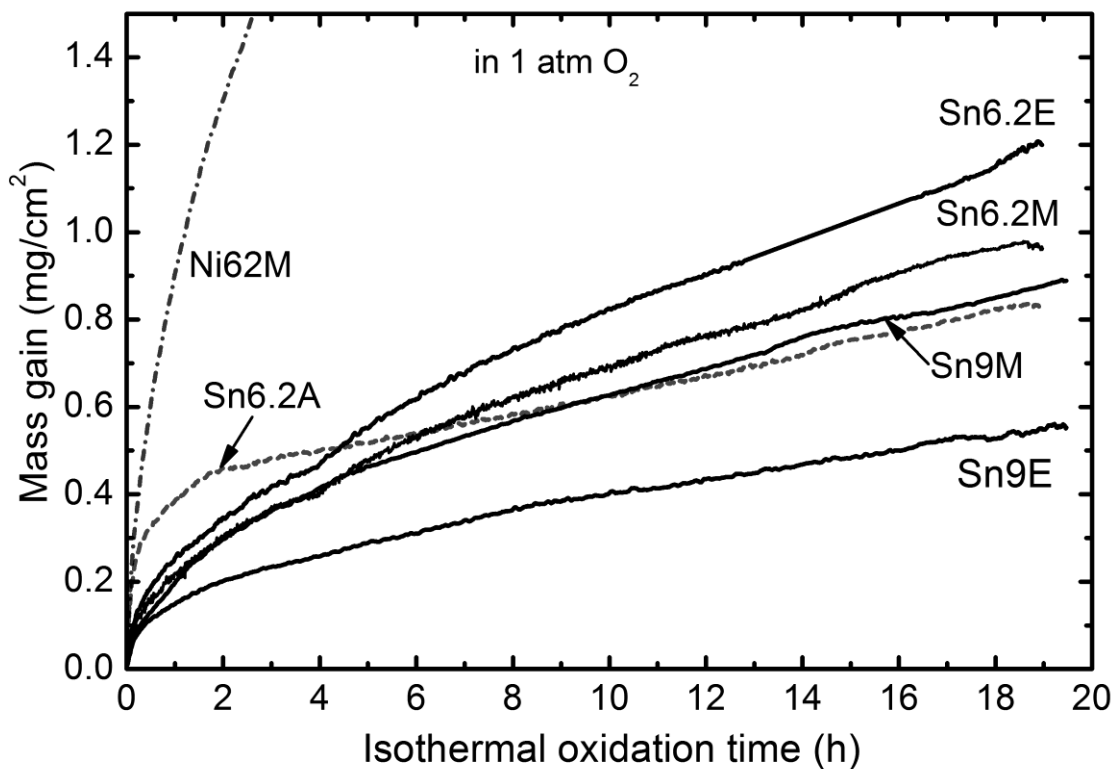


Fig. 33 Oxidation of the microcrystalline samples with the $\text{Ni}_{59.35}\text{Nb}_{34.45}\text{Sn}_{6.2}$ and $\text{Ni}_{57}\text{Nb}_{34}\text{Sn}_9$ compositions at 831 K and 816 K, respectively. The sample names and thermal treatments are listed in the Table 2.

The TG curves shown in Fig. 33 are the curves of the master alloy and equilibrium cooled specimens with the $\text{Ni}_{59.35}\text{Nb}_{34.45}\text{Sn}_{6.2}$ and the $\text{Ni}_{57}\text{Nb}_{34}\text{Sn}_9$ compositions (Table 2), which were oxidized at 831 K and 816 K, respectively. The TG curves of the as-cast amorphous specimens

with the $\text{Ni}_{59.35}\text{Nb}_{34.45}\text{Sn}_{6.2}$ (Sn6.2A) composition and the master alloy specimen of the binary $\text{Ni}_{62}\text{Nb}_{38}$ (Ni62M) are also shown in Fig. 33. The mass gain due to oxidation is lower for the crystalline samples of the ternary alloys, $\text{Ni}_{59.35}\text{Nb}_{34.45}\text{Sn}_{6.2}$ and $\text{Ni}_{57}\text{Nb}_{34}\text{Sn}_9$, than for the binary $\text{Ni}_{62}\text{Nb}_{38}$ and comparable to the mass gain of the amorphous ternary $\text{Ni}_{59.35}\text{Nb}_{34.45}\text{Sn}_{6.2}$. All four studied crystalline specimens obey parabolic oxidation. The master alloys of $\text{Ni}_{59.35}\text{Nb}_{34.45}\text{Sn}_{6.2}$ (Sn6.2M) and $\text{Ni}_{57}\text{Nb}_{34}\text{Sn}_9$ (Sn9M) compositions have similar rate constants, $k_p = 1.44 \times 10^{-5}$ and $1.11 \times 10^{-5} \text{ mg}^2/\text{cm}^4\text{s}$, respectively. The equilibrium cooled specimen $\text{Ni}_{57}\text{Nb}_{34}\text{Sn}_9$ (Sn9E) has a smaller k_p of $4.28 \times 10^{-6} \text{ mg}^2/\text{cm}^4\text{s}$, and the equilibrium cooled $\text{Ni}_{59.35}\text{Nb}_{34.45}\text{Sn}_{6.2}$ (Sn6.2E) has a higher k_p of $2.064 \times 10^{-5} \text{ mg}^2/\text{cm}^4\text{s}$, than the corresponding master alloys under the same conditions.

4.3.1.3. Oxidation of $\text{Ni}_{60}\text{Nb}_{36}\text{Sn}_3\text{B}_1$

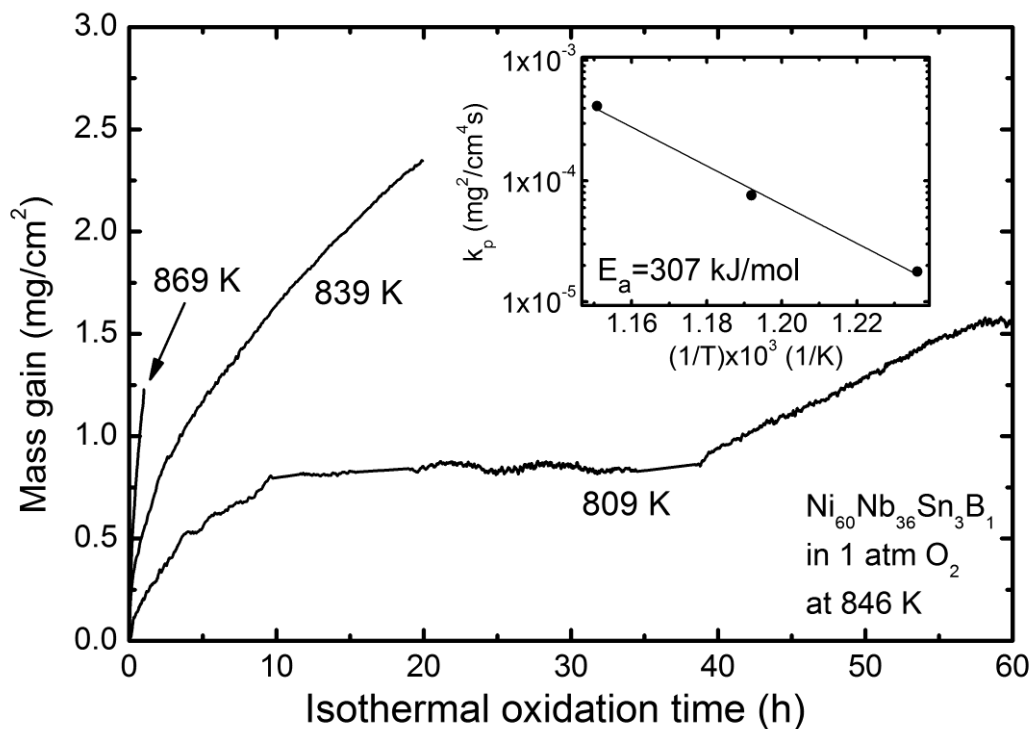


Fig. 34 Oxidation of the as-cast amorphous $\text{Ni}_{60}\text{Nb}_{36}\text{Sn}_3\text{B}_1$ alloy at three different temperatures below the glass transition: $T_g - 20 \text{ K}$ (846 K), $T_g - 50 \text{ K}$ (816 K) and $T_g - 80 \text{ K}$ (786 K). Inserted in the upper right corner is the plot of the parabolic rate constants as a function of $1/T$ and a corresponding Arrhenius fit.

The TG curve of the as-cast amorphous $\text{Ni}_{60}\text{Nb}_{36}\text{Sn}_3\text{B}_1$ oxidized isothermally at three different temperatures below the glass transition is shown in Fig. 34. At T_g-20 K and T_g-50 K, parabolic oxidation is obeyed within the whole oxidation time, with $k_p = 4.17 \times 10^{-4}$ and $7.63 \times 10^{-5} \text{ mg}^2/\text{cm}^4\text{s}$, respectively. At T_g-80 K, oxidation also follows a parabolic equation ($k_p = 1.78 \times 10^{-5} \text{ mg}^2/\text{cm}^4\text{s}$) within the first 9.4 h. Between 9.4 and 38.6 h, oxidation undergoes a passivation period and then continues to oxidize linearly with $k_l = 9.83 \times 10^{-6} \text{ mg}/\text{cm}^2\text{s}$. Inserted in the upper corner of the Fig. 34 is a plot of the parabolic rate constants as a function of reciprocal oxidation temperature and a corresponding Arrhenius fit. From this plot E_a is calculated as 307 kJ/mol (or 3 eV/atom). The TG curve of the master alloy with the $\text{Ni}_{60}\text{Nb}_{36}\text{Sn}_3\text{B}_1$ composition (see Fig. 35) obeys parabolic oxidation within the whole period of oxidation (20h) at 839 K.

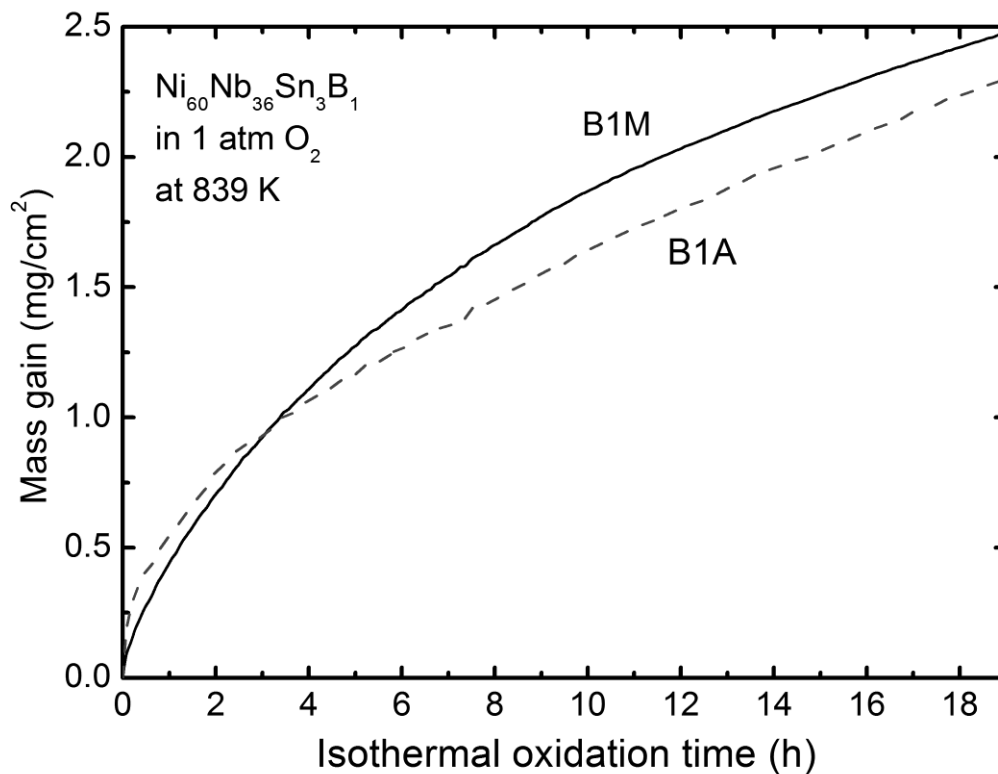


Fig. 35 Oxidation of the master alloy with the $\text{Ni}_{60}\text{Nb}_{36}\text{Sn}_3\text{B}_1$ composition (B1M), at 839 K for 20 h. The TG curve of the as-cast amorphous sample with the same composition (B1A) is shown for comparison.

4.3.1.4. Oxidation of $\text{Ni}_{58.85}\text{Nb}_{34.34}\text{Sn}_{6.2}\text{Si}_{0.5}$

The TG curve of the as-cast amorphous quaternary $\text{Ni}_{58.35}\text{Nb}_{34.45}\text{Sn}_{6.2}\text{Si}_{0.5}$ alloy (Si0.5A), oxidized at 820 K (T_g-50 K) for 17 h, is shown in Fig. 36. The TG curve of ternary as-cast $\text{Ni}_{59.35}\text{Nb}_{34.45}\text{Sn}_{6.2}$ with the similar composition is also shown in the Fig. 36, for comparison. Similar to the corresponding ternary composition, $\text{Ni}_{58.35}\text{Nb}_{34.45}\text{Sn}_{6.2}\text{Si}_{0.5}$ oxidizes in a parabolic manner, with k_p and k_l similar to the $\text{Ni}_{59.35}\text{Nb}_{34.45}\text{Sn}_{6.2}$ (see Table 8). The compositions of the oxidized samples, their short names and oxidation conditions, as well as the parameters determined from the TG curves are given in Table 8.

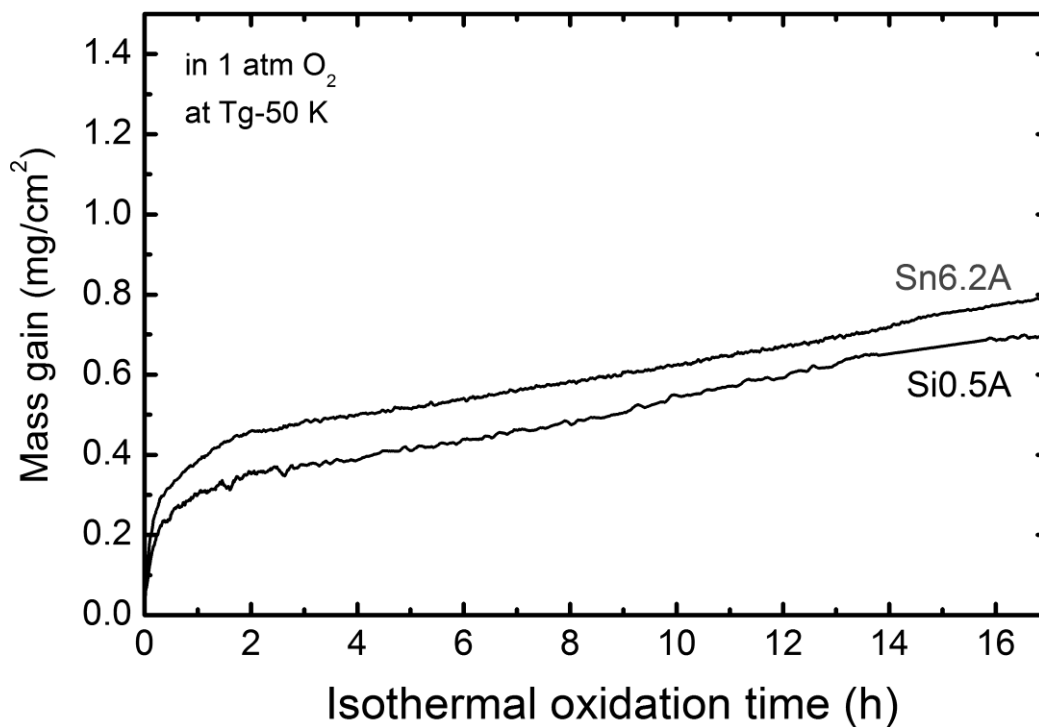


Fig. 36 Oxidation of the quaternary as-cast amorphous $\text{Ni}_{58.85}\text{Nb}_{34.34}\text{Sn}_{6.2}\text{Si}_{0.5}$ alloy at T_g-50 for 17 h. For comparison, TG curve of the as-cast amorphous ternary $\text{Ni}_{59.35}\text{Nb}_{34.34}\text{Sn}_{6.2}$ composition (Sn6.2A) is also shown.

Table 8 The compositions, names, oxidation temperatures and times as well as the oxidation parameters determined from the TG curves: parabolic (k_p) and linear (k_l) rate constants, time of the parabolic oxidation (τ_p), onset of linear oxidation (τ_l) and the overall mass gain after 15 h of isothermal oxidation

Composition	Sample	T_{ox}	τ_{ox}	k_p	τ_p	τ_l	k_l	m_{15h}
	Name ^a	K	h	mg ² /cm ⁴ s	h	h	mg/cm ² s	mg/cm ²
<i>Ni₆₂Nb₃₈</i>	Ni62M	842	15	2.68×10^{-4}	15			3.73
<i>Ni₆₂Nb₃₈</i>	Ni62A	842	15	2.32×10^{-4}	3	5 ^b	^{-b}	2.92
<i>Ni₇₀Nb₃₀</i>	Ni70A	842	15	1.09×10^{-4}	2.4			1.18
<i>Ni₅₇Nb₃₄Sn₉</i>	Sn9M	816	19.5	1.11×10^{-5}	19			0.79
<i>Ni₅₇Nb₃₄Sn₉</i>	Sn9E	816	19.5	4.28×10^{-6}	19			0.48
<i>Ni₅₇Nb₃₄Sn₉</i>	Sn9A	816	19.5	4.97×10^{-5}	0.61	2.14	8.47×10^{-6}	0.87
<i>Ni₅₇Nb₃₄Sn₉</i>	Sn9A	786	80	6.53×10^{-6}	5	23.8	2.28×10^{-6}	0.36
<i>Ni₅₇Nb₃₄Sn₉</i>	Sn9A	846	1	1.54×10^{-4}	0.5	0.73	5.37×10^{-5}	
<i>Ni₅₇Nb₃₄Sn₉</i>	Ni28h	816	19.5	6.93×10^{-6}	2.58	2.58	passive	0.34
<i>Ni_{59.35}Nb_{34.45}Sn_{6.2}</i>	Sn6.2M	831	19	1.44×10^{-5}	19			0.87
<i>Ni_{59.35}Nb_{34.45}Sn_{6.2}</i>	Sn6.2E	831	19	2.06×10^{-5}	19			1.03
<i>Ni_{59.35}Nb_{34.45}Sn_{6.2}</i>	Sn6.2A	831	19	5.00×10^{-5}	0.61	2.14	6.36×10^{-6}	0.75
<i>Ni_{59.35}Nb_{34.45}Sn_{6.2}</i>	R2.5h	831	19	4.10×10^{-5}	2.14	2.14	passive	0.53
<i>Ni_{59.35}Nb_{34.45}Sn_{6.2}</i>	R15h	831	19	5.30×10^{-5}	2.14	2.14	passive	0.665
<i>Ni_{59.35}Nb_{34.45}Sn_{6.2}</i>	Ni15h	831	19	2.46×10^{-6}	9.1	9.1	passive	0.3
<i>Ni_{59.35}Nb_{34.45}Sn_{6.2}</i>	Ni19h	831	19	7.67×10^{-6}	0.83	5.9	9.99×10^{-6}	0.41
<i>Ni_{59.35}Nb_{34.45}Sn_{6.2}</i>	Nq1223K	831	19	6.76×10^{-6}	0.83			0.51
<i>Ni_{58.85}Nb_{34.45}Sn_{6.2}Si_{0.5}</i>	Si0.5A	820	17	2.36×10^{-5}	0.56	1.39	6.98×10^{-6}	0.67
<i>Ni₆₀Nb₃₆Sn₃B₁</i>	B1M	839	20	9.30×10^{-5}	20			2.24
<i>Ni₆₀Nb₃₆Sn₃B₁</i>	B1A	839	20	7.63×10^{-5}	20			2.03
<i>Ni₆₀Nb₃₆Sn₃B₁</i>	B1A	809	80	1.78×10^{-5}	9.4	38.6	9.83×10^{-6}	0.83
<i>Ni₆₀Nb₃₆Sn₃B₁</i>	B1A	869	1	4.17×10^{-4}	20			

a- Sample names and descriptions can be found in Table 2

b- The binary amorphous $Ni_{62}Nb_{38}$ after 5 h of oxidation assumes a new parabolic behaviour with a rate constant of $1.36 \cdot 10^{-4} \text{ mg}^2/\text{cm}^4\text{s}$

4.3.2. XRD Characterizations

The XRD patterns of the oxidized surfaces, of the as-cast amorphous (curve a) and crystalline master alloy (curve b) of binary $\text{Ni}_{62}\text{Nb}_{38}$ are shown in Fig. 37. Crystalline reflections of Nb_2O_5 , NiO and Ni were identified. Since the main reflections of Ni_3Nb overlap with Nb_2O_5 , the actual presence of a small amount of Ni_3Nb in the measured volume cannot be verified.

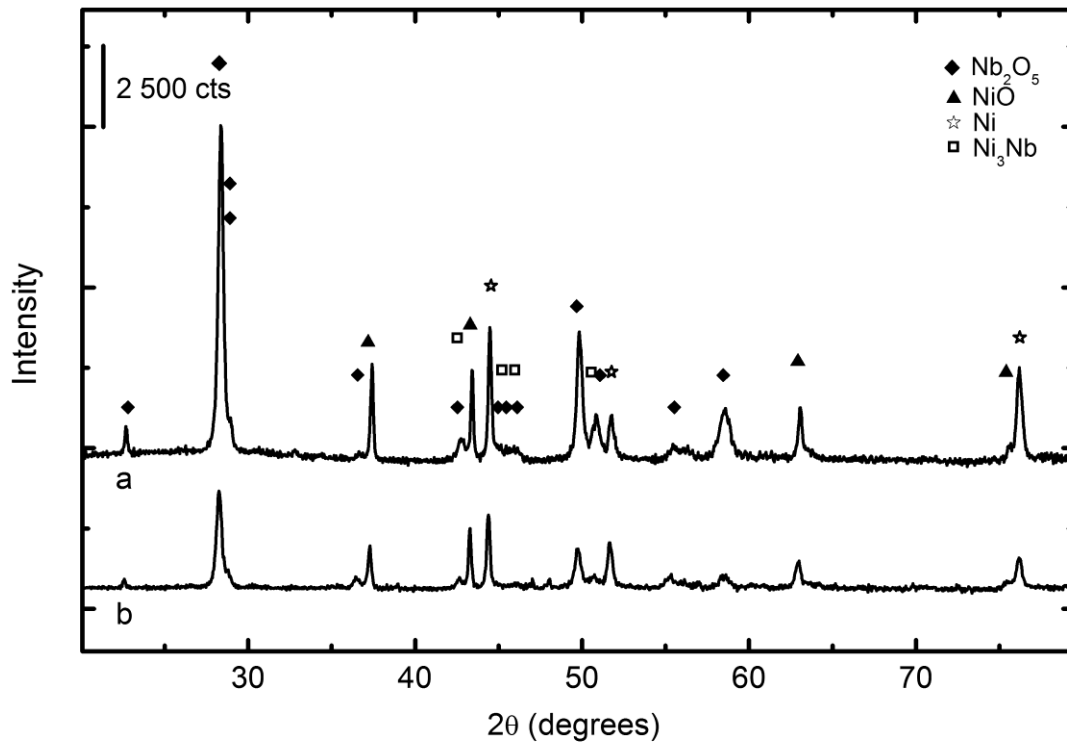


Fig. 37 XRD pattern taken from the surfaces of the binary $\text{Ni}_{62}\text{Nb}_{38}$ specimens oxidized at 842K for 15 h: (a) oxidized as-cast amorphous Ni62A and (b) oxidized master alloy Ni62M (Table 2). The curves have been vertically shifted.

The XRD patterns taken from the surfaces of the specimens Sn9A, Ni28h, Sn9M and Sn9E with the $\text{Ni}_{57}\text{Nb}_{34}\text{Sn}_9$ composition, after oxidation at 816 K for 19.5 h are shown in Fig. 38. The phases identified from these diffractograms (a-d in Fig. 38) are Nb_2O_5 , NbO_2 , NiO , Ni_3Sn and Ni_3Nb . On the diffractogram taken from the oxidized surface of the sample with an equilibrium cooled structure (curve d in Fig. 38), reflections of CaCO_3 were found in addition to the above mentioned phases. These reflections originate from the putty used as the sample holder. The assigned symbols are, for better clarity, shown only over the curves where the specific peak is clearly observed for the first time. One can observe that the intensities of the NbO_2 reflections, compared to the reflections of other phases are more pronounced in the oxidized nanocrystalline Ni28h sample (curve b), than in any other of the four samples and that the reflections of Nb_2O_5 are not as evident

(Fig. 38). The diffractograms taken from the oxidized as-cast amorphous surfaces of the $\text{Ni}_{58.85}\text{Nb}_{34.45}\text{Sn}_{6.2}\text{Si}_{0.5}$ and the $\text{Ni}_{59.35}\text{Nb}_{34.34}\text{Sn}_{6.2}$ compositions are shown in Fig. 39. These same phases were identified as on the above shown $\text{Ni}_{57}\text{Nb}_{34}\text{Sn}_9$ composition (Fig. 38).

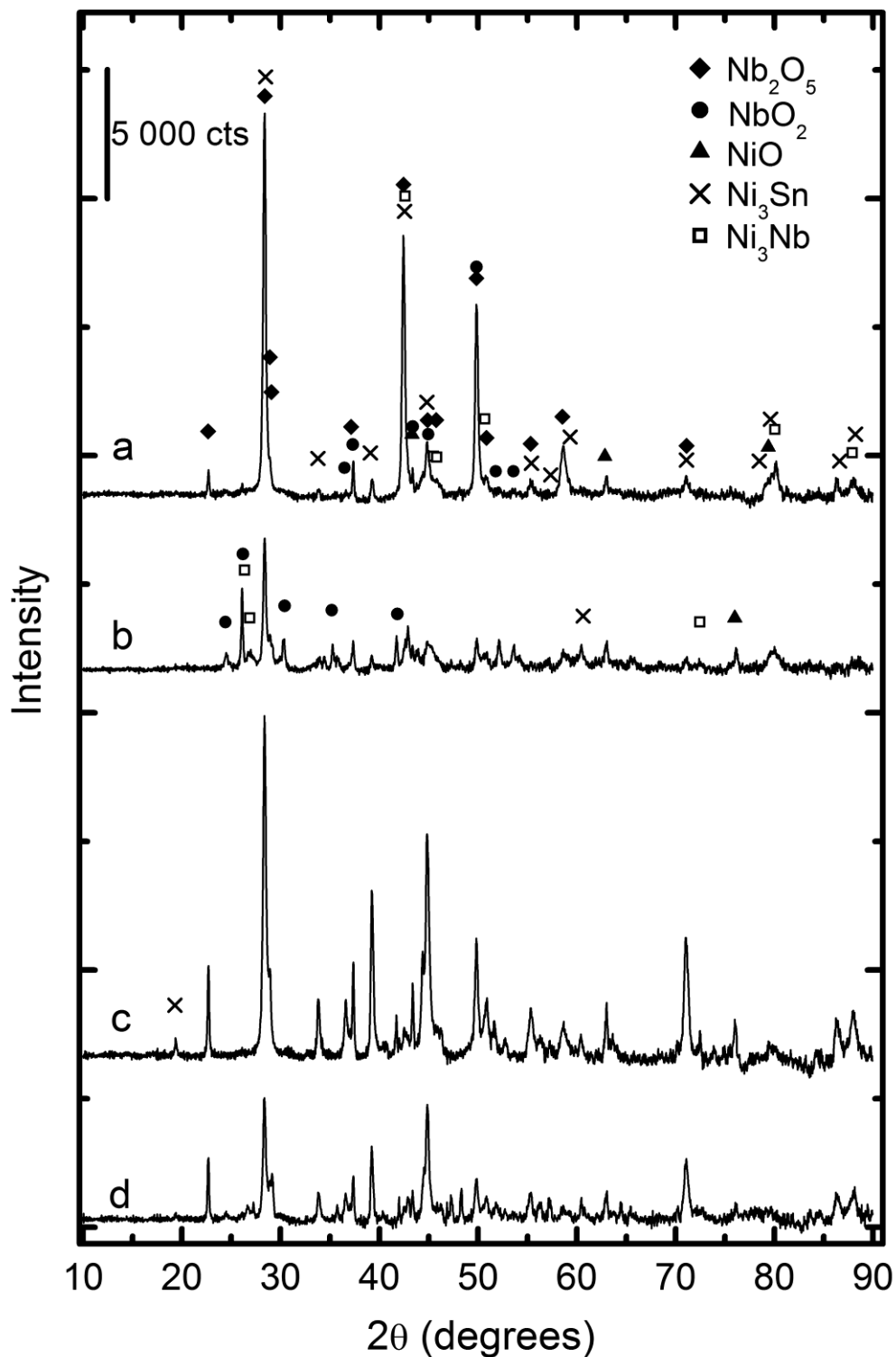


Fig. 38 XRD patterns taken from the oxidized surfaces of the $\text{Ni}_{57}\text{Nb}_{34}\text{Sn}_9$ specimens: (a) Sn9A, (b) Ni28h, (c) Sn9M and (d) Sn9E (Table 2). Oxidation was performed at 816 K for 19.5 h. The curves have been vertically shifted.

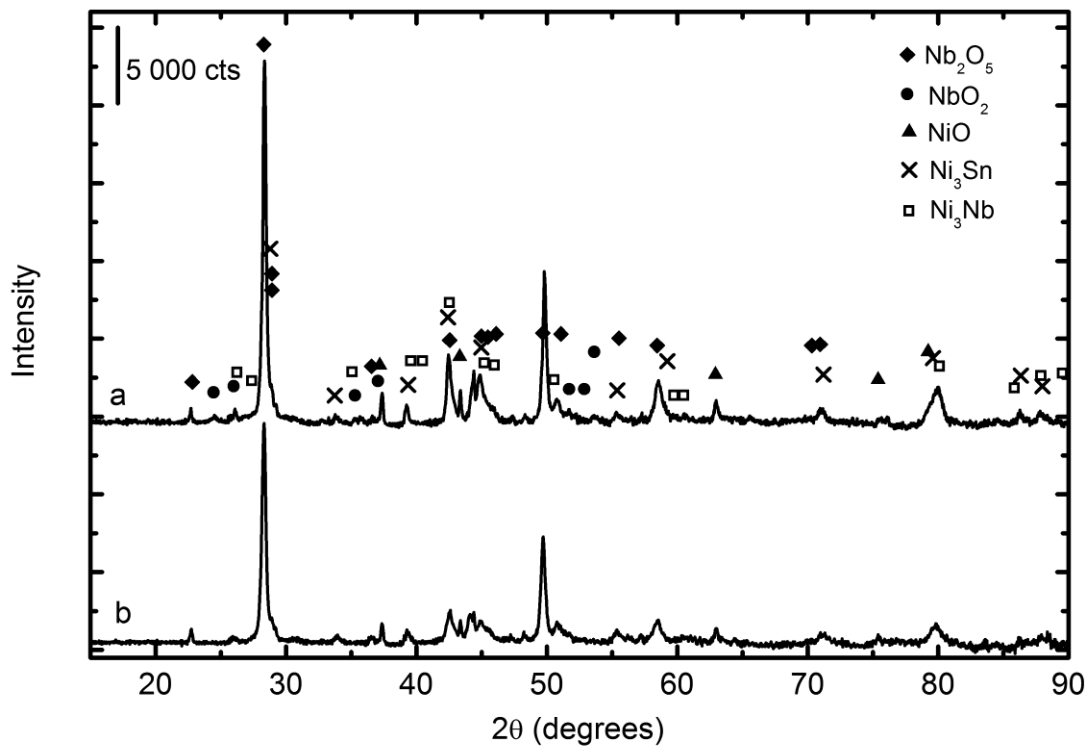


Fig. 39 XRD patterns taken from the oxidized surfaces of the (a) as-cast amorphous $\text{Ni}_{59.35}\text{Nb}_{34.45}\text{Sn}_{6.2}$ (Sn62A), oxidized at 831 K for 19 h and (b) as-cast amorphous $\text{Ni}_{58.85}\text{Nb}_{34.45}\text{Sn}_{6.2}\text{Si}_{0.5}$ (Si0.5A), oxidized at 820 K for 17 h. The curves have been vertically shifted.

The XRD patterns taken from the oxidized surfaces of the specimens with the $\text{Ni}_{59.35}\text{Nb}_{34.34}\text{Sn}_{6.2}$ composition and different types of structures, from the as-cast amorphous (Sn6.2A), annealed amorphous (specimens R2.5h and R15h), nanocrystalline (specimens Ni15h, Ni19h and Nq1223K), to the master alloy and equilibrium cooled specimen, show same crystalline phases as the samples of the $\text{Ni}_{57}\text{Nb}_{34}\text{Sn}_9$ composition, which are shown in Fig. 38. These diffractograms are therefore given in the Appendix (see page 143).

The XRD patterns taken from the surfaces of the oxidized (at 839 K ($T_g - 50$ K) for 20 h) $\text{Ni}_{60}\text{Nb}_{36}\text{Sn}_3\text{B}_1$ composition with the starting as-cast amorphous structure (B1A) and a master alloy (B1M), are shown in Fig. 40. The phases identified on these diffractograms are Ni- and Nb-oxides (Nb_2O_5 , NbO_2 and NiO), Ni-rich intermetallics Ni_3Nb and Ni_3Sn and one Ni-Nb-boride with the formula $\text{Ni}_{21}\text{Nb}_2\text{B}_6$.

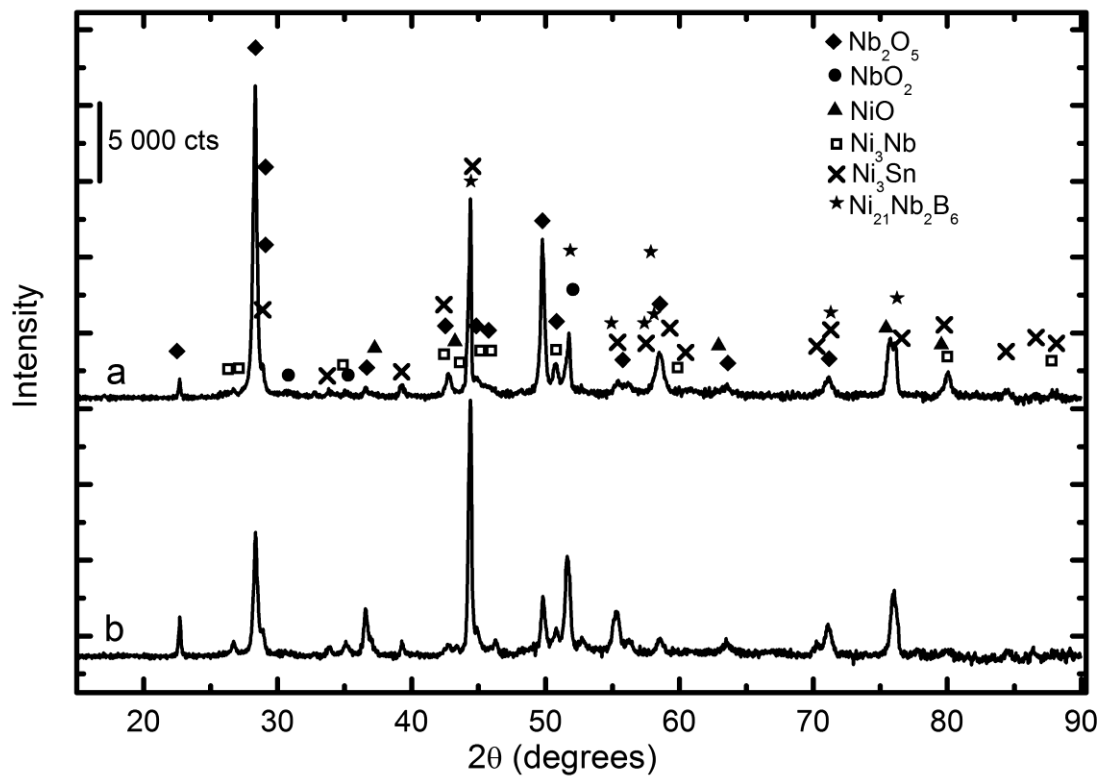


Fig. 40 XRD patterns taken from the surfaces of the specimens with composition $\text{Ni}_{60}\text{Nb}_{36}\text{Sn}_3\text{B}_1$, oxidized at 839 K for 20 h: (a) as-cast amorphous (B1A) and (b) master alloy (B1M). The curves have been vertically shifted.

In order to establish the bulk structure of the oxidized samples, i.e. the structure of the material after the as-cast amorphous samples were oxidized, the oxidized ternary sample was ground with 320 and 600 SiC paper until a thickness of $\sim 50 \mu\text{m}$ was removed and then the XRD method was used for crystallographic characterization (Fig. 41). The XRD pattern of the prepared sample shows only the broad amorphous halo between 35° and 55° .

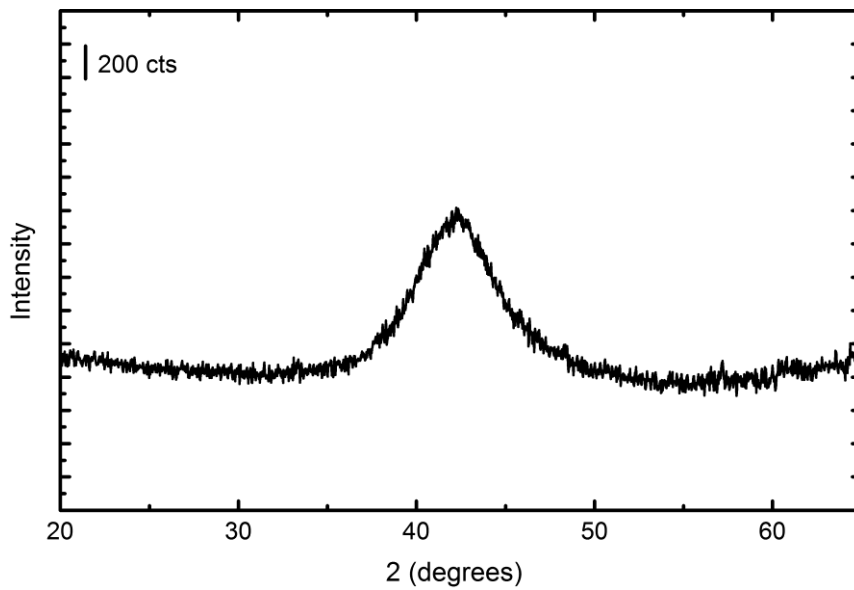


Fig. 41 XRD pattern taken from the surface of the oxidized (T_g -50 K) Ni-Nb-Sn specimen, after grinding away the oxidized surface.

4.3.3. Microstructure Characterizations

4.3.3.1. Binary Ni-Nb Alloys

The BS images taken from the cross-sections of the binary Ni-Nb samples oxidized at 842 K for 15 h in dry O_2 are shown in Fig. 42. The master alloy specimen of the $Ni_{62}Nb_{38}$ composition shows a matrix composed of two types of phases, darker and lighter with the Ni/Nb atomic ratios of $X_{Ni}/X_{Nb} = 3.0$ and 1.2, respectively. The oxide scale consists of alternating darker and brighter contrast phases. One can distinguish areas with finer and coarser alternating features (perlitic-like structure) having different contrast (F and C in Fig. 42a, respectively). The areas marked with F have a higher $X_{Ni}/X_{Nb} = 2.4$ and less oxygen (15 at %) than the areas marked with C, where $X_{Ni}/X_{Nb} = 0.8$ with 24 at.% oxygen. The overall oxide layer thickness is $27.5 \pm 0.4 \mu m$.

The cross-section of oxidized amorphous $Ni_{62}Nb_{38}$ is shown in Fig. 42b. The oxide scale appears similar to that observed on microcrystalline $Ni_{62}Nb_{38}$, consisting of alternating darker and brighter phases. Nevertheless, the areas with a finer and coarser perlitic-like structure, i.e. F and C in Fig. 42a, are not observable here. The oxide scale is richer in Nb ($X_{Ni}/X_{Nb} = 0.4$) than both the average $Ni_{62}Nb_{38}$ composition ($X_{Ni}/X_{Nb} = 1.63$) and the oxide scale of the microcrystalline $Ni_{62}Nb_{38}$. Also, the oxide scale is thinner ($19 \pm 2 \mu m$ thick) than that of the microcrystalline $Ni_{62}Nb_{38}$. The top of the oxide scale is a very thin layer ($0.8 \pm 0.2 \mu m$), marked with A and white

arrows in Fig. 42b. There are indications from the EDX analysis that the Nb concentration in this external layer is limited (~ 1.2 at.% Nb) and $X_{\text{Ni}}/X_{\text{O}} = 1$. The matrix underneath the oxide shows a homogeneous gray contrast. Furthermore, in the oxidized amorphous sample, the oxide scale and bulk appear to be separated by a 1.6 ± 0.6 μm thick layer marked with B in Fig. 42b. In this layer, $X_{\text{Ni}}/X_{\text{Nb}} = 2.8$, which indicates an enrichment in Ni or depletion in Nb with respect to the overall composition where $X_{\text{Ni}}/X_{\text{Nb}} = 1.63$. No significant amount of oxygen was measured by the EDX in this layer.

A melt spun amorphous ribbon of the $\text{Ni}_{70}\text{Nb}_{30}$ composition, oxidized at 842 K for 15 h, is shown in Fig. 42c. The upper and the lower surface of the strip are marked with S1 and S2 in Fig. 42c. The adhesive tape used to affix the strip to the sample holder can be observed underneath S2. Parallel to the interfaces S1 and S2, the darker line, running through the middle of the strip (marked with a white arrow in Fig. 42c) is noticeable. These appear to be pores, remaining after the oxidation front has reached the sample center. In the middle of the cross-section, i.e. in the vicinity to the white arrow in Fig. 42c, $X_{\text{Ni}}/X_{\text{Nb}}$ was determined by EDX to be 1.9-1.7 and the oxygen concentration 21 at.%. The thin, Ni-rich surface layer (like layer A in Fig. 42b) was not visible. Nevertheless, the EDX measurements showed that there is a Ni enrichment close to the surface where $X_{\text{Ni}}/X_{\text{Nb}} = 12.5$ having an oxygen concentration of 9 at.%.

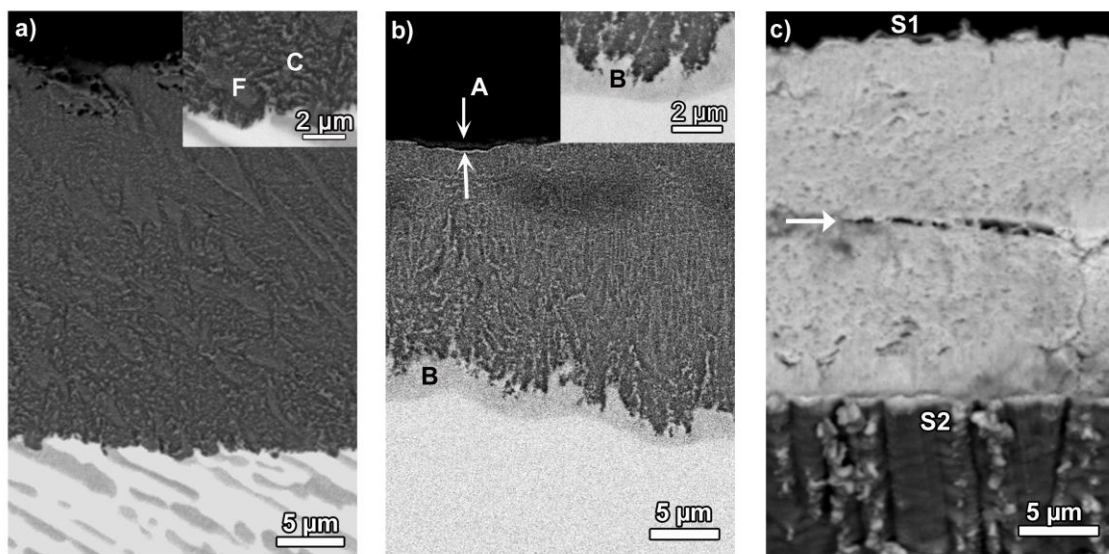


Fig. 42 The BS images in cross-sections of the binary Ni-Nb samples after oxidized at 842 K for 15 h: **a)** master alloy of the $\text{Ni}_{62}\text{Nb}_{38}$ composition (Ni62M), **b)** as-cast amorphous $\text{Ni}_{62}\text{Nb}_{38}$ (Ni62A), and **c)** melt spun amorphous ribbon of $\text{Ni}_{70}\text{Nb}_{30}$ composition (Ni70A). The matrix is located at the bottom of image and the oxide layer on top of it.

4.3.3.2. Microstructure of the Oxidized Ternary Ni-Nb-Sn Alloys

The BS images of the as-cast amorphous specimens (Sn6.2A), oxidized for 2.5 h and 19 h at 831 K, are shown in Fig. 43, under a and b, respectively. Thermally treated amorphous specimens R2.5h and R15h (Table 2), oxidized at 831 K for 19 h, are shown under c and d in Fig. 43, respectively. Generally, in the oxidation penetration distance, four different zones or, as will be referred to hereafter, layers can be noticed. These layers are marked with L1 to L4 in Fig. 43b. The external L1 layer is not observable on all specimens, namely in images a and c of Fig. 43. The reason for this might be that this thin layer (0.4 to 0.5 μm) is highly detachable and easily breaks-off during metallographic preparation. The interface between the L2 and L3 layers is very irregular so the thickness from the point where L2 loses its continuity to the point where the darker contrast phases are no longer observable will be referred to as the *transition zone* (or L3 layer). The L4 layer separates the L3 layer from the matrix. These definitions of layers L1-L4 will be used throughout the text, also for other samples that exhibit similar microstructure in the oxidation penetration distance.

The thicknesses of the L2, L3 and L4 layers on the Sn6.2A sample oxidized for 19 h are bigger compared to the corresponding layers on the sample oxidized for 2.5 h (Fig. 44). The total thickness of the oxidation penetration distance (L1 + L2 + L3 + L4) on the Sn6.2A sample is the same as in R2.5h and R15h (Fig. 44). In contrast, the thicknesses of the corresponding separate layers are different. The oxidized Sn6.2A sample has a thicker L2 layer than R2.5h and R15h. The thickness of the L4 layer decreases in the order R2.5 > R15 > Sn6.2A. In the right side of Fig. 43c, SE (upper image) and BS (lower image) images of the same area of the L2 layer under higher magnification, are shown. A very fine structure composed of at least three gray contrasts (from light gray to dark gray) can be observed. Additionally, a fine porosity within the oxide layer is noticed. The matrix of the specimens in Fig. 43 a-c show a uniform gray contrast. Only in the oxidized R15h sample are very fine contrast variations observed (*inset* in Fig. 43d).

The external L1 layer is not suitable for EDX compositional quantification due to its small thickness (0.4 to 0.5 μm). Nevertheless, a higher Ni content with respect to Nb and Sn together with an oxygen content of 17 to 24 at.% indicates that this layer could be a NiO layer. The L2 layers of the samples presented in Fig. 43 a-d are oxygen rich, with 32 to 35 at.% oxygen. Oxygen concentrations in the L4 layers (Fig. 43) were 9 to 18 at.%. The values of $X_{\text{Ni}}/X_{\text{Nb}}$, $X_{\text{Ni}}/X_{\text{Sn}}$ and $X_{\text{Nb}}/X_{\text{Sn}}$, of these samples in the L2 and L4 layers are given in Tables 9 and 10, respectively. The $X_{\text{Ni}}/X_{\text{Nb}}$, $X_{\text{Ni}}/X_{\text{Sn}}$ and $X_{\text{Nb}}/X_{\text{Sn}}$ of the matrix underneath the L4 layer are similar to the nominal alloy composition (1.65 - 1.72, 8.2 - 8.8 and 4.9 - 5.2, respectively).

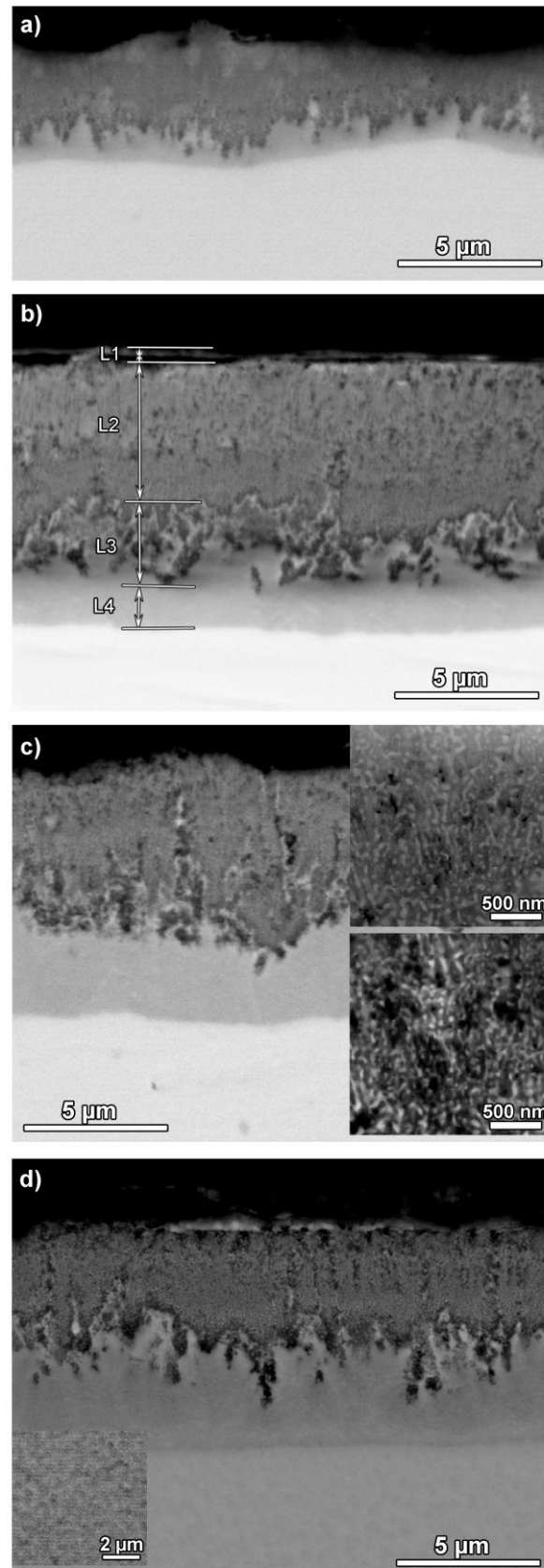


Fig. 43 BS images of the oxidized (at 831 K) amorphous specimens of the $\text{Ni}_{59.35}\text{Nb}_{34.45}\text{Sn}_{6.2}$ composition: **a)** Sn6.2A specimen oxidized for 2.5 h, **b)** Sn6.2A specimen oxidized for 19 h, **c)** specimen R2.5h, oxidized for 19 h, and **d)** specimen R15h oxidized for 19 h. Specimen labels are shown in Table 2.

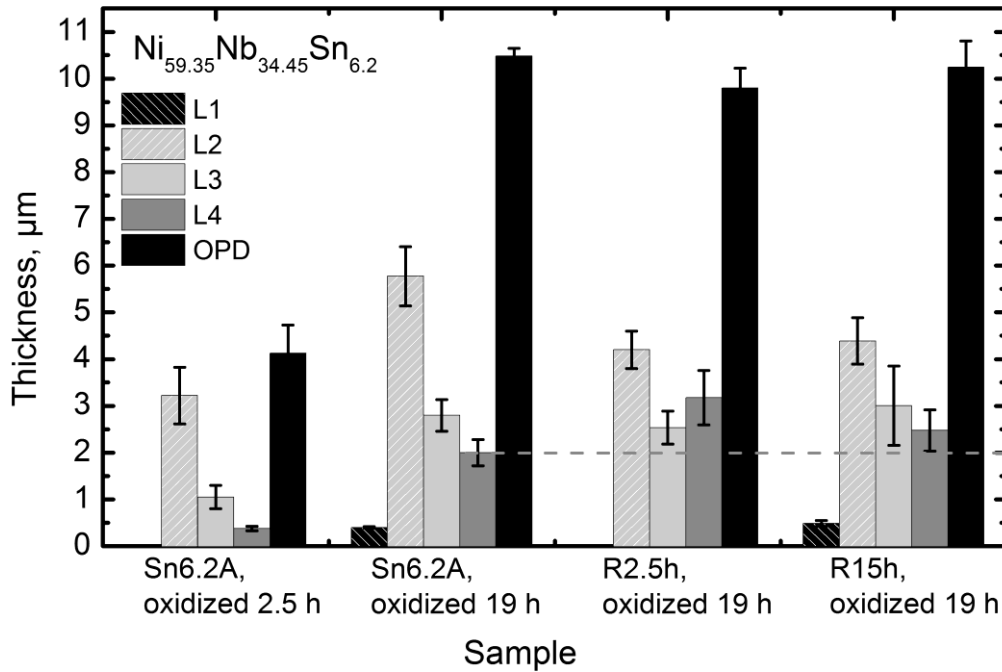


Fig. 44 The thicknesses of different layers formed in the oxidation penetration distance (OPD) of amorphous specimens with the $\text{Ni}_{59.35}\text{Nb}_{34.45}\text{Sn}_{6.2}$ composition, oxidized at 831 K. The first and the second sample from the left are the as-cast amorphous specimens (Sn6.2A) after 2.5h and 19 h of oxidation, respectively. The third and the fourth samples are thermally treated amorphous R2.5h and R15h (see Table 2). The layers L1 –L4 are as defined in Fig. 43.

Table 9 Atomic ratios calculated from the EDX measurements performed on the L2 layers of the amorphous $\text{Ni}_{59.35}\text{Nb}_{34.45}\text{Sn}_{6.2}$ samples (Sn6.2A, R2.5h and R15h, Table 2), oxidized at 831 K.

<i>at.% ratios in L2 layer (main oxide scale)</i>	<i>Ni_{59.35}Nb_{34.45}Sn_{6.2}</i>			
	Sn6.2A, oxidized 2.5 h	Sn6.2A, oxidized 19 h	R2.5h, oxidized 19 h	R15h, oxidized 19 h
$X_{\text{Ni}}/X_{\text{Nb}}$	1.0	0.6	0.6	0.6
$X_{\text{Ni}}/X_{\text{Sn}}$	5.3	2.6	2.6	2.7
$X_{\text{Nb}}/X_{\text{Sn}}$	5.1	4.2	4.5	4.7

Table 10 Atomic ratios calculated from the EDX measurements performed on the L4 layers of the $\text{Ni}_{59.35}\text{Nb}_{34.45}\text{Sn}_{6.2}$ samples (Sn6.2A, R2.5h and R15h, Table 2), oxidized at 831 K.

<i>at. % ratios in L4 layer (Nb depleted zone)</i>	<i>Ni_{59.35}Nb_{34.45}Sn_{6.2}</i>				
	Nominal	Sn6.2A, oxidized 2.5 h	Sn6.2A, oxidized 19 h	R2.5h, oxidized 19 h	R15h, oxidized 19 h
$X_{\text{Ni}}/X_{\text{Nb}}$	1.7	2.8	3.1	3.1	3.0
$X_{\text{Ni}}/X_{\text{Sn}}$	9.6	20.2	15.9	21.1	21.4
$X_{\text{Nb}}/X_{\text{Sn}}$	5.6	7.2	5.9	6.9	7.1

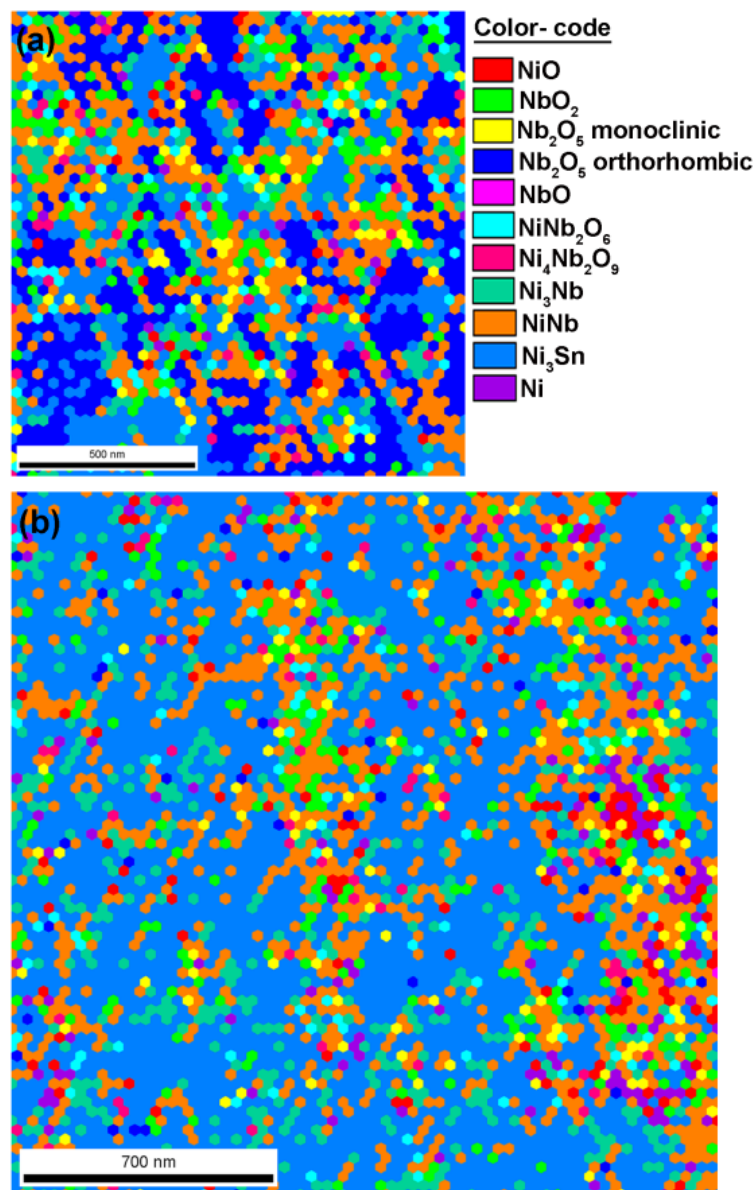


Fig. 45 EBSD phase maps taken from the oxidized ternary amorphous $\text{Ni}_{59.35}\text{Nb}_{34.45}\text{Sn}_{6.2}$ samples (Fig. 43) with a 30 nm step size: a) L2 layer of the sample R15h and b) L4 layer of the sample R2.5h. Sample labels are given in Table 2.

The EBSD phase maps (Fig. 45) were taken with a step size of 30 nm for the amorphous $\text{Ni}_{59.35}\text{Nb}_{34.45}\text{Sn}_{6.2}$ composition. The EBSD map of the L2 layer was taken from the R15h specimen, in the deeper parts of the oxide scale, close to the L3 layer (Fig. 45a). The structure appears to be very fine, approximately the same size as the measurement step. Oxide phases take up 40 % of the image area, where the Nb_2O_5 alone takes up 27 % of the area. The remaining 60 % is taken by a mixture of Ni-Nb intermetallic phases (Ni_3Nb and Ni_6Nb_7) and Ni_3Sn . The Ni_2NbSn phase was not available in the database and its presence can therefore not be determined. In the L4 layer of the specimen R2.5h, the same types of phases are identified as in the L2 layer of the R15h specimen. The oxide phases comprise only 13.2 % of the area, most abundant from which is NbO_2 with 4.5 %; however, 3 % Nb_2O_5 and 2.6 % NiO were also found. The remaining area (86.7 %) is taken up by the Ni-Nb intermetallic phases and Ni_3Sn , where Ni_3Sn alone takes up 54.5 % of the image area. The structure appears to consist of coarser Ni_3Sn grains (120 ± 40 nm in diameter), compared to the Ni_3Sn found in the L2 layer, and very fine grains of the other phases.

The specimen Ni15h (see Table 2), oxidized at 831 K for 19 h, is shown in Fig. 46. Two types of areas, marked with A and B in Fig. 46, can be distinguished. In the area marked with A, a thin dark scale, which corresponds to the L2 layer in Fig. 43, is formed externally. This layer is separated by a well defined planar interface from the underlying L4 layer (depleted matrix). In the thicker areas (e.g. the area marked with B), the oxide scale (L2 layer) appears to be composed of at least three phases distinguishable by differing gray contrasts (Fig. 46). The L1 layer is not observed on the surface of the oxidized Ni15h. The L3 layer is defined as a transition zone between the L2 and L4 layers (see Fig. 43). On the oxidized sample Ni15h, parts of the area B marked with m in Fig. 46, could be classified as a transition zone but, as will be shown below, compositionally it is identical to the average composition of the typical L2 layer.

The compositions of the above mentioned layers of the oxidized Ni15h sample were characterized by EDX. The composition of the L2 layer in the area B was determined in three characteristic points marked with l, n and m in Fig. 46, respectively. The measured oxygen concentrations were 29, 34 and 34 at.% on l, n and m, respectively. $X_{\text{Ni}}/X_{\text{Nb}} = 0.5$ for all three measuring areas (l, n and m in Fig. 46). $X_{\text{Ni}}/X_{\text{Sn}}$ was 2.3 on l and n, and 2.8 on m. Furthermore, the value of $X_{\text{Nb}}/X_{\text{Sn}}$ was determined to be 5.0 on l and n, and 5.8 on m. The L2 layer, in the area A (Fig. 46) contains 56 at.% oxygen and the values of $X_{\text{Ni}}/X_{\text{Nb}}$, $X_{\text{Ni}}/X_{\text{Sn}}$ and $X_{\text{Nb}}/X_{\text{Sn}}$ are 0.1, 0.9 and 6.1, respectively. The L4 layer on the oxidized Ni15h contains 15 at.% oxygen with the atomic ratios $X_{\text{Ni}}/X_{\text{Nb}}$, $X_{\text{Ni}}/X_{\text{Sn}}$ and $X_{\text{Nb}}/X_{\text{Sn}}$ of 2.8, 21.9 and 7.7, respectively.

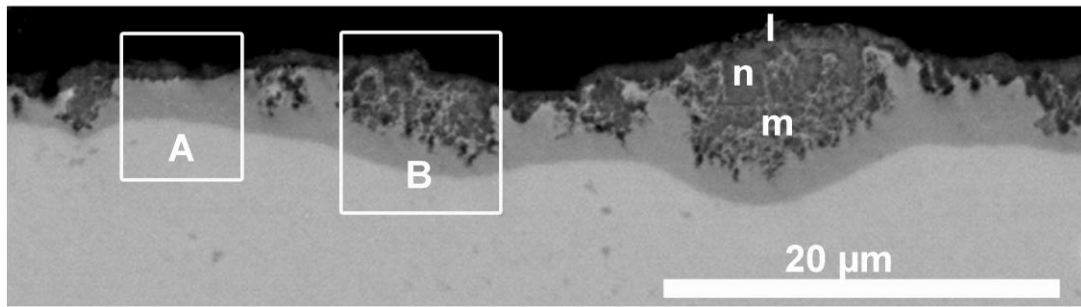


Fig. 46 The BS image of the oxidized nanocrystalline Ni15h sample, of the $\text{Ni}_{59.35}\text{Nb}_{34.45}\text{Sn}_{6.2}$ composition. Oxidation was performed for 19 h at 831 K.

From the oxidized Ni15h sample, one TEM sample in the area of the L2 layer (see Section 3.2.1.2) was prepared. The bright field image is shown in Fig. 47, on the left. Two coarser types of phases were observed: a lighter gray phase (position marked with 1 in Fig. 47) and a darker phase (marked with 2 in Fig. 47). EDX measurements were performed on these phases. The lighter gray phase was determined to be a Nb- and O-rich phase with a 41 at.% Nb, 58 at.% O and 1 at.% Ni. The darker phase, with a composition of 60 at.% Ni, 12 at.% Nb, 13 at.% Sn and 15 at.% O, is a Ni-rich phase. The electron diffraction pattern taken on positions 1 and 2 were also measured and

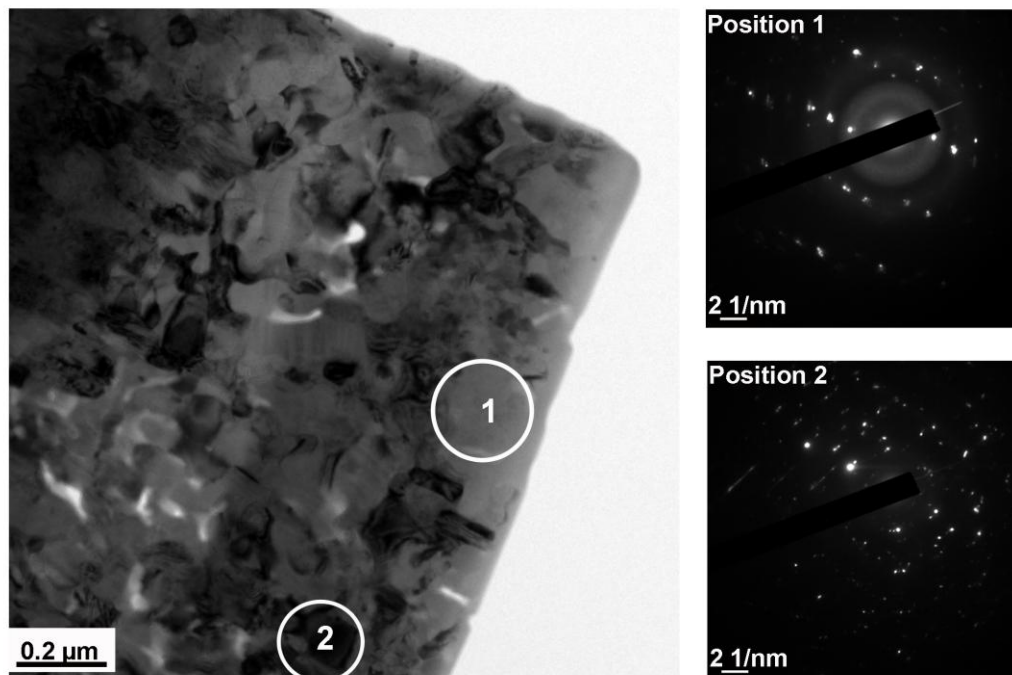


Fig. 47 The TEM images of the nanocrystalline Ni15h sample with $\text{Ni}_{59.35}\text{Nb}_{34.45}\text{Sn}_{6.2}$ composition, after oxidation at 831 K for 19 h: bright field (on the left) and the diffraction patterns taken from positions 1 and 2.

are shown in Fig. 47 on the right. The diffraction areas of position 1 correspond to the size of the lighter gray phase. Nb_2O_5 was identified from the diffraction pattern in position 1. The diffraction area of position 2 is bigger than then the size of the darker phase (schematically shown with a circle in Fig. 47a). In position 2 a polycrystalline pattern was obtained.

The cross-section of the nanocrystalline Nq1223K specimen (see Table 2) of the $\text{Ni}_{59.35}\text{Nb}_{34.45}\text{Sn}_{6.2}$ composition, oxidized at 831 K for 19 h, is shown in Fig. 48. On top of the matrix, with a fine grain-like structure, the oxide scale and Nb-depleted matrix were observed. In Fig. 48, layers L2 and L3, according to general definitions given in connection to Fig. 43b, are defined.

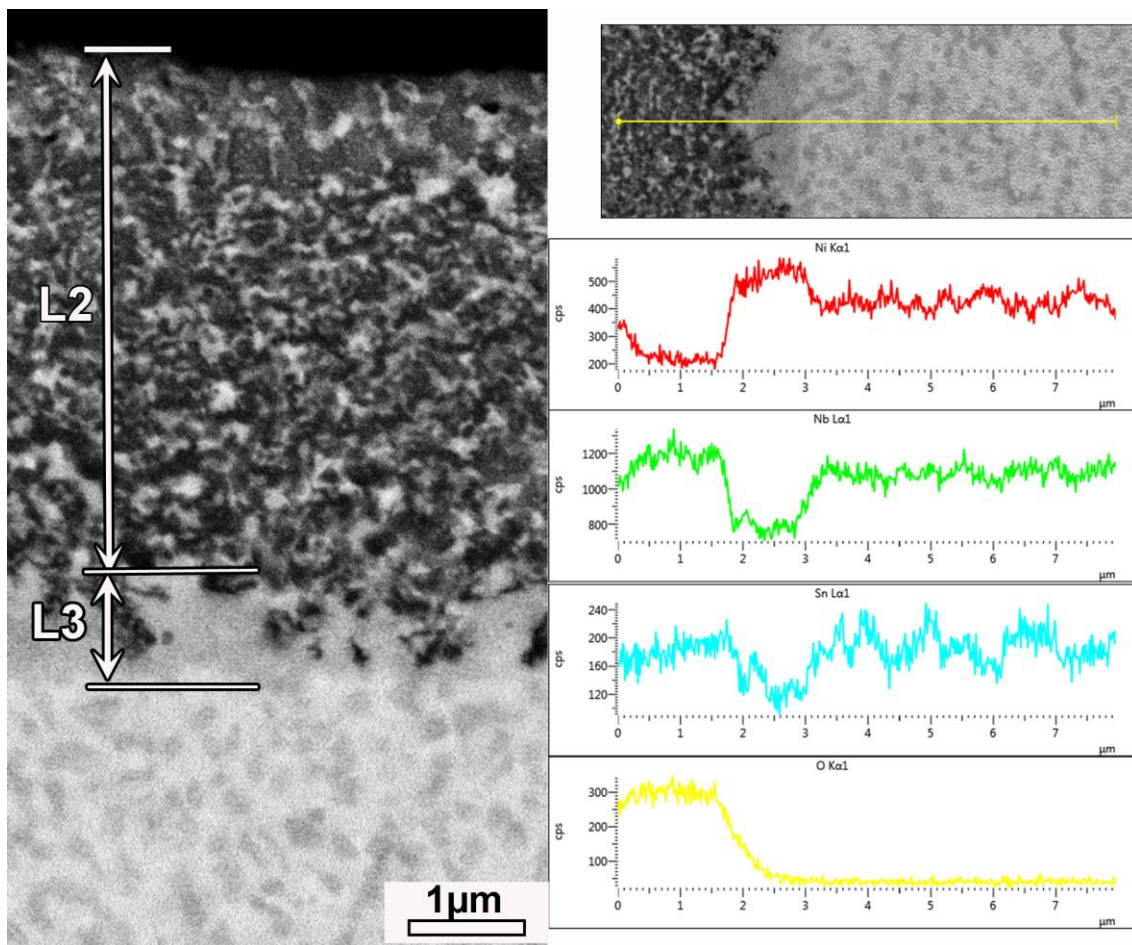


Fig. 48 The BS image of the Nq1223K specimen (Table 2) of the $\text{Ni}_{59.35}\text{Nb}_{34.45}\text{Sn}_{6.2}$ composition, which was oxidized at 831 K for 19 h (on the left). The EDX line-scan performed on the same sample is shown on the right, where vertical axes are in counts per second (cps) and horizontal axes are in μm . The elements are shown in the order: Ni, Nb, Sn and O (top to bottom).

The compositional changes from the oxide scale through the Nb-depleted matrix and further through the matrix are shown with the EDX line-scan (on the right of the Fig. 48). As it can be seen in the image in the upper right side of the Fig. 48, the measurement starts in the oxide scale, 1.5 μm

away from the interface with the Nb-depleted matrix (L2/L3 interface in Fig. 48). From 1.5 to 3.2 μm , the measurement transects the L3 layer (Fig. 48). The last 4.8 μm of the measuring line is the matrix, i.e. the bulk composition of the sample. Within the matrix, the concentration of O is insignificant. Furthermore, the composition just underneath the oxidation penetration distance corresponds to the nominal composition of this alloy, which was confirmed by additional EDX measurements in the matrix. Fine periodic variations in concentration level of Ni, Nb and Sn are also noticeable through the matrix (line-scan in the Fig. 48). The line-scan shows in general that the content of Ni in the Nb-depleted matrix is higher than in the average concentration of the alloy, and that the contents of Nb and Sn are lower than the in the matrix values. In the oxide scale, close to the L2/L3 interface, the Ni concentration is lower, the Nb concentration higher and the concentration of Sn is unchanged compared to the corresponding concentrations in the matrix. As the distance from the interface L2/ L4 increases (throughout the L2 layer), the concentration of Ni starts to increase, and the concentrations of Nb and O decrease.

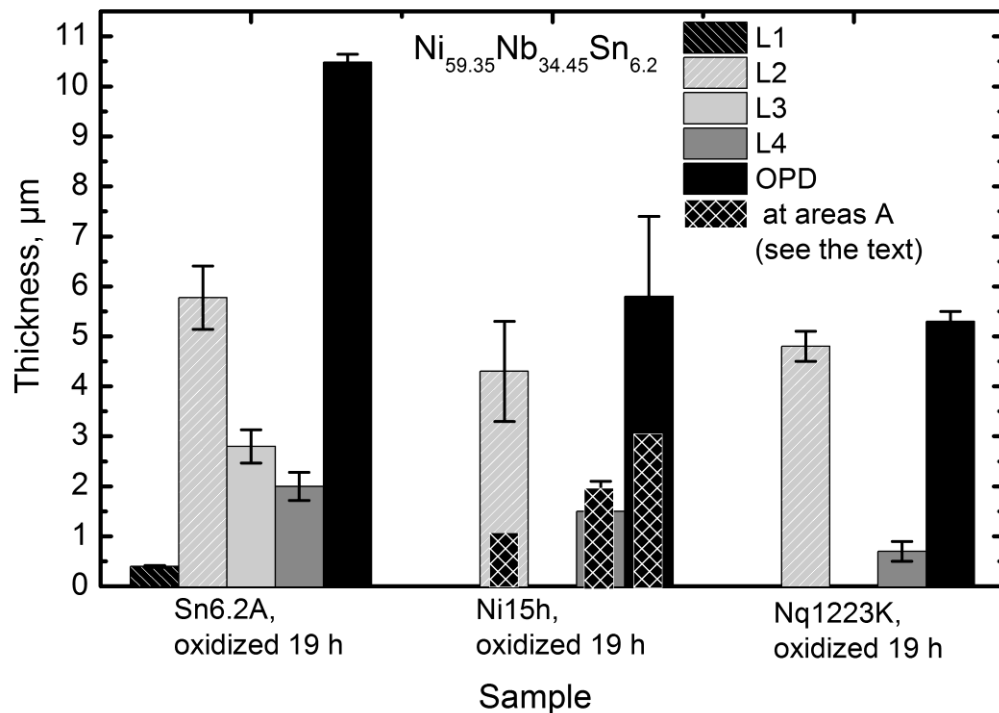


Fig. 49 The thicknesses of the oxidation penetration distance (OPD) and L1 to L4 layers formed after oxidation at 831 K for 19 h on the Sn6.2A, Ni15h and Nq1223K samples (Table 2) with the $\text{Ni}_{59.35}\text{Nb}_{34.45}\text{Sn}_{6.2}$ composition. The layers are defined in Fig. 43. For the sample Ni15h, thicknesses of different layers were determined separately on areas B and A (bars with square pattern which are superimposed onto the corresponding bars of the areas B).

The thickness of the oxidation penetration distance, OPD, and separate layers within the OPD are determined for specimens Sn6.2A, Ni15h and Nq1223K (Table 2), oxidized at 831K for 19 h (Fig. 49). For the specimen Ni15h, the layer thicknesses (L2, L4 and oxidation penetration distance,

OPD) are determined in the areas A and B (Fig. 46) and shown separately in Fig. 49. The OPD-, L4- and L2- layer thicknesses determined in the B areas are shown in the black, dark gray and patterned gray bars, respectively. Inside these three bars, thinner black bars with a square pattern are inserted. These bars represent thicknesses of the corresponding layers (OPD, L4 and L2 layers) as determined on the thinner A areas (Fig. 46). The total thickness of the OPD in B areas is 47 % thicker than in the A areas (Fig. 49). The thickness of the L2 layer in the A areas is also smaller than in the B areas (72 % decrease) but the L4 thickness is greater in the A areas than in the B areas (21 % increase). When the oxidation of the B areas of the sample Ni15h (Fig. 46) is compared to the thicknesses of the corresponding layers in the amorphous oxidized sample with the same composition (Sn6.2A), the total thickness of the oxidation penetration distance (L1 to L4) is 59 % smaller. The thicknesses of the OPD of the oxidized Nq1223K sample appear to be the same as the corresponding thicknesses determined in the B areas of the oxidized Ni15h sample (Fig. 49).

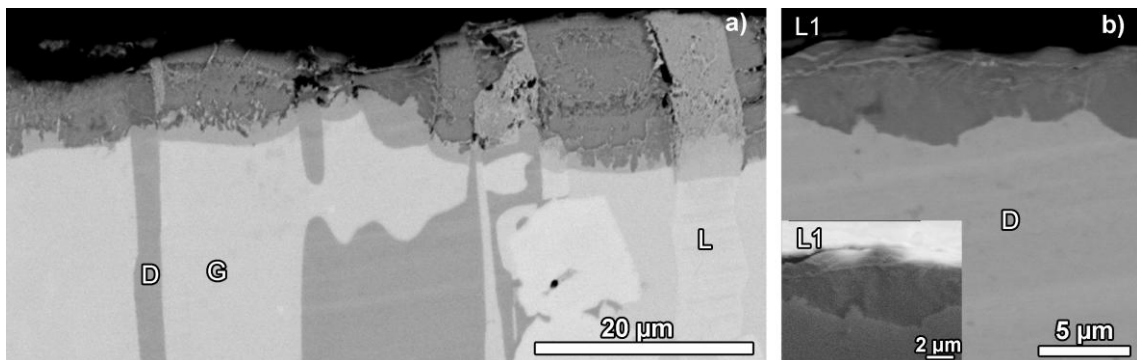


Fig. 50 The BS images taken from the equilibrium cooled specimen (Sn6.2E) with the $\text{Ni}_{59.35}\text{Nb}_{34.45}\text{Sn}_{6.2}$ composition, after oxidation at 831 K for 19h: **a)** overview of the oxide scale formed on different phases and **b)** oxide scale formed on the phase D (see Table 7) including an SE image inserted in the lower left corner of this image.

The BS images taken from the equilibrium cooled $\text{Ni}_{59.35}\text{Nb}_{34.45}\text{Sn}_{6.2}$ specimen of the $\text{Ni}_{59.35}\text{Nb}_{34.45}\text{Sn}_{6.2}$ composition (Sn6.2E in Table 2), after oxidation at 831 K for 19 h, are shown in Fig. 50. A view of the oxidation affected zone over different phases is shown in Fig. 50a. The compositions of these phases, as determined by EDX on the oxidized samples close to the oxidation affected area (D, G and L in Fig. 50) correspond well with the compositions of the crystalline phases shown in Table 7 and are therefore marked with the same symbols as in Table 7 and Fig. 28. The BS image of the oxide scale formed on the phase D (Table 7) is shown in Fig. 50b, and the SE image of the scale is inserted into the lower left corner. The thicknesses and the microstructures of the oxidation layers are different over different phases. On top of the phase D (Fig. 50a), in addition to the thin external layer L1 only the oxide scale (dark layer) was observed on top of the matrix. On top of the phases G and L, the external L1 oxide layer is not observable

but the three morphologically different L2, L3 and L4 layers, as defined in Fig. 43, can be observed. These layers on top of the L phase are comparatively thicker and with lighter contrasts than the corresponding layers on top of the phase G. One can observe that the oxide scale is formed directly on top of the matrix in the case of the phase D, and a matrix depletion layer, which would correspond to the lighter layers on top of G and L, was not observed. The EDX characterization showed that the oxide L2 layer formed on the phase D contains very low Sn concentration (0.3 at %), 17 at.% oxygen and only a slightly lower X_{Ni}/X_{Nb} of 2.6 compared to the D phase (3.0). In the L2 layers of the G and L phases, oxygen concentrations of 31 and 19 at.% were determined, respectively. In the layer L4 of the L and G phases, less than 7 at.% oxygen was detected. The values of X_{Ni}/X_{Nb} , X_{Ni}/X_{Sn} and X_{Nb}/X_{Sn} in the L2 oxide layer on top of the L phase are 1.5, 2.4 and 1.6, respectively; on top of the G phase, 0.5, 2.5 and 5.1, respectively. The values of X_{Ni}/X_{Nb} , X_{Ni}/X_{Sn} and X_{Nb}/X_{Sn} determined in the matrix, beneath the oxidation penetration distance, on the L phase are 2.1, 2.0 and 1, respectively and those determined on the G phase are 1.2, 10.6 and 8.4, respectively. X_{Ni}/X_{Nb} , X_{Ni}/X_{Sn} and X_{Nb}/X_{Sn} in the L4 layer on the L phase are determined to be 3.1, 4.6 and 1.5, respectively.

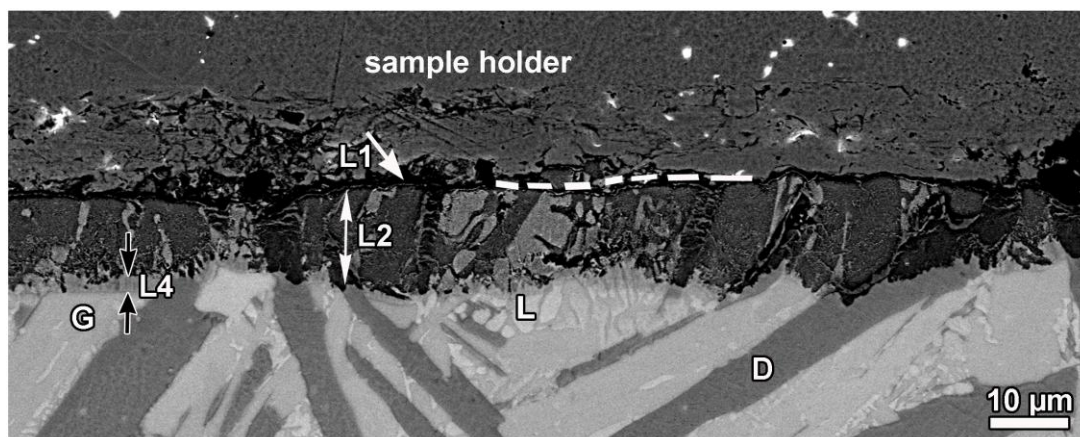


Fig. 51 The BS image taken from the cross-section of the master alloy of the $Ni_{59.35}Nb_{34.34}Sn_{6.2}$ composition, after oxidation at 831 K for 19 h.

The BS image taken from the cross-section of the master alloy of the $Ni_{59.35}Nb_{34.45}Sn_{6.2}$ composition, oxidized at 831 K for 19 h, is shown in Fig. 51. The bulk structure of the sample can be seen in the lower part of the image in Fig. 51. In the upper part of this image, the sample holder (used for the metallographic sample preparation) can be seen. The interface between the oxidized sample and the sample holder is marked with a white dashed line in Fig. 51. A very thin layer, marked with L1 in Fig. 51, can be observed on the surface. The layer directly underneath is marked with L2. This layer consists of differently contrasting areas which appear to be morphologically similar to the bulk structure underneath.

4.3.3.3. Microstructure of the Oxidized Quaternary $\text{Ni}_{58.85}\text{Nb}_{34.45}\text{Sn}_{6.2}\text{Si}_{0.5}$ Alloy

The BS image taken from the as-cast amorphous specimen with the composition $\text{Ni}_{58.85}\text{Nb}_{34.45}\text{Sn}_{6.2}\text{Si}_{0.5}$, after oxidation at 820 K for 17h, is shown in Fig. 52. The microstructure in the oxidation penetration distance is generally similar to that observed on the as-cast amorphous $\text{Ni}_{59.35}\text{Nb}_{34.45}\text{Sn}_{6.2}$ (Fig. 43). The oxide scale appears locally broken-off close to the surface as a result of metallographic preparation (Fig. 52). In its lower part, the structure of this layer becomes coarser, with (horizontally) alternating darker and brighter contrast layers. The matrix depletion layer, between the oxide scale and the matrix contains vertically oriented dark features which often extend to the matrix. The EDX line-scan through the oxidation affected volume, from the oxide layer near the surface, to the matrix, is shown in Fig. 52 on the right. The concentrations of Nb and Sn increase, starting from the right, from 0 to 3 μm . In the same interval the Ni concentration decreases. From 3 to 6 μm , the Ni concentration increases and the concentrations of Nb and Sn decrease. Around 6 μm (interface between the oxide scale and Nb-depleted matrix) and up to 6.5 μm the Ni concentration increases and the Nb and Sn decrease continually, but with higher rates. From 6.5 to 7.5 μm , the concentration of Ni decreases again, while the Nb and Sn concentrations increase. From 7.5 to 9 μm , the concentrations of Ni, Nb and Sn remain constant. The composition of the bulk, away from the oxidation affected zone, was determined to be 56.6 at.% Ni, 36.2 at.% Nb, 6.3 at.% Sn and 0.9 at.% Si.

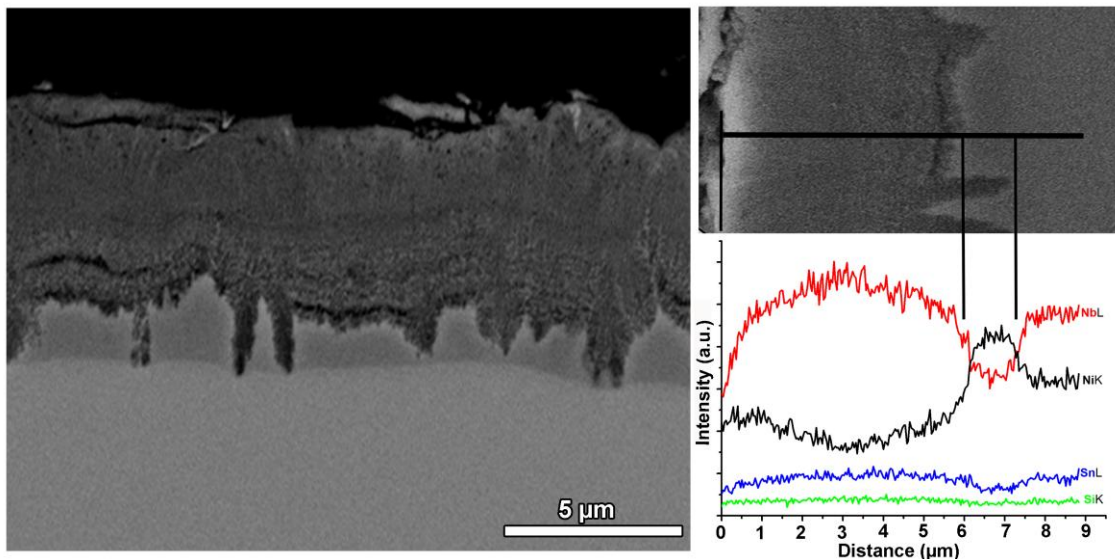


Fig. 52 The BS image taken from the as-cast amorphous $\text{Ni}_{58.85}\text{Nb}_{34.45}\text{Sn}_{6.2}\text{Si}_{0.5}$ after oxidation at 820 K for 17 h (on the left) and the EDX line-scan (on the right).

4.3.3.4. Microstructure of the Oxidized Quaternary $\text{Ni}_{60}\text{Nb}_{34}\text{Sn}_3\text{B}_1$ Alloy

The BS images of the as-cast amorphous specimen B1A of the $\text{Ni}_{60}\text{Nb}_{36}\text{Sn}_3\text{B}_1$ composition, after oxidation at 839 K for 20 h, are shown in Fig. 53. Two types of layer can be differentiated in the oxidation penetration distance: the oxide scale (L2 layer) and the transition zone (L3 layer), as defined in Fig. 43. The oxide scale consists of a cellular structure, where the cells have a faceted morphology with a well defined vertical orientation. The cell boundaries appear to have a lighter contrast. A depleted matrix layer had formed between the oxide layer and the matrix. The faceted vertical cells of the dark layer frequently continue through the depleted matrix layer and often extend to the bulk material. In the bulk, just underneath the L3 layer, the material also has a cellular appearance (image inserted in the lower left corner of the Fig. 53). It was determined from the EDX measurements that $X_{\text{Ni}}/X_{\text{Nb}}$, $X_{\text{Ni}}/X_{\text{Sn}}$ and $X_{\text{Nb}}/X_{\text{Sn}}$ have higher values in the depleted matrix

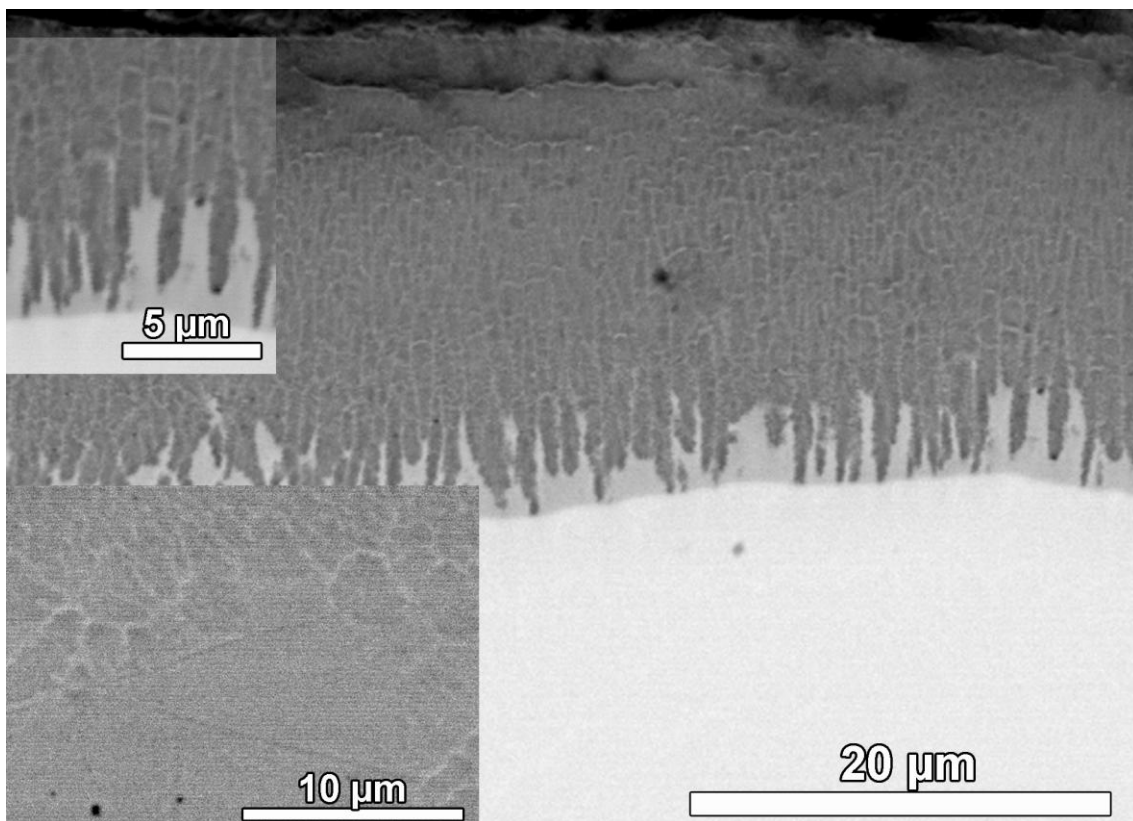


Fig. 53 BS image of the as-cast amorphous B1A specimen with the $\text{Ni}_{60}\text{Nb}_{36}\text{Sn}_3\text{B}_1$ composition, oxidized at 839 K for 20 h, is shown. Inset in the upper left corner of the main image represents the magnification of the L3 layer. In the lower left corner of the figure, the BS image of the bulk, taken underneath the oxidation affected distance, is shown.

than in the matrix or in the oxide layer. The oxygen concentration in the darker layer (L2) is determined to be 32 to 42 at % and in the lighter gray layer (L3) 13 at.%.

In Fig. 54, the total oxidation penetration distance and the thicknesses of the oxide layer (L2) and the transition layer (L3) of the oxidized $\text{Ni}_{60}\text{Nb}_{36}\text{Sn}_3\text{B}_1$, as determined from the BS images, are shown. For comparison, the thicknesses of the layers formed in the oxidation penetration distance of the oxidized as-cast amorphous $\text{Ni}_{59.35}\text{Nb}_{34.45}\text{Sn}_{6.2}$ are also shown in Fig. 54. The total oxidation penetration distance and the thickness of the L2 layer are four times greater than the thicknesses of the corresponding layers on the oxidized as-cast amorphous $\text{Ni}_{59.35}\text{Nb}_{34.45}\text{Sn}_{6.2}$. The thicknesses of the transition L3 layers on the two above mentioned samples are practically the same (Fig. 54). On the oxidized sample of the $\text{Ni}_{60}\text{Nb}_{36}\text{Sn}_3\text{B}_1$ composition, a layer corresponding to the L4 layer of the $\text{Ni}_{59.35}\text{Nb}_{34.45}\text{Sn}_{6.2}$ composition (Fig. 43) was not observed.

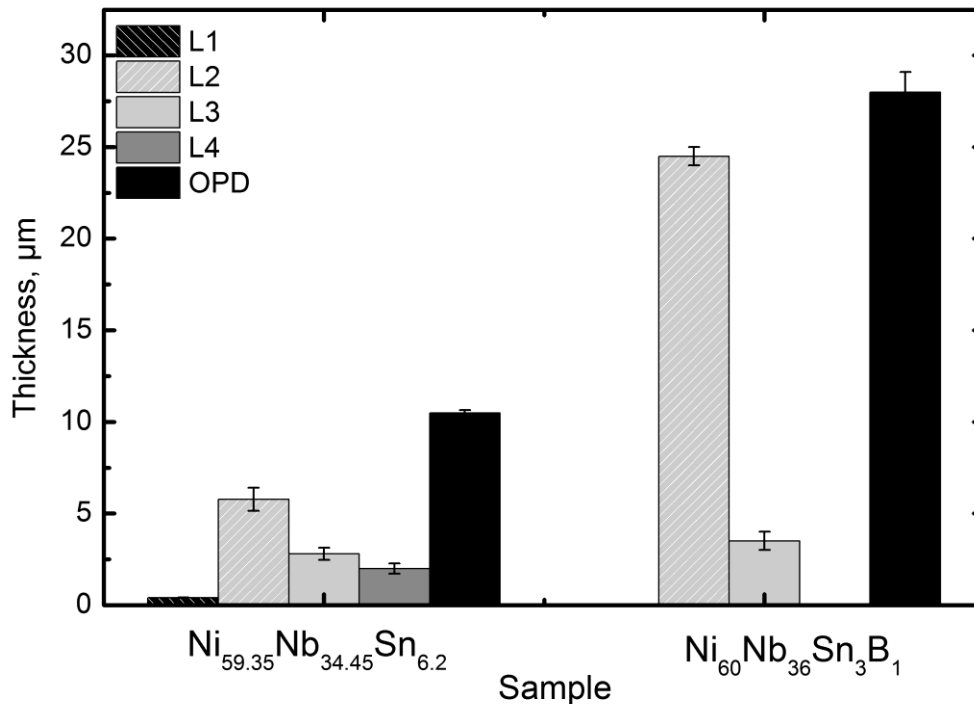


Fig. 54 The thicknesses of the layers formed in the oxidation penetration distance (OPD) of the as-cast amorphous $\text{Ni}_{60}\text{Nb}_{36}\text{Sn}_3\text{B}_1$ (B1A) and for comparison oxidized as-cast amorphous ternary $\text{Ni}_{59.35}\text{Nb}_{34.45}\text{Sn}_{6.2}$ (Sn6.2A) sample, as determined from the BS images.

4.3.4. Calorimetric Characterizations of the Oxidized Ni-Nb-Sn Alloys

The constant heating rate calorimetric thermograms of the as-cast amorphous $\text{Ni}_{57}\text{Nb}_{34}\text{Sn}_9$ are shown in Fig. 55 together with the thermogram taken from the oxidized (816 K for 19.5 h) as-cast amorphous $\text{Ni}_{57}\text{Nb}_{34}\text{Sn}_9$. The oxidation conditions, time and temperature, are chosen to be at $T_g - 50$ K and 75 % of the time to the onset of crystallization of the $\text{Ni}_{57}\text{Nb}_{34}\text{Sn}_9$. The thermogram of the oxidized sample shows a smaller exothermic event in the region before the glass transition than the sample with the as-cast amorphous structure. Enthalpy recovery (at 900 K) is also observable in the oxidized sample. The onset temperatures of the glass transition and crystallization were determined to be 881 and 911 K, respectively. These values are in comparison to the corresponding values of the as-cast amorphous structure 15 K higher and 2 K lower, respectively. The enthalpy of crystallization of the oxidized sample was calculated to be only 5 % smaller than the corresponding value of the as-cast amorphous structure (Table 4).

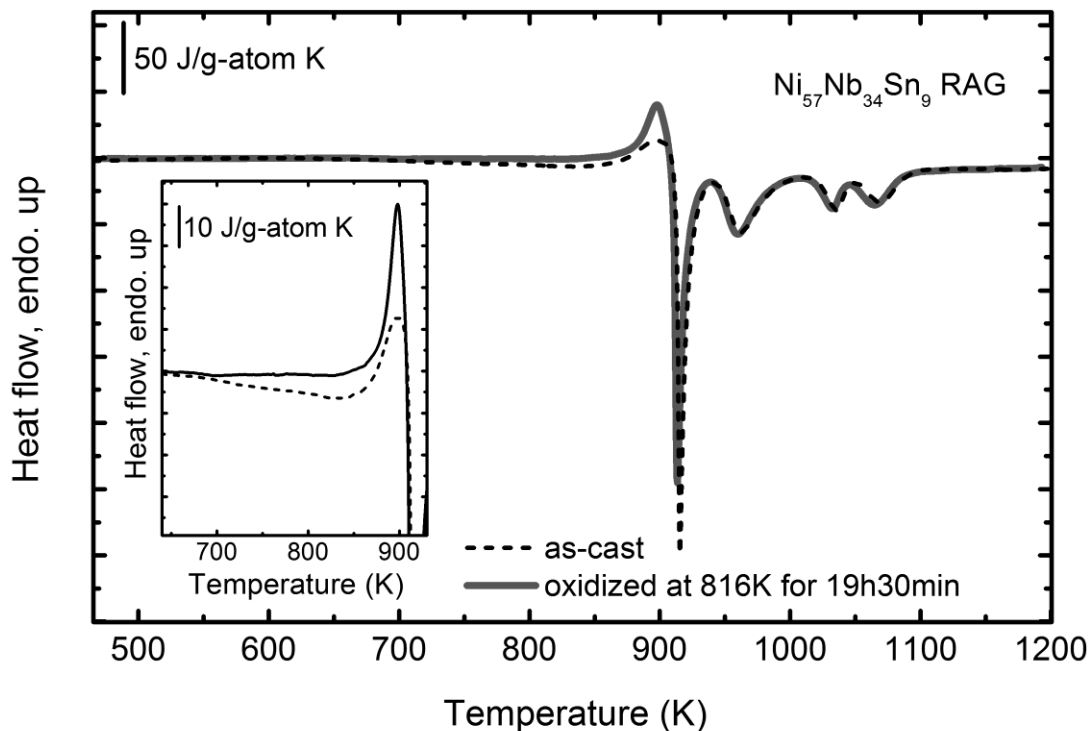


Fig. 55. Comparison of the calorimetric up-scans of the as-cast amorphous $\text{Ni}_{57}\text{Nb}_{34}\text{Sn}_9$, before (dashed line) and after oxidation (solid gray line). Inset represents magnification around glass transition region (630-940 K).

4.3.5. Atom Probe Microscopy Characterization of the Oxidized Ni-Nb-Sn RAG Alloys

The 3D reconstruction of one of the measured tips (Tip 1) of the specimen Si0.5A (Table 2) with the $\text{Ni}_{58.85}\text{Nb}_{34.45}\text{Sn}_{6.2}\text{Si}_{0.5}$ composition, oxidized at 820 K for 17 h, is shown in Fig. 56. The tip was prepared from the deeper parts of the oxide layer (Fig. 11). Two different types of phases can be differentiated in the reconstruction: 1) Nb oxide phase (dominantly red areas in Fig. 56) and 2) the Ni-Nb-Sn based phase (dominantly green and blue areas in Fig. 56). The overall compositions

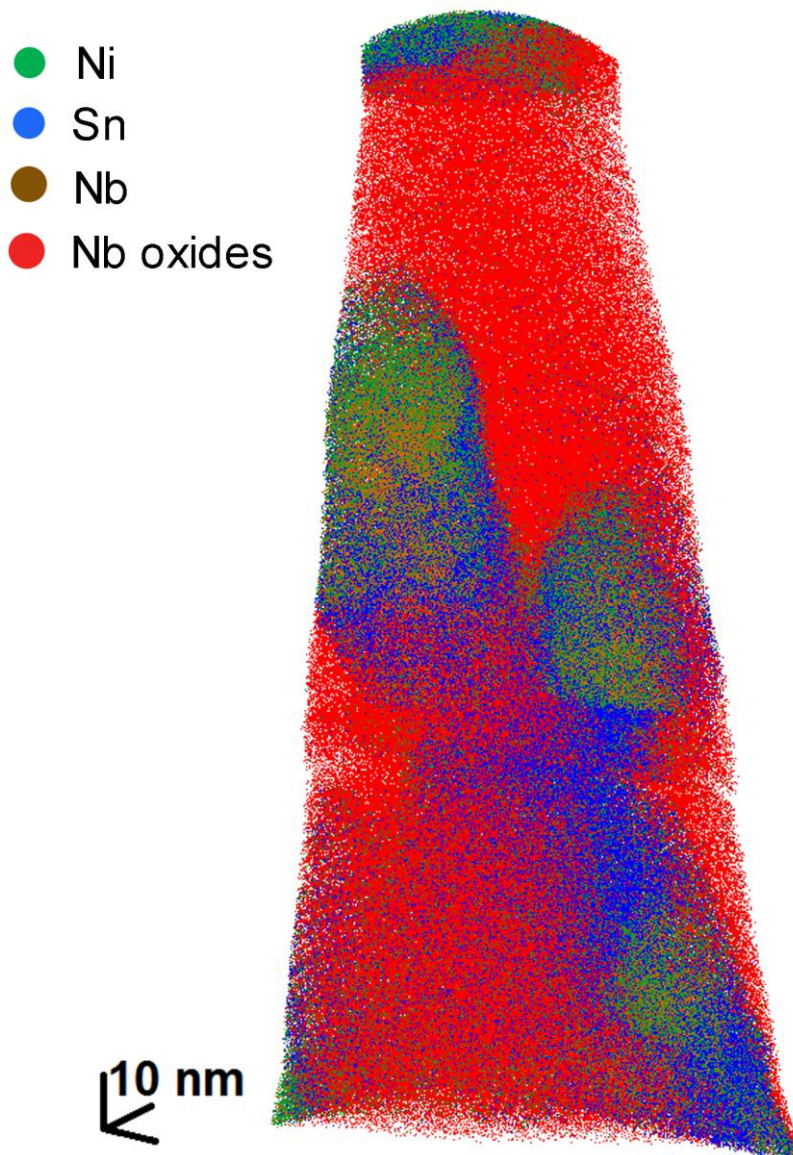


Fig. 56 3D reconstruction of one of the tips (Tip 1) representing the internal oxide scale morphology of the specimen Si0.5A (Table 2) with the $\text{Ni}_{58.85}\text{Nb}_{34.45}\text{Sn}_{6.2}\text{Si}_{0.5}$ composition, oxidized at 820 K for 17 h. Two types of phases can be identified: a Nb oxide phase (red) and the Ni-Nb-Sn based intermetallic phase characterized with an inhomogeneous distribution of Ni and Sn (blue and green, respectively).

of these phases are shown in Table 11.

The reconstruction of another measurement (Tip 2) taken from a similar position in the oxide scale as Tip 1 (Fig. 11) is shown in Fig. 57a. The same two types of phases observed in Tip 1 were also observed in Tip 2. The composition of the oxide phase detected in Tip 2 corresponds well with the composition of the oxide phase determined in Tip 1 (Table 11). The Ni-Nb-Sn based phase in the lower left corner of the reconstruction was extracted and shown separately in Fig. 57b. Typical artifacts resulting from the different evaporation rates of Ni and Sn are observable in the upper parts of the phase. However, the segregation of Ni and Sn, which could not be connected to reconstruction artifacts, was observed in the lower part of the Ni-Nb-Sn based phase. The zones observed as Sn-rich and Ni-rich, are marked A and B in Fig. 57b, respectively. The bottom view of the Ni-Nb-Sn based phase, is shown in the iso-density surfaces in Fig. 57c. The compositions of the Ni-Nb-Sn based phase in the zones A and B are determined from the mass spectra of the two zones and shown in Table 11. The determined compositions of the zones A and B are comparatively different and also different compared to the Ni-Nb-Sn based phase composition determined on Tip 1. This may be an indication that the areas here referred to as Ni-

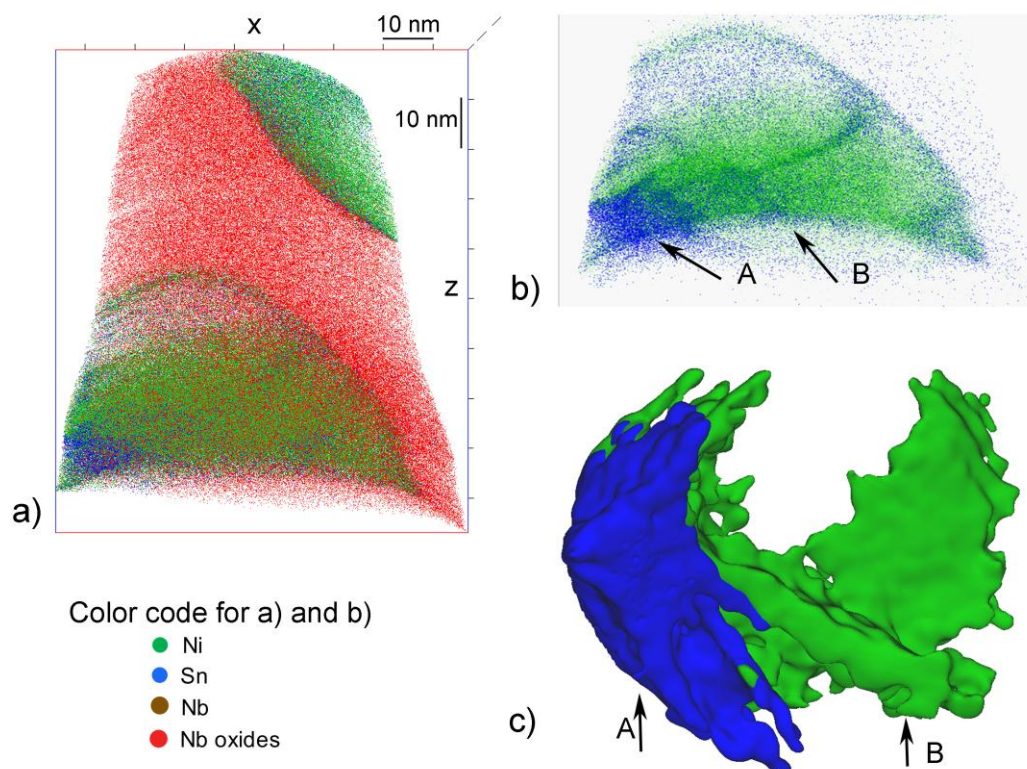


Fig. 57 Reconstructions of one of the measured tips (Tip 2) taken from the oxidized sample (Fig. 11): a) 3D reconstruction where the Nb-oxide phase and the Ni-Nb-Sn based intermetallic phase can be differentiated, b) the extracted Ni-Nb-Sn based phase from the reconstruction in a. The zones marked with A and B show the material characteristic variations in the composition within this phase, c) bottom view of the phase in b), shown through the iso-density surfaces (1.8 ion/nm³ for Sn and 5.5 ion/nm³ for Ni). Zones A and B marked in b) are also indicated in image c).

Nb-Sn based phase represent one phase areas where the Ni, Nb and Sn are inhomogeneously distributed, or that these are the multy phase areas.

Table 11 Compositions of the Nb-oxide phase and Ni-Nb-Sn based phase measured on Tip 1 (Fig. 56) and 2 (Fig. 57).

<i>Ion/at.%</i>	<i>Tip 1</i>			<i>Tip 2</i>		
	<i>Oxide phase</i>	<i>Ni-Nb-Sn based phase (overall)</i>	<i>Oxide phase</i>	<i>Ni-Nb-Sn based phase</i>		
				<i>overall</i>	<i>Zone A</i>	<i>Zone B</i>
<i>Ni</i>	0.0887	71.681±0.048	0.0956	72.134±0.003	68.509±0.233	74.931±0.188
<i>Sn</i>	0.0282	22.363±0.049	0.1001	14.736±0.079	27.485±0.229	15.683±0.17
<i>Nb</i>	31.9017	4.28±0.016	31.5828	11.464±0.048	2.942±0.053	8.688±0.087
<i>O</i>	67.9285	1.351±0.003	68.1038	1.329±0.001	0.914±0.013	0.583±0.010
<i>Si</i>	0.0306	0.041±0.001	0.0303			
<i>Other^a</i>	0.0223	0.284	0.0874	0.337	0.150	0.115

a- Difference to 100 at.% representing sum of other detected elements like H, C, Ga, OH, H₂O, etc.

Despite the difficulties and limitations encountered during analysis of the atom probe measurements on the oxidized samples, the following information was obtained (Table 11):

- The oxide phase determined on two tips of the specimen Si0.5A with the Ni_{58.85}Nb_{34.45}Sn_{6.2}Si_{0.5} composition has the same composition, which stoichiometrically corresponds to the NbO₂ phase.
- This oxide phase contains very low concentrations of the Ni, Sn, and Si
- The distribution of Ni, Nb and Sn in the Ni-Nb-Sn based phase is very inhomogeneous. In some parts of the reconstruction this is the consequence of different evaporation rates of Ni and Sn but the inhomogeneous distribution appears also to be artifact independent. Therefore, the Ni-Nb-Sn based phase represents either one phase areas where the Ni, Nb and Sn are inhomogeneously distributed, or these are in fact multy phase areas.
- The overall content of Si in the alloy was 0.5 at.% (as determined by EDX). In the oxide scale Si was found in very small concentrations in the oxide phase (an order of magnitude lower than the average Si concentration in the alloy) and was not found in the Ni-Nb-Sn based phase. Since the interfaces between the different phases were systematically removed from the analysis, the segregation of Si on the interfaces is not detected, but cannot be excluded.

5. Discussion

Alloying and suction casting of Ni-Nb-Sn RAGs is discussed in Section 5.1. In Section 5.2 the microstructures formed under equilibrium and non-equilibrium cooling conditions are discussed. The results from the amorphous structure characterization, as well as characterization of devitrification sequences in Ni-Nb(-Sn) based alloys are also addressed in Section 5.2. In Section 5.3, the oxidation behavior of the Ni-Nb(-Sn) RAGs is discussed.

5.1. Processing

The arc melting method was chosen for alloying the pure elements into the master alloys as it provides temperatures high enough for melting pure Nb ($T_m = 2750$ K). In the cases of the binary Ni-Nb compositions, the process of alloying together Ni and Nb, as described in the Section 3.1.1, was conducted without any practical difficulties being encountered. Efficient mixing of the two elements in their molten states is attributed to their negative heat of mixing (-30 kJ/mol [60]). The structure of the master alloy of the $Ni_{62}Nb_{38}$ composition was characterized, in the polished cross-section of the ingot, by XRD (Fig. 24a). Identified crystalline phases were the intermetallic Ni_3Nb and Ni_6Nb_7 phases. The reflections of the pure Ni and/or Nb were not identified in the XRD pattern, indicating that the process of alloying was complete.

In first alloying trials of the ternary Ni-Nb-Sn compositions, the position of Ni, Nb and Sn in the spherical impression of the melting chamber was chosen based on the melting temperatures of these elements. The Sn ($T_m=505$ K) was placed directly onto the Cu-plate and the pieces of Ni ($T_m=1726$ K) were placed on top of the Sn, on top of which the Nb ($T_m=2750$ K) pieces were placed. It was attempted in this way to shield the low melting Sn from the extreme temperatures that are necessary to melt the Nb and may cause the Sn to evaporate (Sn $T_b = 2543$ K). After the elements were melted and left to solidify, a strong adhesion between the ingot and the Cu-plate was observed. In the binary Cu-Sn phase diagram, a low melting eutectic can be observed at 500 K, on the Sn-rich side (98.7 at.% Sn) of the diagram [61]. Since Sn was in direct contact with the Cu-plate, this type of reaction could have taken place at the Cu-Sn interface, during melting of the pure elements (Ni, Nb and Sn) and resulted in alloying between the ingot and the Cu-plate. By changing the position of the elements (Fig. 7a), i.e. by placing the Ni pieces in direct contact with the Cu-plate, this low temperature reaction with the Cu-plate was prevented. It was observed that during melting of Nb, the Sn and Ni also melted from the indirect heat. Since the Ni-Sn enthalpy of mixing is negative (-4 kJ/mol) [62], the good mixing during melting was observed. On the other

hand, the Nb-Sn heat of mixing has a small positive value (+7 kJ/mol [60]). This could presumably cause ineffective mixing during melting and lead to problems in the sense of compositional homogenization. The fact that the Sn was already mixed with Ni before final mixing with the Nb is favorable in the sense of obtaining a homogeneous composition of the ingot. After the melt was left to solidify and cool, it was turned upside down and melted again. This process was repeated 3 to 5 times. The structures of the ingots' cross-section (master alloys) were characterized by x-ray diffraction (Fig. 24). The identified crystalline phases were of the Ni_3Nb , Ni_6Nb_7 and Ni_2NbSn -type phase. This indicated, similar to the binary master alloys, that the alloying was complete, i.e. there were no traces of the elemental high-melting Nb found in the ingot. Furthermore, the Ni-Nb-Sn based alloys contain elements with very different melting temperatures. In the cases when such elements are melted together concerns regarding mass loss of the low-melting element exists. The composition of the $\text{Ni}_{59.35}\text{Nb}_{34.45}\text{Sn}_{6.2}$ alloy was experimentally determined from an atom probe mass spectrum (see Section 4.1.2). This experimentally determined composition corresponds well with the nominal values of the $\text{Ni}_{59.35}\text{Nb}_{34.45}\text{Sn}_{6.2}$ alloy (see Section 4.1.2), which confirms that the alloying method is adequate.

The master alloys were re-melted by arc-melting and suction casting into plate-like specimens as described in Section 3.1. At first, many specimens were found to have crystalline phases imbedded in the amorphous matrix. The microstructural characterization of one of these castings can be found in Appendix A1. Improvements to the suction casting conditions, such as the application of higher vacuum (7×10^{-3} mbar) during preparation of chamber atmosphere, resulted in casting specimens with the completely amorphous structures (Section 4.1). The critical casting thicknesses of different compositions, obtained in the casting setup used in this work, are shown in Table 3. These values are slightly lower than the reported values (see Table 1). It can be assumed, however, that further improvement to the casting conditions, such as an even higher vacuum and higher purity Ar, can result in higher casting thicknesses.

5.2. Crystallization

5.2.1. Solidification

The microstructures formed during solidification were characterized for the master alloys of one binary $\text{Ni}_{62}\text{Nb}_{38}$ and three ternary Ni-Nb-Sn compositions ($\text{Ni}_{62}\text{Nb}_{35}\text{Sn}_3$, $\text{Ni}_{59.35}\text{Nb}_{34.45}\text{Sn}_{6.2}$ and $\text{Ni}_{57}\text{Nb}_{34}\text{Sn}_9$). In addition, the microstructures of the $\text{Ni}_{59.35}\text{Nb}_{34.45}\text{Sn}_{6.2}$ and $\text{Ni}_{57}\text{Nb}_{34}\text{Sn}_9$ alloys, equilibrium cooled from molten states, were also characterized.

$\text{Ni}_{62}\text{Nb}_{38}$ is a near-eutectic composition, on the Ni-rich side of the eutectic at 40.5 at.% Nb (Fig. 4), for which primary crystallization of the Ni_3Nb followed by the eutectic crystallization of Ni_3Nb and Ni_6Nb_7 is expected in conditions of equilibrium cooling. In the master alloy structure of the binary $\text{Ni}_{62}\text{Nb}_{38}$, the two mentioned intermetallic phases (Ni_3Nb and Ni_6Nb_7) were indeed identified (Fig. 24, curve a).

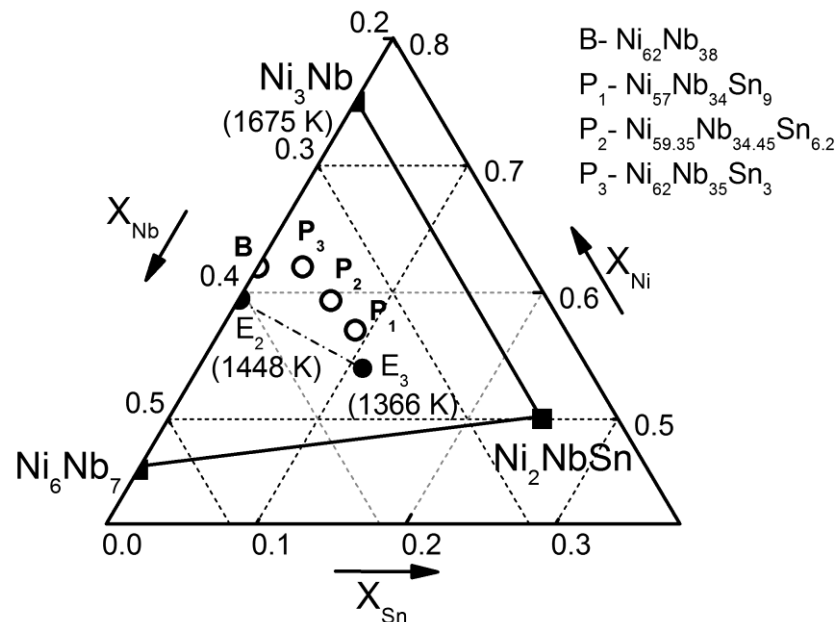


Fig. 58 Schematic representation of a section of the Ni-Nb-Sn diagram showing the compositions of the binary $\text{Ni}_{62}\text{Nb}_{38}$ and three ternary investigated alloys (marked with open circles), as well as the positions of the binary, E_2 (eutectic phases: Ni_3Nb and Ni_6Nb_7) and ternary, E_3 [10] (eutectic phases: Ni_3Nb , Ni_6Nb_7 and Ni_2NbSn) eutectics. Temperatures given in parentheses represent the congruent melting temperature of Ni_3Nb and the eutectic temperatures of E_2 (Fig. 4) and E_3 [10].

The investigated ternary alloys ($\text{Ni}_{62}\text{Nb}_{35}\text{Sn}_3$, $\text{Ni}_{59.35}\text{Nb}_{34.45}\text{Sn}_{6.2}$ and $\text{Ni}_{57}\text{Nb}_{34}\text{Sn}_9$) are compositionally in the vicinity of the Ni_3Nb , Ni_6Nb_7 and Ni_2NbSn -type phase. Also, the compositions of the binary E_2 and ternary E_3 eutectic points are in the proximity of these compositions (Fig. 58). Here it was identified by EDX, that the microstructures of the equilibrium cooled $\text{Ni}_{59.35}\text{Nb}_{34.45}\text{Sn}_{6.2}$ and $\text{Ni}_{57}\text{Nb}_{34}\text{Sn}_9$ specimens are composed of the above mentioned intermetallic phases: Ni_3Nb , Ni_6Nb_7 and a Ni_2NbSn -type phase (marked D, G and L in Fig. 28a and b and Table 7). These three phases combined constitute more than 95 % of the volume of both specimens. Ni_3Nb and the Ni_6Nb_7 appear in the microstructure (Fig. 28a and b) as coarse, randomly oriented, plate-like crystals (phase marked with D and G in Fig. 28a). Between these coarse crystals, the fine eutectic-like features, composed of the phases with three different contrasts (marked with E_{DGL} in Fig. 28) have formed. According to these microstructural characterizations and a general position of the investigated ternary alloys in the phase diagram (schematically shown

in Fig. 58), it is expected that the crystallization of coarse plate-like crystals of Ni_3Nb and Ni_6Nb_7 may have preceded the ternary eutectic reaction ($\text{Liquid} \rightarrow \text{Ni}_3\text{Nb} + \text{Ni}_6\text{Nb}_7 + \text{Ni}_2\text{NbSn}$).

In the microstructures of the $\text{Ni}_{62}\text{Nb}_{35}\text{Sn}_3$, $\text{Ni}_{59.35}\text{Nb}_{34.45}\text{Sn}_{6.2}$ and $\text{Ni}_{57}\text{Nb}_{34}\text{Sn}_9$ master alloys, Ni_3Nb , Ni_6Nb_7 and a Ni_2NbSn -type phase were identified (Fig. 24). The dark plate-like Ni_3Nb phase (Fig. 28) has the same chemical composition in the equilibrium cooled as in the master alloys (Table 7). In both specimens the Ni_3Nb crystallizes as a Sn free phase. The Ni_6Nb_7 phase also has the same chemical composition in the master alloy as in the equilibrium cooled microstructures. About 5 to 7 at % Sn is found as a solute in Ni_6Nb_7 . This shows that, in regard to the formation of Ni_3Nb and the Ni_6Nb_7 , an order of magnitude change in the cooling rate (from 0.1 K/s and 1 K/s) has no significant influence on the compositions of these phases. In connection to this, an important result is that the formation of the Ni_3Nb is only possible in Sn- free areas while the Ni_6Nb_7 can dissolve up to 5-7 at.% Sn. The obtained compositions of Ni_3Nb and Ni_6Nb_7 correspond well with the compositions of these phases obtained on the $\text{Ni}_{59}\text{Nb}_{35}\text{Sn}_6$ master alloy by Zhang et al. [10]. The third phase in the microstructure is the Ni_2NbSn -type phase, which compositionally appears to be dependent on the cooling rate. In the case of slow equilibrium cooling, Ni_2NbSn forms with a chemical composition closer to the stoichiometric Ni_2NbSn composition (see Table 7). When moderate cooling rates are applied (~ 1 K/s for the master alloys), the composition of Ni_2NbSn is more different than the expected stoichiometric composition (50 at.% Ni, 25 at.% Nb and 25 at.% Sn). It is enriched in Nb and poor in Ni and Sn, compared to the stoichiometric values (Table 7). This may indicate that Ni_2NbSn nucleates with this metastable composition, and if cooling is slow enough to allow long range diffusion, it will change its composition closer towards that of the equilibrium composition.

By comparing the equilibrium cooled microstructure with the microstructure of the master alloy (comparison of Fig. 28a - Fig. 28e and Fig. 28b - Fig. 28e), it can be observed that the increase in the cooling rate results in microstructure refinement in both investigated compositions ($\text{Ni}_{59.35}\text{Nb}_{34.45}\text{Sn}_{6.2}$ and $\text{Ni}_{57}\text{Nb}_{34}\text{Sn}_9$). Also, the microstructure of the master alloy with the lower Sn concentration ($\text{Ni}_{59.35}\text{Nb}_{34.45}\text{Sn}_{6.2}$) is coarser than the corresponding microstructure in the alloy with the higher Sn concentration ($\text{Ni}_{57}\text{Nb}_{34}\text{Sn}_9$). This points to the role of mass transport in the crystallization, namely the role of Sn, which is the largest atom with presumably the slowest diffusivity in the Ni-Nb-Sn alloys. It was further observed that the plate-like Ni_6Nb_7 crystals, which were found in equilibrium cooled specimens of both compositions ($\text{Ni}_{59.35}\text{Nb}_{34.45}\text{Sn}_{6.2}$ and $\text{Ni}_{57}\text{Nb}_{34}\text{Sn}_9$), as well as the master alloy of $\text{Ni}_{59.35}\text{Nb}_{34.45}\text{Sn}_{6.2}$, do not form in the master alloy of $\text{Ni}_{57}\text{Nb}_{34}\text{Sn}_9$ (Fig. 28). The Ni_6Nb_7 phase was observed only within the eutectic-like features (marked with E_{DGL} and E_{GL} in Fig. 28f), which appear to form in this case right after the primary crystallization of Ni_3Nb .

5.2.2. Amorphous Structure and Devitrification

5.2.2.1. Devitrification of binary Ni-Nb Alloys

The binary $\text{Ni}_{59.5}\text{Nb}_{40.5}$ and $\text{Ni}_{62}\text{Nb}_{38}$ alloys were cast into amorphous plates of 0.5 mm thicknesses by suction casting. The $\text{Ni}_{70}\text{Nb}_{30}$ binary composition was melt spun into amorphous ribbons. The structure of these specimens was characterized to be amorphous based on their XRD patterns (Fig. 15), which showed only broad amorphous halos in the 2θ interval between 35° and 55° and no sharp crystalline reflections.

The crystallization of the three studied binary Ni-Nb compositions was characterized using calorimetric methods (Fig. 19). It was observed that upon heating from room temperature, with a constant rate of 0.33 K/s using DTA, to the temperature above the end of the crystallization process (1154 K for $\text{Ni}_{70}\text{Nb}_{30}$) only the amorphous sample with a $\text{Ni}_{62}\text{Nb}_{38}$ composition exhibited a glass transition (T_g) before the onset of crystallization (T_x). Also, the T_x of $\text{Ni}_{62}\text{Nb}_{38}$ (937 K) was higher than the T_x of $\text{Ni}_{59.5}\text{Nb}_{40.5}$ and $\text{Ni}_{70}\text{Nb}_{30}$ (918 K and 913 K, respectively). This corresponds well with the findings in Ref. [27], where a maximum temperature of the onset of crystallization in the binary Ni-Nb system was found around 60 at.% Ni. It was also observed in Ref. [27] that T_x increases with increasing heating rate, this effect appears to be the greatest in the Ni-Nb system at around 60 at.% Ni. It therefore appears that at the heating rate of 0.33 K/s, $T_x > T_g$ only for the $\text{Ni}_{62}\text{Nb}_{38}$ composition, causing the glass transition region to be observable in calorimetric up-scans (Fig. 19). In the cases of the other two binary compositions, $\text{Ni}_{59.5}\text{Nb}_{40.5}$ and $\text{Ni}_{70}\text{Nb}_{30}$, $T_x < T_g$. The glass transition is therefore not observable, because the glass crystallizes before relaxing in the supercooled liquid.

The crystallization of the three investigated binary compositions, upon constant heating with 0.33 K/s, proceed in three exothermic events in $\text{Ni}_{62}\text{Nb}_{38}$ and $\text{Ni}_{70}\text{Nb}_{30}$ and in four exothermic events in the $\text{Ni}_{59.5}\text{Nb}_{40.5}$ composition (Fig. 19). The application of the isothermal Gibbs free energy diagram is not appropriate for the discussion of the crystallization under the conditions of constant heating rate. Nevertheless, when constructed at the temperatures around the onset of crystallization (Fig. 19), it can give general information about the driving forces for nucleation of different phases. Therefore, the Gibbs free energy curves of different phases in the binary Ni-Nb system at 925 K, which is close to the T_x of the investigated compositions, are shown in the Fig. 59. These curves are calculated according to the parameters determined by the CALPHAD (Calculation of Phase Diagrams) method in Ref. [27]. In Fig. 59, Gibbs free energy curves of the amorphous phase (A) and two equilibrium intermetallic phases, Ni_3Nb and Ni_6Nb_7 , are shown. The Gibbs free energy curves of the Ni- and Nb-based solid solutions lie at much higher values than those shown in Fig. 59, and therefore do not appear here. In addition to the Gibbs free energy curves, the positions of

the three binary compositions that were studied here, $\text{Ni}_{59.5}\text{Nb}_{40.5}$, $\text{Ni}_{62}\text{Nb}_{38}$ and $\text{Ni}_{70}\text{Nb}_{30}$ are also shown in Fig. 59 (marked with a, b and c, respectively), on the curve of the amorphous phase (A). The parallel tangent construction is shown for the three indicated compositions. With the vertical arrows the thermodynamic driving force for nucleation of the Ni_3Nb and the Ni_6Nb_7 equilibrium phases, from the amorphous phase (with compositions a, b and c), is indicated. It can be observed that the driving force for Ni_6Nb_7 nucleation is lower than for Ni_3Nb nucleation, for all investigated compositions. Furthermore, the driving force for the Ni_6Nb_7 nucleation decreases with increase of the Ni concentration in the alloy (in the order of $a < b < c$) and it even becomes thermodynamically unfavorable for the composition marked with c. The driving force for the nucleation of the Ni_3Nb , on the other hand, increases in the same order ($a > b > c$).

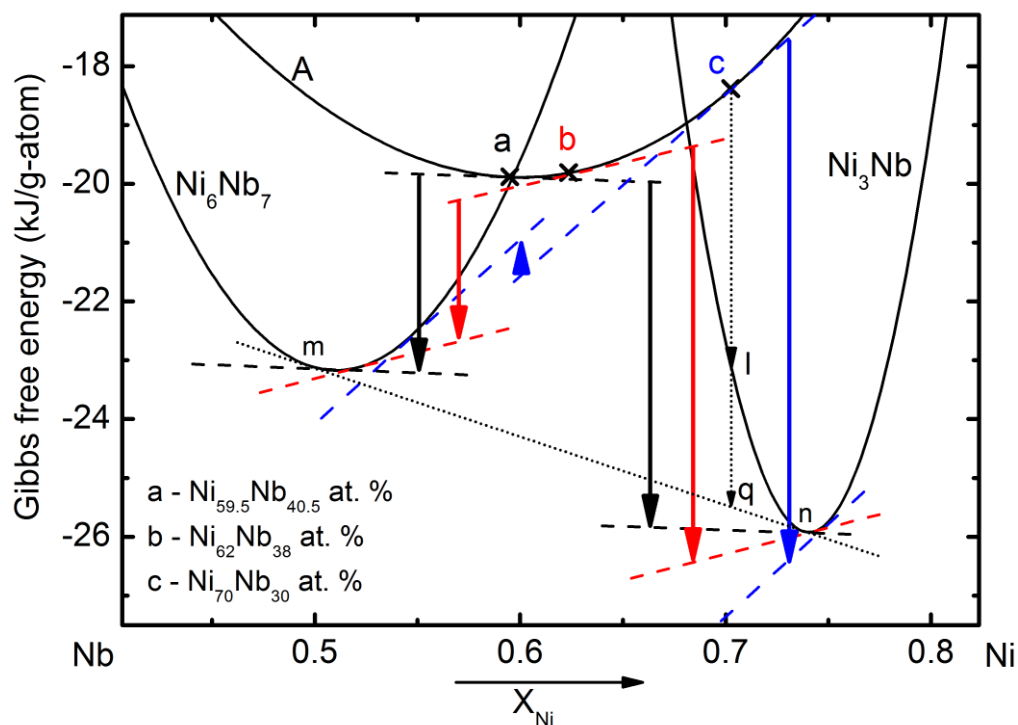


Fig. 59 The Gibbs free energy curves of the Ni_3Nb , Ni_6Nb_7 and amorphous phase in the binary Ni-Nb system at 925 K, calculated using interaction parameters determined by CALPHAD in Ref. [27]. The three binary compositions, $\text{Ni}_{59.5}\text{Nb}_{40.5}$, $\text{Ni}_{62}\text{Nb}_{38}$ and $\text{Ni}_{70}\text{Nb}_{30}$ are indicated on the Gibbs free energy curve of the amorphous phase (A) with a, b and c, respectively. For these three amorphous compositions, the parallel tangent construction over Ni_3Nb and Ni_6Nb_7 phases is shown with dashed lines, and the driving force for nucleation of Ni_6Nb_7 (on the left) and Ni_3Nb (on the right) are shown with the solid arrows. With a dotted line, a common tangent of Ni_3Nb and Ni_6Nb_7 , is shown.

It was mentioned in the previous paragraph that for all three compositions, the thermodynamic driving force for nucleation of Ni_3Nb is higher than that of Ni_6Nb_7 . It can be therefore expected in all three compositions, that Ni_3Nb will be the first phase to crystallize from the amorphous phase. Structural characterizations of the thermally treated Ni-Nb specimens were not carried out in this

work; results reported elsewhere [27,28] for the Ni-Nb system will be used for further discussion. It was reported in Ref. [27] that, upon heating with 0.017 K/s, after the first crystallization event, only Ni_3Nb was identified in the structure and the remaining amorphous phase was not reported to have been observed. It was further reported there, that after the second crystallization event Ni_6Nb_7 was identified in addition to Ni_3Nb . At the composition of 70 at.% Ni, the Ni_3Nb Gibbs free energy curve lies well below the amorphous curve (composition c in Fig. 59). Crystallization may have therefore proceeded according to polymorphic transformation of the amorphous phase into Ni_3Nb . The formation of the Ni_3Nb phase with the same composition as the starting amorphous phase would result in the decrease of Gibbs free energy from the point c to point l, as indicated with an arrow in Fig. 59. Equilibrium would then be reached with a consequent transformation into the Ni_3Nb phase with the composition n and Ni_6Nb_7 with a composition m, as indicated on the common tangent (dotted line) in Fig. 59. The structural changes corresponding to the third crystallization event (Fig. 19) are not clear due to insufficient structural information.

In the structure of the Ni-Nb amorphous alloys with 60 and 65 at.% Ni, upon heating with 0.017 K/s above the first exothermic event, Ni_3Nb along with the amorphous phase were identified [27]. This type of transformation is a non-polymorphic, diffusion controlled transformation, which is believed to take place also in the $\text{Ni}_{62}\text{Nb}_{38}$ composition investigated here. The lower T_x of $\text{Ni}_{70}\text{Nb}_{30}$ compared to that of $\text{Ni}_{62}\text{Nb}_{38}$ could therefore be a result of the higher driving force for Ni_3Nb nucleation and, possibly, the fast polymorphic type of transformation in $\text{Ni}_{70}\text{Nb}_{30}$.

The calorimetric measurements have also shown that $\text{Ni}_{59.5}\text{Nb}_{49.5}$ has a lower T_x than $\text{Ni}_{62}\text{Nb}_{38}$ (Table 4). The crystallization behavior of the amorphous $\text{Ni}_{60}\text{Nb}_{40}$ alloy, very similar to the $\text{Ni}_{59.5}\text{Nb}_{49.5}$ characterized here, was reported in Ref. [28]. According to those findings, the formation of the metastable M-phase can be assigned to the first crystallization event in amorphous $\text{Ni}_{60}\text{Nb}_{40}$. The formation of the M-phase, prior to the formation of Ni_3Nb , may also be considered to be the reason why $\text{Ni}_{59.5}\text{Nb}_{49.5}$ exhibits a lower T_x compared to that of $\text{Ni}_{62}\text{Nb}_{38}$.

5.2.2.2. Amorphous Structure of Ternary Ni-Nb-Sn Alloys

The 1 mm thick suction cast plates of different ternary compositions were characterized by XRD. When no sharp crystalline reflections were observed, i.e. only presence of the broad amorphous halo on the diffraction pattern was detected, the sample was considered amorphous (Fig. 15). However, the limitation of the XRD method in regard to the minimal crystalline structure size which can be identified should be considered to be at about 2 nm. By fitting the amorphous halos formed between 35 and 55° with the Voigt function, the positions of the amorphous halo maxima (x_c) were determined. From x_c the average interatomic distances were calculated. In this way, four different ternary compositions: $\text{Ni}_{57}\text{Nb}_{34}\text{Sn}_9$, $\text{Ni}_{59.35}\text{Nb}_{34.45}\text{Sn}_{6.2}$, $\text{Ni}_{35}\text{Nb}_{35}\text{Sn}_5$ and

$\text{Ni}_{62}\text{Nb}_{35}\text{Sn}_3$, were analyzed. The Nb content in these four compositions varies very little (2 at.%) in comparison with the Ni and Sn compositions. The calculated interatomic distances showed a decreasing trend with the decrease in the Sn concentration in the alloy (see Section 4.1.1). Since Sn, with its atomic radius of $r_{\text{Sn}}=1.62 \text{ \AA}$, is the largest element in the ternary Ni-Nb-Sn alloys ($r_{\text{Nb}}=1.46$ and $r_{\text{Ni}}=1.28 \text{ \AA}$), the trend of decreasing interatomic distances with the decrease of Sn content is expected. The interatomic distance determined for the composition with the lowest Sn content, $\text{Ni}_{62}\text{Nb}_{35}\text{Sn}_3$, (2.12 \AA) is similar to the interatomic distances determined in the binary samples with the intermediate compositions $\text{Ni}_{59.5}\text{Nb}_{40.5}$ and $\text{Ni}_{62}\text{Nb}_{38}$ (2.12 and 2.13 \AA , respectively). Since the focus of this work is on the ternary Ni-Nb-Sn system, the amorphous structure of the suction cast ternary $\text{Ni}_{59.35}\text{Nb}_{34.45}\text{Sn}_{6.2}$ sample, characterized above by XRD (Section 4.1.1) is investigated further by the APT (Section 4.1.2). The composition of the as-cast $\text{Ni}_{59.35}\text{Nb}_{34.45}\text{Sn}_{6.2}$ alloy, as determined by the complete peak decomposition analysis of the mass spectrum (58.18 at.% Ni, 34.549 at.% Nb and 6.396 at.% Sn) showed a good agreement with the nominal composition (59.35 at.% Ni, 34.45 at.% Nb and 6.2 at.% Sn). The 1D profiles of the Ni, Nb and Sn concentrations in two directions, x and z (Fig. 17), show constant values of Ni, Nb and Sn; i.e. the differences between the maximal and minimal measured concentrations of each of the three elements is not larger than 3 at %, within the measured distances of 30 and 18 nm, respectively. Keeping in mind the high spatial resolution of the APT – better than 0.04 nm in z direction and 0.2 nm in both lateral directions, x and y [57] – any significant compositional variations would have been noticeable in the 1D profile (Fig. 17) already at the sub-nm scale. Additionally, a method of random comparators was used in order to obtain more information about the atomic arrangement in the sample. Since in this case the experimental curves correspond well with the curves representing an ideally random element distribution, it can be said that the as-cast amorphous structure exhibits no characteristics typical of phase separation or formation of fine crystalline particles.

5.2.2.3. Devitrification of Ni-Nb-Sn Based Alloys

Calorimetric measurements with a constant heating rate of 0.33 K/s were used to characterize the crystallization behavior of the ternary Ni-Nb-Sn RAG alloys from the glassy state. It was observed that among the three investigated compositions, both T_g and T_x increase significantly in the order $\text{Ni}_{57}\text{Nb}_{34}\text{Sn}_9 < \text{Ni}_{59.35}\text{Nb}_{34.45}\text{Sn}_{6.2} < \text{Ni}_{62}\text{Nb}_{35}\text{Sn}_3$ (T_g : 869 K < 881 K < 894 K and T_x : 913 K < 924 K < 940 K). It was also observed that the $\text{Ni}_{57}\text{Nb}_{34}\text{Sn}_9$ and $\text{Ni}_{59.35}\text{Nb}_{34.45}\text{Sn}_{6.2}$ compositions crystallize in four exothermic events, while the $\text{Ni}_{62}\text{Nb}_{35}\text{Sn}_3$ composition crystallizes in three (Fig. 20). In order to obtain more information about which crystalline phases form during each of these exothermic events, the up-scans of the $\text{Ni}_{59.35}\text{Nb}_{34.45}\text{Sn}_{6.2}$ composition were stopped at four different

temperatures (schematically marked with the specimen names in Fig. 60), and the obtained structure was characterized by XRD. In the case of the $\text{Ni}_{57}\text{Nb}_{34}\text{Sn}_9$ composition only the specimen heated just above the first crystallization event was prepared (Sn9Nq933K in Table 2) and characterized.

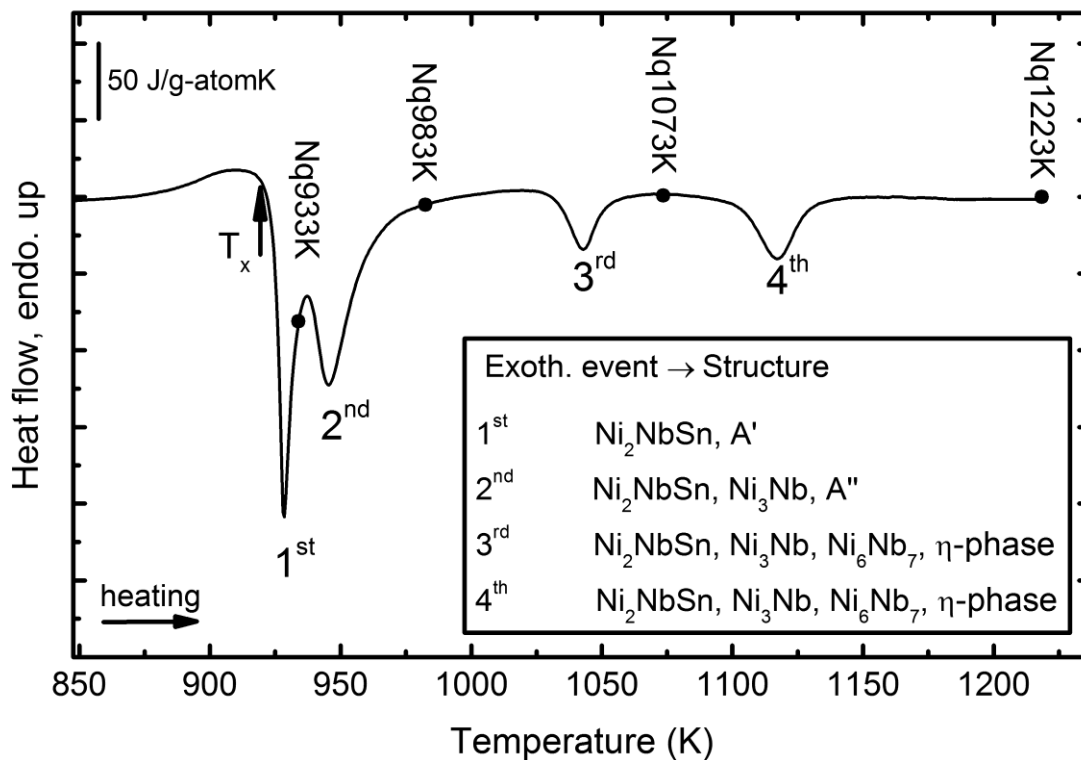


Fig. 60 Constant heating rate thermogram of the as-cast amorphous $\text{Ni}_{59.35}\text{Nb}_{34.45}\text{Sn}_{6.2}$ RAG alloy, with the solid circles indicating temperatures at which the up-scans were stopped for specimens Nq933K, Nq983K, Nq1073K and Nq1223K (Table 2). The phases identified in the structure after each of the crystallization events, as determined by x-ray diffraction, are shown below the heat flow curve.

After the first crystallization event, according to the XRD patterns of $\text{Ni}_{57}\text{Nb}_{34}\text{Sn}_9$ and $\text{Ni}_{59.35}\text{Nb}_{34.45}\text{Sn}_{6.2}$ compositions (Fig. 25a and b, respectively), the structure consists of an amorphous phase (A') and a crystalline phase identified as a Ni_2NbSn -type phase (Fig. 60).

After the second crystallization event, in addition to the Ni_2NbSn -type phase, one other crystalline phase, Ni_3Nb , appears in the structure. At this point, the amorphous halo is still observable in the XRD pattern (Fig. 25c), which indicates the presence of the amorphous phase (A'' in Fig. 60). Finally, after the third and fourth crystallization events, Ni_6Nb_7 and a metastable η -phase are observed in the structure in addition to the previously formed Ni_2NbSn and Ni_3Nb phases. Already after the third crystallization event, the amorphous halo cannot be identified in the structure with certainty (Fig. 25c).

The thermodynamic parameters required for the construction of the Gibbs free energy curves of the phases: Ni_3Nb , Ni_6Nb_7 , Ni_2NbSn and the amorphous phase in the ternary Ni-Nb-Sn system, are not available from the literature. A hypothetical quasi-binary section of a Gibbs free energy diagram at 773 K is shown in Fig. 61a. The position of the quasi-binary section is along the AB line, shown schematically in the isothermal ternary Ni-Nb-Sn diagram (insertion in Fig. 61a). This section corresponds to a constant Sn concentration of 6.2 at.%, which itself corresponds to the Sn concentration in one of the investigated ternary compositions, $\text{Ni}_{59.35}\text{Nb}_{34.45}\text{Sn}_{6.2}$. The positions of the minima of the Gibbs free energy curves of Ni_3Nb , Ni_6Nb_7 and Ni_2NbSn are projected onto the AB section from their stoichiometric points in the ternary diagram. The Ni_3Nb phase is presented with the Gibbs free energy curve with steeper slopes compared to Ni_6Nb_7 . This corresponds to the facts that in the binary Ni-Nb system Ni_6Nb_7 forms in a wider concentration interval than Ni_3Nb (Fig. 4) and, in ternary Ni-Nb-Sn alloys, Ni_3Nb crystallizes only Sn-free and Ni_6Nb_7 can contain up to 7 at.% Sn solute (see Section 5.2.1). The minimum of the Gibbs free energy curve (y-axis in Fig. 61) of the Ni_3Nb is at lower energy values compared to Ni_6Nb_7 , which roughly reflects the positions of these phases in the binary Ni-Nb diagram at the same temperature. The thermodynamic parameters required for the construction of the Ni_2NbSn Gibbs free energy curve are also not available. According to the EDX measurements on the equilibrium cooled and master alloy structures it was concluded that Ni_2NbSn can form in a broad concentration range (35 – 56 at.% Ni from Table 7) and was therefore constructed with less steep slopes than the Ni_3Nb , which forms in a narrow concentration range. The Gibbs free energy curve minimum of the Ni_2NbSn -type phase was chosen at the position which gives the common tangent with the other two equilibrium phases (Ni_3Nb and Ni_6Nb_7). In Fig. 61a, the amorphous curve is marked with A and the ternary composition $\text{Ni}_{59.35}\text{Nb}_{34.45}\text{Sn}_{6.2}$ is marked on the amorphous curve with P. At 773 K, according to the isothermal section of the Ni-Nb-Sn system [63], the composition marked with P should be in the three phase field of the Ni_3Nb , Ni_6Nb_7 and Ni_2NbSn phases, which is indeed the case in this hypothetical diagram. The common tangent of the three discussed phases is shown with a dotted line marked with e in Fig. 61a.

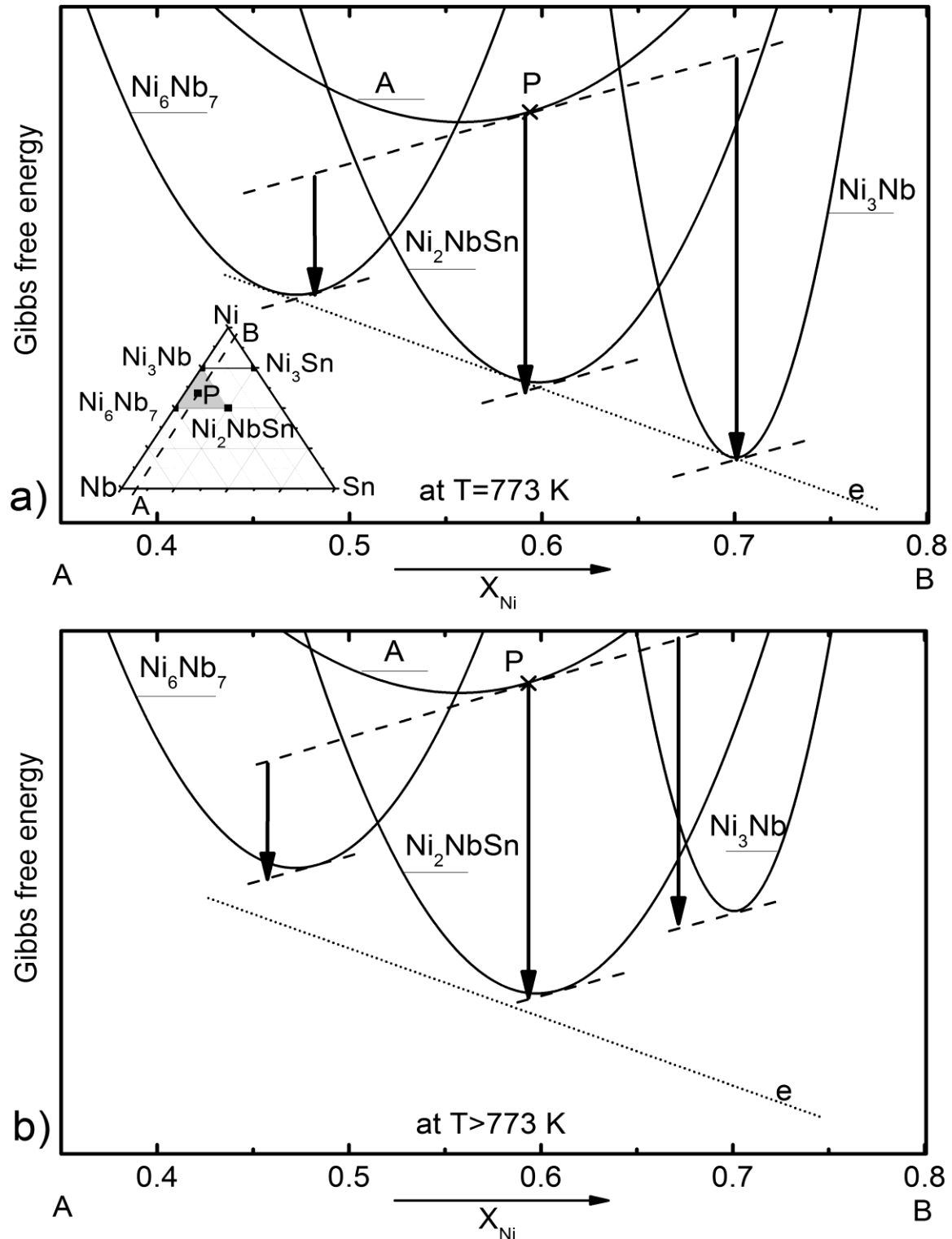


Fig. 61 The Hypothetical quasi-binary diagrams, presenting isothermal Gibbs free energies of different phases along the AB cross-section (see inserted schematic representation of the isothermal ternary Ni-Nb-Sn diagram): **a)** at $T = 773$ K and **b)** at $T > 773$ K. Phases presented on this diagram are the equilibrium Ni_3Nb , Ni_6Nb_7 and Ni_2NbSn as well as the amorphous phase (A). The position of *tangent e* (marked with dotted line) is identical in a) and b), for visual orientation.

According to the Gibbs free energy diagram in Fig. 61a and the parallel tangent construction over the amorphous phase with the composition P and the three equilibrium intermetallic phases, Ni_3Nb , Ni_6Nb_7 and the Ni_2NbSn -type phase, it would appear that the thermodynamic driving force for nucleation decreases in the order $\text{Ni}_3\text{Nb} > \text{Ni}_2\text{NbSn} > \text{Ni}_6\text{Nb}_7$, as indicated with the arrows in Fig. 61a. This would suggest that the first phase to form from the amorphous phase (with the composition P) would be Ni_3Nb . This doesn't correspond with the experimentally observed behavior, where the Ni_2NbSn -type phase is identified to be the first and the Ni_3Nb only second crystalline phase to form from the amorphous phase Fig. 60. The reason for this may be the fact that the hypothetical diagram in Fig. 61a is made to correspond to information available for 773 K, that the three phases form a three phase field in the compositional interval roughly corresponding to the interval between the tangent intersects on Ni_6Nb_7 and Ni_3Nb (Fig. 61a). The temperature T_x , as observed in the heat flow curve of the discussed composition is at 924 K (Fig. 20a), which is significantly higher than the temperature of the hypothetical Gibbs free energy diagram shown in Fig. 61a. It might be the case that with the increase in temperature the position of the Gibbs free energy curve of Ni_3Nb increases to higher energy values faster than those of the other phases, especially Ni_2NbSn . Ultimately, the situation shown in Fig. 61b might be more likely to expect, where the driving force for nucleation of $\text{Ni}_2\text{NbSn} > \text{Ni}_3\text{Nb} > \text{Ni}_6\text{Nb}_7$ (indicated with arrows in Fig. 61b).

It should be also noted that, since Ni_3Nb forms as a Sn-free phase, significant structural rearrangements are needed for its nucleation and growth, especially with regard to Sn (formation of Sn-poor areas). Therefore, kinetic factors might also contribute to primary nucleation of Ni_2NbSn instead of Ni_3Nb .

As already stated, after the first crystallization event of as-cast amorphous $\text{Ni}_{57}\text{Nb}_{34}\text{Sn}_9$ and $\text{Ni}_{59.35}\text{Nb}_{34.45}\text{Sn}_{6.2}$, the structure consists of an amorphous phase (A') and a crystalline phase identified as a Ni_2NbSn -type phase (Fig. 60). The interatomic distances corresponding to maxima of the broad halos of the remaining amorphous phases (A'), in both Sn9Nq933K and Nq933K specimens (2.02 Å and 2.10 Å, respectively), are smaller compared to those of the as-cast amorphous phases with the same composition (2.15 Å in $\text{Ni}_{57}\text{Nb}_{34}\text{Sn}_9$ and 2.14 Å in $\text{Ni}_{59.35}\text{Nb}_{34.45}\text{Sn}_{6.2}$). This is in agreement with the fact that a phase rich in Sn compared to the average alloy composition has crystallized, leaving the remaining amorphous matrix (A') poorer in Sn than the as-cast amorphous phase. Since Sn is the largest atom in the Ni-Nb-Sn alloy system the average interatomic distance may decrease in Sn- poorer amorphous matrix (A').

Based on the available information, it cannot be determined with certainty whether the formation of Ni_3Nb within the second exothermic event (Fig. 60) involves only its crystallization from the remaining amorphous phase, A', or if it also involves some type of reaction with previously crystallized Ni_2NbSn . Nevertheless, it is very possible that the partial elimination of Sn

from the amorphous phase during primary crystallization of Ni_2NbSn (Sn poorer A') is favorable for the consequent nucleation of Ni_3Nb in A' . After the second exothermic event, it was determined that the structure consists of Ni_2NbSn , Ni_3Nb and a remaining amorphous phase, A'' , (Fig. 60). If, as proposed, Ni_3Nb had formed from A' , then based on the fact that Ni_3Nb can be considered to be a Ni-rich phase compared to the A' composition, the remaining A'' amorphous phase should be enriched in Nb compared to A' . It can be assumed that this Nb enrichment in the remaining amorphous phase may have caused the crystallization of Nb-rich Ni_6Nb_7 and η -phase from A'' , within the last two crystallization events (Fig. 60). The broad halo of the amorphous phase is, however, no longer observable after the third exothermic event, which may mean that the last crystallization event involves partial transformations of the previously crystallized phases.

The as-cast amorphous sample of the $\text{Ni}_{57}\text{Nb}_{34}\text{Sn}_9$ composition was isothermally heat treated for 28 h at 846 K (sample Ni28h). The structure of this specimen after the heat treatment consists of an amorphous phase and a crystalline Ni_2NbSn -type phase (Fig. 26d). This is in agreement with the results obtained from the samples treated with a constant heating rate (Sn9Nq933K in Fig. 25), which suggests primary crystallization of a Ni_2NbSn -type phase. When the TTT diagram of the $\text{Ni}_{60}\text{Nb}_{35}\text{Sn}_5$ composition is modified (as explained in Section 3.2.4) for the $\text{Ni}_{57}\text{Nb}_{34}\text{Sn}_9$ composition, the time to the onset of crystallization at 846 K of 2 h is determined. It appears therefore, that during following 26 h of the isothermal heat treatment additional crystalline phases (like Ni_3Nb) have not formed. This can be compared to the DSC up-scan of the as-cast amorphous $\text{Ni}_{57}\text{Nb}_{34}\text{Sn}_9$ (Fig. 20) which shows that the crystallization of the first event (Ni_2NbSn) is completely finished before the onset of the second crystallization event (Ni_3Nb). From the XRD pattern of the Ni28h sample (Fig. 26d) and the Scherrer equation, the size of the crystallized Ni_2NbSn phase was determined to be only 10 nm which suggests that the growth of Ni_2NbSn is very slow, probably because long range diffusion of Sn is required. Also, in the XRD pattern of the Ni28h sample (Fig. 26d) the decrease in interatomic distance, corresponding to the peak of the amorphous halo was observed compared to that of the amorphous halo of the as-cast sample of the same composition (2.07 Å compared to 2.15 Å). This fact also correlates well with the results obtained from the sample of the same composition, heat treated with a constant heating rate just above the first crystallization event (Sn9Nq933). For Sn9Nq933K, however, a greater difference is determined compared to the as-cast sample (2.02 Å compared to 2.15 Å). This might be an indication that after 28 h heat treatment at 846 K, the crystallization of Ni_2NbSn -type phase is only partially completed.

The temperatures of the onset of crystallization of the three ternary Ni-Nb-Sn alloys characterized in this work increase significantly in the order $\text{Ni}_{57}\text{Nb}_{34}\text{Sn}_9 < \text{Ni}_{59.35}\text{Nb}_{34.34}\text{Sn}_{6.2} < \text{Ni}_{62}\text{Nb}_{35}\text{Sn}_3$ (913 K < 924 K < 940 K). The compositional differences between these alloys are found mainly in the concentrations of Ni and Sn. Since the first phase formed from the amorphous

matrix is Ni_2NbSn , considerable diffusion is required to achieve the Sn concentration necessary for this phase to nucleate. The incubation time, therefore, for the nucleation of Ni_2NbSn during isothermal heat treatment, or the temperature at which the Ni_2NbSn nucleates when heated with a constant heating rate, are higher for the alloys with a lower Sn content.

Furthermore, upon heat treatment with a constant heating rate of 0.33 K/s, the ternary $\text{Ni}_{62}\text{Nb}_{35}\text{Sn}_3$ and quaternary $\text{Ni}_{60}\text{Nb}_{36}\text{Sn}_3\text{B}_1$, both containing only 3 at.% Sn, crystallize in three exothermic events instead of the four that were observed in Sn-richer $\text{Ni}_{57}\text{Nb}_{34}\text{Sn}_9$ and $\text{Ni}_{59.35}\text{Nb}_{34.34}\text{Sn}_{6.2}$ (Fig. 20a and Fig. 22a, respectively). The temperature of the first exothermic event in $\text{Ni}_{62}\text{Nb}_{35}\text{Sn}_3$ corresponds well with the temperature of the second exothermic event in $\text{Ni}_{59.35}\text{Nb}_{34.34}\text{Sn}_{6.2}$. This might be an indication that the formation of Ni_2NbSn under a constant heating rate of 0.33 K/s, due to the long incubation interval, is completely suppressed in Sn-poorer alloys ($\text{Ni}_{62}\text{Nb}_{35}\text{Sn}_3$ and $\text{Ni}_{60}\text{Nb}_{36}\text{Sn}_3\text{B}_1$).

When, after crystallization from the amorphous phase, these samples are further heated until complete melting, one can observe that the melting intervals (of the two alloys with 3 at.% Sn $\text{Ni}_{62}\text{Nb}_{35}\text{Sn}_3$ and $\text{Ni}_{60}\text{Nb}_{36}\text{Sn}_3\text{B}_1$) are similar (curves marked with A in Fig. 22) and higher than those of other ternary and quaternary alloys with higher Sn concentrations (Figs. 20, 22 and Table 5). When these melted samples are left to solidify under a controlled, moderate cooling rate of 0.33 K/s and then melted again (with the same rate of 0.33 K/s), the melting intervals of the ternary compositions with a 6.2 and 9 at.% Sn remain the same as before, and are therefore not shown in Fig. 20b. The melting interval of the ternary alloy with a 3 at.% Sn is now wider than the melting interval observed during melting of crystallized amorphous sample (curve A compared to B in Figs. 20 and 22). The decrease in the melting temperature is due to the additional small endothermic event, which was not observed during first melting. This event appears at the same temperature as the temperatures of the first melting events observed on the ternary alloys with 6.2 and 9 at.% Sn (Fig. 20b). It is suspected that absence of this first melting event, in those alloys with 3 at.% Sn, melted after the amorphous phase had crystallized, is also an indication that the crystallization of the ternary Ni_2NbSn -type phase from the amorphous phase was completely suppressed due to the low Sn content.

5.3. Oxidation

The Ni-Nb(-Sn) based alloys with different compositions and structures were oxidized using the thermogravimetric method of oxidation in flow of the pure dry oxygen at different conditions (oxidation time and temperature) as described in Section 3.2.4.

In most general terms, it is of interest to identify which of the elements present in the alloy are most susceptible to oxidation. An Ellingham diagram was constructed for this purpose and shown

in Fig. 62. The Gibbs free energies of oxide formation per mol of O_2 are shown for different oxides in the temperature interval in which the oxidation experiments were performed.

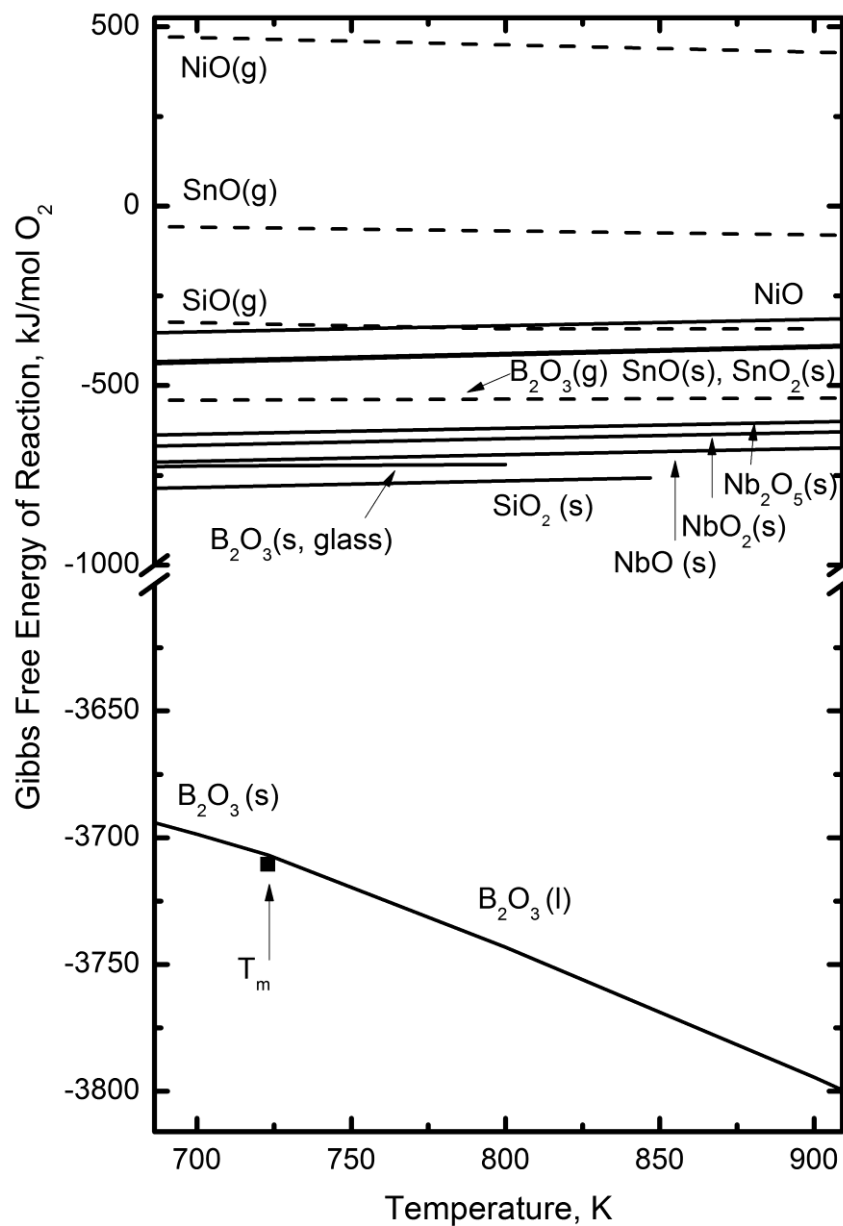


Fig. 62 An Ellingham diagram of Ni, Nb, Sn, B and Si oxides. The square point marked with T_m represents the melting temperature of B_2O_3 . The notations in the brackets, next to the oxides, s, l and g, represent the state of the oxide: solid, liquid and gas, respectively. In the case of B_2O_3 the crystalline and the glassy oxide should be differentiated; hence, next to the mark s, the word 'glass' is added in the parentheses.

The data for the construction of Ellingham diagram (Fig. 62) are taken from Ref. [64] for Nb oxides and from Ref. [65] for all other oxides shown therein. According to the Ellingham diagram in the cases of the binary Ni-Nb alloys, Nb is the less noble element compared to the second

element (Ni). In the ternary Ni-Nb-Sn alloys, the three elements in question have an increasing driving force for oxidation in the order Ni < Sn < Nb. Finally, in cases of the quaternary alloys, either B or Si is added to Ni, Nb and Sn. These two elements are even less noble than Nb in regard to oxidation, especially B, which has a negative slope in Ellingham diagram, in the crystalline and liquid states. From the standard Gibbs free energies of the reactions shown in Fig. 62, the equilibrium constants and the equilibrium partial pressures of the reacting gas, in this case O₂, at

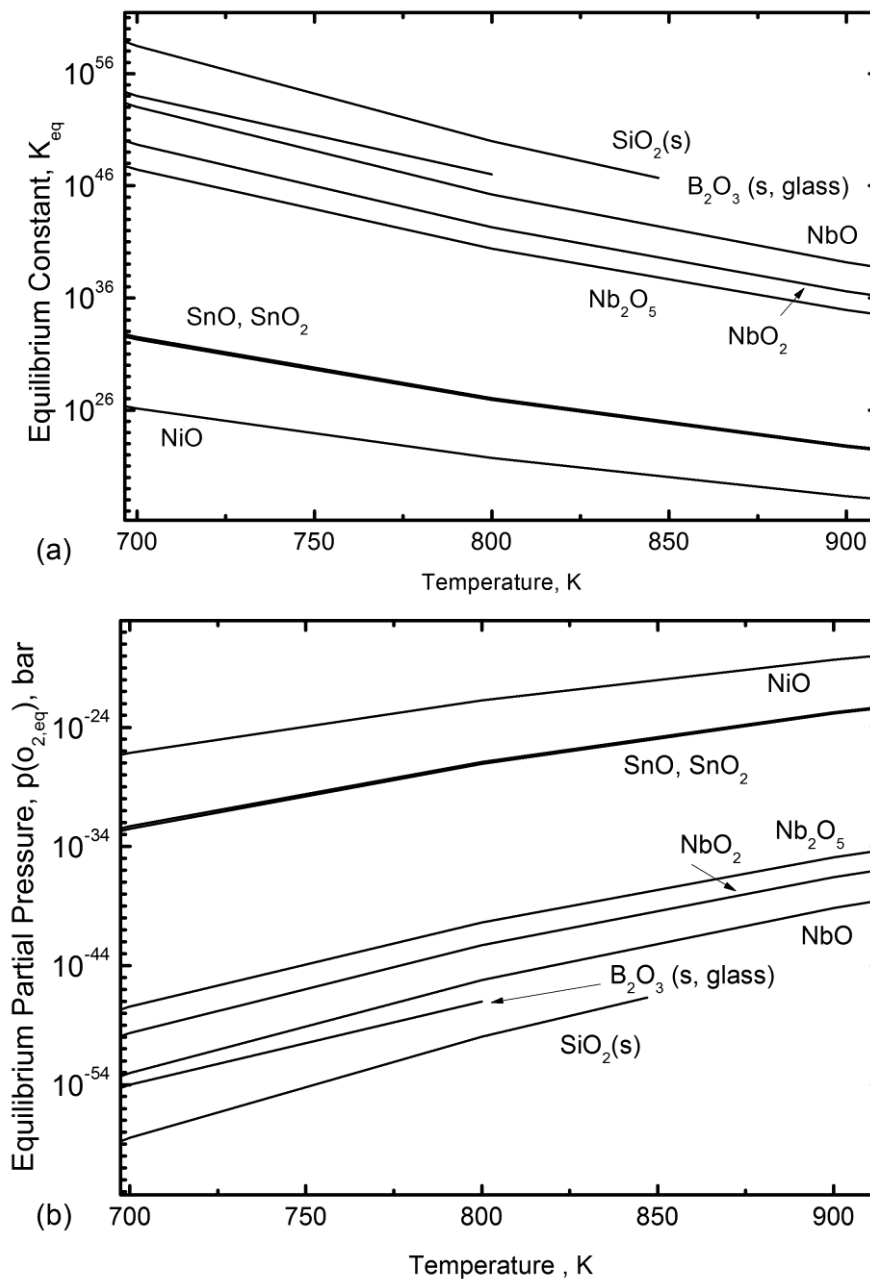


Fig. 63 Calculated values of the **a)** Equilibrium Constants, K_{eq} and the **b)** Equilibrium Partial Pressure of reacting gas (O₂), $p(O_{2,eq})$.

different temperatures were calculated and are shown in Fig. 63.

The Ellingham diagrams give information about the driving force for oxide formation from the pure elements, when the activity of the oxidizing element is 1. In the case of alloy oxidation, the activity of the elements is less than 1 and the free energies of the reactions as well as the equilibrium oxygen partial pressures deviate from the ideal case. On top of this the kinetics should also be taken in consideration when the oxidation behavior of an alloy is characterized. Therefore, TGA experiments were conducted.

5.3.1. Oxidation of the Binary Ni-Nb RAG

The oxidation experiments were conducted at 842 K for 15 h, on two different binary Ni-Nb compositions: 1) the master alloy sample and the suction casted amorphous sample of the $\text{Ni}_{62}\text{Nb}_{38}$ composition and 2) the melt spun amorphous sample of $\text{Ni}_{70}\text{Nb}_{30}$ (Fig. 29).

The results of the two samples with identical compositions ($\text{Ni}_{62}\text{Nb}_{38}$) and different structures (microcrystalline master alloy vs. as-cast amorphous RAG) will be first discussed. In the time frame 0 - 2.4 h the amorphous and the microcrystalline samples oxidize with the same parabolic rates (Fig. 29). After 2.4 h the oxidation behavior of $\text{Ni}_{62}\text{Nb}_{38}$ with the starting microcrystalline structure retains the same oxidation kinetics while the sample with the amorphous starting structure assumes another parabolic law of oxidation with a lower rate. The XRD patterns taken from the oxidized surfaces of these samples (Fig. 37) indicate the presence of the same crystalline phases in both samples: Nb_2O_5 , NiO and Ni. The observed differences in the oxidation kinetics can be connected with the morphology of the oxidized surface (Fig. 42).

In the oxidized surface layer of the microcrystalline sample, two types of areas, marked with C and F in Fig. 42, can be noticed. According to the spatial distribution and the compositions of these areas, it can be noticed that the areas marked with F ($X_{\text{Ni}}/X_{\text{Nb}} = 2.4$) must originate from the Ni_3Nb and the areas C ($X_{\text{Ni}}/X_{\text{Nb}} = 0.8$) from the Ni_6Nb_7 , which are two phases present in the starting microstructure. The oxidized structure in the areas originating from the Nb-richer Ni_6Nb_7 is also oxygen richer (24 at.% oxygen) than in the areas originating from the Nb-poorer Ni_3Nb (15 at.%). This is further connected with the coarseness of the oxide phase, which is coarser in the areas originating from the Ni_6Nb_7 (areas C in Fig. 42) than Ni_3Nb (area F in Fig. 42). The fact that the microstructure of the oxide reflects the starting microstructure points to the fact that the oxidation probably proceeds by oxygen-ion diffusion through the oxide and the oxidation reaction taking place on the oxide-alloy interface. This fact, and the fact that the formation of Nb-depleted sub-oxide layer (between the oxidized- and bulk alloy) was not observed, suggest that the oxidation proceeds almost as the in situ process, when neither of the elements (Ni or Nb) needs to diffuse extensively. This type of behavior corresponds well with earlier studies on two phase binary alloys

[66,67], such as M-Nb, M= Fe, Co, Ni [68]. It was reported by Niu et al. [40] that a Ni-Nb alloy containing 21 at.% Nb and having a two phase structure composed of Ni₈Nb and Ni₃Nb, when oxidized under 1 atm O₂ and 873 K, forms a very thin external NiO layer and a much thicker region of internal oxidation, where the two intermetallic phases (Ni₈Nb and Ni₃Nb) were transformed into a mixture of Ni and Nb-oxides (NbO₂ and/or Nb₂O₅) at the internal oxidation front without involving significant diffusion of Nb. Also, the Nb-depletion sub-oxide layer, beneath the internal oxidation zone was not observed. This type of oxidation is, as already mentioned earlier in this section, observed on microcrystalline (two phase) Ni₆₂Nb₃₈, without the NiO external layer being directly observed in SEM. It is possible that NiO has a very small thickness and poor adhesion, which might have resulted in its inadvertent removal during metallographic preparation.

The above considerations regarding the in situ-like oxidation with the reaction at the oxide-alloy interface and the oxidation front, which might move with different rates through the two constituent phases of these samples, is consistent with the kinetic oxidation behavior observed in the TG curve shown in Fig. 29, where the oxidation proceeds following a single parabolic law within the whole 15 h of oxidation. Since the TG curve of the amorphous sample with the same composition, Ni₆₂Nb₃₈ (Fig. 29), obeys the same oxidation law as the microcrystalline sample within the first 2.4 h, it is reasonable to assume that some diffusion process within the formed oxide layer, like O²⁻-ion diffusion, governs the oxidation process in both cases. After 2.4 h the oxidation of the microcrystalline sample continues to obey the same parabolic law but the amorphous sample changes its behavior by assuming the new parabolic law with the lower rate. More information about oxidation behavior of the amorphous structure was again obtained from the polished cross-section of the sample (Fig. 42b).

A very thin Ni-rich oxide layer was observed on the surface of the oxidized amorphous Ni₆₂Nb₃₈. Underneath this thin layer (marked with A in Fig. 42b), the inner zone rich in Nb oxide is observed with the Nb-depleted zone (marked with B in Fig. 42b) separating the matrix and the internal zone rich in Nb oxide. Generally, the formation of the external NiO scale is in good agreement with the results of earlier oxidation studies carried out on Ni-Nb alloys with similar compositions, having either microcrystalline [40,41] or amorphous structures [69,70]. The general oxidation mechanism, proposed in Ref.[31], for the both amorphous binary Ni-Nb and ternary Ni-Nb-Sn glasses, appears to be in good agreement with the behavior observed in Section 4.3. According to Ref.[31], the NiO and Nb₂O₅ nucleate at the surface, which is exposed to oxygen. Due to the faster Ni-ion diffusion in NiO than Nb-ion diffusion in Nb₂O₅, lateral overgrowth of NiO is induced. As further proposed in Ref. [31], NiO is being reduced to Ni at its interface with Nb according to the reaction:



A lower value of $X_{\text{Ni}}/X_{\text{Nb}}$ in the internal oxidation zone (0.24) compared to that of the average alloy composition (1.63), indicates Nb-enrichment in the internal oxidation zone. This enrichment is a result of the high affinity of Nb to oxygen and therefore its diffusion from the alloy to the oxidation front, where the oxidation reaction takes place.

The formation of a Nb-depletion zone is a significant difference between the oxidized master alloy sample, where only limited diffusion of the elements in the alloy was observed as the result of oxidation, and the amorphous sample, where the formation of the Nb-depletion zone can be connected with the more pronounced Nb diffusion from the alloy to the oxide/ alloy interface. The formation of the Nb-depletion zone can further be connected with the change in the parabolic rate constant after 3 h of oxidation in the amorphous structure, which was not observed on the microcrystalline sample. Compositionally, the Nb-depletion zone is Nb-poorer than the average alloy composition and it might therefore play a role in slowing down the oxidation rate.

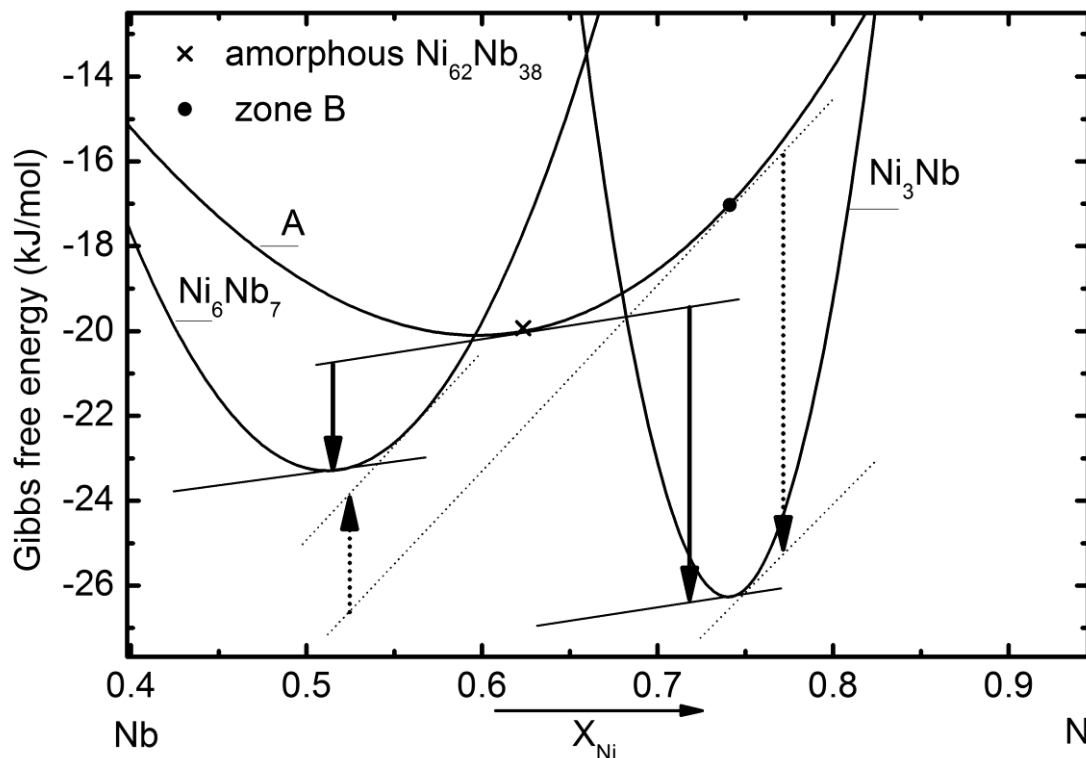


Fig. 64 The Gibbs free energy curves of the Ni_3Nb , Ni_6Nb_7 and amorphous phase in the binary Ni-Nb system at 842 K, between the Ni mol fraction 0.4 and 1, calculated using interaction parameters determined by CALPHAD in Ref. [27]. For the $\text{Ni}_{62}\text{Nb}_{38}$ and the composition of zone B (in Fig. 42), which are indicated on the Gibbs free energy curve of the amorphous phase (A), parallel tangent construction and driving forces for nucleation of Ni_6Nb_7 and Ni_3Nb are shown with solid and dashed lines, respectively.

According to the TTT diagram (Fig. 5), the onset of crystallization at 842 K is expected in less than one minute, and the end of crystallization after ~ 15 min of isothermal treatment. The influence of crystallization on the oxidation kinetics is not observable in the TG curve shown in Fig. 29, within the time of crystallization. The devitrification of amorphous $\text{Ni}_{62}\text{Nb}_{38}$ in inert atmosphere is discussed in Section 5.2.2.1. Ni_3Nb and Ni_6Nb_7 were found to be the products of devitrification, where Ni_3Nb is the primary phase to crystallize. In addition to that, the Gibbs free energy diagram of the amorphous and two intermetallic phases (Ni_3Nb and Ni_6Nb_7) in the binary Ni-Nb system was constructed at 842 K (Fig. 64). This diagram confirms that for the amorphous $\text{Ni}_{62}\text{Nb}_{38}$ composition, at the oxidation temperature of 842 K driving force for Ni_3Nb nucleation is greater than that for the nucleation of Ni_6Nb_7 . As the oxidation of Nb proceeds, its concentration in the remaining amorphous alloy close to the oxidation front decreases, e.g. zone B of Fig. 64. This means that the driving force for formation of Ni_3Nb is also locally even greater than in the average composition. Ni_3Nb is therefore very likely to form during crystallization in such conditions. However, Ni_3Nb was not identified in the XRD pattern of the oxidized surface. It therefore appears that, at least in the oxide thickness of $\sim 4 \mu\text{m}$ from the surface (from which the information in XRD pattern originates), a complete amount of crystallized Ni_3Nb must have been consequently oxidized.

The as-cast amorphous $\text{Ni}_{70}\text{Nb}_{30}$ oxidizes within the first 2.4 h at 842 K following a parabolic law, after which it exhibits a slowing down of the oxidation rate until the passive region is reached (after 3 h of oxidation). The XRD pattern of the oxidized $\text{Ni}_{70}\text{Nb}_{30}$ ribbon was not obtained in this work. Nevertheless, SEM and EDX analyses were performed and compared to earlier studies. The SEM image of the oxidized $\text{Ni}_{70}\text{Nb}_{30}$ cross-section (Fig. 42c) shows that after 15 h of oxidation at 842 K, the oxidation front has passed throughout the entire sample thickness. This is apparent from the morphology of the material (porosity), especially the porosity in the middle of the ribbon, marked with a white arrow in Fig. 42c. The time when the oxidation front has reached the sample center can be connected with the time when passivation on the TG curve was observed (~ 3 h, Fig. 29). The EDX analysis showed that close to the middle of the ribbon's cross-section the $X_{\text{Ni}}/X_{\text{Nb}} = 1.7\text{-}1.9$. This is slightly lower than that of the average alloy composition, $X_{\text{Ni}}/X_{\text{Nb}} = 2.3$. The oxygen concentration at the same position was determined to be 21 at.%. The region close to the surface was observed to be Ni-rich, $X_{\text{Ni}}/X_{\text{Nb}} = 12$, with about 9 at.% oxygen. According to these results, the formation of at least two layers is apparent.

Since the specimen mass before oxidation is known, as well as its surface area and composition, the mass gain due to oxidation can be calculated. Under assumption that both Ni and Nb are completely oxidized and that Ni oxidizes to NiO and Nb to Nb_2O_5 , which were observed to be the oxidation products of amorphous $\text{Ni}_{62}\text{Nb}_{38}$ (this work), as well as of the microcrystalline $\text{Ni}_{75}\text{Nb}_{25}$ (reported in Ref. [41]), the calculated mass gain is 78 % higher than the mass gain observed in the TG experiment (Fig. 29). If it is assumed that only Ni or only Nb oxidizes, the calculated mass gain

is 14 % and 7.9 % lower than the experimentally observed mass gain, respectively. This suggests, since Nb has a higher affinity to oxygen than Ni, that the entirety of the Nb is oxidized to Nb_2O_5 and part of the Ni content is oxidized to NiO (formation of NiNb_2O_6 is not excluded). The formation of an external NiO layer and internal layer rich in Nb_2O_5 containing Ni can be assumed. Furthermore, after the Nb atoms have oxidized, the remaining Ni, in the deeper parts of the samples are not susceptible to oxidation due to the low oxygen partial pressure, at which time the oxidation passivates (~ 3 h in Fig. 29). More detailed discussion on oxidation mechanism can be found in Section 5.3.2.2.

The oxidation of the amorphous samples with the $\text{Ni}_{62}\text{Nb}_{38}$ and the $\text{Ni}_{70}\text{Nb}_{30}$ compositions proceed according to the parabolic laws of oxidation within the first 2.4 h. The parabolic rate constant of the Nb- richer $\text{Ni}_{62}\text{Nb}_{38}$ is higher than that of $\text{Ni}_{70}\text{Nb}_{30}$. Since both samples have the same starting type of structure (as-cast amorphous) and are oxidized under the same conditions, the compositional differences are the most probable cause of different parabolic oxidation rates. The oxidation rate is higher in the alloy with the higher Nb concentration.

5.3.2. Oxidation of the Amorphous Ni-Nb(-Sn) Based Alloys

With the exception of the quaternary $\text{Ni}_{60}\text{Nb}_{36}\text{Sn}_3\text{B}_1$ and the earlier discussed binary Ni-Nb RAGs, all of the other investigated amorphous samples, such as ternary as-cast amorphous Sn6.2A and Sn9A, thermally treated amorphous R2.5h and R15h (Table 2) and as-cast amorphous $\text{Ni}_{58.85}\text{Nb}_{34.45}\text{Sn}_{6.2}\text{Si}_{0.5}$ (Si0.5A) exhibit generally similar oxidation behavior at T_g-50 K. These characteristics of oxidation, common for all of the above samples, will be discussed further in this section. More specific discussion on thermally treated amorphous R2.5h and R15h, and the quaternary $\text{Ni}_{58.85}\text{Nb}_{34.45}\text{Sn}_{6.2}\text{Si}_{0.5}$ and $\text{Ni}_{60}\text{Nb}_{36}\text{Sn}_3\text{B}_1$ will be given in next sections.

In terms of oxidation kinetics, after initial parabolic oxidation the amorphous samples undergo a transition to linear oxidation (Figs. 30, 31 and 36). On the surface of the oxidized samples, a Ni-rich oxide layer, poor in both Nb and Sn, is formed (marked with L1 in Fig. 43b). The thickness of this layer, which is apparently the NiO layer, is very small (~ 0.5 μm). This thin layer is also highly detached from the underlying oxide and appears to be often absent, at places, as a result of the metallographic sample preparation. Therefore, the NiO layer was in some cases not observed at the surface in BS images (Fig. 43a and c). Underneath the NiO, the main oxidation zone, which is rich in Nb and oxygen, had formed (marked L2 in Fig. 43). Below it, the Nb-depleted zone (marked with L4 in Fig. 43) is found. The interface between the main oxide layer, L2 (darker layer in Fig. 43), and the Nb-depleted zone (brighter zone in Fig. 43) is very irregular.

The EDX analysis of the L4 layer had shown that it contains ~ 35 at.% oxygen and, as calculated for R2.5h from Table 9, ~ 36 at.% Nb, ~ 22 at.% Ni and ~ 7 at.% Sn. It appears that the

$X_{\text{Nb}}/X_{\text{O}} \sim 1$. This would suggest, assuming preferential oxidation of Nb, that the Nb is completely oxidized to NbO or that at lower O_2 pressures the Nb_2O_5 and NbO_2 reduce to NbO. It can also be noticed that the Ni content in L4 layer (~ 22 at.%) is smaller than in the average alloy composition (59.35 at.%). Nevertheless, the Ni and Sn concentrations in the main oxidation layer are significant. In the XRD pattern taken from the surfaces of the oxidized amorphous samples (Figs. 38 and 39), the reflections of three types of oxide phases were found: NiO, Nb_2O_5 and the NbO_2 , as well as two types of intermetallic phases; namely, Ni_3Nb and Ni_3Sn . The Ni_2NbSn -type phase was not identified in the XRD pattern, however, due to the overlap of Ni_2NbSn reflections with other phases, such as Nb_2O_5 , small amounts of Ni_2NbSn would have gone unnoticed. In correlation with the XRD results with a rough estimation based on EDX measurements, it appears that the Nb is indeed partially oxidized to its higher oxygen content oxides (Nb_2O_5 and NbO_2) and partially bound in intermetallic phases, such as Ni_3Nb and perhaps as a solute in Ni_3Sn .

The information from the deeper parts of the main oxide layer, L2, beyond the XRD penetration depth were obtained from the EBSD map in Fig. 45a. It appeared that in the deeper parts of the oxide layer (L2), in addition to the phases identified in XRD, Ni_6Nb_7 was observed. The Ni_2NbSn phase was not included in the EBSD map, as it was not present in the available database. Its formation in the deeper parts of the oxide cannot be therefore excluded. Information from the deeper parts of the oxidation penetration distance, namely the Nb-depleted zone (L4 as marked in Fig. 43b) is also obtained from the EBSD map (Fig. 45b). The same type of phases, oxide and intermetallic, are found here as in L4 layer. The amount of specific phases in oxide layer L2 compared to the Nb-depleted zone L4 is different. The Nb-depleted zone is poorer in oxide phases and richer in intermetallic phases (13.2 % and 86.7 %, respectively) compared to the oxide L2 layer (40 % and 60 %, respectively). In the Nb-depleted zone, the most abundant phase among the oxide phases is NbO_2 and, among the intermetallic phases, Ni_3Sn , which is the most abundant and coarsest.

The information about the bulk alloy, beyond the oxidation penetration depth, is also of interest, since the oxidation conditions were chosen according to the modified TTT diagram (see Section 3.2.4) so that that the oxidation was interrupted before the onset of bulk crystallization. The XRD pattern was taken from the oxidized sample after the 50 μm -thick surface layer (which is thicker than the oxidation penetration distance) was removed. This XRD pattern (Fig. 41) suggests that the bulk was still amorphous after oxidation, as predicted by the TTT diagram. The DTA up-scan of the amorphous sample oxidized at $T_g - 50$ K also showed that the crystallization enthalpy is the same as the crystallization enthalpy of the as-cast structure with the same composition (Fig. 55). Also, the absence of a relaxation signal in the up-scan of the oxidized compared to the as-cast sample indicates that the bulk material of the oxidized sample has undergone complete relaxation during oxidation.

This suggests that the intermetallic phases found to form during oxidation are localized within the oxidation penetration distance and a direct consequence of the compositional changes at the oxidation front. For a better understanding of which intermetallic phases are likely to form due to oxidation, the driving forces for crystallization of different phases in the ternary Ni-Nb-Sn system are discussed in Section 5.3.2.1.

5.3.2.1. Driving Forces for Nucleation of Different Phases at the Oxidation Front

For this purpose the hypothetical quasi-binary Gibbs free energy diagram, constructed according to the one used in Section 5.2.2.3 (Fig. 61), was used. In Fig. 65a, the schematic representation of the Ni-rich side of the isothermal Ni-Nb-Sn diagram is shown. The hypothetical quasi-binary Gibbs free energy diagram is made for the section along the dashed AB line. It is assumed that the $\text{Ni}_{59.35}\text{Nb}_{34.45}\text{Sn}_{6.2}$ composition falls on this section (marked with P in the Fig. 65a). The arrow in Fig. 65a points to the corrected composition of the Nb-depleted zone (calculated by neglecting the oxygen concentration and according to the atomic ratios of the $X_{\text{Ni}}/X_{\text{Nb}}$, $X_{\text{Ni}}/X_{\text{Sn}}$ and $X_{\text{Ni}}/X_{\text{Sn}}$ for sample R2.5h in Table 10). This composition was also projected to the AB section and marked as L4 in Fig. 65b. The amorphous phase and the intermetallic Ni_3Nb , Ni_6Nb_7 and Ni_2NbSn phases are constructed as in Fig. 61b. Since Ni_3Sn was found to be one of the phases to form during oxidation, it was also projected onto this quasi-binary Gibbs free energy diagram. The Ni_3Sn curve was constructed with steep slopes because it forms in a narrow composition interval in the binary Ni-Sn system.

The overall alloy composition changes at the oxidation front along the quasi-binary AB section of Fig. 65a from P to L4. The parallel tangent construction is shown over both the starting composition of the amorphous alloy, P (dashed lines), and the amorphous Nb-depleted composition, L4 (dotted lines). The driving force for nucleation of the indicated intermetallic phases (Ni_2NbSn , Ni_6Nb_7 , Ni_3Nb and Ni_3Sn) from the amorphous phases with the compositions P and L4 are indicated with solid and dotted arrows, respectively. In the case shown in Fig. 65b, the driving force for nucleation from the amorphous composition P is highest for the Ni_2NbSn -type phase and it decreases in the order $\text{Ni}_2\text{NbSn} > \text{Ni}_3\text{Nb} > \text{Ni}_6\text{Nb}_7 > \text{Ni}_3\text{Sn}$. For the amorphous composition L4, on the other hand, the driving force for nucleation is highest for Ni_3Sn and Ni_3Nb . In fact, the nucleation of Ni_6Nb_7 from the amorphous composition L4 is thermodynamically unfavorable. It appears that, generally, as the composition of the amorphous phase changes from P to L4, the driving force for nucleation of Ni_3Nb and especially Ni_3Sn increase. On the other hand, the driving force for nucleation of Ni_2NbSn generally decreases as the composition changes from P to L4, but the observed decrease is not as large as that observed for Ni_6Nb_7 (Fig. 65b).

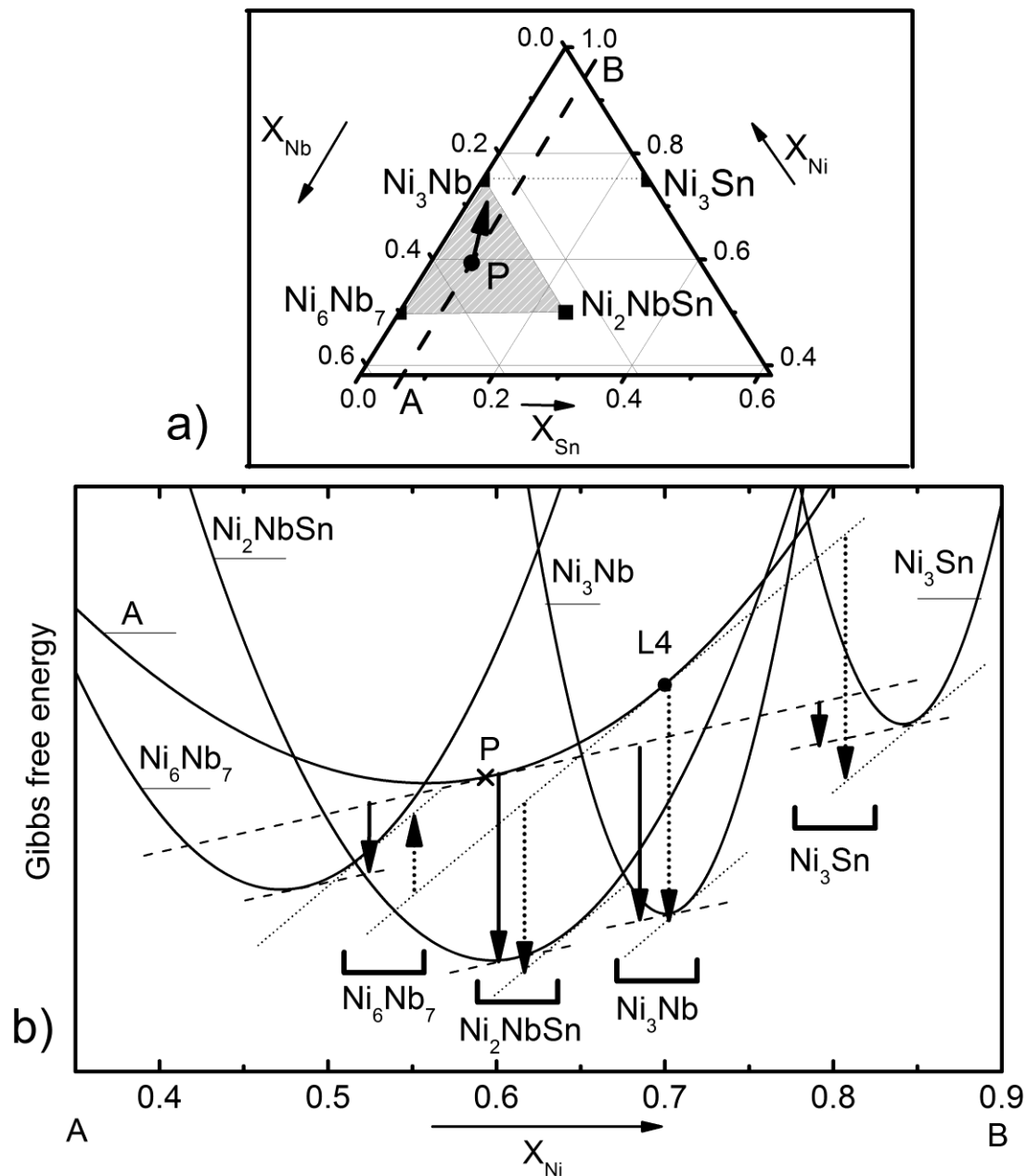


Fig. 65 a) Schematic representation of the isothermal ternary Ni-Nb-Sn diagram on the Ni-rich side ($0.35 \leq X_{Ni} \leq 0.9$), with indicated intermetallic phases: Ni_3Nb , Ni_6Nb_7 and Ni_2NbSn , the $Ni_{59.35}Nb_{34.45}Sn_{6.2}$ composition (marked with P) and the quasi-binary cross-section AB (dashed line); b) The hypothetical Gibbs free energy diagram of the quasi-binary AB cross-section, showing the Gibbs free energy curves of Ni_2NbSn , Ni_6Nb_7 , Ni_3Nb , Ni_3Sn and the amorphous phase (A). Parallel tangent constructions over the amorphous compositions P and L4 are shown with dashed and dotted lines, respectively. The driving forces for nucleation of different intermetallic phases from the amorphous P and L4 compositions are indicated with solid and dotted arrows, respectively.

5.3.2.2. Oxidation Mechanism

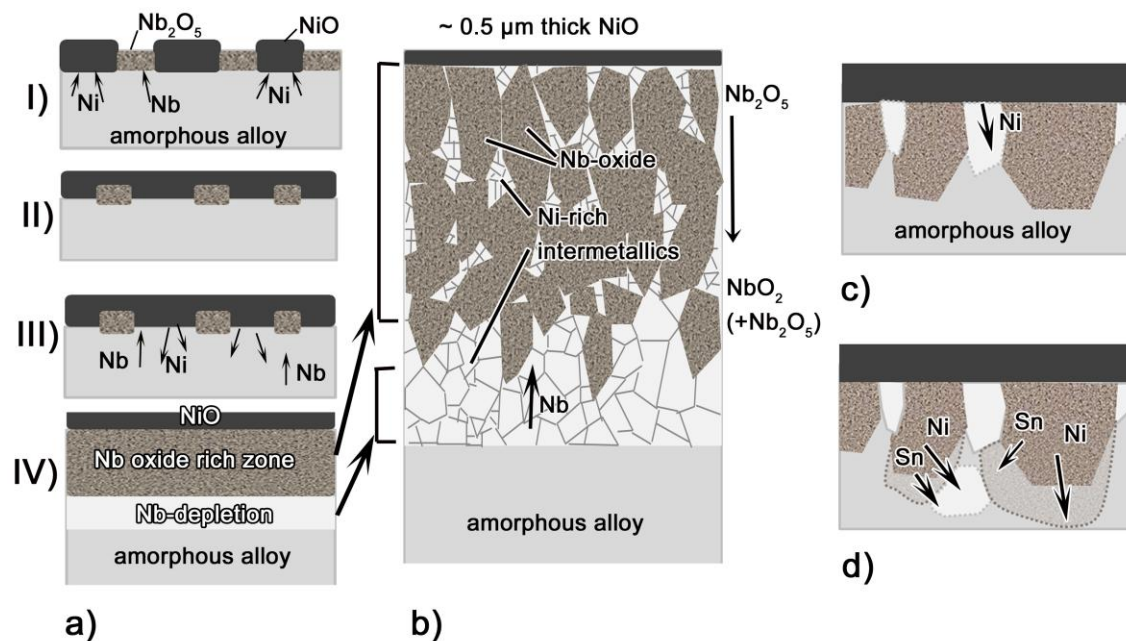


Fig. 66 Schematic representation of: **a)** oxidation mechanism as proposed by I Gallino et al [31], **b)** microstructure of the oxidation penetration depth and **c)** crystallization of Ni-rich intermetallics as a result of Ni enrichment of the amorphous phase at the oxidation front, **d)** Ni and Sn diffusion out from the oxidation front, due to the oxide grain growth and the compositional changes at the oxidation front causing crystallization of intermetallic phases.

The results of an earlier study on the oxidation behavior of $\text{Ni}_{60}\text{Nb}_{35}\text{Sn}_5$ RAGs in synthetic air by I. Gallino et al. [31], showed a parabolic oxidation kinetics, which is in good agreement with the results obtained here, taken in dry oxygen. They also reported the formation of an outer layer of Ni oxide and a continuous inner layer of Nb oxide (Nb_2O_5 and NbO_2). It was suggested there that the depletion of Nb in the alloy underneath the scale induces crystallization of Ni-rich intermetallics such as Ni_3Nb and Ni_2NbSn . These findings are also in good general agreement with the oxidation behavior observed here; furthermore, the oxidation mechanism proposed in Ref. [31] appropriately describes the oxidation behavior of Ni-Nb-Sn RAGs below T_g observed in this work.

According to the proposed oxidation mechanism [31], when the surface of amorphous Ni-Nb-Sn is exposed to the oxidizing atmosphere, both NiO- and Nb_2O_5 -nuclei are formed at the surface (I in Fig. 66a). Both types of nucleus will proceed to grow, but due to the faster diffusion of Ni^{2+} in NiO than Nb^{5+} in Nb_2O_5 , lateral overgrowth of NiO will be induced (II in Fig. 66a). At the same time, atoms of the less noble Nb will diffuse to the oxide layer/alloy interface and reduce NiO to Ni (Eq. 35), which will then diffuse back into the alloy (III in Fig. 66a).

As a result, Nb will become depleted (i.e. Ni-enriched) in a zone at the alloy/oxide interface. In this way, four typical zones (NiO-layer, Nb-oxide rich inner layer and the Nb-depletion zone) in the oxidation penetration distance have formed (IV in Fig. 66a). The growth of the NiO layer appears to be suppressed compared to the other two zones (Nb-oxide rich and Nb-depletion zone), as its thickness does not exceed $\sim 0.5 \mu\text{m}$. The Nb oxide rich zone grows due to the Nb reaction with oxygen at the Nb-oxide/alloy interface. The Nb-depletion zone is constantly renewed by Nb diffusion to the oxidation front and the Ni diffusion from the oxide/alloy interface into the alloy.

Based on the XRD of the oxidized surfaces (Figs. 38a and 39) and characterizations of the oxidized samples' cross-sections by SEM (Fig. 43), EBSD maps (Fig. 45a) and APT characterizations (Figs. 56 and 57), it can be stated that the Nb oxide rich zone is not a pure oxide layer. Rather, it is consisted of Nb oxides and Ni-rich intermetallics (Fig. 66b). Two Nb oxides found in the Nb oxide rich zone are Nb_2O_5 and NbO_2 . Although the amount of NbO_2 in the XRD pattern of the oxidized surfaces appears to be very low (Fig. 39) in the deeper parts of the oxide layers higher amounts of the NbO_2 compared to Nb_2O_5 may be expected due to the lower equilibrium partial pressure of NbO_2 compared to Nb_2O_5 (Fig. 63b).

Ni-rich intermetallics, such as Ni_3Nb and especially Ni_3Sn , were found to form within the Nb oxide rich zone and in the Nb-depletion zone. It was shown in Section 5.3.2.1 how the nucleation of Ni_3Nb and especially Ni_3Sn becomes more favorable thermodynamically, as the amorphous phase becomes richer in Ni, compared to nucleation of Ni_2NbSn -type phase and especially Ni_6Nb_7 . The driving force for nucleation of Ni_2NbSn appears to be slightly decreasing as the amorphous phase becomes Ni-richer (Fig. 65). This decrease is however only very slight. Additionally, the formation of Ni_2NbSn based on the available experimental results cannot be established with complete certainty. In XRD pattern of the oxidized surface (Figs. 38a and 39), small amounts of Ni_2NbSn could have gone undetected due to the overlap with the peaks of other phases such as Nb-oxides. The results of APT indicated the formation of phases containing Ni, Nb and Sn but the stoichiometry corresponding roughly to the Ni_2NbSn -type phase was not found. Nevertheless, the presence of the two phases expected to form most likely in the structure, according to Fig. 65 (Ni_3Sn and Ni_3Nb), was confirmed. It is possible therefore that the Ni atoms diffusing back from the oxide interface react with the amorphous alloy at the oxidation front causing it to gradually become enriched in Ni. This further causes the amorphous matrix to destabilize and, depending on the locally achieved concentrations, to crystallize in one of the Ni-rich phases.

It should be also mentioned that Ni_3Sn is not expected as a product of $\text{Ni}_{59.35}\text{Nb}_{34.45}\text{Sn}_{6.2}$ devitrification in Ar (see Section 5.2.2.3). However, Ni_3Sn is among the observed intermetallic phases in the oxidation penetration distance the most abundant one. The influence of oxidation on the type of crystalline phases formed was also observed in Zr-based BMGs [46]. It was reported there that a product of $\text{Zr}_{55}\text{Cu}_{30}\text{Al}_{10}\text{Ni}_5$ crystallization in vacuum was a Zr-rich $\text{Zr}_2(\text{NiCu})$ phase. On the other hand, in an oxidizing atmosphere, a Cu-rich $\text{Cu}_{10}\text{Zr}_7$ phase was found instead. The

reason for such behavior was found to be a slight Cu enrichment at the interface between the oxide and alloy [46].

The activation energy for oxidation, E_a , of the as-cast amorphous $\text{Ni}_{57}\text{Nb}_{34}\text{Sn}_9$ was determined from the isothermal oxidation measurements at different temperatures below the T_g (see Section 4.3.1.2) to be about 298 kJ/mol. The E_a for oxidation of the as-cast amorphous $\text{Ni}_{57}\text{Nb}_{34}\text{Sn}_9$ appears to be much higher than the E_a for oxidation of pure Nb, Ni or Ni_3Nb (Appendix A5). The APT results (Section 4.1.2) show that the concentrations of the Ni and Sn, in the Nb oxide phase, are very low (Table 11). This suggests that for the growth of the oxide in the ternary Ni-Nb-Sn based alloys, it is necessary for Ni and Sn to diffuse out, ahead of the oxidation front, through the alloy (Fig. 66d). It could be therefore possible, according to determined E_a , that some of the diffusion processes in the amorphous matrix (96.5 - 289.5 kJ/mol [22]) or crystallized Nb-depleted zone, could be the limiting process. A roughly similar mechanism was proposed by Köster [50] for Zr-based BMGs such as Zr-Cu-Ni-Al, where beneath the surface film, which mainly consisted of Al- and Zr-oxides, in deeper parts of the oxide scale zirconia and (Cu, Ni) solid solution were found. According to the proposed model, as pure zirconia crystallizes, the Ni and Cu are being rejected into the surrounding amorphous phase, which further crystallizes into (Cu, Ni) solid solution around zirconia.

As a larger atom, Sn is expected to have a lower diffusivity than Ni and therefore could be the limiting factor for oxidation in ternary Ni-Nb-Sn. Furthermore, since the ternary Ni-Nb-Sn RAGs show considerably smaller mass gain within 15 h of oxidation at T_g-50 K (Fig. 67) than the binary $\text{Ni}_{62}\text{Nb}_{38}$ (with the same $X_{\text{Ni}}/X_{\text{Nb}}$), it can be also deduced that the large Sn atoms retard oxidation due to their sluggish mobility. A high E_a for oxidation (528 kJ/mol) was also determined for Zr-based $\text{Zr}_{69.5}\text{Cu}_{12}\text{Ni}_{11}\text{Al}_{7.5}$ in temperature interval 603-643 K [47]. Despite the fact that the oxygen diffusion through the oxide layer was apparent, it was noticed that the E_a for oxygen diffusion in ZrO_2 (200 kJ/mol [71]) as well as the E_a for crystallization of these glasses (345 kJ/mol [72]) are significantly lower than that for oxidation. A high observed E_a for oxidation was then interpreted as a result of a complex overlap of different nucleation and growth processes during oxidation.

5.3.2.3. Influence of the Thermal Treatment on the Oxidation Behavior of the Amorphous Structure

It was shown in Section 5.2.2.2 that the as-cast amorphous structure is compositionally homogeneous without any signs of segregation or phase separation. The structure of the thermally treated R2.5h sample (Table 2) was calorimetrically characterized with a constant heating rate (Fig. 21) and compared to the up-scan of the as-cast sample with the same composition (Fig. 20a). The R2.5h sample shows a smaller exothermic event prior to the onset of glass transitions than that of

the as-cast amorphous sample. Also, the crystallization enthalpies of the as-cast amorphous and R2.5h sample differ only very slightly, with the maximal difference of 6.7 % observed in the first crystallization event (Table 6). This suggests that only enthalpy relaxation took place during isothermal treatment of R2.5h, i.e. based on the measured enthalpies of crystallization determined after treatment, no crystallization processes would have taken place during isothermal treatment.

The structure of the R15h sample was characterized with XRD (Fig. 26) and calorimetry (Fig. 21). Although the XRD pattern showed only a broad halo belonging to the amorphous phase, the crystallization enthalpy of R15h is significantly smaller than that of the as-cast amorphous sample. The difference is observed within the first crystallization event, where ΔH_{x1} of R15h is 26.7 % lower than that of the as-cast amorphous sample. This suggests that structural changes beyond the relaxation, i.e. some phase separation or fine nuclei formation under the x-ray resolvability, have taken place. According to TTT diagram modified for the $\text{Ni}_{59.35}\text{Nb}_{34.45}\text{Sn}_{6.2}$ composition (see Section 3.2.4), the time to the onset of crystallization at 831 K in Ar is 25 h. Samples of R2.5h and R15h were isothermally treated before oxidation at 831 K (in vacuum) for 2.5 h and 15 h, respectively. Subsequent oxidation of both samples was conducted at the same temperature for 19 h. It is expected therefore, that unlike R2.5h, R15h will start to crystallize, in the bulk, after 10 h of oxidation. This crystallization can indeed be observed in the BS images taken from the matrix of the R15h sample after oxidation (inserted in the lower left corner of the Fig. 43d), where a fine grained structure is apparent.

As already indicated in Section 5.3.2, the oxidation behavior of the thermally treated R2.5h and R15h samples is generally very similar to that of the as-cast sample with the same composition. Nevertheless, some fine differences were also noticed. The most pronounced difference can be observed in the oxidation kinetics (Fig. 31). After initial parabolic oxidation, where the as-cast and thermally treated samples (R2.5h and R15h) exhibit similar oxidation rates, the thermally treated samples passivate instead of assuming the linear oxidation behavior of the as-cast sample. Therefore, after 15 h of oxidation at 831 K, the thermally treated samples (R2.5h and R15h) exhibited significantly smaller mass gain compared to that of the oxidized as-cast amorphous sample (Table 8). Differences in the morphologies and thicknesses of different layers in the oxidation affected zones are also observable in Figs. 43 and 44. More specifically, although the total thicknesses of the oxidation affected zones in the as-cast sample and thermally treated R2.5h and R15h samples are approximately the same, the thicknesses of the specific layers separately are different (Fig. 44). The L2 layer is observed to be the thicker on the oxidized as-cast amorphous sample compared to that on the thermally treated R2.5h and R15h samples, where it is of about the same thicknesses (Fig. 44). The thickness of the L4 layer is the thickest on the R2.5h sample and it decreases in the order R2.5h > R15h > as-cast. It thus appears that a fully relaxed amorphous structure is more oxidation resistant due to its apparently slower atomic mobility (lower diffusivity).

5.3.3. Oxidation of the Quaternary Ni-Nb-Sn-X (X=Si, B)

As already mentioned in Section 5.3.2, the oxidation behavior of the as-cast amorphous quaternary $\text{Ni}_{58.85}\text{Nb}_{34.45}\text{Sn}_{6.2}\text{Si}_{0.5}$ is similar to that of the ternary as-cast amorphous $\text{Ni}_{59.35}\text{Nb}_{34.45}\text{Sn}_{6.2}$. Although the amount of Si in this alloy is very low (0.5 at.%), some differences in the oxide layer morphologies of the ternary $\text{Ni}_{59.35}\text{Nb}_{34.45}\text{Sn}_{6.2}$ (Fig. 43) and the corresponding quaternary $\text{Ni}_{58.85}\text{Nb}_{34.45}\text{Sn}_{6.2}\text{Si}_{0.5}$ (Fig. 52) compositions could be noticed in the BS images of the polished cross-sections, as well as in the inner Nb oxide rich zone close to the L4 layer. The Si content within the matrix was determined by EDX to be 0.9 at.%. The EDX line-scan (Fig. 52), in the interval 0-7.5 μm shows that the composition changed within the oxidation penetration distance. This line-scan, however, does not start at the surface, because part of the oxide layer was broken-off, probably during metallographic preparation. Therefore, it does not give information about the outer most part of the oxidation penetration distance, such as NiO layer. In the interval 7.5 - 9 μm , the line-scan shows the composition of the matrix below the oxidation penetration distance. Within this EDX line-scan, the content of Si appears to be constant within the oxidation penetration distance and about equal to that in the bulk. The APT characterizations showed that the Si concentration in either of the two types of phases observed on the measured tips, i.e. oxide and Ni-Nb-Sn based phase, is very low (Table 11). These compositions are however obtained by systematic elimination of the interface-areas (see Section 3.2.1.3). The information from the surface layer and interfaces is therefore not available. Due to its high affinity to oxygen, Si may be diffusing to the interfaces with the oxide phase and further to the surface in order to form amorphous SiO_2 .

The as-cast amorphous $\text{Ni}_{60}\text{Nb}_{34}\text{Sn}_3\text{B}_1$ is the sample that shows the most different oxidation behavior of all the ternary and quaternary compositions characterized here. These differences are observable in the oxidation kinetics, where the as-cast amorphous $\text{Ni}_{60}\text{Nb}_{34}\text{Sn}_3\text{B}_1$ sample follows at T_g-20 K and T_g-50 K a purely parabolic law of oxidation instead of a parilinear law, in contrast to the two ternary (Figs. 30 and 31) and the quaternary $\text{Ni}_{58.85}\text{Nb}_{34.45}\text{Sn}_{6.2}\text{Si}_{0.5}$ (Fig. 36) compositions. The total thickness of the oxidation affected surface, determined on the as-cast amorphous sample oxidized at T_g-50 K is almost three times that of as-cast amorphous $\text{Ni}_{59.35}\text{Nb}_{34.45}\text{Sn}_{6.2}$, also oxidized at T_g-50 K (Fig. 54). It is also apparent from Fig. 54 that most of the total thickness corresponds to the L2 layer (87.5 %). The L3 layers in the as-cast amorphous $\text{Ni}_{59.35}\text{Nb}_{34.45}\text{Sn}_{6.2}$ and $\text{Ni}_{60}\text{Nb}_{34}\text{Sn}_3\text{B}_1$ samples are of approximately the same size and the L4 layer is completely absent in $\text{Ni}_{60}\text{Nb}_{34}\text{Sn}_3\text{B}_1$. Very intense oxidation is also reflected through the mass gain recorded on as-cast amorphous $\text{Ni}_{60}\text{Nb}_{34}\text{Sn}_3\text{B}_1$ at T_g-50 K after 15 h of oxidation compared to the other compositions, which is shown in Fig. 67. Furthermore, in the XRD pattern of the oxidized surface of the as-cast

amorphous $\text{Ni}_{60}\text{Nb}_{34}\text{Sn}_3\text{B}_1$ at T_g-50 K, in addition to the phases already found to form on the other amorphous samples (Ni and Nb oxides, Ni_3Nb and Ni_3Sn) of the Ni-Nb-Sn based alloys, a boride phase, $\text{Ni}_{21}\text{Nb}_2\text{B}_6$, was identified. Since the time for which the $\text{Ni}_{60}\text{Nb}_{34}\text{Sn}_3\text{B}_1$ sample was oxidized was determined based on the modified TTT diagram of the ternary $\text{Ni}_{60}\text{Nb}_{35}\text{Sn}_5$ composition (as described in Section 3.2.4), as-cast $\text{Ni}_{60}\text{Nb}_{34}\text{Sn}_3\text{B}_1$ was also vacuum annealed, using the same time and temperature as used for the oxidation, in order to determine if the modified diagram of the $\text{Ni}_{60}\text{Nb}_{35}\text{Sn}_5$ composition is still applicable, i.e. if the addition of B in the ternary system might not have resulted in a new phase forming as a devitrification product.

The XRD pattern of vacuum annealed $\text{Ni}_{60}\text{Nb}_{34}\text{Sn}_3\text{B}_1$ showed that the structure is still amorphous (Fig. 27). This shows that the as-cast structure is thermally stable within the whole oxidation time at the T_g-50 K, similar to the case of the ternary compositions, and that the boride phase is the crystallization product forming as the consequence of the oxidation, i.e. the Ni enrichment close to the oxidation reaction zone due to the Nb elimination from the amorphous structure. The identified boride phase is found to be one of the equilibrium phases in the ternary Ni-Nb-B system at 773 K, close to the Ni corner, between Ni_3Nb , Ni_3B , Ni_2B and $\text{Ni}_5\text{Nb}_3\text{B}_2$ [73,74]. The formation of this boride phase could not be directly connected to the low oxidation resistance of $\text{Ni}_{60}\text{Nb}_{34}\text{Sn}_3\text{B}_1$. In fact, the $X_{\text{Ni}}/X_{\text{Nb}}$ in the $\text{Ni}_{60}\text{Nb}_{34}\text{Sn}_3\text{B}_1$ is not significantly different either from the ternary ($\text{Ni}_{59.35}\text{Nb}_{34.45}\text{Sn}_{6.2}$ and $\text{Ni}_{57}\text{Nb}_{34}\text{Sn}_9$) or binary $\text{Ni}_{62}\text{Nb}_{38}$.

The determined value of E_a for the oxidation of the as-cast ternary $\text{Ni}_{57}\text{Nb}_{34}\text{Sn}_9$ composition (289 kJ/mol) is very similar to that of the $\text{Ni}_{60}\text{Nb}_{34}\text{Sn}_3\text{B}_1$ composition (307 kJ/mol). This suggests the same oxidation mechanism in both compositions. The reason for the slower oxidation kinetics of the ternary as-cast samples compared to the binary was suggested to be the sluggish Sn diffusion. This correlates well with the increasing parabolic oxidation rates of the as-cast structures with the decrease in Sn concentration ($\text{Ni}_{59.35}\text{Nb}_{34.45}\text{Sn}_{6.2} < \text{Ni}_{60}\text{Nb}_{34}\text{Sn}_3\text{B}_1 < \text{Ni}_{62}\text{Nb}_{38}$).

Furthermore, the assumed role of the Ni-rich layer (L4) in the oxidation passivation is also in agreement with the observed behavior. The L4 layer was defined and measured on the BS images of the polished cross-section taken from the oxidized samples, as the distance between the deepest oxide grains and the interface with the alloy, as shown in Fig. 43. It was already indicated in Section 5.3.2.3 that the composition and the thickness of the L4 layer might be crucial in slowing down the oxidation. In oxidized as-cast amorphous $\text{Ni}_{60}\text{Nb}_{34}\text{Sn}_3\text{B}_1$ the L4 layer is not observed, i.e. the oxide grains have well defined directional (undisturbed) growth. Even after 20 h of oxidation at T_g-50 K the oxide grains appear to reach through the Ni-richer area all the way to the interface with the bulk, forming the connection with the Nb-richer matrix and consequently bridging with the Ni-richer zone. This allows the parabolic oxidation to be preserved, unlike in the cases of the amorphous alloys with the higher Sn concentration where the continuous L4 layer is formed and the parabolic to linear oxidation kinetics transition was observed.

It should also be mentioned that B_2O_3 melts at 723 K (Fig. 62). Therefore, if formed during oxidation at 809-869 K, B_2O_3 would be volatile. It is more likely, however, that the cause of the higher oxidation rates in the B-containing composition, $Ni_{60}Nb_{34}Sn_3B_1$, than in the B-free $Ni_{59.35}Nb_{34.45}Sn_{6.2}$ and $Ni_{57}Nb_{34}Sn_9$, lies in size difference between B and Sn. In other words, due to the lower concentration of Sn, which has a sluggish mobility and presence of the highly mobile B, the oxidation resistance is lower in $Ni_{60}Nb_{34}Sn_3B_1$.

5.3.4. Oxidation of the Micro- and Nanocrystalline Ni-Nb-Sn Alloys

Similar to binary $Ni_{62}Nb_{38}$, the microcrystalline samples (equilibrium cooled and master alloys, Table 2) of the investigated ternary Ni-Nb-Sn alloys show purely parabolic oxidation (Fig. 33). In the polished cross-sections of the oxidized equilibrium cooled samples (Fig. 50) the formation of the external NiO layer and the inner zone, rich in Nb oxides, is observable. In the case of phases containing Sn (Ni_2NbSn and Ni_6Nb_7 in Table 7), beneath the Nb oxide rich zone, the Nb-depletion zone forms. It appears that oxidation takes place on the oxide-alloy interface and that the oxidation front progresses with different rates within different phases. The general observation that the amorphous compositions containing Sn oxidize slower than the amorphous binary $Ni_{62}Nb_{38}$ was earlier connected with the sluggish mobility of the large Sn atoms. This observation can be further extended to the microcrystalline structures. Among the microcrystalline samples having intermediate Sn concentrations, i.e. arc melted and equilibrium annealed samples of $Ni_{57}Nb_{34}Sn_9$ and $Ni_{59.35}Nb_{34.45}Sn_{6.2}$, the equilibrium annealed $Ni_{57}Nb_{34}Sn_9$ and $Ni_{59.35}Nb_{34.45}Sn_{6.2}$ were determined to have the highest and the worst oxidation resistance, respectively (Fig. 33). The samples with the arc melted structures of both compositions have, on the other hand, comparatively similar oxidation behavior. Since these four structures differ in more than one factor, i.e. in their compositions as well as in the structure coarseness (grain boundary density), amounts and the compositions of the specific phases (e.g. Ni_2NbSn in the arc melted compared to the same phase in the equilibrium annealed) a more detailed comparison of the oxidation behavior is not obtainable.

In the period of parabolic oxidation, amorphous samples of $Ni_{57}Nb_{34}Sn_9$ and $Ni_{59.35}Nb_{34.45}Sn_{6.2}$ have a higher k_p than the microcrystalline samples, where the highest difference, of almost an order of magnitude, can be observed for the equilibrium annealed $Ni_{57}Nb_{34}Sn_9$. The reason for this may be the more pronounced diffusivity in the amorphous structure compared to the microcrystalline structure.

The oxidation behavior of BMGs was earlier studied and compared with their microcrystalline counterparts for different systems such as the Fe-based $Fe_{61}B_{15}Zr_8Mo_7Co_5Y_2Cr_2$ (in dry air, 823 – 973 K) [48] and $Fe_{72}B_{22}Y_6$ (in dry air, at 873 - 973 K) [49]. The oxidation kinetics of both glassy

and crystalline alloys of these two Fe-based compositions generally followed parabolic laws. In $\text{Fe}_{61}\text{B}_{15}\text{Zr}_8\text{Mo}_7\text{Co}_5\text{Y}_2\text{Cr}_2$ lower oxidation resistance was observed in the glassy state compared to its microcrystalline counterpart below T_x . In contrast, for $\text{Fe}_{72}\text{B}_{22}\text{Y}_6$, better oxidation resistance was observed for the glass compared to the microcrystalline sample. This was observed to be a result of a rich B_2O_3 oxide zone in the glass compared to microcrystalline sample. Better oxidation resistance of the microcrystalline compared to amorphous structure was also found in Zr-based $\text{Zr}_{55}\text{Cu}_{30}\text{Al}_{10}\text{Ni}_5$ [75]. In this case also, different oxide phases were found in the crystalline state compared to the glass. In contrast to the amorphous samples where pure (at 573 K) or nearly pure ($T > 573$ K) tetragonal ZrO_2 was found in the oxide zone, the oxide zone on the crystalline samples as richer on Al_2O_3 and $\text{CuO/Cu}_2\text{O}$, which is believed to be responsible for the better oxidation resistance of the microcrystalline samples.

The oxidation behaviors of the nanocrystalline structures Ni28h, Ni15h, Ni19h and Nq1223K (Table 2) of the ternary $\text{Ni}_{57}\text{Nb}_{34}\text{Sn}_9$ and $\text{Ni}_{59.35}\text{Nb}_{34.45}\text{Sn}_{6.2}$ compositions are characterized in Fig. 32. The Ni28h and Ni15h samples are characterized as having structures composed of the amorphous phase with fine crystals of a Ni_2NbSn -type phase (Fig. 26). In the XRD pattern of the Ni15h sample some small reflections, which could not be assigned to any specific phase could be additionally observed at 36.86° , 47.41° , 48.32° and 57.25° . After short initial parabolic oxidation

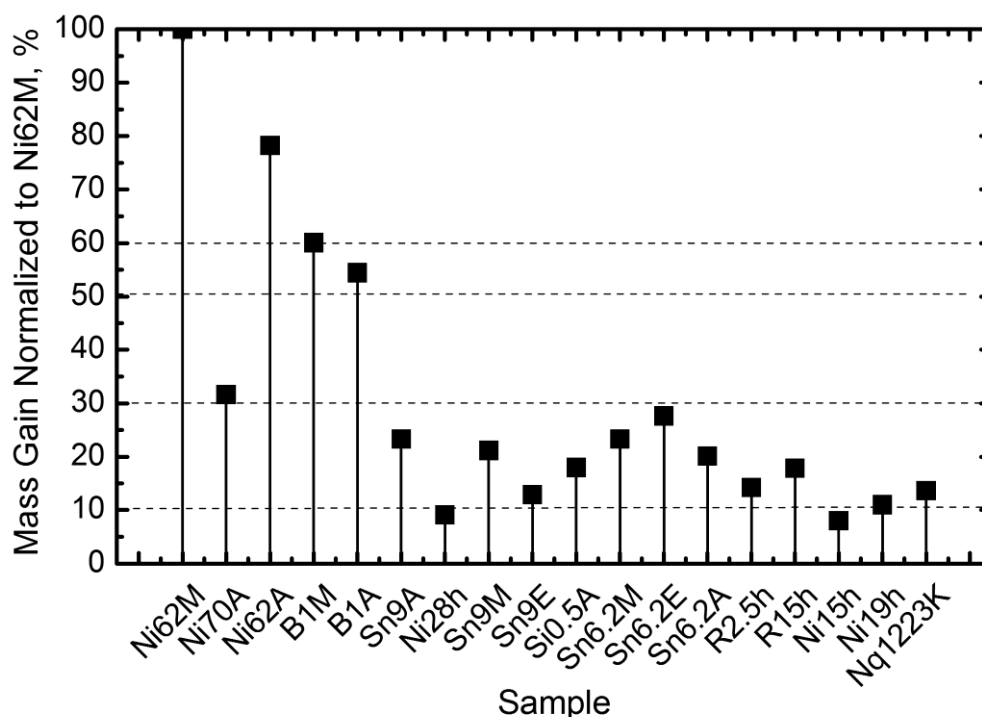


Fig. 67 The mass gain of different samples after 15h oxidation at T_g-50 K. The short names of the samples are given in Table 2. The mass gain is normalized to the microcrystalline $\text{Ni}_{62}\text{Nb}_{38}$ (Ni62M), the sample with the most intensive oxidation kinetics among all characterized samples.

these samples go into a passive period of oxidation. According to the XRD pattern of Ni19h, crystalline reflections of Ni_2NbSn , Ni_6Nb_7 and Ni_3Nb as well as the remaining amorphous halo, were observed (Fig. 26). This sample shows passivation after a short initial period of oxidation, followed by a period of linear oxidation and a new passivation afterwards (Fig. 32). The Nq1223K structure can be considered as being completely nanocrystalline, without any remaining amount of the amorphous phase, and containing Ni_2NbSn , Ni_6Nb_7 and Ni_3Nb phases (Fig. 25). This sample exhibits a purely parabolic oxidation behavior within the whole period of oxidation (Fig. 32). Generally this corresponds to the kinetic behavior observed in the microcrystalline samples (Fig. 33), except that a significantly slower oxidation rate was determined for Nq1223K (k_p in Table 8).

The mass gain observed after 15h of oxidation at $T_g-50\text{K}$, normalized to the mass gain observed on the sample with the most intense oxidation kinetics, the microcrystalline $\text{Ni}_{62}\text{Nb}_{38}$ (Ni62M), is shown in the Fig. 67. All of the samples of the ternary $\text{Ni}_{57}\text{Nb}_{34}\text{Sn}_9$ and $\text{Ni}_{59.35}\text{Nb}_{34.45}\text{Sn}_{6.2}$ compositions have mass gains only up to 30 % of the mass gain observed on the microcrystalline $\text{Ni}_{62}\text{Nb}_{38}$. Furthermore, nanocrystalline samples, especially Ni28h and Ni15h, with mass gain less than 10 % of that observed on microcrystalline $\text{Ni}_{62}\text{Nb}_{38}$, are the samples with the best oxidation resistance of all the investigated structures.

In summary, the higher oxidation resistance of the samples consisting of fine intermetallic phases within the amorphous matrix (Ni28h, Ni15h or Ni19h) compared to the as-cast amorphous structure, may be due to the fully relaxed amorphous matrix, for which lower diffusivity can be assumed. Furthermore, finely dispersed intermetallic crystallites may also influence the nucleation and growth processes. It was observed in BS images of the Ni15h sample that on the oxidized surface, different types of areas form, marked with A and B Fig. 46. It was further found from the EDX measurements that the oxygen concentration and the $X_{\text{Ni}}/X_{\text{Nb}}$, $X_{\text{Ni}}/X_{\text{Sn}}$ and $X_{\text{Nb}}/X_{\text{Sn}}$ in the Nb oxide rich zone of the areas B are very similar compositionally to those of the oxidized as-cast sample. In the areas marked with A on the other hand, a Nb oxide rich zone is O- and Nb-richer and Ni-poorer than on the as-cast sample. It might be the case here, that in the nanocrystalline Ni15h sample, a more protective Nb oxide rich zone forms, at least locally, in the areas marked with A. Additionally, in these types of nanocrystalline samples, which are composed of fine nanocrystalline phases in the remaining matrix, the content of the NbO_2 phase compared to Nb_2O_5 might be higher compared to the oxidized as-cast sample (Fig. 38a and b). This could have an influence on the properties of the oxide zone, since NbO_2 provides better protection than Nb_2O_5 . In Zr-based alloys, for example, Refs. [47,50,53] compare the oxidation behavior of the nanocrystalline and glassy states. It was found that the nanocrystalline alloys have better oxidation resistance than the amorphous due to the lower driving force for oxidation of the nanocrystalline compared to amorphous. These findings are in accord with the results reported here in Sections 4.3.1.2 and 4.3.3.2.

6. Conclusions

The main part of the research carried out in this work was focused on the characterization of the crystallization and oxidation behavior, as well as the interdependence between these two processes, in Ni-Nb(-Sn) based alloys. The following section will summarize the most important findings reported here with respect to processing, crystallization and oxidation.

1) Processing

- It was shown that the method of arc melting is a good method for alloying pure elements (Ni, Nb and Sn) into a master alloy. A positioning scheme of the pure elements on the Cu-plate was proposed, which would prevent direct contact between the Sn and the Cu and a consequent strong adhesion. This, combined with 3 to 5 times re-melting (for homogenization) results in the ingot with homogeneous structure and desired composition.
- The suction casting method was successfully applied for casting 0.5 and 1 mm thick amorphous plates of Ni-Nb and Ni-Nb-Sn based samples.

2) Amorphous Phase and Crystallization

- Upon the equilibrium solidification, three types of phases were identified: orthorhombic Ni_3Nb , hexagonal Ni_6Nb_7 and the fcc Ni_2NbSn . The primary Ni_3Nb phase is a Sn-free phase while the Ni_6Nb_7 contains 5 and 7 at.% Sn in $\text{Ni}_{59.35}\text{Nb}_{34.45}\text{Sn}_{6.2}$ and $\text{Ni}_{57}\text{Nb}_{34}\text{Sn}_9$, respectively. The Ni_2NbSn -type phase is formed with a composition close to the stoichiometric values (50 at.% Ni, 25 at.% Nb and 25 at.% Sn), i.e. 53 at.% Ni, 25 at.% Nb and 22 at.% Sn in $\text{Ni}_{59.35}\text{Nb}_{34.45}\text{Sn}_{6.2}$ and 56 at.% Ni, 23 at.% Nb and 21 at.% Sn in $\text{Ni}_{57}\text{Nb}_{34}\text{Sn}_9$.
- When faster cooling rates were applied, as in the case of solidification on a water cooled Cu-plate (arc melted structure), the three equilibrium phases are still identified, but a much finer grained structure has formed, especially in the case of the Sn-richer composition ($\text{Ni}_{57}\text{Nb}_{34}\text{Sn}_9$ compared to $\text{Ni}_{59.35}\text{Nb}_{34.45}\text{Sn}_{6.2}$). Ni_3Nb and Ni_6Nb_7 form with

the same compositions as in the equilibrium annealed structures. The composition of Ni_2NbSn changes significantly with increasing the cooling rate, e.g. from 53 at.% Ni, 25 at.% Nb and 22 at.% Sn in the equilibrium annealed $\text{Ni}_{59.35}\text{Nb}_{34.45}\text{Sn}_{6.2}$ to 35 at.% Ni, 49 at.% Nb and 16 at.% Sn in the arc melted structure of the same composition.

- The as-cast amorphous phase of the suction casted 1 mm thick plates was characterized with the XRD and the APT. Within the resolution of these two methods, it was shown that the amorphous phase is homogeneous, without any signs of phase separation or formation of crystalline phases.
- The crystallization of the amorphous Ni-Nb-Sn phase, upon heating with the constant heating rate of 0.33 K/s, begins with the primary crystallization of Ni_2NbSn . The next phase to form is Ni_3Nb . In the later stages of the thermal treatment the metastable η and the stable Ni_6Nb_7 phases form.

3) Oxidation

The oxidation behavior of amorphous binary ($\text{Ni}_{70}\text{Nb}_{30}$ and $\text{Ni}_{62}\text{Nb}_{38}$), ternary ($\text{Ni}_{59.35}\text{Nb}_{34.45}\text{Sn}_{6.2}$ and $\text{Ni}_{57}\text{Nb}_{34}\text{Sn}_9$) and quaternary ($\text{Ni}_{58.85}\text{Nb}_{34.45}\text{Sn}_{6.2}\text{Si}_{0.5}$ and $\text{Ni}_{60}\text{Nb}_{36}\text{Sn}_3\text{B}_1$) Ni-Nb(-Sn) base alloys was characterized under dry oxygen flow, below the glass transition temperature. For comparison, microcrystalline and nanocrystalline structures of some of the above compositions have also been characterized. The following conclusions could be made:

- All characterized ternary and quaternary compositions containing Sn show considerably lower mass gain within 15h of oxidation at T_g-50 K compared to the binary Ni-Nb alloy with the same $X_{\text{Ni}}/X_{\text{Nb}}$. This implies that the sluggish mobility of the large Sn atoms plays an important role in the improvement of the oxidation resistance in the Ni-Nb(-Sn) alloys compared to the binary Ni-Nb
- At T_g-50 K, the as-cast amorphous structures of $\text{Ni}_{59.35}\text{Nb}_{34.45}\text{Sn}_{6.2}$, $\text{Ni}_{57}\text{Nb}_{34}\text{Sn}_9$ and $\text{Ni}_{58.85}\text{Nb}_{34.45}\text{Sn}_{6.2}\text{Si}_{0.5}$ obey a parabolic law of oxidation. All microcrystalline samples of different compositions as well as the as-cast amorphous binary $\text{Ni}_{62}\text{Nb}_{38}$ and the quaternary $\text{Ni}_{60}\text{Nb}_{36}\text{Sn}_3\text{B}_1$ obey parabolic laws of oxidation within the whole period of oxidation also at T_g-50 K. The formation of a Ni-rich layer between

the bulk and the oxide layer have been shown to play an important role in the transition from parabolic to linear oxidation behavior.

- The fully relaxed amorphous phase appears to be more oxidation resistant, due to its apparent slower atomic mobility (lower diffusivity).
- All studied nanocrystalline structures of the ternary $\text{Ni}_{59.35}\text{Nb}_{34.45}\text{Sn}_{6.2}$ and $\text{Ni}_{57}\text{Nb}_{34}\text{Sn}_9$ have shown to have significantly lower oxidation rates compared to their microcrystalline and amorphous counterparts at T_g-50 K. This is possibly the result of the formation of a more protective Nb oxide rich scale.

Appendix

A1. Suction Casting - Experimental Difficulties

After re-melting master alloys by arc melting and suction casting into specimens as described in Section 3.1. the suction cast specimens were, in some cases, not completely amorphous but were observed to have a few crystalline features embedded in an amorphous matrix. In the following, the microstructure of one of such casting is described.

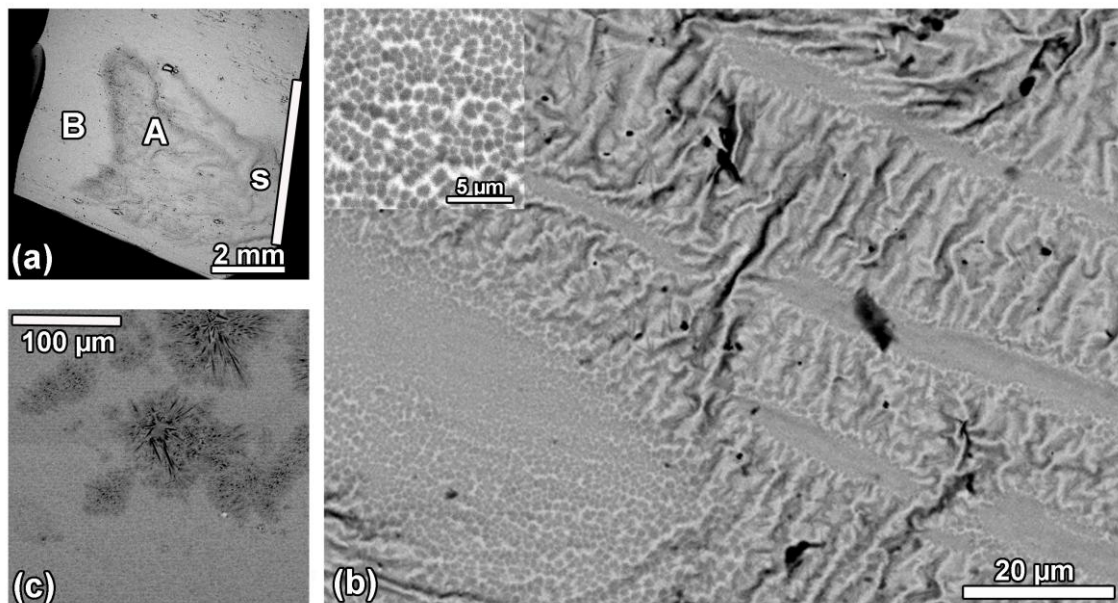


Fig. A1 a) Overview taken from the as-cast surface of the $\text{Ni}_{59.35}\text{Nb}_{34.45}\text{Sn}_{6.2}$ plates. Suction casting was performed after the melting chamber was prepared by three evacuations to 10^{-1} mbar and back filling with Ar 4.6. Two types of areas, marked with A and B can be distinguished in this overview: b) the BS image of the zone A with a detail under high magnification in its upper right corner; c) the BS image of the polished cross-section taken along line *s*, as marked in a.

The atmosphere of the melting chamber was prepared by three evacuations to 10^{-1} mbar and back filling with Ar 4.6 (purity $\geq 99.996\%$). The final condition in the chamber was 0.2 bar overpressure with Ar 4.6. The residual oxygen in the atmosphere was gettered by melting a piece of Ti placed in a separate impression of the Cu-plate. After the Ti re-solidified, it was visually observed that its surface was metallic, with no indications of oxidation. This was an indication of the low oxygen content in the chamber. An overview of the as-cast surface of the $\text{Ni}_{59.35}\text{Nb}_{34.45}\text{Sn}_{6.2}$ plate is shown in Fig. A1a. Two types of morphologies, marked with A and B in Fig. A1a, can be noticed. The areas marked B appear flat but the morphology of the areas A is more complex, as it can be seen under higher magnification of the area A in Fig. A1b. First, the as-cast surface in the area A appears to be wrinkled. Secondly, two different types of phases can be differentiated. This consists of fine spherical particles having a darker contrast, about $1\ \mu\text{m}$ in diameter, embedded in a brighter matrix (*inset* in Fig. A1b). The cross-section taken across area A, as indicated with the line s in Fig. A1a is shown in Fig. A1c. The upper edge of the Fig. A1c corresponds to the plate surface. Two different contrasts can be observed: a dark phase with strongly faceted morphology and two finer phases with the brighter contrasts.

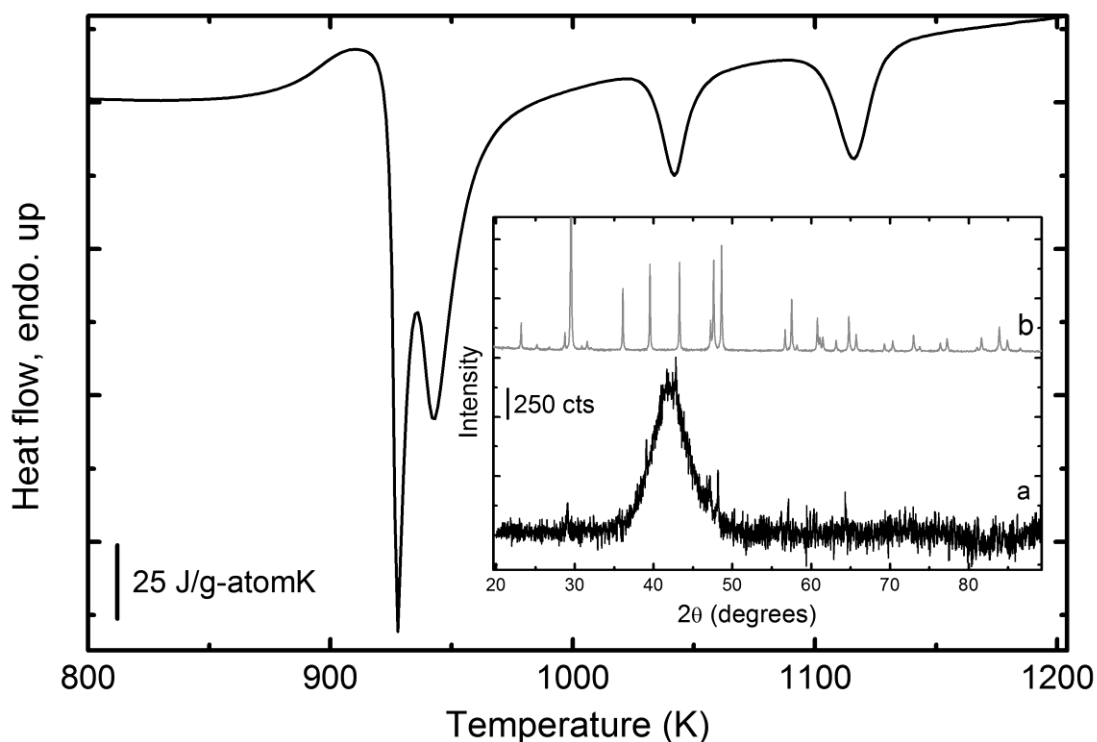


Fig. A2 Thermogram of the specimen from area B measured with a heating rate of 0.33 K/s, as indicated in Fig. A1a. *Inset (a)* is the XRD pattern taken from the polished surface of the same specimen before the calorimetric measurement and the (b) holding putty material.

One specimen was cut-off from the region B of Fig. A1a. After grinding the surface with 320 and 600 SiC grinding paper, XRD was performed followed by a calorimetric measurement under

constant heating rate of 0.33 K/s up to 1200 K (Fig. A2). From the thermogram shown in Fig. A2, the values of T_g , T_x and ΔH_x were determined to be 878 K, 924 K and 5.0 kJ/g-atom, respectively. These values correspond to those obtained from the fully amorphous plates of the same composition (Table 4). The XRD pattern (*inset* in the Fig. A2) shows a typical amorphous halo. In addition to the amorphous halo, small crystalline reflections (at $2\theta = 29.2, 35.8, 39.0, 42.9, 47.1$ and 48.2°) correspond to the reflections of the putty used as the sample holder. This is also, in addition to results of the calorimetric measurement, an indication that the observed crystalline phases had formed only locally (i.e., in areas A of Fig. A1a).

A2. Gibbs Free Energy Functions and Coefficients

The phase diagram and the thermodynamic properties of the binary Ni-Nb system were modeled in Ref. [27] using the Calculation of Phase Diagrams (CALPHAD) method [76–80]. In multicomponent systems, the Gibbs free energy of each phase, G^ϕ , can be described as:

$$G^\phi = {}^{ref}G^\phi + {}^{id}G^\phi + {}^{ex}G^\phi. \quad (A1)$$

${}^{ref}G^\phi$ represents the Gibbs free energy contributions of the mechanical mixture of the pure elements. ${}^{id}G^\phi$ corresponds to the Gibbs free energy of mixing of the ideal solution ($\Delta H_{mix} = 0$), i.e. it contains only the contribution of the ideal entropy of mixing, $\Delta {}^{id}S_{mix}$. ${}^{ex}G^\phi$ is the excess Gibbs free energy term, which contains the contributions from interatomic interactions and defines the phase as a regular solution ($\Delta H_{mix} \neq 0$). The expressions used for the three above mentioned parts of the Gibbs free energy, G^ϕ , in the binary Ni-Nb system are:

$${}^{ref}G^\phi = X_{Ni}G_{Ni} + X_{Nb}G_{Nb} \quad (A2)$$

$${}^{id}G^\phi = RT(X_{Ni} \ln X_{Ni} + X_{Nb} \ln X_{Nb}) \quad (A3)$$

$${}^{ex}G^\phi = A_1 X_{Ni} X_{Nb} + A_2 X_{Ni} X_{Nb} (X_{Ni} - X_{Nb}) + BTX_{Ni} X_{Nb} + CT^{-1} X_{Ni} X_{Nb}. \quad (A4)$$

G_{Ni} and the G_{Nb} are the Gibbs free energies of Ni and Nb in their reference states, respectively. X_{Ni} and X_{Nb} are the molar fractions of Ni and Nb, respectively. The constants A_1 , A_2 , B and C are the excess term parameters. The temperature dependence of the Gibbs free energies for different phases and the values of the parameters A_1 , A_2 , B and C , which were applied in Eqs. (A1-A4), are shown below:

$$G_{Nb}^{bcc} = -7254 + 100T + 23.73T(1 - \ln T) - 0.00402 \left(\frac{T^2}{2} \right) \quad (A5)$$

$$G_{Nb}^{fcc} = 14745 + 97.8T + 23.73T(1 - \ln T) - 0.00402 \left(\frac{T^2}{2} \right) \quad (A6)$$

$$G_{Ni}^{bcc} = -3393 + 140.7T + 29.73(1 - \ln T) - 0.00417 \left(\frac{T^2}{2} \right) + 933660 \left(\frac{1}{2T} \right) \quad (A7)$$

$$G_{Ni}^{fcc} = -10882 + 143.2T + 29.73T(1 - \ln T) - 0.00417 \left(\frac{T^2}{2} \right) + 9336600 \left(\frac{1}{2T} \right) \quad (A8)$$

$$G_{Nb}^{Ni_6Nb_7} = 101200 + 84.9T + 23.73T(1 - \ln T) - 0.00402 \left(\frac{T^2}{2} \right) \quad (A9)$$

$$G_{Ni}^{Ni_6Nb_7} = 76200 + 141.0T + 29.73T(1 - \ln T) - 0.00417 \left(\frac{T^2}{2} \right) + 933660 \left(\frac{1}{2T} \right) \quad (A10)$$

$$G_{Nb}^{Ni_3Nb} = 1052100 + 88.7T + 23.73T(1 - \ln T) - 0.00402 \left(\frac{T^2}{2} \right) \quad (A11)$$

$$G_{Ni}^{Ni_3Nb} = 98200 + 141.0T + 29.73T(1 - \ln T) - 0.00417 \left(\frac{T^2}{2} \right) + 933660 \left(\frac{1}{2T} \right) \quad (A12)$$

$$G_{Nb}^{amorphous} - G_{Nb}^{bcc} = 22010 - 6.3T \quad (A13)$$

$$G_{Ni}^{amorphous} - G_{Ni}^{fcc} = 14190 - 7.4T \quad (A14)$$

Table A1 The excess term parameters used in Eq. (A4)

Parameter	bcc	fcc	Ni ₆ Nb ₇	Ni ₃ Nb	amorphous
A ₁	-57900	-27100	-488500	-2.006·10 ⁶	-158200
A ₂	0	13500	0	0	32700
B	26.0	-40.5	63.0	70.3	62.8
C	0	0	0	0	0

A3. XRD Pattern of Different Phases

Identification of crystalline phases in XRD patterns of different specimens was conducted according to the information obtained from the database of the X'Pert HighScore Plus Software, Version 2.2.3 (2007). The XRD patterns of crystalline phases identified in the samples throughout this work are shown in *Fig. A3*. In the upper right corner of each XRD pattern in *Fig. A3*, the number of the PDF card (PDF-Nr.) and the chemical formula of the crystalline phase to which the pattern belongs are shown. The available database does not contain the XRD pattern of the Ni₂NbSn-type phase. The 2θ positions of the characteristic crystalline reflections of the Ni₂NbSn-type phase were taken from the indexed XRD patterns of the Ni-Nb-Sn master alloys published in Ref. [10].

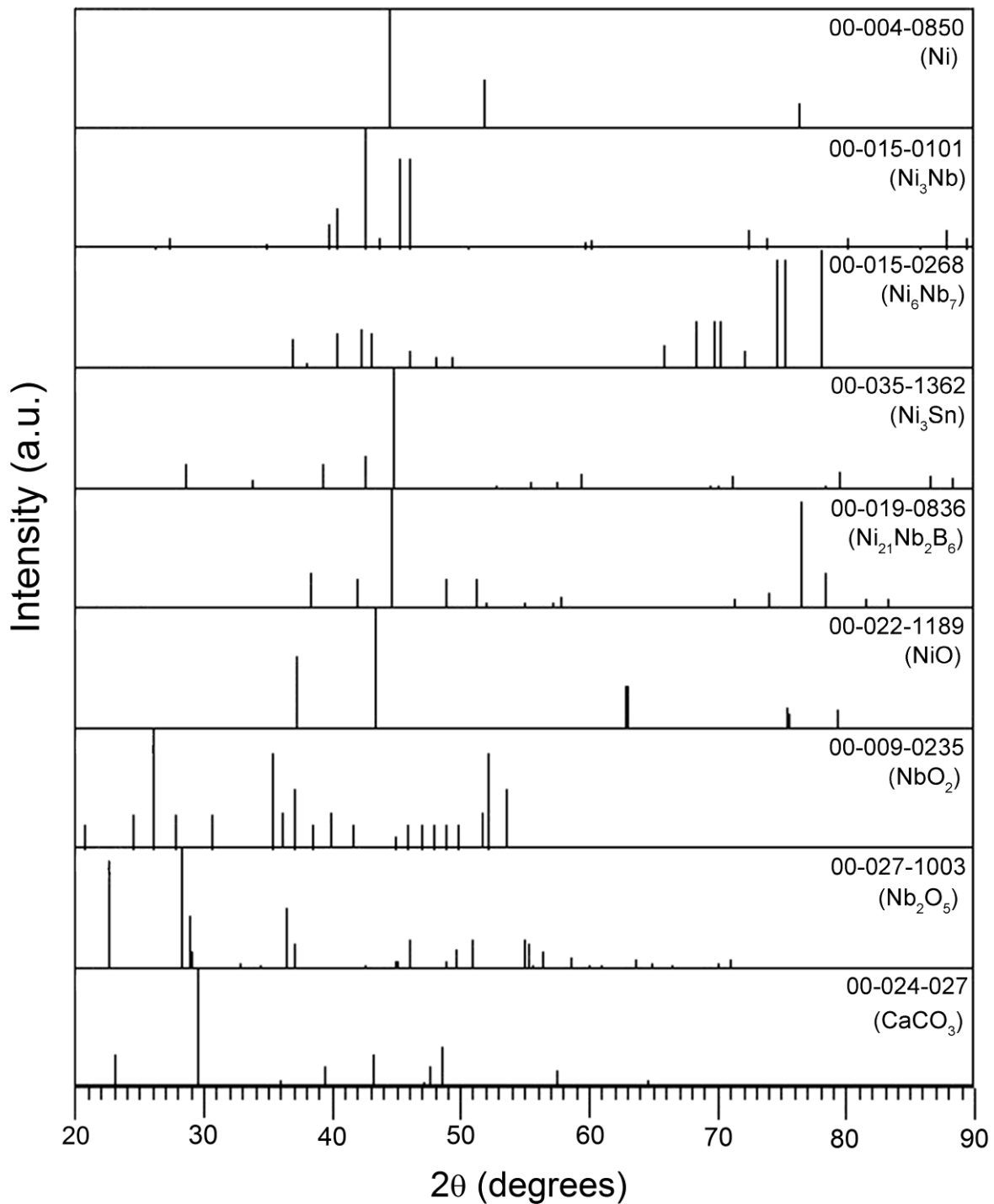


Fig. A3 XRD patterns of crystalline phases taken from the database of X'Pert HighScore Plus Software. In the upper right corner of each XRD pattern the PDF-Nr and the chemical formula of the crystalline phase, to which the pattern belongs are shown.

A4. XRD Pattern of the Oxidized $\text{Ni}_{59.35}\text{Nb}_{34.45}\text{Sn}_{6.2}$ Alloy

The XRD patterns taken from the oxidized samples of the $\text{Ni}_{59.35}\text{Nb}_{34.45}\text{Sn}_{6.2}$ composition with different starting structures are shown in Figs. A4 - A7. All samples were isothermally oxidized in dry oxygen at 831 K. Nb_2O_5 , NbO_2 and NiO are the identified oxide phases. The intensities of the NbO_2 reflections are most pronounced on the surfaces of the oxidized nanocrystalline Ni15h and Ni19h. In addition to the oxide phases, the intermetallic Ni_3Nb and Ni_3Sn phases are observed in Figs. A4 - A7. Indications of the Ni_2NbSn reflections are also found on the oxidized surface of the Nq1223K sample. In some cases reflections of CaCO_3 , which is a component of the putty used as a sample holder, were observed.

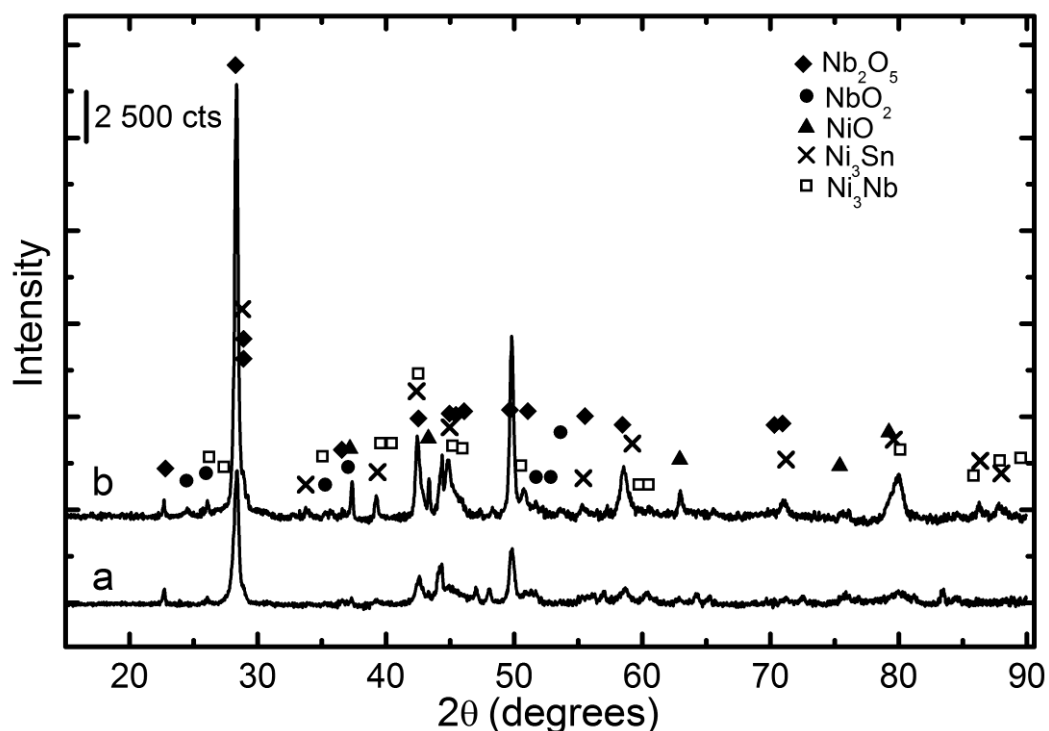


Fig. A4 XRD patterns made on the oxidized surfaces of the as-cast amorphous $\text{Ni}_{59.35}\text{Nb}_{34.45}\text{Sn}_{6.2}$ alloy after oxidation at 831 K for: **a)** 2.5 h and **b)** 19 h. The curves are for better comparison shifted vertically.

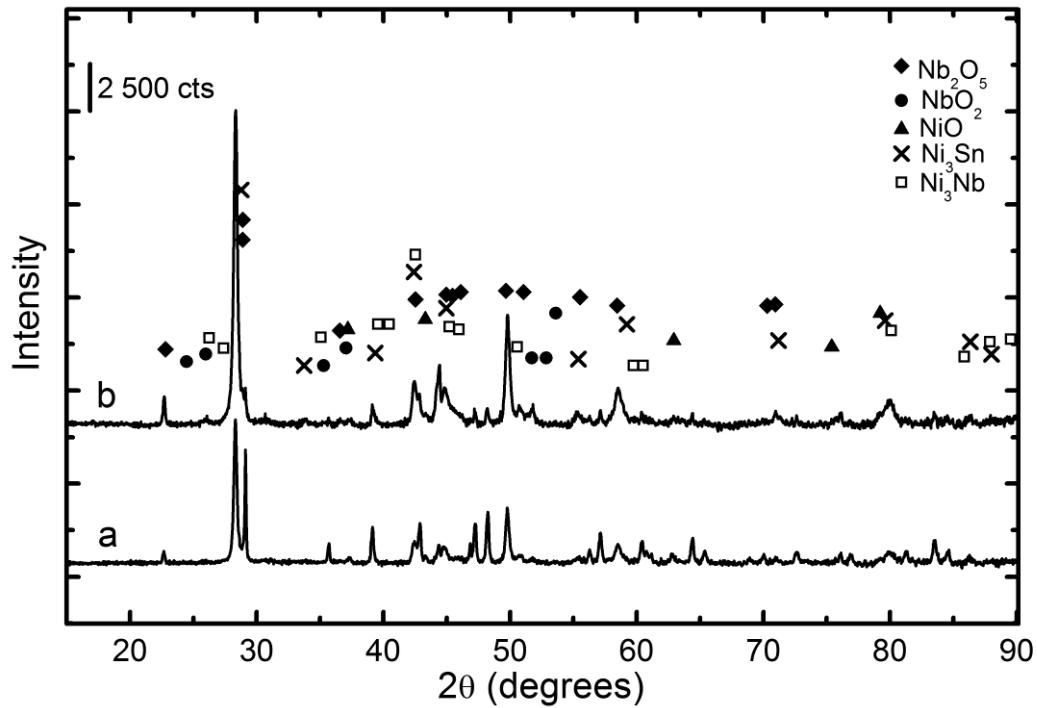


Fig. A5 XRD patterns made on the oxidized surfaces of the: (a) R2.5h and (b) R19h (see Table 2). Samples were oxidized at 831 K for 19 h. The curves are shifted vertically.

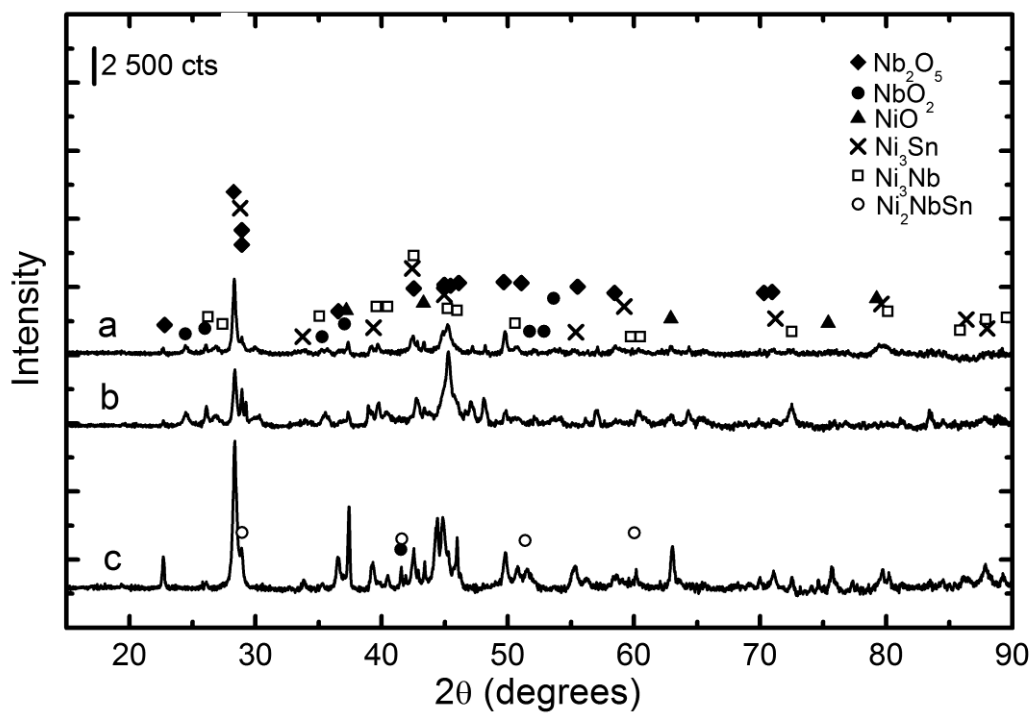


Fig. A6 XRD patterns made on the oxidized surfaces of the: (a) Ni15h, (b) Ni19h and (c) Nq1223K (Table 2). Oxidation was performed at 831 K for 19 h. The curves are vertically shifted.

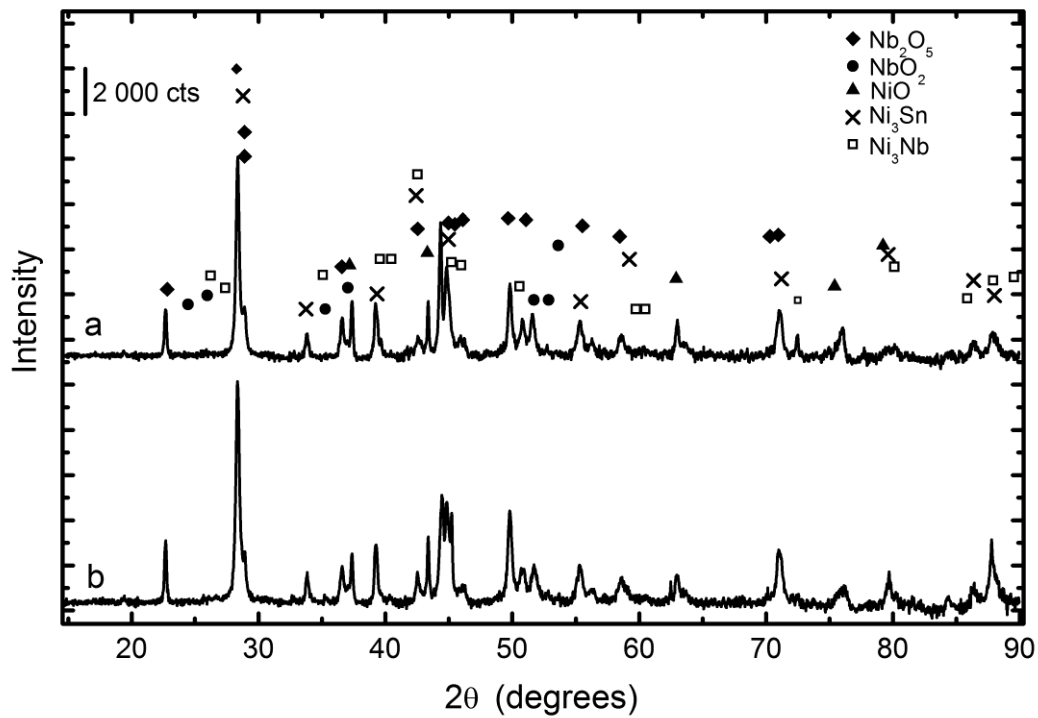


Fig. A7 XRD patterns made on the oxidized surfaces of the (a) master alloy and (b) equilibrium cooled specimen. Oxidation was performed at 831 K for 19 h. The curves are vertically shifted.

A5. Overview on E_a of Various Processes

In Table A2, the values of E_a for different diffusion controlled processes, such as diffusion in Ni- and Nb-oxides, as well as diffusion processes in different crystalline materials containing Ni, Nb or Sn, are tabulated. Descriptions of diffusion processes and the temperature intervals for which the E_a were determined (third column in Table A2) are given in the first and the second column, respectively. Some additional remarks and publications from which the values originate are given in the fourth and the fifth columns, respectively.

Table A2 Activation energies determined for different diffusion processes along with a corresponding temperature ranges, additional remarks and references

<i>Process</i>	<i>Temperature range (K)</i>	<i>Activation energy (kJ/mol)</i>	<i>Remarks</i>	<i>Ref.</i>
<i>Ni lattice self-diffusion in NiO</i>	793-1673	247		[36]
<i>Ni diffusion in NiO dislocations</i>	795-1073	192		
<i>Ni grain boundary diffusion in NiO</i>	Temperature independent	171		
<i>Oxygen self-diffusion in single crystal NiO</i>	1473-1873	540		
<i>Oxygen diffusion in Nb₂O_{4.978}</i>	773-1173	118.1		[81]
<i>Nb diffusion in NbO</i>	1173-1373	123.9		
<i>Nb diffusion in Nb₂O₄ and Nb₂O₅</i>	1173-1373	217.7-221.9		
<i>Ni diffusion in Nb oxide</i>	549-996	195		[82]
<i>Ni lattice self-diffusion. in Ni</i>	748-923	279.7		

<i>Process</i>	<i>Temperature range (K)</i>	<i>Activation energy (kJ/mol)</i>	<i>Remarks</i>	<i>Ref.</i>
<i>Ni grain boundary diffusion in Ni</i>		114.7		
<i>Volume diffusion of Nb in Nb</i>	1273 and 1276	401.7	<i>Diffusive transport is proportional to dislocation density including the subgrain boundary dislocation density</i>	
<i>Sn diffusion in polycrystalline Nb</i>	2123-1233	302.1		[83]
<i>Sn diffusion in polycrystalline Ni</i>	1373-973	248.4		
<i>Grain boundary diffusion of Sn in Ni</i>	973-1373	128.7	<i>For diffusion of Sn in Ni-Sn, 0.42 at % Sn had drastically reduced self-diffusivity at 873 K [84]</i>	
<i>NiO oxide growth on pure nanocrystalline Ni</i>	973-1173	108	<i>In good agreement with Ni grain boundary diffusion, as determined in the same study to be 103.1 kJ/mol for nanocrystalline Ni</i>	[38]
<i>Oxidation of pure Nb</i>	773-1073 K	37.6-41.8		[85]
<i>Oxidation of Ni₃Nb</i>	873-1073	159.1		[41]
<i>Diffusion in Ni₆Nb₇ phase</i>	1200-1450	271	<i>Activation energy for interdiffusion</i>	[86]
		319		
	1323-1423	321	<i>Activation energy for intrinsic Ni diffusion. The Ni atoms diffuse faster than the Nb atoms</i>	[87,88]
		315	<i>Activation energy for intrinsic Nb diffusion</i>	

Reference List

- [1] Klement W, Willens RH, Duwez P. *Nature* 1960;187:869.
- [2] Peker A, Johnson WL. *Appl Phys Lett* 1993;63:2342.
- [3] Choi-Yim H, Xu D, Johnson WL. *Appl Phys Lett* 2003;82:1030.
- [4] Choi-Yim H, Xu D, Lind ML, Löffler JF, Johnson WL. *Scripta Mater* 2006;54:187.
- [5] Choi-Yim H, Xu D, Johnson WL. *Mater Sci Eng A* 2007;449-451:134.
- [6] Gorman BP, Puthucode A, Diercks DR, Kaufman MJ. *Mater Sci Technol* 2008;24:682.
- [7] Mukherjee S, Zhou Z, Johnson WL, Rhim W-K. *J Non-Cryst Solids* 2004;337:21.
- [8] Shadowspeaker L, Busch R. *Appl Phys Lett* 2004;85:2508.
- [9] Xie G, Li S, Louzguine-Luzgin DV, Cao Z, Yoshikawa N, Sato M, Inoue A. *Metall Mater Trans A* 2010;41A:1714.
- [10] Zhang L, Zhuo M-J, Xu J. *J Mater Res* 2008;23:688.
- [11] Kim YJ, Busch R, Johnson WL, Rulison AJ, Rhim WK. *Appl Phys Lett* 1994;65:2136.
- [12] Peker A, Johnson WL. *Appl Phys Lett* 1993;63:2342.
- [13] Xu D, Johnson WL. *Phys Rev B* 2006;74.
- [14] Schroers J, Johnson WL, Busch R. *Appl Phys Lett* 2000;77:1158.
- [15] Inoue A, Nishiyama N, Kimura H. *Mater T JIM* 1997;38:179.
- [16] Xia L, Li WH, Fang SS, Wei BC, Dong YD. *J Appl Phys* 2006;99:026103.
- [17] Zhang W, Inoue A. *Scripta Mater* 2003;48:641.
- [18] Turnbull D, Cech RE. *J Appl Phys* 1950;21:804.
- [19] Porter DA, Easterling KE. *Phase Transformations in Metals and Alloys*, second ed. Chapman & Hall; 1992.
- [20] Inoue A. *Acta Mater* 2000;48:279.
- [21] Johnson WL. *Prog Mater Sci* 1986;30:81.
- [22] Faupel F, Frank W, Macht M-P, Mehrer H, Naundorf V, Rätzke K, Schober HR, Sharma S, Teichler H. *Rev Mod Phys* 2003;75:237.
- [23] Kelton KF, Greer AL. *Nucleation in Condensed Matter*. Elsevier; 2010.
- [24] TAPP, Thermochemical and Physical Properties, Software Package, E. S. Microware, Hamilton, OH; 1991.
- [25] Sprengel W, Denking M, Mehrer H. *Intermetallics* 1994;2:127.
- [26] Chen H, Du Y. *Calphad* 2006;30:308.
- [27] Busch R. *Thermodynamische Beschreibung Von Phasentransformationen Metastabiler NbNi- Und NbCo-Legierungen*. Der Georg-August-Universität zu Göttingen, 1988.
- [28] Collins L, Grant N, Sande J. *J Mater Sci* 1983;18:804.
- [29] Shoemaker CB, Shoemaker DP. *Acta Cryst* 1967;23:231.
- [30] Bergmann H, Fritsch H, Hunger G. *J Mater Sci* 1981;16:1935.

- [31] Gallino I, Busch R, Yim HC, Jastrow L, Köster U. *J Alloy Compd* 2007;434-435:225.
- [32] Khanna AS. *Introduction to High Temperature Oxidation and Corrosion*. ASM International; 2002.
- [33] Scully JC. *The Fundamentals of Corrosion*, third ed. Pergamon Press; 1990.
- [34] McNallan M and ESM and ESHTMD and ESCD. *High Temperature Corrosion and Materials Chemistry*. Electrochemical Society; 2000.
- [35] Kubaschewski O, Hopkins BE. *Oxidation of Metals and Alloys*, second ed. London: Butterworth and Co; 1962.
- [36] Kofstad P. *High Temperature Corrosion*. Elsevier Applied Science; 1988.
- [37] Khoi N, Smeltzer W. *J Electrochem Soc* 1975;122.
- [38] Rashidi AM. *Surf Coat Tech* 2011;205:4117.
- [39] Gmelin L. *Gmelins Handbuch Der Anorganischen Chemie*, eight ed. Verlag Chemie; 1965.
- [40] Niu Y, Gesmundo F, Viani F, Rizzo F. *Corros Sci* 1995;37:2043.
- [41] Arbuzov MP, Chuprina VG. *Izv VUZ Fiz+* 1969;12:75.
- [42] Miller C, Simmons G, Wei R. *Scripta Mater* 2000;42:227.
- [43] Caron A, Qin CL, Gu L, González S, Shluger A, Fecht H-J, Louzguine-Luzgin D V, Inoue A. *Nanotechnology* 2011;22:095704.
- [44] Gallino I, Shah MB, Busch R. *Acta Mater* 2007;55:1367.
- [45] Kai W, Kao PC, Lin PC, Ren IF, Jang JSC. *Intermetallics* 2010;18:1994.
- [46] Liu L, Chan KC. *Appl Phys A-Mater* 2005;80:1737.
- [47] Triwikantoro. *Oxidation Metallener Gläser Auf Zr-Basis*. Technische Universität Dortmund, 2001.
- [48] Kai W, Ren LF, Kao PC, Huang RT, Liu CT. *Intermetallics* 2009;17:205.
- [49] Hsieh HH, Kai W, Huang RT, Lin CY, Chin TS. *Intermetallics* 2006;14:917.
- [50] Köster U, Triwikantoro. *Mater Sci Forum* 2001;360-362:29.
- [51] Dark AM, Wei G, Cantor B. *Mater Sci Eng* 1988;99:533.
- [52] Wei G, Candor B. *Acta Metall Mater* 1988;36:167.
- [53] Köster U, Zander D. *Mater Sci Forum* 2000;343-346:203.
- [54] Russ J. *Practical Stereology*. Plenum Press; 1986.
- [55] Underwood E. *Quantitative Stereology*. Addison-Wesley Publishing Company; 1970.
- [56] Delesse A. *Comptes Rendus Hebdomadaires des Sciences de L'Academie de Sciences* 1947;25:544.
- [57] Gault B, Moody M, Cairney J, Ringer S. *Atom Probe Microscopy*. Springer; 2012.
- [58] Spieß L, Teichert G, Schwarzer R, Behnken H, Genzel C. *Moderne Röntgenbeugung*, second ed. Wiesbade: Vieweg+Teubner; 2009.
- [59] G.W.H.Höhne, W.F.Hemminger H-JF. *Differential Scanning Calorimetry*, second ed. Springer Verlag; 2003.

- [60] Takeuchi A, Inoue A. *Mater Trans* 2000;41:1372.
- [61] Saunders N, Miodownik AP. *J Phase Equilib* 1990;11:278.
- [62] Ichitsubo T, Matsubara E, Fujiwara K, Yamaguchi M, Irie H, Kumamoto S, Anada T. *J Alloy Compd* 2005;392:200.
- [63] Skolozdra R V., Okhrimovich KO. *Russ Metall* 1971;6:135.
- [64] Chase MW. *NIST-JANAF Thermochemical Tables*, fourth ed. American Chemical Society; 1998.
- [65] Barin I. *Thermochemical Data of Pure Substances Part I, II*. Wiley-VHC; 1989.
- [66] Gesmundo F, Viani F, Niu Y. *Oxid Met* 1994;42:409.
- [67] Gesmundo F, Niu Y, Viani F. *Oxid Met* 1995;43:379.
- [68] Gesmundo F, Niu Y, Viani F, Rizzo FC. *Oxid Met* 1996;46:441.
- [69] Cense WA, Klerk M, Albers W. *J Mater Sci* 1977;12:2184.
- [70] Song Z, Tan D, He F, Bao X. *Appl Surf Sci* 1999;137:142.
- [71] Köster U, Meinhardt J. *Mater Sci Eng A* 1994;178:271.
- [72] Köster U, Meinhardt J, Roos S, Liebertz H. *Appl Phys Lett* 1996;69:179.
- [73] Fadeeva VI, Kubalova LM, Sviridov IA. *Steel Transl* 2011;41:451.
- [74] Kubalova LM, Fadeeva VI, Sviridov IA, Fedotov SA. *J Alloy Compd* 2009;483:86.
- [75] Kai W, Hsieh HH, Nieh TG, Kawamura Y. *Intermetallics* 2002;10:1265.
- [76] Katter UR. *JOM* 1997;49:14.
- [77] Wanqi J, Ruijie Z, Zhi H. *Mater Sci Eng A* 2005;413-414:497.
- [78] Schmid-Fetzer R, Andersson D, Chevalier PY, Eleno L, Fabrichnaya O, Kattner UR, Sundman B, Wang C, Watson A, Zabdyr L, Zinkevich M. *CALPHAD* 2007;31:38.
- [79] Palumbo M, Battezzati L. *CALPHAD* 2008;32:295.
- [80] Kroupa A. *Comp Mater Sci* 2013;66:3.
- [81] Harrop P. *J Mater Res* 1968;3:206.
- [82] Wazzan AR. *J Appl Phys* 1965;36:3596.
- [83] Kaur I, Gust W, Kozma L. *Handbook of Grain and Interphase Boundary Diffusion Data*. Ziegler Press; 1989.
- [84] Padgett R, White C. *Scr Metall*;1984;18:459.
- [85] Bridges DW, Fassell WM. *J Electrochem Soc* 1956;103:326.
- [86] Sprengel W, Denkinge, Martin, Mehrer H. *Intermetallics* 1994;2:137.
- [87] Balam, S., S. K, Ravi R, Paul A. *Defect Diffus Forum* 2012;323-325:497.
- [88] Balam SSK, Dong HQ. *Metall Mater Trans A* 2011;42A:1727.